

STAVEBNÍ OBZOR

ČÍSLO 4/2017

Obsah čísla:

PHYSICAL AND MECHANICAL CHARACTERISTICS OF BUILDING MATERIALS OF HISTORIC BUILDINGS <i>Jiří Witzany, Radek Zigler, Tomáš Čejka, Pavel Pospíšil, Milan Holický, Jan Kubát, Aneta Maroušková, Klára Kroftová</i>
STUDY ON DE-NOISING METHODS FOR SOIL COMPRESSIVE STRESS SIGNAL DURING VIBRATION COMPACTION <i>Qingzhe Zhang, Meng Ji, Qian Zhang, Zhi Qin</i>
STUDY ON THE INFLUENCE OF BOLT ANCHORED CATENARY ON TUNNEL LINING UNDER THE AERODYNAMIC LOAD <i>Zhong-xin Ren, Hong Guo, Yong-tao Su</i>
INFLUENCE OF GLASS POWDER AND STEEL SLAG ON PROPERTIES OF CONCRETE: A REVIEW <i>Sajjad Ali, Zia ur Rahman, Muhammad Kamran Khan</i>
STUDY ON ANTI-CRACKING PERFORMANCE EVALUATION METHOD OF STEEL FIBER REINFORCED CERAMITE CONCRETE (SFRCC) BASED ON PARTLY-RESTRAINED SHRINKAGE RING <i>Zhang Yi-fan</i>
EXPERIMENTAL AND NUMERICAL INVESTIGATION OF BLASTING-INDUCED GROUND VIBRATION FROM TUNNEL UNDERCROSSING A VILLAGE <i>Fan Haobo, Yu Deqiang, Zhao Dongping, Lai Jinxing, Xie Yongli</i>
PROGRESSIVE COLLAPSE ANALYSIS OF 2-D RC FRAMES USING AEM <i>Osama El-Mahdy, El-Sayed El-Kasaby, Hala Abusaf, Amr El-Gamal</i>
FAULT-RELATED INSTABILITY PROBLEMS OF TUNNELS – THE HOST ROCK SLIP CRITERION AND CHARACTERISTICS OF THE TUNNELING-INDUCED SHEAR DISPLACEMENTS <i>Jian-guo Liu, Xiao-jun Zhou, Qing-hua Xiao, Wei Zhao</i>
DESIGN OF AN ACTIVE LOW FREQUENCY VIBRATION ISOLATION SYSTEM FOR ATOM INTERFEROMETRY BY USING SLIDING MODE CONTROL <i>Dong-Yun Luo, Bing Cheng, Bin Wu, Xiao-Long Wang, Qiang Lin</i>
INPUT DATA OF BURNING WOOD FOR CFD MODELLING USING SMALL-SCALE EXPERIMENTS <i>Petr Hejtmánek, Libor Ševčík, Kamila Cábová</i>
RELATIONSHIP BETWEEN FOAMING BEHAVIOR AND SURFACE ENERGY OF ASPHALT BINDER <i>Jian-ping Xu, Kai Zhang, Yao-ting Zhu</i>
NUMERICAL SIMULATION OF ULTRASONIC DETECTION FOR CONCRETE STRUCTURE BASED ON EQUIVALENT OFFSET MIGRATION <i>Mingshun Hu, Juanjuan Li, Dongming Pan, Shenen Chen</i>
A MECHANISTIC-EMPIRICAL IMPACT ANALYSIS OF DIFFERENT TRUCK CONFIGURATIONS ON A JOINTED PLAIN CONCRETE PAVEMENT (JPCP) <i>Lubinda F. Walubita, Tito P. Nyamuhokya, Stefan A. Romanoschi, Xiaodi Hu, Mena I. Soulimans</i>

FINITE ELEMENT ANALYSIS OF THE BEHAVIOUR OF REINFORCED CONCRETE COLUMNS CONFINED BY OVERLAPPING HOOPS SUBJECTED TO RAPID CONCENTRIC LOADING

Xiang Zeng

EXPERIMENTAL STUDY ON THE SOFTENING CHARACTERISTICS OF ARGILLACEOUS SLATE WITH WATER

Chengzhong Yang, Yuqiang Tang, Wei Wang, Shufang Wang

**HOW MUCH DOES A MINUTE OF COMMUTING TIME COST?
AN EXAMINATION OF PROPERTY PRICES IN RELATION TO DISTANCE TO THE CITY CENTER IN PRAGUE, CZECH REPUBLIC**

Martin Lukavec, Božena Kadeřábková

PHYSICAL AND MECHANICAL CHARACTERISTICS OF BUILDING MATERIALS OF HISTORIC BUILDINGS

Jiří Witzany¹, Radek Zigler¹, Tomáš Čejka¹, Pavel Pospíšil², Milan Holický³, Jan Kubát¹, Aneta Maroušková¹ and Klára Kroftová⁴

1. CTU in Prague, Faculty of Civil Engineering, Department of Building Structures, Prague, Thákurova 7, Czech Republic; wizany@fsv.cvut.cz, zigler@fsv.cvut.cz, cejka@fsv.cvut.cz, jan.kubat.2@fsv.cvut.cz, aneta.marouskova@fsv.cvut.cz
2. VŠB Ostrava, Faculty of Civil Engineering, Department of Geotechnics and Underground Engineering, L. Podéšť 1875/17, Ostrava – Poruba, Czech Republic; pavel.pospisil@vsb.cz
3. CTU in Prague, Klokner Institute, Prague, Šolínova 7, Czech Republic; milan.holicky@klok.cvut.cz
4. CTU in Prague, Faculty of Civil Engineering, Department of Architecture, Prague, Thákurova 7, Czech Republic; klara.kroftova@seznam.cz

ABSTRACT

The article presents partial results of laboratory research into physical and mechanical characteristics of materials most commonly used as walling units in masonry structures of historic and heritage buildings. Core boreholes and specimens for the laboratory research of selected characteristics were sampled from accessible places of historic buildings, which had not been restored or reconstructed.

The results of the research brought new knowledge about the unreliability (variance) of the properties of historical, mainly natural building materials, and, at the same time, pointed out the need for further research and extension of knowledge necessary for the assessment of residual physical and mechanical characteristics of historic masonry structures.

KEYWORDS

physical and mechanical characteristics, unreliability, masonry components, heterogeneous nature, variable factors

INTRODUCTION

Individual masonry components – walling units and binder – manifest a considerable variability of initial physical and mechanical characteristics. The manufacturing, extraction and processing methods of individual masonry components – walling units and binder – and the walling technology are processes with a relatively high degree of variability. Their contribution to the heterogeneous nature of masonry in terms of its mineralogical, chemical, physical, mechanical and other significant characteristics is crucial.

In the case of natural building blocks, the above variable factors are further assisted by other effects, e.g. the effect of the locality, extraction method and processing of natural stone, in the case of bricks, in turn, the effect of the brick clay quality, manufacturing technology, mainly the firing time

and technology, ceramic body composition and porosity, in the case of binder, the effect of individual components, their ratio and processing method. Subsequently, due to the effect of degradation processes, changes in these major characteristics of masonry and its components occur over time, the structure is impaired, there are changes in porosity, mineralogical composition, chemical changes, etc. The intensity of degradation processes depends on the aggressiveness of the external environment to which the masonry is exposed, the effects of moisture and ongoing transport processes which trigger off chemical, biochemical and physical changes in the masonry.

There are many historical methods of mutual bonding of building blocks, so-called masonry bonds, a large number of assembly and composition types of load-bearing masonry members. The size, shape and structure of bricks, the working method, shape and dimensions of building blocks of natural stone, various stiffening methods of e.g. historic masonry also play their role here, plus other facts significantly affecting the load-bearing capacity and failure mechanisms of masonry, mechanical and physical characteristics of brick, stone and mixed masonry which must be considered while assessing residual load-bearing capacity of masonry.

Despite relatively extensive research into masonry structures, the issue of a reliable identification of the load-bearing capacity (loadability) of existing, mainly historic masonry structures still has not been solved in a satisfactory way [1]. The identification of the load-bearing capacity of existing historic masonry structures is an extremely difficult task because of the variability and vagueness of the parameters [2, 3] describing the physical and mechanical characteristics of masonry – walling units and mortar. Moreover, there is a great variability in the quality and characteristics of masonry structures used e.g. within the masonry structure of a building, one storey, within a masonry member (e.g. wall, pillar) along its height and length [4].

The decreasing reliability in the identification of mechanical characteristics of historical materials requires a corresponding scope and number of diagnosed elements and parts of historic masonry (e.g. number of core boreholes) and, during the interpretation of the results of this research, the adequate setting of the ratio between e.g. experimentally identified and design strength.

DEGRADATION EFFECTS ON PHYSICAL AND MECHANICAL CHARACTERISTICS OF BUILDING MATERIALS OF HISTORIC BUILDINGS

All building materials used for the masonry of historic buildings have a porous structure, most frequently a system of open pores, which allows the transport of moisture through the pore system. These transport processes are related to the pore system, specific surfaces, moisture content in the masonry, etc. and are essential in terms of the mechanism of degradation processes, their intensity and kinetics. Moisture in the liquid and gaseous phase is the principal carrier of various aggressive substances transported into the interior structure of building materials.

An inseparable part of degradation processes caused by moisture are chemical degradation processes. Chemical corrosion of building materials is an action or a series of actions during which as a consequence of the effects of the aggressive environment the major physical and mechanical characteristics of materials fall below values necessary for their serviceability.

The basis of these actions are chemical reactions, reactions between the solid and liquid or gaseous phase. During the reactions, apart from the chemical reaction itself, transfer phenomena interact at the phase interface supplying reacting substances and removing reaction products. So that the reaction can run, permanent mass transfer – transport – of the reacting liquid phase and its effective substances must be provided.

Salt crystallization in pores or hydration pressures produce pressures inside the building material structure which gradually impair this structure and cause so-called physical degradation processes. The volume expansion of some salts which pass into hydrates (increased water content)

causes crystallization hydration pressures reaching values in the order of tens of MPa, which exceed common real tensile strengths of building materials. The growth of crystals is limited by small pore spaces and the crystals develop considerable expansive pressures which grow with temperature. Water evaporation leads to the dehydration of crystals and to their disintegration. With a new increase in moisture, hygroscopic salts reabsorb water and recrystallize. This repetitive process (crystallization and recrystallization), together with the washout of binder components, leads to a gradual disintegration of the structure.

A significant physical property which substantially conditions the successive course of degradation processes is the porosity of building materials, which changes over time and affects their water absorption.

Building materials and, hence, entire structures, have some infiltration capacity. Building stone (clastic sediments – sandstones) offers very favourable conditions for infiltration. Different materials differ by their grain size, pore size and distribution and are inhomogeneous in their microstructure.

As a consequence of and in direct proportion to the intensity and kinetics of degradation processes, the parameters describing the characteristics of masonry components – walling units and binder – must be assessed as time variable values.

BUILDING MATERIALS USED IN HISTORIC AND HERITAGE MASONRY BUILDINGS

Masonry structures of historic and heritage buildings, such as strip footings, walls, pillars and vaults, are most frequently made up of walling units of sandy marlstone, sandstone and limestone, granite, trachyte and fired bricks. Experimental research [5, 6] pointed out the severe effect of the moisture content, mineralogical composition and porosity (number, distribution and type of pores) on the intensity of chemical degradation processes and their effect on the mechanical characteristics of walling units.

In the Middle Ages, apart from local resources, relatively easily accessible and workable **sandy marlstone** belonged to the most common walling materials. It was the main material used for the construction of religious as well as civic buildings in the Romanesque to the early Gothic period. Judging by the quality of sandy marlstone, the durability of sandy marlstone masonry exposed to the present-day environment with its growing aggressiveness may be, in some cases, assessed for less than 50 years (depending on the intensity of degradation processes).

Note: Sandy marlstones are marlites to spongillites (or spongolites), mostly with slight sand contents, composed of various forms of SiO₂ (opal, chalcedony, cristobalite or micro-grained quartz), consolidated clay (aqueous aluminium silicates) and variable amounts of calcite (mostly as a binder), substances of biological origin (opal needles of sea sponges, etc., hence spöngillite) [2, 7]. The mechanical strength of sandy marlstone grows with higher contents of SiO₂, and, on the contrary, falls with higher porosity and higher contents of CaCO₃. Decalcified sandy marlstone (calcium carbonate is washed out) is highly porous, it has extremely low specific mass and low strength and is used for the production of lightweight building materials.

From the start of the 15th century, **sandstone** belonged to the main building materials. The turning point in using sandy marlstone is the end of the 14th century and the start of the 15th century, when sandy marlstone was gradually replaced with sandstone. The evident reason was higher resistance of sandstone to weathering. The collective term – building sandstone – covers a series of rock types of sedimentary origin, variable chemical composition, age and physical characteristics (water absorption, strength, porosity, frost resistance).

Note: Sandstones form a large group of clastic consolidated sediments, most often with quartz grains, but also with calcite, 0.063-2 mm in size. They are classified as fine-grained (grains in an interval of 0.063-0.5 mm), medium-grained (grains of 0.5-1.0 mm) and coarse-grained (grains larger than 1.0 mm). The space between the grains can be void space or can be filled with a binder – fine-grained sedimentary rock component of a

different structure, which makes the rock cohesive [7, 8]. The properties of sandstone (porosity, mechanical characteristics, colour, chemical resistance) are significantly affected by the binder quality and amounts. A considerably lower water absorption and porosity are the precondition for high strength and resistance to weathering and are typical of sandstones with a porous or filler binder. Sandstones mostly tend to be more resistant to the effects of degradation agents (water, acid exhalations from the air) than e.g. sandy marlstone.

Limestones belonged to rock types, less frequently used in the construction of historic buildings, they were used in historic buildings on a relatively small scale and, as a rule, in the locality where they were quarried; in Bohemia, a major area with limestone quarries are the surroundings of the town of Beroun.

Note: Limestones are non-clastic, compact to fine-grained sedimentary rocks (marbles have visible grains) formed by calcite CaCO_3 (rhombohedral calcite and its orthorhombic modification – aragonite, in two-component rocks they must be represented by at least 50%) with a smaller proportion of admixtures (admixtures of clastic particles do not exceed 10%), which colour them. Aragonite is more soluble, therefore, it tends to be easily leached and, for this reason, it cannot be found in geologically older limestones. Limestones are connected via continuous interfaces mainly with clay sediments (marl, marlite), sandy sediments (sandy limestones and lime sandstones) and very often with dolomite. In relation to the proportion of carbonate contents, some types of sandstone can be classified as sandy limestones or lime sandstones.

Walling units were also prepared from granites, e.g. from granite, **trachyte** and others. Like in the case of limestone, their use in the construction of historic buildings was linked to a respective locality of their quarrying.

Note: Trachyte is an extrusive magmatic rock, light whitish to grey in colour, of very fine-grained, porous structure. By its mineralogical composition, it is mostly formed by feldspar (potassium feldspars prevail over plagioclases), foide (representative of feldspars) - nepheline, sodalite and leucite, smaller amounts of quartz or smaller amounts of tridymite. In the Czech Republic, it is found sporadically, e.g. near the settlement of Úterý close to Mariánské lázně.

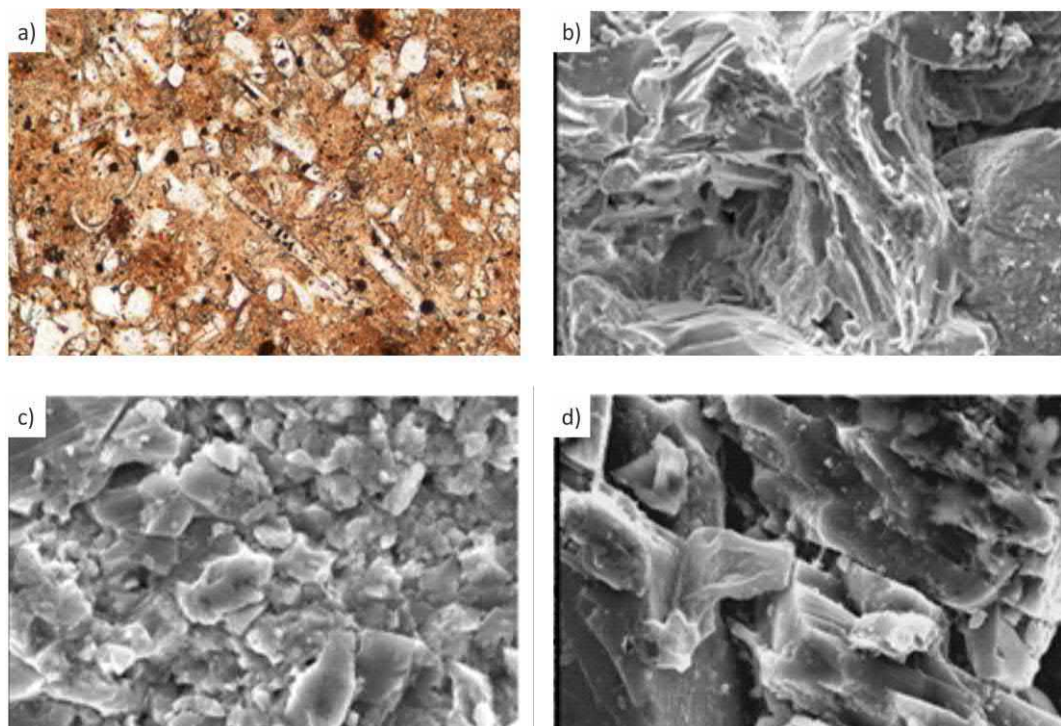


Fig. 1 - Microscopic images of walling materials, a) Sandy marlstone (photo by P. Pospíšil), b) Sandstone [9], c) Limestone [9], d) Trachyte [9]

Starting from the Middle Ages, **burnt bricks** have been used for the construction of masonry buildings. They were used for brickwork or mixed masonry structures, together with walling units of natural materials, or they formed their reinforcing parts, e.g. outside corners of stonework and mixed masonry walls, linings, etc. Depending on the firing temperature and brick mix composition, bricks with different strengths, porous systems, etc. were manufactured.

Note: The basic raw material for burnt bricks are loams based on clay minerals (mainly illite, montmorillonite and kaolinite). Non-clay components (mainly quartz, to a lesser extent calcite, mica, chlorite, etc.) are added to them. The dehydration of clay minerals takes place at temperatures of 500 - 600°C, while at 950°C amorphous SiO₂ parts split off and dehydrated aluminosilicates change into a spinel-type compound. This, in turn, starts to pass into mullite 3Al₂O₃ • 2SiO₂ at temperatures above 1100°C. At temperatures higher than 1200°C, the split-off amorphous SiO₂ changes into cristobalite. The manufacturing technology and brick mix composition are essential for the physical and mechanical characteristics of burnt bricks, e.g. a higher firing temperature also increases the amount of melt (glass phase) thus increasing the strength of the resulting product. [7, 8].

EXPERIMENTAL RESEARCH INTO SELECTED MECHANICAL CHARACTERISTICS OF HISTORICAL MATERIALS

The specimens sampled from selected historic buildings differing in age were exposed to laboratory research focused on the identification of mechanical characteristics (tensile and compressive strength, dynamic modulus of elasticity, modulus of elasticity in compression) and selected physical characteristics (overall porosity, pore distribution) and chemism.

*Note: Uniaxial compressive strength was identified using procedures under ČSN EN 1926:2007. The test pieces used for the tensile strength test had the same dimensions as those used for the uniaxial compressive strength test, whose bases were fitted with anchoring steel elements glued with two-component epoxy adhesive. The dynamic modulus of elasticity of the test pieces was identified on all test pieces before the compressive or tensile tests using the TICO device. Water absorption up to a constant mass was tested by the immersion of the whole specimen in water. Mercury porosimetry performed on chips of sedimentary rocks 10-20 g in weight served to identify overall porosity and pore distribution in a range of 1 to 60*10³ nm. Moisture profiles and basic chemism were detected on powder specimens (samples were performed in three different height levels – 0.25m, 0.75m and 1.3m above terrain level to assess the moisture distribution in masonry).*

The experimental, predominantly laboratory research conducted within the Ministry of Culture research project NAKI II was primarily concentrated on research into sedimentary rocks – sandy marlstone, sandstone, lime sandstone – from granites on trachyte and from artificial building materials on burnt bricks. The dimensions of partial specimens for the identification of the required characteristics obtained from core boreholes were modified to comply with ČSN standards (ČSN EN 1926:2007, ČSN EN 1996-1-1+A1:2013). Tab. 1 presents the list of sampled specimens which were the subject of laboratory research.

Tab. 1 - List of test specimens

Sampled specimens	Labelling	Sampling site	Type of structure	Age (years)	Locality
Sandy marlstone	M1 - M3	quarry	quarry	0	Přední Kopanina
	M4 - M5	farmstead	barn	170	Tuchoměřice
	M6 - M9	Václav Havel Library	library	345	Praha
	M10 - M16	Ursuline Convent	convent	340	Praha
Sandstone	S1	quarry	quarry	0	Hořovice
	S2	quarry	quarry	0	Božanov
	S3 - S8	church	church	340	Fořt
	S9 - S14	former poorhouse	residential building	350	Kutná Hora
	S15	quarry	quarry	0	Hořice v Podkrkonoší
	S16 - S17	Jeřice Castle	barn	170	Jeřice
	S18 - S20	farmstead	barn	140	Chotíkov
	S21 - S23	farmstead	stable	350	Boseň
Lime sandstone	LS1 - LS6	former vicarage	vicarage	340	Hořovice
Trachyte	T1 - T6	farmstead	stable	270	Teplá, Ovčí Dvůr
	T7 - T10	farmstead	stable	270	Teplá, Hájčí Dvůr
	T11 - T14	Premonstrate Monastery	fence	370	Teplá
Bricks	B1 - B4	from manufacture	from manufacture	0	Praha
	B5 - B7	carpenter's workshop	carpenter's workshop	120	Kutná Hora
	B8 - B11	printing house	printing house	120	Humpolec
	B12 - B13	church	church	340	Fořt
	B14 - B17	former poorhouse	residential building	350	Kutná Hora
	B18 - B20	Václav Havel Library	library	345	Praha

STATISTICAL ANALYSIS OF LABORATORY OBTAINED VALUES

The section below presents the results of statistical analysis subdivided according to materials. Due to the limited scope of data, together with the mean measured values, coefficients of variation, skewness of a distribution, etc., other theoretical assumptions supported by previous findings and experience are used [10, 11].

Tab. 2 - Results of laboratory research – sandy marlstone

Labelling	f_b	f_t	E.	E_{dyn}	Water absorption	Porosity
	(Mpa)	(Mpa)	(Mpa)	(Mpa)	(%)	(%)
M01	76.15	-	11755	-	10.24	26.15
M02	49.63	-	6388	-	10.04	32.08
M03	72.69	-	21200	-	10.16	26.15
M04	29.57	1.47	4514	3700	10.27	-
M05	29.12	1.39	5184	10644	9.74	-
M06	39.4	3.52	6556	12241	4.86	-
M07	45.81	3.48	5749	2149	8.31	-
M08	35.29	1.97	6515	14053	-	-
M09	46.91	1.53	5023	25950	-	-
M10	29.35	2.97	3980	7144	16.09	27.42
M11	19.92	1.45	3300	5518	20.85	30.2
M12	66.81	4.14	5035	6765	4.22	22.33
M13	43.62	0.34	4930	6668	12.76	-
M14	39.27	3.36	4995	10751	16.39	-
M15	38.41	3	4324	12236	11.86	-
M16	34.43	4.49	4180	10609	12.6	-

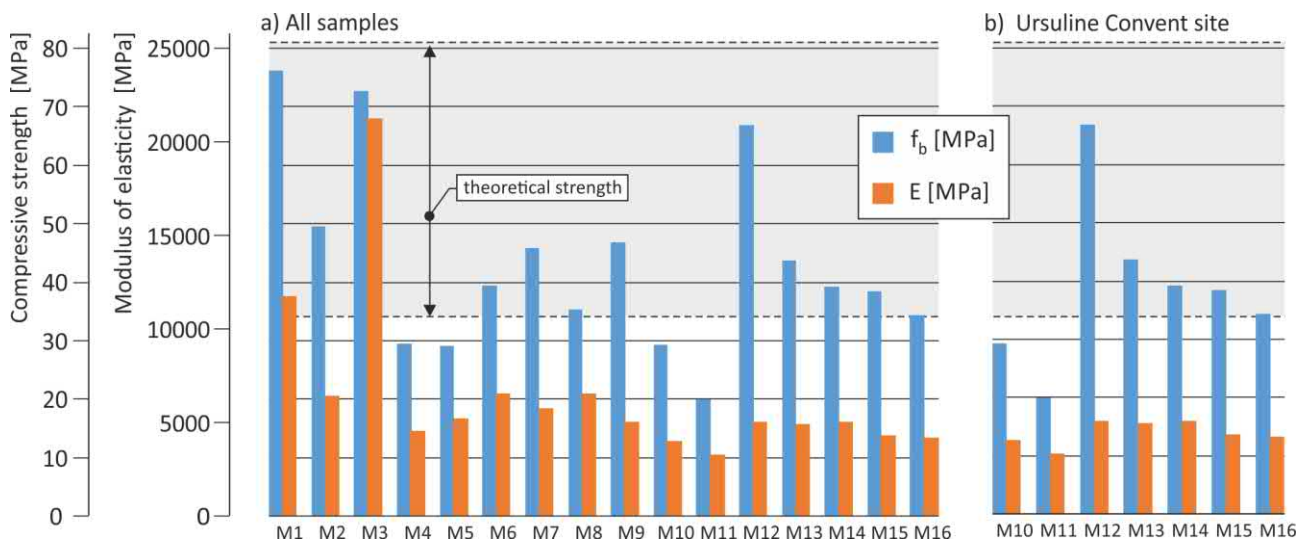


Fig. 2 - Results of laboratory research – sandy marlstone

Tab. 3 - Statistical analysis – sandy marlstone (entire data set)

	arithmetic mean	median	lower quartile	upper quartile	standard deviation	coeff. of variation	coeff. of kurtosis	coeff. of skewness
f_b (MPa)	43.5	39.3	33.2	47.6	15.6	35.8%	0.151	0.81
E (MPa)	6476.75	5029	4466.5	6419.8	4225.8	62.25%	9.471	2.688

Tab. 4 - Statistical analysis – sandy marlstone (selected locality – Ursuline Convent)

	arithmetic mean	median	lower quartile	upper quartile	standard deviation	coeff. of variation	coeff. of kurtosis	coeff. of skewness
f_b (MPa)	38.8	38.4	31.9	41.4	13.5	34.7%	2.37	0.83
E (MPa)	4392.0	4324.0	4080.0	4962.5	595.01	14%	-0.37	-0.5

The entire data set of compressive strengths f_b shows a significant dispersion of measured values (coefficient of variation of 0.36) corresponding to a slightly peaked probability density distribution (positive kurtosis of 0.151) and a markedly positive skewness (0.81). It is a slightly peaked distribution with a positive skew.

The strengths from a selected locality (Ursuline Convent) are of a similar nature, but the probability density distribution has a higher degree of peakedness (positive kurtosis of 2.37).

The entire data set of the modulus of elasticity E shows a very significant dispersion of measured values (coefficient of variation of 0.63) with a very sharp peaked probability density distribution (positive kurtosis of 9.471) and a markedly positive skewness (2.69). It is a sharp peaked and positively skewed distribution.

The modulus of elasticity values from a selected site (Ursuline Convent) show a markedly lower dispersion of measured values (coefficient of variation of 0.14) corresponding to a flat probability density distribution (negative kurtosis of 0.37) with a negative skewness (-0.5).

The normal and three-parametric lognormal distribution for the entire data set of sandy marlstone strengths (derived from the mean value of 43.5 MPa, standard deviation of 15.6 and skewness of 0.81), including the minimum (19.92) and the maximum (76.15) measured values, is presented in Figure 3.

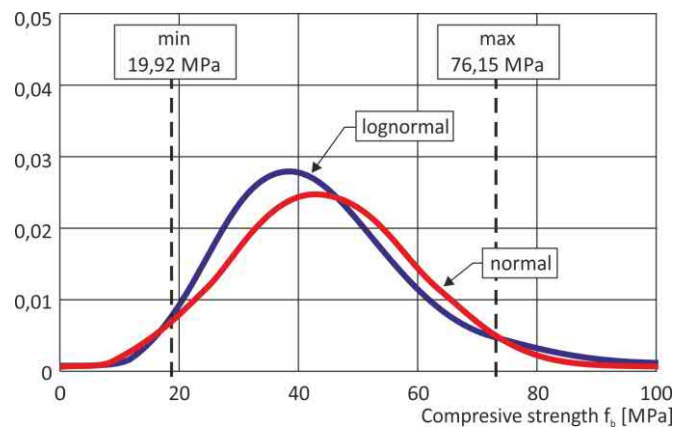


Fig. 3 - Normal and three-parametric lognormal distribution for the entire data set of sandy marlstone strengths showing minimum and maximum measured values

Tab. 5 - Results of laboratory research – sandstone

labelling	f_b	f_t	E.	E_{dyn}	water absorption	porosity
	(Mpa)	(Mpa)	(Mpa)	(Mpa)	(%)	(%)
S01	30.9	-	4100	-	5.24	22.13
S02	43.91	-	19500	-	5.64	19.06
S03	52.16	-	3900	-	3.44	13.63
S04	29.16	-	3800	-	5.6	15.12
S05	71.07	-	8900	-	-	14.72
S06	41.1	-	4900	-	4.28	14.3
S07	33.49	-	5369	-	-	13.63
S08	50.39	-	6272	-	-	14.72
S09	39.7	-	2879	15156	1.06	-
S10	39	1.35	3009	24270	-	-
S11	48.29	-	3103	-	-	-
S12	47.39	-	5777	-	-	-
S13	45.03	-	5334	-	-	-
S14	47.39	-	5524	-	-	-
S15	36.8	-	11800	-	-	16.26
S16	44.79	1.48	6355	8174	-	5.53
S17	48.63	1.65	7111	16000	-	5.36
S18	55.1	1.04	3097	8010	8.67	-
S19	60.48	0.58	3942	5401	13.54	-
S20	31.16	1.48	3120	3953	3.73	8.25
S21	1.83	-	400	-	-	23.89
S22	1.93	-	300	-	-	26.01
S23	4.31	-	1100	-	-	23.89

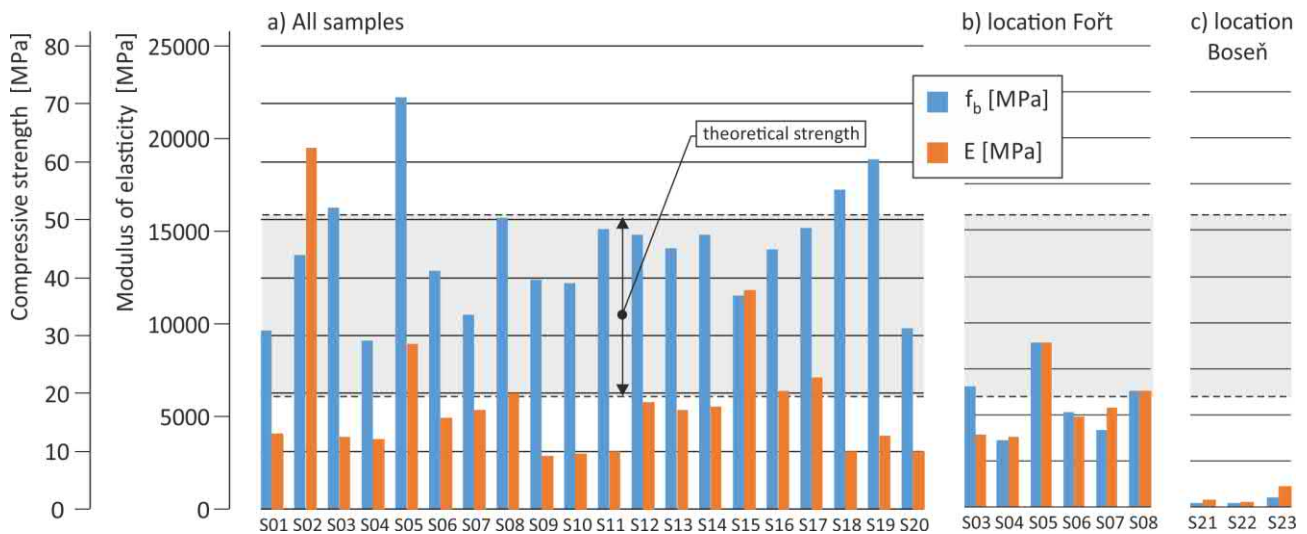


Fig. 4 - Results of laboratory research – sandstone

Tab. 6 - Statistical analysis – sandstone (entire data set)

	arithmetic mean	median	lower quartile	upper quartile	standard deviation	coeff. of variation	coeff. of kurtosis	coeff. of skewness
f_b (MPa)	44.8	44.91	38.45	49.07	10.14	22.64%	0.813	0.595
E (MPa)	5889.6	5117.0	3630.0	6292.8	3799.5	64.51%	7.727	2.379

Tab. 7 Statistical analysis – sandstone (selected locality - Fořt)

	arithmetic mean	median	lower quartile	upper quartile	standard deviation	coeff. of variation	coeff. of kurtosis	coeff. of skewness
f_b (MPa)	46.23	45.75	35.39	51.72	13.84	29.94%	0.296	0.530
E (MPa)	5523.5	5134.5	4150.0	6046.3	1731.08	31.34%	1.665	0.940

The entire data set of compressive strengths f_b shows a significant dispersion of measured values (coefficient of variation of 0.23) with a peaked probability density distribution (positive kurtosis of 0.813) and a positive skew (0.595). It is a slightly peaked and positively skewed distribution.

The strengths from a selected site (Fořt) are of a similar nature with a positive skew (positive skewness of 0.53), but their probability density distribution is flatter (positive kurtosis of 0.296).

The entire data set of the modulus of elasticity E shows a significant dispersion of measured values (coefficient of variation of 0.65) with a markedly sharp peaked probability density distribution (positive kurtosis of 7.727) and a significantly positive skewness (2.38). It is a sharp peaked and positively skewed distribution.

The modulus of elasticity values from a selected site (Fořt) have a lower dispersion of measured values (coefficient of variation of 0.31), their probability density distribution is less sharp peaked (positive kurtosis of 1.67) with a positive skew (0.94).

The normal and three-parametric lognormal distribution for the entire data set of sandstone strengths (derived from the mean of 44.8 MPa, standard deviation of 10.1 and skewness of 0.59),

including the minimum (29.16) and the maximum (71.07) measured values, is presented in Figure 5.

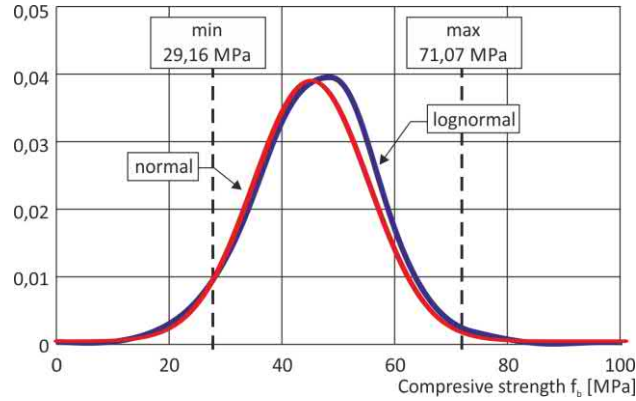


Fig. 5 - Normal and three-parametric lognormal distribution for the entire data set of sandstone strengths showing minimum and maximum measured values

Tab. 8 - Results of laboratory research – lime sandstone

labelling	f_b	f_t	E.	E_{dyn}	water absorption	porosity
	(Mpa)	(Mpa)	(Mpa)	(Mpa)	(%)	(%)
LS01	173.35	2.52	6320	15476	1.31	-
LS02	155.27	6.23	5971	18540	0.69	-
LS03	103.53	3.77	6210	9080	1.99	7.53
LS04	98.59	2.75	6153	12991	2.25	7.75
LS05	105.6	3.99	60478	12278	3.0	7.24
LS06	81.62	2.39	4754	17075	3.14	9.98

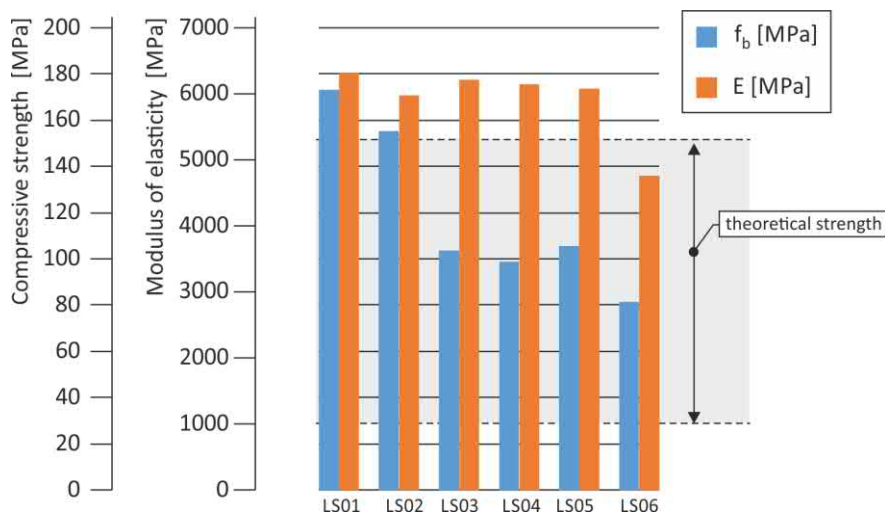


Fig. 6 - Results of laboratory research – lime sandstone

Tab. 9 - Statistical analysis – lime sandstone (entire data set)

	arithmetic mean	median	lower quartile	upper quartile	standard deviation	coeff. of variation	coeff. of kurtosis	coeff. of skewness
f_b (MPa)	119.66	104.56	99.83	142.86	32.91	27.51%	-1.148	-0.731
E (MPa)	5916.0	6115.5	6005.3	6195.8	530.18	8.96%	5.210	-1.633

The entire data set of compressive strengths f_b shows a dispersion of measured values (coefficient of variation of 0.28) corresponding to a flat probability density distribution (negative kurtosis of -1.15) and a negative skew (-0.731). It is a flat and negatively skewed distribution.

The entire data set of the modulus of elasticity E shows a lower dispersion of measured values (coefficient of variation of 0.09) corresponding to a sharp peaked probability density distribution (positive kurtosis of 5.21) and a markedly negative skewness (-1.63). It is a sharp peaked and negatively skewed distribution.

The normal and three-parametric lognormal distribution for the entire data set of lime sandstone strengths (derived from the mean of 119.66 MPa, standard deviation of 32.91 and skewness of -0.731), including the minimum (81.62) and the maximum (173.35) measured values, is presented in Figure 7.

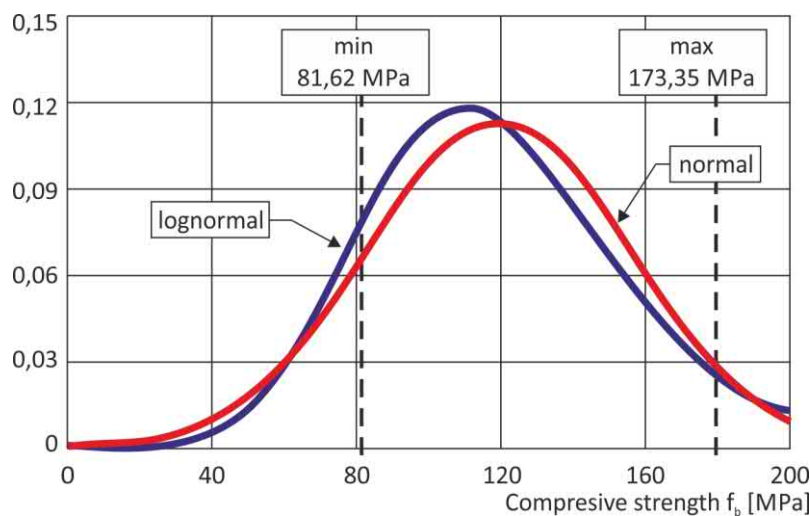


Fig. 7 - Normal and three-parametric lognormal distribution for the entire data set of lime sandstone strengths showing minimum and maximum measured values

Tab. 10 - Results of laboratory research – trachyte

labelling	f_b	f_t	E.	E_{dyn}	water absorption	porosity
	(Mpa)	(Mpa)	(Mpa)	(Mpa)	(%)	(%)
T01	55.07	1.2	10700	9984	3.45	-
T02	53.31	1.37	12900	12100	-	-
T03	76.16	-	8666	-	-	-
T04	85.39	-	9366	-	-	-
T05	82.63	3.31	8486	14096	-	-
T06	71.11	4.76	8754	17226	-	-
T07	55.61	1.02	8331	5094	3.49	-
T08	54.91	0.78	9007	7497	-	-
T09	42.03	-	8726	-	-	-
T10	51.92	-	8919	-	-	-
T11	75.74	3.85	6530	8676	1.19	10.28
T12	77.12	3.86	5543	6569	2.81	10.5
T13	58.635	1.38	4015	8488	2.05	10.93
T14	67.48	1.78	3619	6317	2.17	12.18

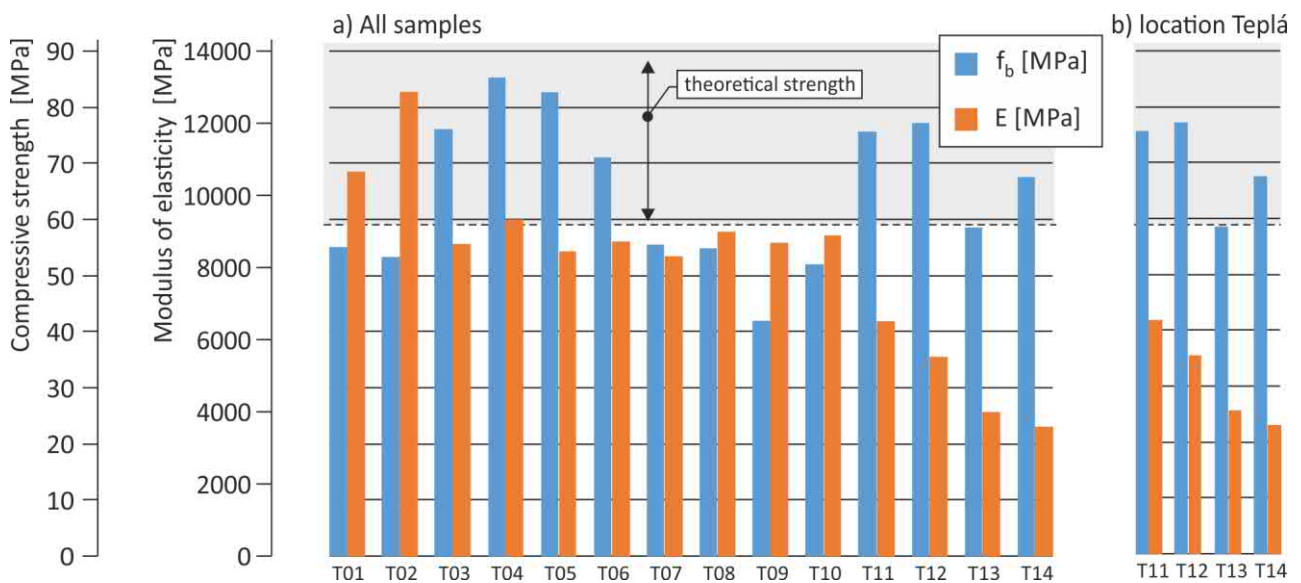


Fig. 8 - Results of laboratory research – trachyte

Tab. 11 - Statistical analysis – trachyte (entire data set)

	arithmetic mean	median	lower quartile	upper quartile	standard deviation	coeff. of variation	coeff. of kurtosis	coeff. of skewness
f_b (MPa)	64.79	63.06	54.95	76.06	12.87	19.87%	-1.240	0.033
E (MPa)	8111.6	8696.0	6980.3	8985.0	2390.6	29.47%	0.403	-0.257

Tab. 12 - Statistical analysis – trachyte (selected locality - Teplá)

	arithmetic mean	median	lower quartile	upper quartile	standard deviation	coeff. of variation	coeff. of kurtosis	coeff. of skewness
f_b (MPa)	69.74	71.61	65.27	76.09	7.40	10.61%	-1.286	-0.473
E (MPa)	4926.8	4779.0	3916.0	5789.8	1171.7	23.78%	-3.178	0.211

The entire data set of compressive strengths f_b shows a significant dispersion of measured values (coefficient of variation of 0.20) corresponding to a flat probability density distribution (negative kurtosis of -1.24) and a nearly negligible skewness (0.03). It is a flat and nearly symmetrical distribution.

The strengths from a selected locality (Teplá) are of a similar nature, but the value of the probability density distribution coefficient of variation is by one half lower (0.11) and the distribution is negatively skewed (skewness of -0.47).

The entire data set of the modulus of elasticity E shows a significant dispersion of measured values (coefficient of variation of 0.29) with a slightly peaked probability density distribution (positive kurtosis of 0.403) and a negative skewness (-0.257). It is a slightly peaked and negatively skewed distribution.

The modulus of elasticity values from a selected site (Teplá) show a similar dispersion of measured values (coefficient of variation of 0.24), but their probability density distribution is markedly flat (negative kurtosis of 3.18) with a positive skewness (0.21).

The normal and three-parametric lognormal distribution for the entire data set of trachyte strengths (derived from the mean of 64.79 MPa, standard deviation of 12.87 and skewness of 0.03), including the minimum (42.03) and maximum (85.39) measured values, is presented in Figure 9.

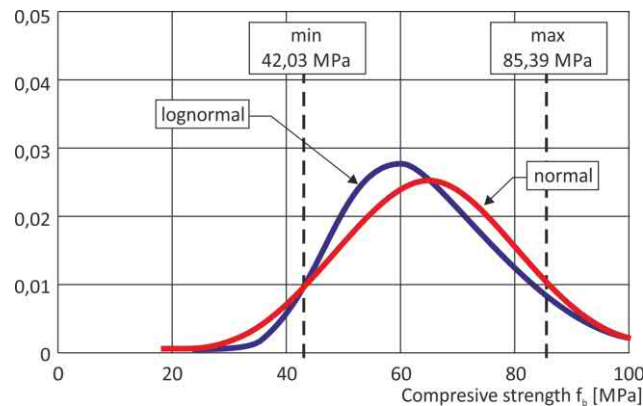


Fig. 9 - Normal and three-parametric lognormal distribution for the entire data set of trachyte strengths showing minimum and maximum measured values

Tab. 13 -Results of laboratory research – burnt bricks

labelling	f_b	f_t	E.	E_{dyn}	water absorption	porosity
	(Mpa)	(Mpa)	(Mpa)	(Mpa)	(%)	(%)
B01	14.31	-	5600	-	20.88	31.92
B02	26.23	-	8500	-	18.49	34.36
B03	20.02	-	2600	-	11.9	38.41
B04	17.76	-	2400	-	16.4	37.4
B05	17.08	-	2300	-	18.3	37.5
B06	34.78	-	5300	-	22.5	31.27
B07	21.39	-	3200	-	19.2	31.78
B08	19.57	-	2400	-	-	26.15
B09	23.82	-	3100	-	-	18.44
B10	12.02	-	1400	-	-	24.93
B11	11.21	-	3072	-	-	18.44
B12	11.15	-	2200	-	-	31.8
B13	7.59	-	1400	-	-	34.32
B14	9.28	1.15	2710	3684	17.44	-
B15	16.17	1.45	4763	6652	16.27	-
B16	21.4	-	5090	2477	-	-
B17	32.54	-	6630	6104	-	-
B18	8.28	0.5	1522	1130	12.95	-
B19	6.82	0.8	1768	-	-	-
B20	8.08	2.13	2072	-	-	-

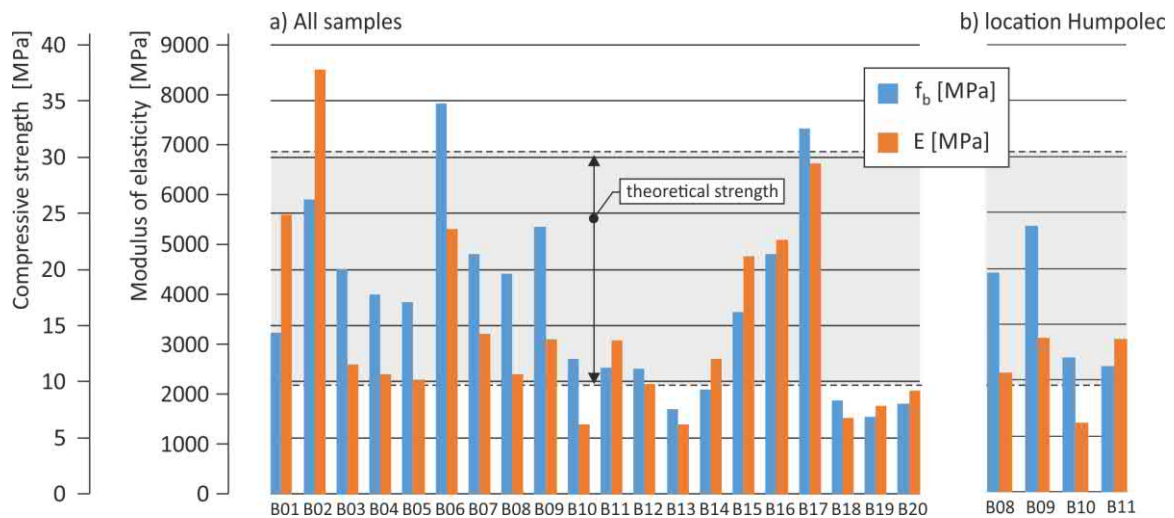


Fig. 10 - Results of laboratory research – burnt bricks

Tab. 14 - Statistical analysis – burnt bricks (entire data set)

	arithmetic mean	median	lower quartile	upper quartile	standard deviation	coeff. of variation	coeff. of kurtosis	coeff. of skewness
f_b (MPa)	16.98	16.63	10.68	21.39	7.91	46.61%	-0.106	0.659
E (MPa)	3401.4	2655.0	2168.0	4844.8	1891.6	55.61%	1.010	1.150

Tab. 15 - Statistical analysis – burnt bricks (selected locality - Humpolec)

	arithmetic mean	median	lower quartile	upper quartile	standard deviation	coeff. of variation	coeff. of kurtosis	coeff. of skewness
f_b (MPa)	16.66	15.80	11.82	20.63	5.27	31.62%	-3.637	0.225
E (MPa)	2493.0	2736.0	2150.0	3079.0	690.47	27.70%	0.321	-0.675

The entire data set of compressive strengths f_b shows a significantly high dispersion of measured values (coefficient of variation of 0.47) corresponding to a flat probability density distribution (negative kurtosis of -0.11) and a significantly positive skewness (0.66). It is a slightly flat and positively skewed distribution.

The strengths from a selected site (Humpolec) are of a similar nature, but their probability density distribution is significantly flatter (negative kurtosis of -3.64).

The entire data set of the modulus of elasticity E shows a significant dispersion of measured values (coefficient of variation of 0.56) with a peaked probability density distribution (positive kurtosis of 1.01) and a positive skewness (1.15). It is a sharp peaked and positively skewed distribution.

The modulus of elasticity values from a selected site (Humpolec) show a lower dispersion of measured values (coefficient of variation of 0.28), their probability density distribution is less peaked (positive kurtosis of 0.32) with a negative skewness (-0.68).

The normal and three-parametric lognormal distribution for the entire data set of brick strengths (derived from the mean of 16.98 MPa, standard deviation of 7.91 and skewness of 0.66), including the minimum (6.82) and the maximum (34.78) measured values, is presented in Figure 11.

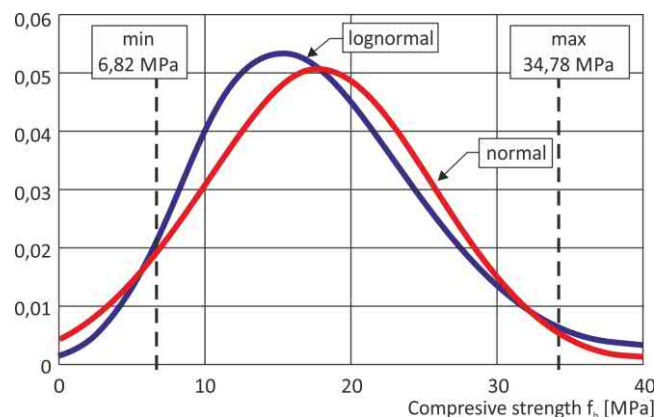


Fig. 11 - Normal and three-parametric lognormal distribution for the entire data set of brick strengths showing minimum and maximum measured values

Overall assessment

The statistical analysis of major mechanical characteristics (compressive strength f_b , modulus of elasticity E) of selected materials (sandy marlstone, sandstone, lime sandstone, trachyte, burnt bricks) has manifested a significant to a very significant dispersion of measured values (coefficient of variation ϵ (0.11; 0.47)) corresponding to a flat probability density distribution except for sandstone, whose measured values have a sharp peaked distribution.

The standard deviations ϵ (5.3; 32.9) where the lowest standard deviation values were calculated for burnt bricks (7.9 for the entire data set, 5.3 for a selected locality – structure), and the highest standard deviation values were calculated for lime sandstone (32.9 for the entire data set) and for sandy marlstone (15.6 for the entire data set of values, 13.5 for a selected locality – structure).

CONCLUSION

The significant dispersion of measured values of major mechanical characteristics of natural stone and burnt bricks requires obtaining the values describing the major characteristics of walling units (strength, modulus of elasticity and others) from a sufficient number of sampling sites in order to identify the residual loading capacity of particularly stonework and mixed masonry. The values obtained on the basis of e.g. sampled core boreholes are valid mainly in the immediate vicinity of the sampling site and cannot be extrapolated for larger masonry parts. The residual load-bearing capacity of masonry, identified on the basis of an insufficient number of sampling sites or values obtained from respective regulations and literature can only be classified as approximate.

ACKNOWLEDGEMENTS

The article was written with support from the NAKI DG16P02M055 project “Development and Research into Materials, Procedures and Technologies for Restoration, Conservation and Strengthening of Historic Masonry Structures and Surfaces and Systems of Preventive Care of Historic and Heritage Buildings Threatened by Anthropogenic and Natural Risks”.

REFERENCES

- [1] Witzany, J. et al.: Chemická a biochemická degradace Karlova mostu, analýza odolnosti a bezpečnosti kamenné mostní konstrukce při povodni, průzkum základového zdiva a základů mostních pilířů, Stavební obzor, 12, 2003, No. 6, pp. 161–180.
- [2] Kotlík, P., Šrámek, J., Kaše, J.: Opuka, STOP, Praha, 2000, ISBN 80-902668-5-1.
- [3] Hanykýř, V., Kloužková, A., Bouška, P., Vokáč, M.: Stárnutí pórovitého keramického střepu, In: SILIS - Keramický zpravodaj, Vol. 25, No. 6/2009, pp. 5-10, Praha, ISSN 1210-2520.
- [4] Heidingsfeld, V.: Fyzikální a chemická koroze stavebních materiálů. In: Voda nepřítel památek. Odborný seminář STOP. Praha: 1997, pp. 9-12
- [5] Witzany, J., Čejka, T., Výzkum fyzikálně mechanických vlastností porézních zdících prvků, Stavební obzor. 2008, 17(10), 289-292. ISSN 1210-4027.
- [6] Witzany, J., Čejka, T., Kroftová, K., Šmidtová, M., The effect of degradation processes on the serviceability of building materials of historic buildings, The Civil Engineering Journal. 2016,(3), ISSN 1805-2576.
- [7] Kotlík, P. et al.: Stavební materiály historických objektů – Materiály, koroze, sanace, Vydavatelství VŠCHT, 1999, ISBN 80-7080-347-9.
- [8] Hošek, J., Stavební materiály pro rekonstrukce. 1st edition 1996. ISBN 80-01-01156-9.
- [9] Neubergová, S., Analýza vlivu vybraných degradačních činitelů na fyzikálně mechanické vlastnosti přírodního kamene, DDP, Praha: České vysoké učení technické v Praze, 2015.

[10] Holický, M., Introduction to Probability and Statistics for Engineers, Heidelberg: Springer, 2013. ISBN 978-3-642-38299-4.

[11] Holický, M., Aplikace teorie pravděpodobnosti a matematické statistiky, Praha: České vysoké učení technické v Praze, Kloknerův ústav, 2015. ISBN 978-80-01-05803-9.

STUDY ON DE-NOISING METHODS FOR SOIL COMPRESSIVE STRESS SIGNAL DURING VIBRATION COMPACTION

Qingzhe Zhang, Meng Ji, Qian Zhang, and Zhi Qin

1. *Chang'an University, Key Laboratory for Highway Construction Technique and Equipment of Ministry of Education of China, Xi'an, China; e-mail: zqzh@chd.edu.cn*

ABSTRACT

The compressive stress signal of soil during vibration compaction is an unstable and transient saltation signal accompanied by broadband noise, and the spectra of the signal and noise always overlap. To extract the ideal original signal from noisy data, this paper studies several signal de-noising methods such as low-pass filtering, multi-resolution wavelet transform, spectrum subtraction and independent component analysis. Experiments show that the traditional low-pass filter is only applicable when the spectra of the signal and noise can be separated in the frequency domain. The multi-resolution wavelet transform can decompose the signal into different frequency bands and remove the noise efficiently by extracting useful the frequency band of the signal, but this method is not reliable when the signal to noise ratio (SNR) is low. Spectrum subtraction can remove strong background noise with stationary statistical characteristics even if the noise level is high and the spectrum of the signal overlaps with that of the noise. Independent component analysis can extract weak signals which are combined with heavy noise and can separate the noise from signal effectively when the independent channel hypothesis holds. These de-noising methods are of great importance for further analysing vibration signals in engineering.

KEYWORDS

Compressive stress signal, Low-pass filter, multi-resolution wavelet transform; spectrum subtraction; independent component analysis; de-noising methods

INTRODUCTION

Signals can be easily degraded by noise due to signal generators, sensors and other equipment during the acquisition and transmission process. In practical applications, most received signals are accompanied by noise. Processing the noisy signals directly will affect the feature recognition, classification and other subsequent steps [1]. Therefore, it is very important that signal de-noising is performed and the original signal information is preserved and extracted.

The soil compressive stress signal contains important physical information about the process of vibration compaction. It not only reflects the distribution of the compressive stress in each layer, but the distribution, absorption and transfer of the compaction energy in the soils. The compressive stress signal of soil during vibration compaction is an unstable transient saltation signal accompanied by broadband noise, and the noise and signal spectra always overlap [2]. In order to study the joint time-frequency property and the laws of distribution and transfer of the soil compressive stress signal in each layer, so as to reveal the vibration compaction mechanism, it is crucial to extract the ideal original signal from noisy data for further processing and analysis. In recent years, a large number of novel algorithms have appeared in the study of unstable and transient saltation signal de-noising [3-6]. Considering the soil compressive stress signal during vibration compaction, this paper discusses and studies the effect of de-noising methods on vibration signals; such methods include low-pass filters, multi-resolution wavelet transforms,

spectrum subtraction and independent component analysis. A comparative analysis of the experimental results is presented and the applicability of the algorithms is discussed.

1. SOIL VIBRATION COMPACTION TEST

A soil vibration compaction test was implemented in the large soil tank of Key Laboratory for highway construction techniques and equipment of the Ministry of Education, Chang'an University. The test equipment used a custom-designed vibratory roller model [7]. The compaction test section length was 8 m, with a width of 1 m. Based on the test conditions and vibratory roller that used during vibration compaction, the nominal amplitude, vibration frequency and running speed of the roller are the main influencing factors in the test. An orthogonal experiment scheme of the 3 factors at 3 levels was implemented, resulting in nine tests that fully reflect the influence of various factors. For each condition, static compaction was first performed 2 times, then the vibration compaction was repeated for 12 times [8].

Before the test, turned loose soil to 35cm in soil tank by hand, and watering in order to achieve the appropriate moisture content. Then, three dynamic strain gauge pressure cells were placed on 3 layers under the soil at depths of 5cm, 15cm and 25cm, respectively. A DEWE-2010 data logger recorded the soil compressive stress signals of the pressure cells during the vibration compaction process, capturing stress signals on an oscilloscope in real time, as well as storing and processing data. The experimental setup is shown in Figure 1. The sampling frequency of the soil compressive stress signal in the test was 2000Hz.

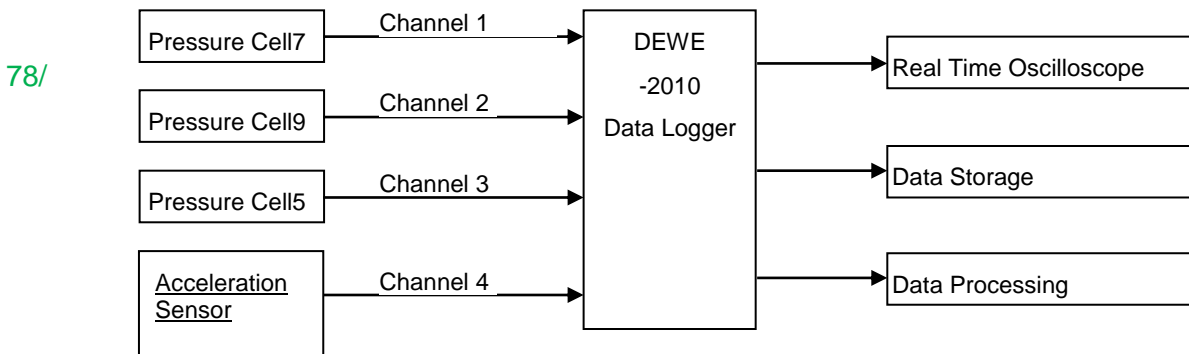


Fig.1 - Experimental setup

2. DE-NOISING METHODS OF COMPRESSIVE STRESS SIGNALS

This paper considers the case of the soil compressive stress signal, and assumes a signal S_1 with a low amount of noise and signal S_2 with heavy noise. Signal S_1 retains the waveform characteristics of stress signal generally, but due to the heavy noise, the waveform of signal S_2 has been distorted. The vibration compaction operating parameters in the test were: vibration frequency-- 30Hz, nominal amplitude-- 1.2mm, and running speed--1.12 km/h. According to the analysis, the ideal compressive stress signal is an unstable transient signal which has a peak value at the moment of impact, but is a stable signal with zero mean at other times.

2.1 Low-pass filtering

When the signal is band-limited and the signal and noise spectra can be separated in the frequency domain, a low-pass filter can filter out the noise spectrum by multiplying a window function in the frequency domain, thus separating the noise from signal through a purpose-

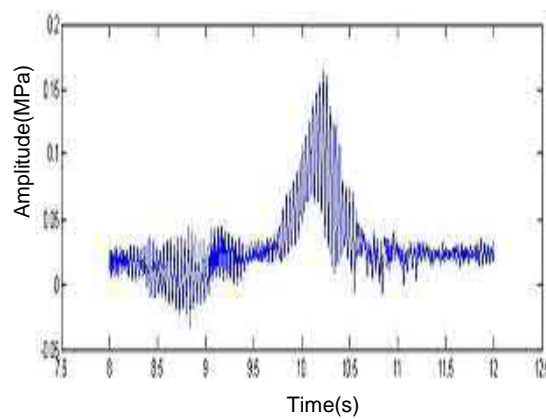
designed filter [3, 9], as long as the cut-off frequency of the signal is known. Then, the de-noised signal can be obtained in the time-domain through the Inverse Fourier Transform.

By low-pass filtering signal $y(t)$, we can obtain the signal $x(t)$ as follows:

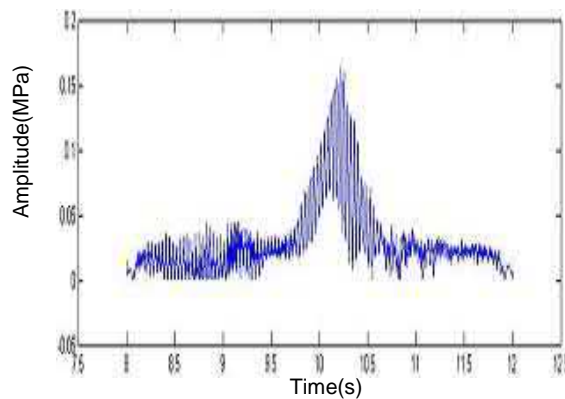
$$x(t) = IFFT(Y(\omega)W(\omega)) \quad (1)$$

Where $W(\cdot)$ is window function.

The spectra of the signal and noise overlap in most cases. Low-pass filtering can remove high-frequency noise but low frequency noise is still mixed with the signal and is difficult to separate. The influence of the noise spectrum is more obvious when the SNR is low. Therefore, the de-noising effect of the low-pass filter degrades greatly with the decrease of the SNR.

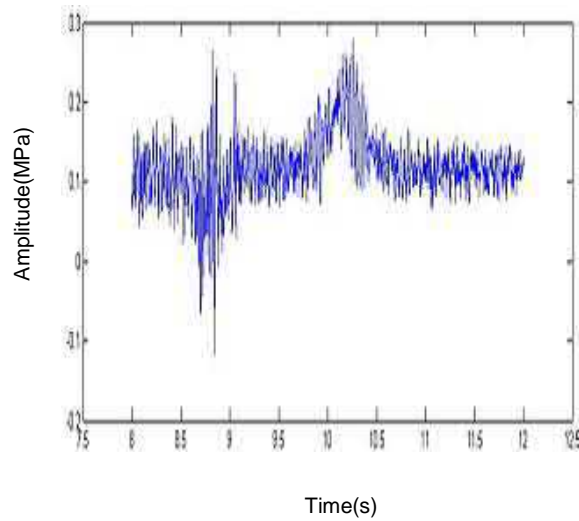


(a) Noisy compressive stress signal

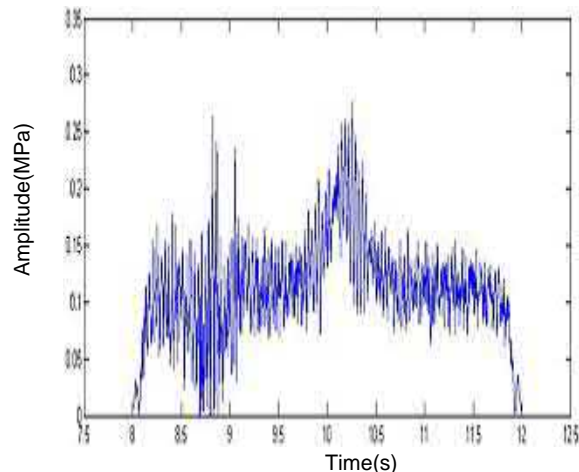


(b) Signal de-noised through frequency domain low-pass filtering

Fig. 2 - Low-pass filtering of noisy signal S1



(a) Noisy compressive stress signal



(b) Signal de-noised through frequency domain low-pass filtering
 Fig.3 - Low-pass filtering of noisy signal S₂

The vibration compaction operating parameters show that the main frequency of the signal is close to 30Hz. Therefore, the width of the pass-band of the low-pass filter applied was about 30Hz with a width of 35%. Figure 2(a) shows the compressive stress signal S₁ with small noise, Figure 3(a) shows compressive stress signal S₂ with heavy noise, Figure 2(b) and Figure 3(b) shows the de-noised signals S₁ and S₂ through the low-pass filter.

Comparing the de-noised result of Figure 2(b) with that of Figure 3(b), it can be seen that the de-noising effect is not significant when the noise is small, and we cannot reconstruct the ideal compressive stress signal through low-pass filtering when the noise level is high. This is because the compressive stress signal of the soil during vibration compaction is a mutation signal and contains high frequency information which is useful for signal processing. However, the low-pass filter filtered out the high frequency components over $1.35 * 30\text{Hz}$ as noise. Therefore, the low-pass filter cannot separate high frequency components of the signal from the noise effectively.

2.2 Multi-resolution wavelet transform

2.2.1 Signal analysis principle of wavelet transform [10]

The wavelet transform is a novel signal analysis method gaining popularity in recent years [4,11-13], and it is widely used in de-noising of transient saltation vibration signals accompanied by noise.

Let $\psi(t) \in L^2(R)$, and $\hat{\Psi}(\omega)$ be the result of the Fourier transform of $\psi(t)$. If $\hat{\Psi}(\omega)$ meets the admissibility condition: $C_\psi = \int_{-\infty}^{\infty} \left(|\hat{\Psi}(\omega)|^2 / |\omega| \right) d\omega < \infty$, then we consider $\psi(t)$ as a basic wavelet function, through the scale transformations and translations of which a group of wavelet functions can be obtained.

$$\psi_{a,b}(t) = \frac{1}{\sqrt{|a|}} \psi((t-b)/a); a, b \in R, a \neq 0 \quad (2)$$

In Equation (2), 'a' is the scale factor which controls the time window width of the wavelet function, and 'b' is the displacement factor which controls the translation of the wavelet function on the time axis. The bigger |a| is, the wider the time window is and the narrower the frequency window is. It can be proved that the product of the time window width and the frequency window width of the wavelet function is constant.

The dyadic wavelet transform is used widely in practice. By letting $a = 2^j, b = 2^j \cdot k$, a group of dyadic wavelet functions can be obtained.

$$\psi_{j,k}(t) = 2^{-\frac{j}{2}} \psi(2^{-j}t - k); j, k \in Z \quad (3)$$

The wavelet transform of signal $f(t)$ is defined as:

$$W_f(j, k) = \langle f(t), \psi_{j,k}(t) \rangle = \frac{1}{2^j} \int_{-\infty}^{\infty} f(t) \cdot \psi(2^{-j}t - k) dt \quad (4)$$

From the perspective of signal processing, changes in 'a' are equivalent to a continuous change of the transmission bands of a band-pass filter and changes of 'b' are equivalent to the band-pass filtering of the signal at different times. By varying 'a', the signal can be observed through the wavelet transform on a wide time window (which corresponds to a narrow frequency window) at low frequency, but on a narrow time window (that is a wide frequency window) at high frequency. The local time-frequency characteristics of the wavelet transform are very suitable for the analysis of signals that change slowly at low-frequencies but rapidly at high-frequencies.

2.2.2 Wavelet transform principles for de-noising

The fundamental principle of wavelet transform for de-noising is to let some high-frequency components be zero selectively and retaining some useful frequency band, then reconstruct the signal through the wavelet reconstruction algorithm.

Mallat [4] proposed a multi-resolution wavelet transform based on a orthogonal wavelet basis. Let $\psi(n)$ be a wavelet function representing a band-pass filter, and $\phi(n)$ be a scaling function representing a low-pass filter. From the perspective of multi-resolution analysis, wavelet decomposition is equivalent to applying the low-frequency signal $c_{j-1,n}$ with scale $j-1$ through the band-pass filter $\psi(-k)$ and the low-pass filter $\phi(-k)$. Then, after downsampling, we can get a low-

frequency signal $c_{j,n}$ and a high-frequency signal $d_{j,n}$ with scale j . The principle of multi-resolution wavelet decomposition is shown in Figure 4.

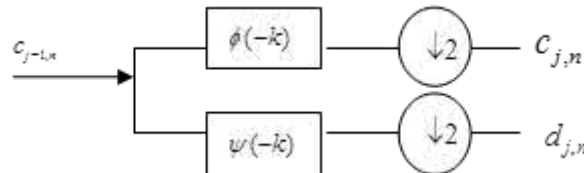


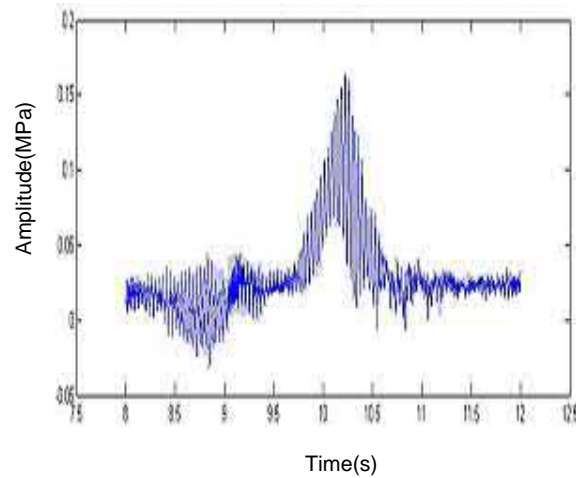
Fig.4 - Multi-resolution wavelet decomposition

The low-frequency signal can be decomposed step by step using a multi-resolution wavelet transform. In every decomposition, the signal can be divided into a low-frequency band and a high-frequency band. Let the frequency band of the original signal be $[0, f_{\max}]$. Then, for the k -th wavelet decomposition, the signal can be divided into a low-frequency band and a high-frequency band with respective ranges $[0, f_{\max}/2^k]$ and $[f_{\max}/2^k, f_{\max}/2^{k-1}]$.

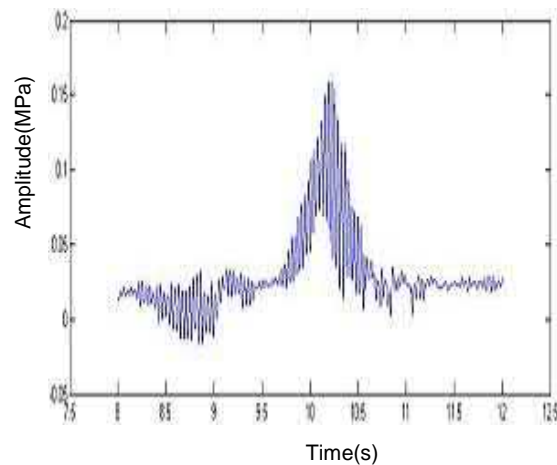
A signal can be decomposed into different frequency bands through multiple multi-resolution wavelet decompositions. By extracting the useful frequency band but suppressing the high-frequency band and applying the wavelet reconstruction algorithm, we can obtain the denoised compressive stress signal.

The vibration frequency of the vibratory roller was 30Hz in the test so, theoretically, the soil compressive stress signal should demonstrate a resonance peak value at about 30Hz. Therefore, the signal within this frequency band is useful and should be retained. In addition, because of the nonlinear characteristics of the vibration, the compressive stress signal not only includes the 30Hz frequency components, but other harmonic components such as those at 60Hz and 90Hz, etc, which should also be selectively retained. According to the sampling theorem, due to the fact that the sampling frequency of the stress signal in the test was 2000Hz, the frequency range analysed using the wavelet transform should be $[0, 1000\text{Hz}]$. Thus, based on the frequency band segregation theorem of wavelet decomposition, the signal should be decomposed to 5 levels.

According to the above analysis, we decomposed the noisy compressive stress signal using the sym8 orthogonal wavelet function to 5 levels. The frequency of the low-frequency signal at the fifth level is $[0, 31.25\text{Hz}]$, which should be completely retained, and the frequency bands of high-frequency signals at the other levels are respectively $[1000/2^k, 1000/2^{k-1}]$ Hz. We can dispose of the high frequency coefficient at different levels by choosing soft thresholds using adaptive thresholding based on the estimated noise levels at each decomposition level. Thus, the signal can be reconstructed by disposing the high frequency coefficients and retaining the low-frequency signal at the fifth level.



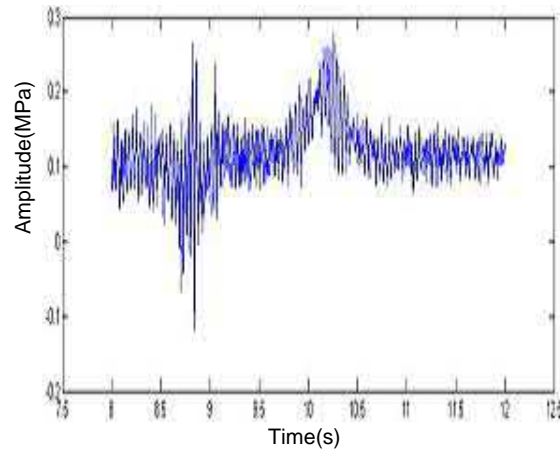
(a) Noisy compressive stress signal



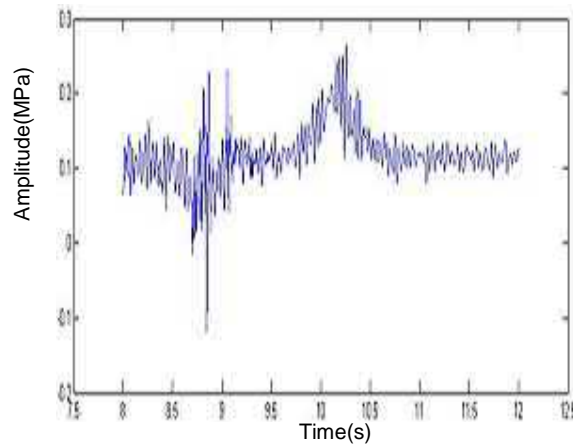
(b) Signal de-noised through the wavelet transform

Fig.5 - Signal S1 before and after application of the wavelet transform.

Figure 5(a) shows the noisy compressive stress signal S_1 , while 5(b) shows the wavelet transform de-noising result. Compared with Figure 2, the de-noising effect using the wavelet transform is better than that obtained using the low-pass filter, and closer to the ideal stress signal. Because the wavelet transform can selectively retain some high frequency information, it is more effective in retaining the high frequency characteristics of signal.



(a) Noisy compressive stress signal



(b) De-noised signal through wavelet transform

Fig.6 - Signal S₂ before and after application of the wavelet transform

Figure 6 shows the wavelet transform de-noising result for signal S₂. It can be seen when noise levels are high, the wavelet transform can remove some noise but cannot reconstruct the ideal original signal. This is because the wavelet transform method is based on the assumption that the spectrum band of the noise and the signal can be separated in the multi-resolution decompositions; this is approximately correct only when the SNR is high. When the noise is of narrow spectrum, its influence can be ignored even its spectrum overlaps with that of the signal. However, when noise level is higher, the influence of the overlapping spectrum cannot be ignored. Therefore, the wavelet transform is only suitable for de-noising signals with a high SNR, as the result is not reliable when the SNR is low and the signal and noise spectra overlap.

2.3 Spectrum subtraction

The fundamental principle of spectrum subtraction is that we subtract the power spectrum of the noise from that of the signal in frequency domain, then obtain the power spectrum estimation of the de-noised signal [5,14-16]. It is essentially a modification of the amplitude of signal by subtracting from its power spectrum while retaining the original phase information. Then, the de-noised signal in the time-domain can be obtained through the Inverse Fast Fourier Transform (IFFT).

Suppose $s(n)$ is an ideal signal and $y(n)$ is an actual observation signal; then

$$y(n) = s(n) + d(n), \quad (5)$$

where $d(n)$ is the additive noise.

When the signal and the noise are stationary random processes, the cross-correlation function $R(\tau)$ and power spectral density function $P(\omega)$ of the signal are related through the Fourier transform. In this case, the power spectrum of the signal is defined as the modular square of the Fourier transform of the signal, which represents its energy density, that is:

$$P_Y(\omega) = |Y(\omega)|^2 = |FFT(R_Y(\tau))|^2, \quad (6)$$

However, $R_Y(\tau) = E(Y(n)Y(n + \tau)) = E[(s(n) + d(n))(s(n + \tau) + d(n + \tau))]$.

If the noise is uncorrelated with the signal, it can be deduced that:

$$R_Y(\tau) = E[s(n)s(n + \tau)] + E[d(n)d(n + \tau)] = R_s(\tau) + R_d(\tau) \quad (7)$$

By applying the Fourier Transform to both sides of Eq. (7), it can be deduced that:

$$|Y(\omega)|^2 = |S(\omega)|^2 + |N(\omega)|^2 \quad (8)$$

The estimated value of the power spectrum of the signal can be obtained using power spectrum subtraction:

$$|\hat{S}(\omega)|^2 = |Y(\omega)|^2 - |\hat{N}(\omega)|^2 \quad (9)$$

Where $\hat{N}(\omega)$ is the estimated value of the power spectrum of the noise, which can be approximated using the variance of the noise.

It can be concluded from Eq. (9) that:

$$|\hat{S}(\omega)| = |Y(\omega)| \cdot (\sqrt{1 - (|\hat{N}(\omega)| / |Y(\omega)|)^2}) \quad (10)$$

Suppose $G = \max(\varepsilon, \sqrt{1 - (|\hat{N}(\omega)| / |Y(\omega)|)^2})$

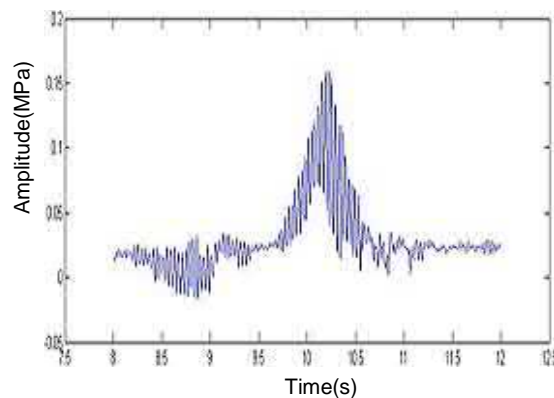
Where ε is a small positive constant. Then:

$$|\hat{S}(\omega)| = |Y(\omega)| \cdot G \quad (11)$$

The estimation of the reconstructed signal can be obtained through IFFT but retains the original phase information of signal, that is:

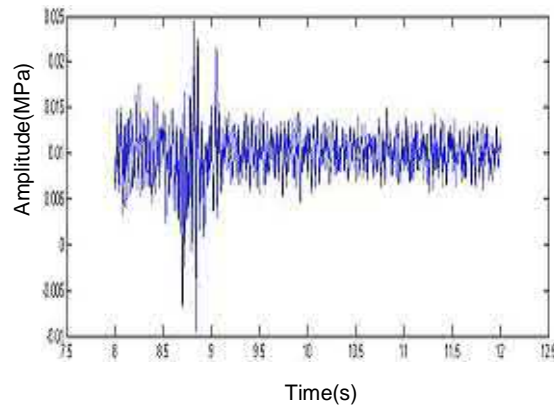
$$\hat{s}(n) = IFFT(|\hat{S}(\omega)| \cdot e^{i\theta}) \quad (12)$$

where θ is the phase function of the original noisy signal. In practice, the compressive stress signal is non-stationary, but each signal segment can be regarded as stationary and can be reconstructed using spectrum subtraction by processing short-time windowing segments in the time-domain.



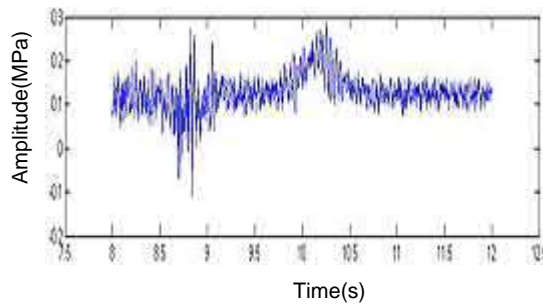
(a) Ideal compressive stress signal

Fig.7 - Ideal compressive stress signal and noise signal

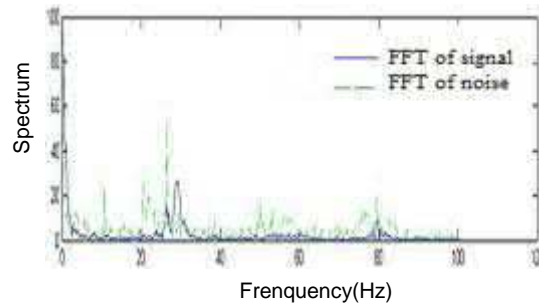


(b) Noise signal

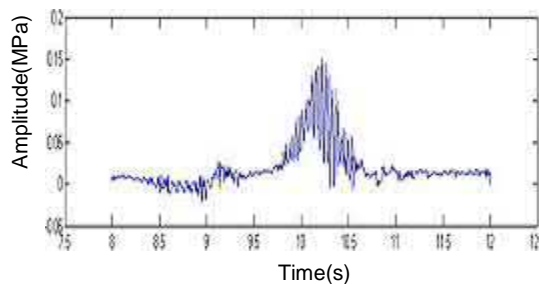
Fig.7 - Ideal compressive stress signal and noise signal



(a) Noisy compressive stress signal



(b) Spectrum of signal and noise

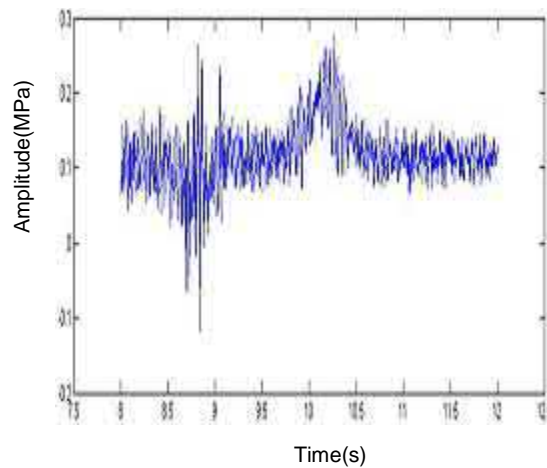


(c) Signal de-noised through spectrum subtraction

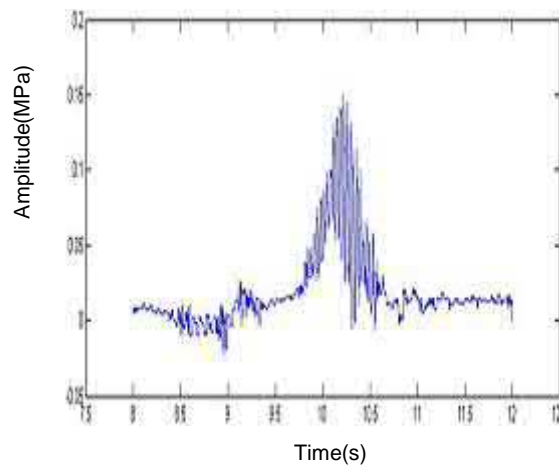
Fig.8 - The original signal, its spectrum and the signal de-noised through spectrum subtraction

The de-noising performance of spectrum subtraction is verified for a segment of a simulated signal. Suppose Figure 7(a) is an ideal compressive stress signal. After the addition of the noise

signal shown in Figure 7(b), we obtain the noisy signal shown in Figure 8(a), whose waveform is distorted seriously because of the noise. Figure 8(b) shows the spectra of the signal and noise which overlap. Figure 8(c) shows the signal de-noised through spectrum subtraction, where it can be seen that the de-noised signal is very close to the ideal compressive stress signal. Therefore, spectrum subtraction performs well when removing strong background noise.



(a) Noisy signal



(b) Signal de-noised through spectrum subtraction

Fig.9 - De-noised signal of noisy signal S₂ through Spectrum subtraction

Figure 9 shows signal S₂ de-noised through spectrum subtraction. The result shows that the de-noised signal has the characteristics of the compressive stress signal and is very close to its ideal form. Obviously, the de-noising results obtained through spectrum subtraction are superior to those obtained using the wavelet transform shown in Fig. 6. Therefore, when the SNR is lower, spectrum subtraction can be used to recover the ideal compressive stress signal even if the signal and the noise spectra overlap.

2.4 Independent component analysis (ICA)

ICA assumes that N source signals are statistically independent instantaneously, there is only one Gaussian-distributed signal at most in the source signals and that the received signal is a linear mixture of these N source signals. The ICA algorithm is essentially an optimization problem. The mixed signal is decomposed into independent components when the degree to which the

components are non-Gaussian reaches a maximum value. Every component obtained is a source signal [6,17-21].

Suppose $x = (x_1, x_2, \dots, x_m)^T$ is the m -dimensional random observation signal vector, which is a linear combination of n independent source signals s_j in the source signal vector $s = (s_1, s_2, \dots, s_n)^T$. Then, we can write

$$x = Hs = \sum_{j=1}^n h_j s_j, j = 1, 2, \dots, n \quad (13)$$

In Eq. (13), H is an unknown $m \times n$ full-rank hybrid matrix. The ICA algorithm is used to estimate the separation matrix W , and the output that represents the source signal obtained by separating $x(t)$ using W is

$$y(t) = Wx(t) = WHs(t) = Gs(t) \quad (14)$$

The separation can be achieved by solving for the optimal G .

The central limit theorem of probability theory states that the probability distribution of sum of each independent random variable tends to be a Gaussian distribution. For the signal under consideration, the higher degree to which the components are non-Gaussian, the higher their mutual independence. Therefore, the signal is decomposed based on the non-Gaussianity measure of the resulting components. When the measure reaches a maximum, this indicates that each independent component has been completely separated. The non-Gaussianity measure can be represented using a probability density function $p(y)$ and the Kullback–Leibler divergence of the Gaussian distribution with the same covariance matrix, which is called negentropy. The negentropy of a random variable y is defined as:

$$N_g(y) = H(y_{Gauss}) - H(y) \quad (15)$$

where $H(y) = -\int p(x) \lg p(x) dx$ is the comentropy of y . $H(y_{Gauss})$ is the comentropy of a Gaussian distribution which has the same covariance matrix with y . According to information theory, the random variable of Gaussian distribution which has the same variance also has the maximum comentropy. The more non-Gaussian y is, the higher of the value of $N_g(y)$. The approximation equation of negentropy in practical applications is defined as follows:

$$N_g(y) = \sum_{i=1}^P k_i \{E[G_i(y)] - E[G_i(v)]\}^2 \quad (16)$$

where k_i is the constant greater than zero; v is the Gaussian random variable that obeys the $N(0,1)$ distribution; and G_i is a non-quadratic function.

In order to maximize the upper equation, according to the Kuhn-Tucker condition, when $E[G(W^T x)^2] = \|W\|^2 = 1$, the optimal value should satisfy the following equation:

$$E[xg(w^T x) - \beta x] = 0. \quad (17)$$

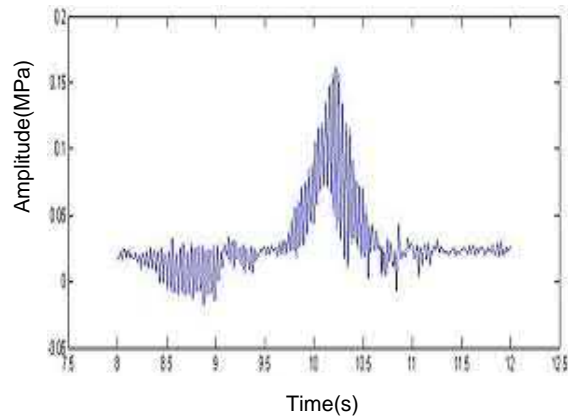
Therefore, the recursion formula of the ICA algorithm can be obtained as follows:

$$w^+ = w - \{E[xg(w^T x)] - \beta w\} / \{E[g'(w^T x)] - \beta\}$$

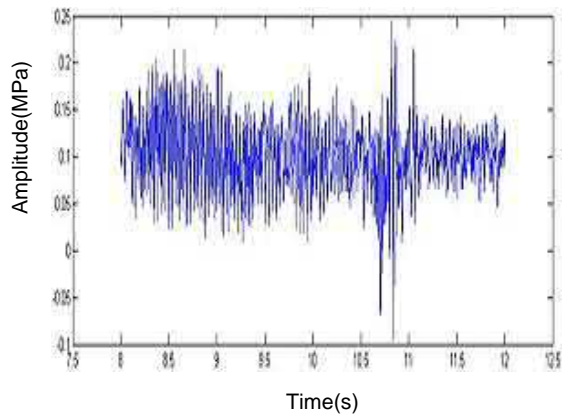
$$w_{new} = \frac{w^+}{\|w^+\|} \quad (18)$$

where $\beta = E[w^T xg(w^T x)]$.

According to the principle of independent component analysis, when the observed data are a random mixture of real signal and noise, they can be separated using the ICA algorithm.

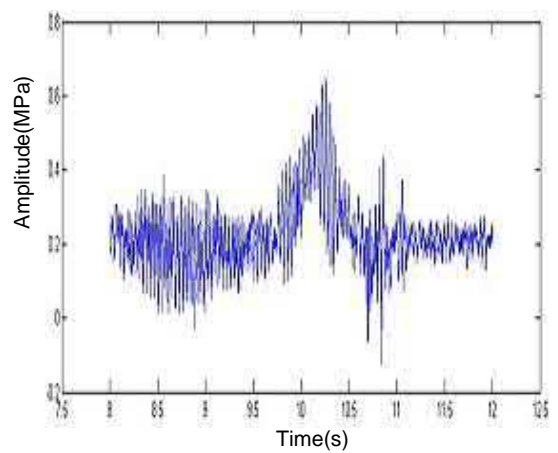


(a) Ideal compressive stress signal



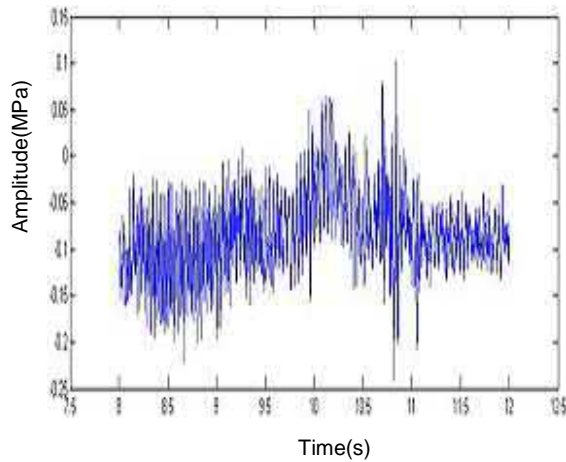
(c) Noise signal

Fig.10 - Ideal compressive stress signal and noise signal



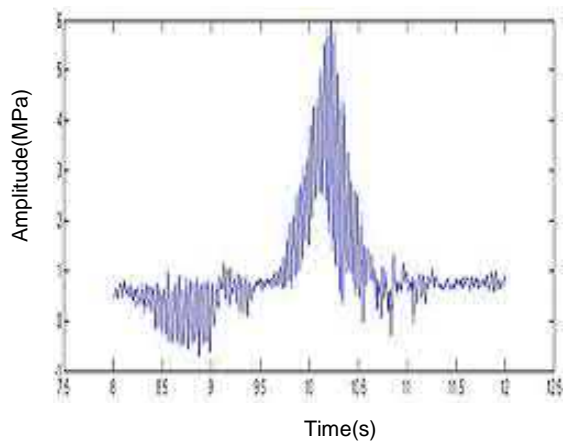
(a) Mixed-signal 1

Fig.11 - Two mixed-signals

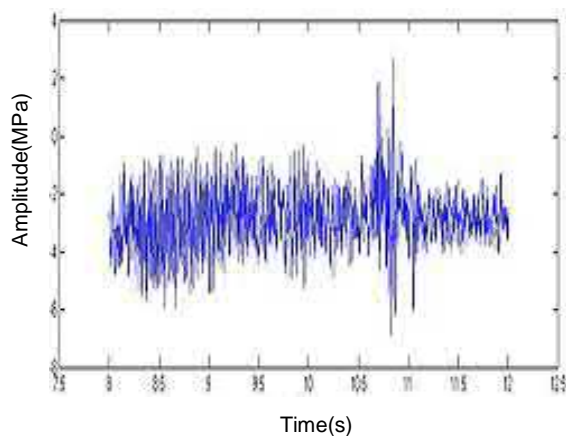


(b) Mixed-signal 2

Fig.11. Two mixed-signals



(a) Isolated stress signal



(b) Isolated noise

Fig.12 - Separation of signal and noise through ICA

Figure 10(a) shows an ideal compressive stress signal, while 10(b) shows a noise signal obtained by extracting and amplifying the time-domain signal from a real compressive stress signal during the stable period. If the noise is independent from the original signal, the signal received by

the system is a random mixture of compressive stress signal and noise, as shown in Figure 11(a) and Figure 11(b), where the two signals are shown after being mixed randomly. Figure 12 shows the separation results of signal and noise obtained through the fast ICA algorithm. In Figure 12(a), it can be seen that the compressive stress signal was successfully separated from the two mixed-signals, and is close to the ideal compressive stress signal. Figure 12(b) shows the separation result of the noise signal.

3. CONCLUSION

This paper studied the principled and applicability of several de-noising methods for the soil compressive stress signal during vibration compaction, with applications on both low- and high-SNR signals. According to the above analyses, the following can be concluded:

1) Traditional low-pass filtering methods assume that the signal and noise are in different frequency bands, so using appropriately designed filters, noise can be removed while retaining the useful signal. When the noise level is low and the frequency band of noise does not overlap with that of the signal significantly, a low-pass filter can separate noise from the signal in frequency domain effectively. However, this method is not applicable when the spectrum of the signal overlaps with that of the noise.

2) The multi-resolution wavelet transform can decompose the signal into different frequency bands, and effectively remove the noise by extracting the signal from the useful frequency bands. However, these methods are based on the assumption that the spectrum band of noise and signal can be separated during the multi-resolution decompositions. This assumption does not hold when the SNR is lower and the spectrum of the noise and signal significantly overlap. In this case, the de-noised result is not reliable. Therefore, the wavelet transform is widely used for signals with a higher SNR.

3) Spectrum subtraction methods require that the noise is statistically stationary. Because spectrum subtraction takes full advantage of the statistical characteristics of the signal and the noise, it can remove the strong background noise. Spectrum subtraction can be applied to remove strong statistically stationary background noise, even in cases where the SNR is lower and the spectrum of the noise and signal overlap significantly.

4) ICA assumes that a multi-channel signal is a random mixture of N independent source signals. When the signal received is such a random mixture of the ideal signal and noise, the ICA algorithm can separate the noise from the signal accurately. In particular, if N independent observation channels received meet the assumption of instantaneous independence, the N -channel original signal can be directly extracted from N -channel noisy observation data through the ICA algorithm. ICA is applied in cases of broadband noise, low SNR and considerable spectrum overlap between signal and noise.

In conclusion, when the noise is small, using the multi-resolution wavelet transform can yield better de-noising results; when the noise level is high and the effect of spectrum overlapping between noise and signal cannot be ignored, spectrum subtraction or ICA algorithm should be used to remove the noise based on the specific signal processing system and the characteristics of the signal and the noise.

REFERENCES

- [1] He Bin.,2002. Visual C++ digital image processing [M].Beijing: Posts and Telecommunications Press.
- [2] Zhang qingzhe.,2010. Study on the Model and Parameters of the Vibration Compaction Systems in the Soil Subgrade[D].Xi'an: Chang'an University.
- [3] Oppenheim A V, Willsky A S, Nawab S H, et al.,2012. EE202 Signals and Systems Fall 2012[J].
- [4] S. G. Mallat.,1989. Multifrequency channel decompositions of images and wavelet models. IEEE Transactions on Acoustics, Speech and Signal Processing. 37(12): 2091- 2110.

- [5] S Boll.,1979. Supp ression of acoustic noise in speech using spectral subtraction[J]. Acoustic Speech and Signal Processing, IEEE Transactions, 27 (2) : 113 - 120.
- [6] Comon P.,1994. Independent component analysis—a new concept Signal Processing. 36: 287-314.
- [7] Yao Yunshi, Xiao Gang, Dong Xiuhui, Feng Zhong-xu.,2006. Experimental Study of Doubl-e Frequency Composed Vibrating Compaction[J], China Journal of Highway and Transport,19(1):122-126.
- [8] PRC National Standard,Vibratory Roller Performance Test Methods (GB4478-1995) [S].1995. China Standards Press.
- [9] Ditommaso R, Mucciarelli M, Ponzio F C.,2012. Analysis of non-stationary structural systems by using a band-variable filter[J]. Bulletin of Earthquake Engineering, 10(3): 895-911.
- [10] Cheng Zhengxing., 2000.The Wavelet Analysis Algorithm and Application[M]. Xi 'an: Xi 'an jiaotong University Press.
- [11] Killick R, Eckley I A.,2013. Jonathan P. A wavelet-based approach for detecting changes in second order structure within nonstationary time series[J]. Electronic Journal of Statistics. 7: 1167-1183.
- [12] Chen Y M, Zi Y Y, Cao H R, et al.,2014. A data-driven threshold for wavelet sliding window denoising in mechanical fault detection[J]. Sci China Tech Sci, 57: 589~597.
- [13] Tao Ke, Zhu Jianjun.,2012. A comparative study on validity assessment of wavelet de-noising[J]. Journal of Geodesy and Geodynamics, 2: 128~133.
- [14] Upadhyay N, Karmakar A.,2013. Spectral Subtractive-Type Algorithms for Enhancement of Noisy Speech: An Integrative Review[J]. International Journal of Image, Graphics and Signal Processing (IJIGSP), 5(11): 13.
- [15] P Lochwood, J Boudy.,1992. Experimentswith a nonlinear spectral subtractor (NSS) , hiddenMarkov models and p rojection for robust recognition in cars [J]. Speech Communication, 11 (6) : 2 15- 228.
- [16] Zhu Jianhua, Tian Lan., 2013. Research on New Speech Denoising Based on Spectral Subtraction and Wavelet Threshold Method[J]. Coal Technology, 01: 171~173.
- [17] Hyvarinen A, Karhunen J, Oja E.,2001. Independent Component Analysis. John Wiley, New York.
- [18] Ella Bingham, Aapo hyvarinen.,2000. A fast fixed-point algorithm for independent component analysis of complex valued signals[J]. International Journal of Neural Systems, Vol.10, No.1(2000)1-8.
- [19] Comon P, Jutten C.,2010. Handbook of Blind Source Separation: Independent component analysis and applications[M]. Access Online via Elsevier.
- [20] Frappart F, Ramillien G, Leblanc M, et al.,2011. An independent component analysis filtering approach for estimating continental hydrology in the GRACE gravity data[J]. Remote Sensing of Environment, 115(1): 187-204.
- [21] P. Capuano,E. De Lauro,S. De Martino,M. Falanga.,2016. Detailed investigation of Long-Period activity at Campi Flegrei by Convolutive Independent Component Analysis[J]. Physics of the Earth and Planetary Interiors, 253: 48~57.

STUDY ON THE INFLUENCE OF BOLT ANCHORED CATENARY ON TUNNEL LINING UNDER THE AERODYNAMIC LOAD

Zhong-xin Ren¹, Hong Guo² and Yong-tao Su¹

1. *Northeast Forestry University, Harbin 150040, China.*
2. *Beijing Municipal Engineering Research Institute, Beijing 100037, China, email: 18515251290@163.com*

ABSTRACT

In order to study the influence of Bolt anchored catenary on tunnel lining under the aerodynamic load, the paper takes a tunnel on Qinhuangdao -Shenyang Railway as an example. The force of lining structure is studied using numerical simulation based on the research and analysis of relevant theory and model test results. Firstly, the variation of the air pressure in the tunnel was calculated caused by the train when it is passing through the tunnel at different speeds (200 ~ 400km/h). Then, by ANSYS the aerodynamic load calculated by FLUENT is applied to the simplified catenary suspension. The main results are as follows: 1. The maximum normal stress of tunnel lining with train speed according to the power law, and maximum normal stress with train speed according to quadratic function relation; 2. Tunnel lining is subjected to push-pull stress because the magnitude and direction of aerodynamic loads change with the advance of the train; 3. The lining structure is mainly subjected to the stress of the Y direction, and this stress should not be neglected when design the structure of tunnel secondary lining. 4. The load spectrum of the lining structure under different train speed is given. The research results of this paper are of great significance to the optimization design of tunnel lining structure.

KEYWORDS

High-speed train, Tunnel lining, Aerodynamics load, Suspended ancillary facilities, Tension and compression cycle

1. INTRODUCTION

It is expected that in 2020, China's high-speed railway mileage will reach 30,000 km, at the same time; the high-speed railway tunnel construction scale will increase with the increasing mileage of high-speed rail in mountainous China. With the increase of the train speed, the aerodynamic effect of the tunnel is more and more obvious, and out of the consideration of the comfort of high-speed railway train, the tunnel construction and the economy of the vehicle manufacturing, many experts in domestic and overseas have conducted a series of numerical simulations, model tests and field experiments on tunnel aerodynamics. For example: Miyachi T and Ozawa S [1], Cross D and Hughes B [2], Luo Jianjun [3-4] Ma Weibin et al. [5-7] improved the computational theory of tunnel aerodynamics further through the numerical simulation study.

In order to ensure the normal operation of the train, the catenary fittings are essential as part of power supply facilities. When the train passes through the tunnel, catenary suspension will also be affected by the aerodynamic effect of the tunnel. Shi Chenghua, Yang Weichao, Wang Zhaowei [8-11] et al. found that long-term aerodynamic loads will accelerate the damage of the attachment fixtures. As for the current situation of railway tunnel design in our country, during the design of the lining structure, the influence of the catenary on the lining under the action of aerodynamic load is not considered. With the increase of railway tunnels in recent years, the

problems are more and more serious. The authors have found that the connection between the auxiliary facilities and the tunnel lining is where the lining cracks begin to form in many tunnels.

In this paper, the bolt anchored catenary in a tunnel of Qinhuangdao -Shenyang railway is studied. Firstly, the ICEM CFD is used to establish a high-speed railway tunnel model whose length is 1000m and blocking ratio is 0.1102 (The train model is CRH_{380A}, the cross sectional area of the tunnel is 100m²). Secondly, the air pressure in tunnel will be acquired by FLUENT when the train speed is 200km / h, 250km / h, 300km / h, 350km / h, 380km / h and 400km / h. Then the ANSYS is used to establish the simplified catenary suspension model and the influence of the catenary on tunnel lining under the action of aerodynamic load is also studied. Last but not least, the load spectrum of the lining structure under different train speed is given, and the load should be considered in combination with the passage frequency of the tunnel when design the secondary lining. The research results of this paper will make a great significance to the design or partial strength of the high-speed railway tunnel lining.

2. AERODYNAMIC LOAD CALCULATION BASED ON FLUENT

Firstly, a numerical model is established according to the data provided by the relevant scholars of Central South University. In order to make the calculated aerodynamic load close to reality, the aerodynamic load calculation model is verified and related calculation parameters is adjusted by comparing with the model test data in the laboratory. Linearity reduced scale of this model test is 1/17.6. The train model is CRH380A and the length of it is 2.92m. The length and sectional area of tunnel are 28m and 0.258 m² respectively. The speed of train is 55.98m/s, the measure point is about 14.2m away from the entrance of tunnel. In order to make the results as accurate as possible, calculate time step size is 0.0005s. Figure 1 shows the test and calculated value.

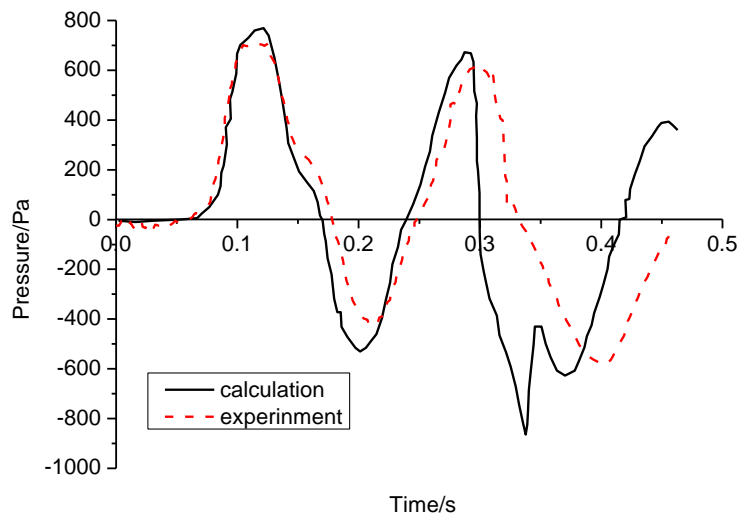


Fig. 1 - Comparison between the test value and the calculated value

As we can see from Figure 1, the difference between the maximum positive pressure obtained from numerical simulation and the model test result is less than 5%. It shows that the parameter setting and the model of numerical simulation are in accord with the actual situation.

Then, the aerodynamic load of CRH_{A380} train caused when going through the tunnel whose cross section is 100m² at different speeds is analyzed by the numerical simulating calculation. According to the results of real vehicle test and numerical simulation, the maximum aerodynamic load is obtained within the range of 100m ~150m from the tunnel entrance. Taking the most

unfavorable situation into account, in this paper, the measuring point of aerodynamic load is set at 120m from the entrance in the tunnel, the calculated results are as shown in Figure 2.

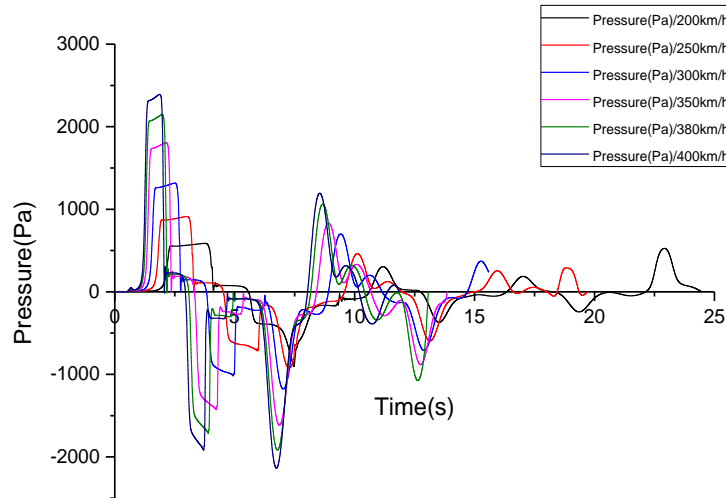


Fig. 2 - Calculation results of aerodynamic loads at different speeds

3. ANSYS COMPUTING MODEL

3.1 Stress analysis of lining

When the tunnel is opened to traffic, the lining structure will be interacted with external loads, such as the surrounding rock pressure, water force and so on, and form a stable tertiary stress field. The bolt anchored catenary is directly fixed on the secondary lining structure by bolts, as shown in Figure 3.

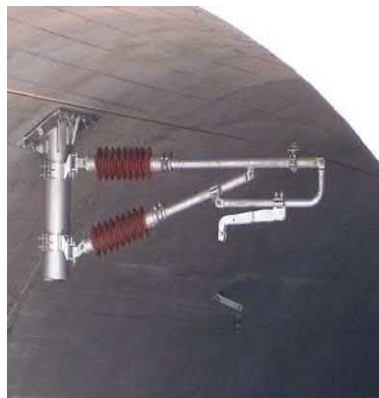


Fig. 3 - Bolt type contact net hanger after installation

Due to the limited space inside the tunnel and the compressibility of air, when high speed train passing through the tunnel, catenary becomes obstacles to train wind, therefore, it will be affected by the aerodynamic load, and all these forces are eventually passed on to the tunnel lining. For the lining structure, the stress direction of the lining structure is along the tunnel axial (X direction) and perpendicular to the tunnel axial (Y direction). This force is only applied to the lining when the train passes, and the size and the direction change with the time. In order to make statistic more convenient, this study determines the positive direction of x and y are as shown in Figure 4, that is, when the y-direction stress is positive, the lining structure is subjected to tensile stress.

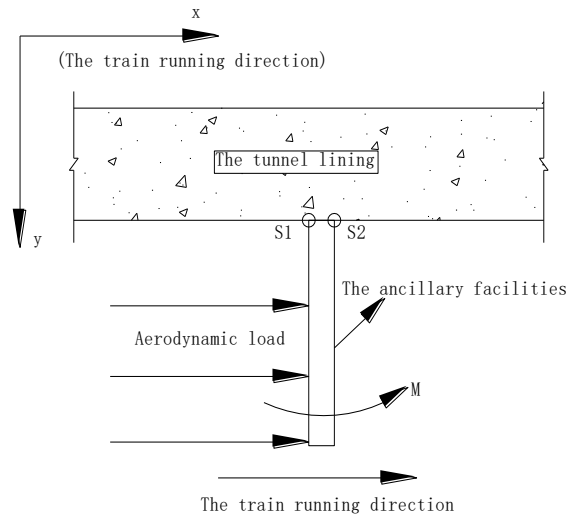


Fig. 4 - Force analysis and measuring point position of bolt anchored catenary under aerodynamic load

3.2 ANSYS APDL simulation implementation process

After making a force analysis of the bolt anchored catenary, the model is established and the grid is divided by ANSYS Parametric Design Language. PLANE42 is used for the unit type of Lining structure and Bolt anchored catenary. The lining concrete is C35 concrete, the density is 2425kg/m^3 , Elastic modulus is $2.83.15 \times 10^4\text{MPa}$, Poisson's ratio is 0.2, material of bolt anchored catenary is Q335. In order to facilitate the calculation, the connection between the tunnel lining and the suspension is set to perfect contact. [9]

Then, the aerodynamic load caused by the train are calculated by FLUENT. The calculated aerodynamic load is applied as a force varying with time to catenary by means of transient analysis, in order to analyze the stress of secondary lining and monitor the stress at the connection point between the lining and catenary. The simplified model and the numerical simulation of the stress distribution of the bolt anchored catenary are shown in Figure 4.

The length of bolt anchored catenary is 500mm in Qinhuangdao-Shenyang Railway. From the current research on the railway tunnel disease(), the lining structure is prone to crack where the suspension is located. The measuring points are as shown in Figure 4 (S1 and S2). The simplified two-dimensional model is established to monitor the X-direction and Y-direction stresses.

4. ANALYSIS OF NUMERICAL SIMULATION RESULTS

4.1 Basic law analysis

Using ANSYS APDL to simulate the X-direction and Y-direction's stress at the two measuring points, it is found that the magnitude of the stress at S1 and S2 are of small differences and are opposite in direction, so just monitor the stress at S1, and, the tunnel lining structure caused by bolt anchored catenary in the aerodynamic loads the directional change of stress is consistent with the aerodynamic loads. In order to save the length of the paper, taking the stress of the tunnel lining as an example at the train speed of 400km/h, the stress distribution of the lining structure is analyzed. The stresses in the tunnel structure are shown in Figures 5 and 6, the magnitude of the stress and its relation to the aerodynamic load are shown in Table 1.

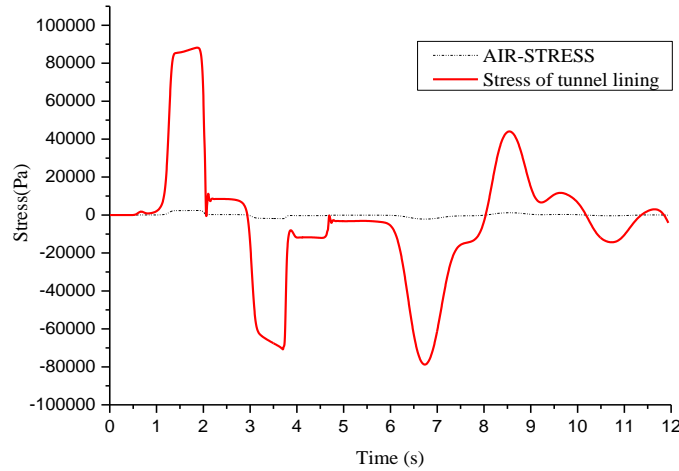


Fig. 5 - The stress of X direction when the train speed is 400km/h

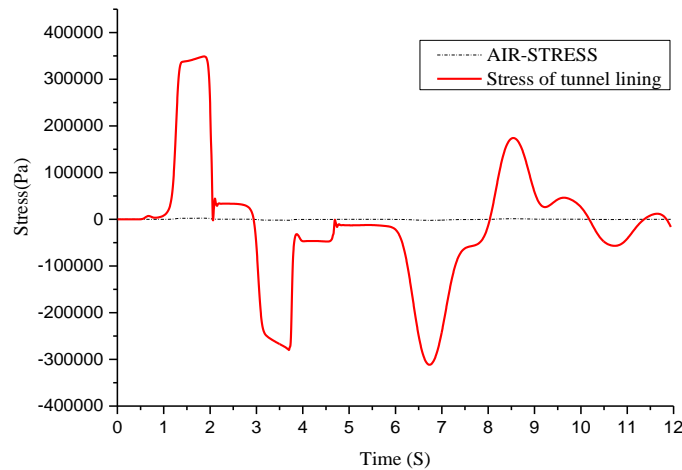


Fig. 6 - The stress of Y direction when the train speed is 400km/h

Tab. 1 - Peak stress of tunnel lining when the train speed is 400km/h

Time/s	AIR-STRESS AIR/ Pa	Stress direction	Peak stress	The relationship
1.87	2392	X	88215	$P=37* \text{AIR-STRESS}$
		Y	348901	$P=146* \text{AIR-STRESS}$
6.735	-2136	X	-78768	$P=37* \text{AIR-STRESS}$
		Y	-311537	$P=146* \text{AIR-STRESS}$

From Figure 5, 6 and Table 1, we can draw the following conclusions:

- (1) When the speed is 400km / h, the aerodynamic load in the tunnel reaches the maximum positive pressure (AIR-STRESS = 2392Pa) when $t = 1.87s$. At this time, the tunnel lining structure is subjected to the maximum horizontal force to the right and maximum pulling force under the action of aerodynamic load;

- (2) When $t = 6.735s$, the aerodynamic load in the tunnel reaches the maximum negative stress (AIR-STRESS = -2136 Pa). At this time, the tunnel lining structure is subjected to the maximum horizontal force to the left and maximum upward pressure under the action of aerodynamic load;
- (3) As shown in Figures 5 and 6, the stress of the lining structure caused by the passing of the train is a cycle of tension, compression and tension;
- (4) The X and Y directional stresses of the tunnel lining reach 37 times and 146 times of the aerodynamic load, respectively.

4.2 Analysis of lining stress without working condition

As shown in Figure 7 to 10, the maximum positive pressure and the maximum negative pressure curve of tunnel lining structure in the direction of X and Y are summarized.

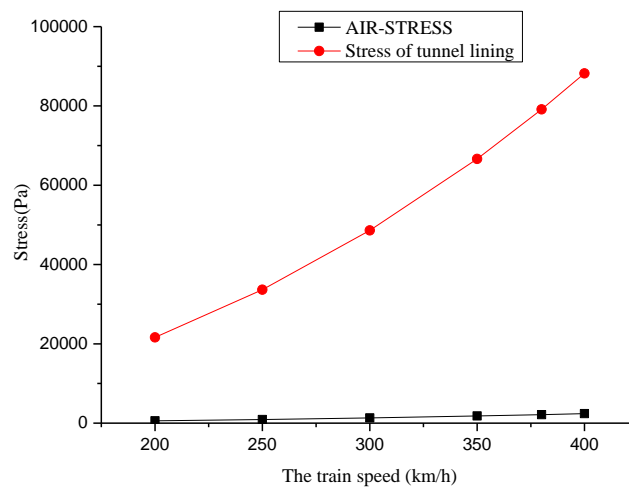


Fig. 7 - Maximum positive pressure in X direction of tunnel lining structure

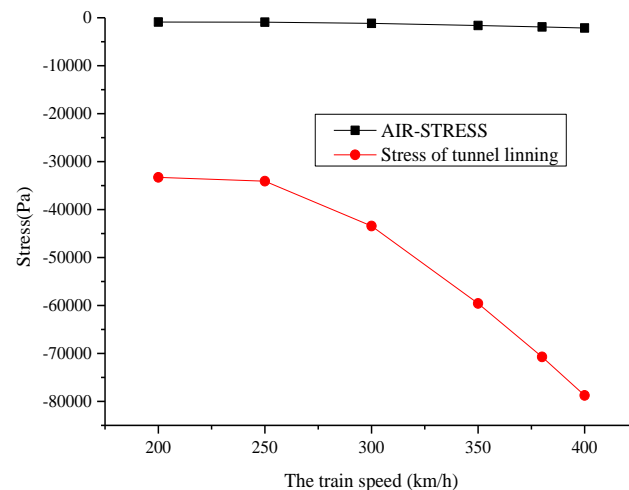


Fig. 8 - Maximum negative pressures in X direction of tunnel lining structure

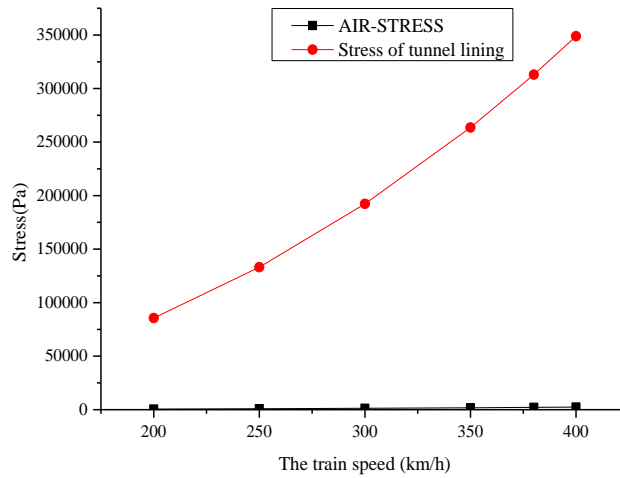


Fig. 9 - Maximum positive pressure in Y direction of tunnel lining structure

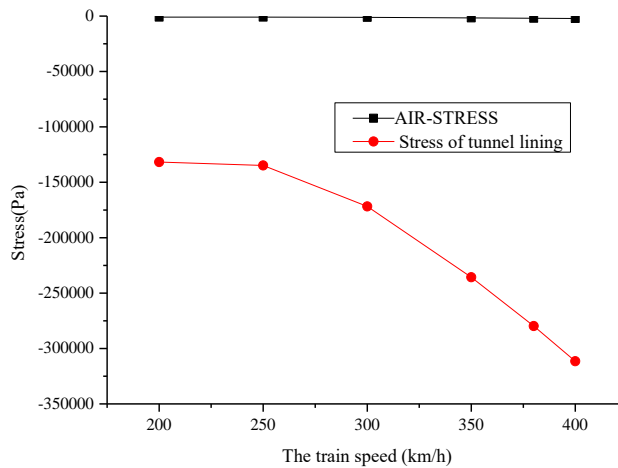


Fig. 10 - Maximum negative pressure in Y direction of tunnel lining structure

As shown in Figure 7 and Figure 10, we can see that the stress value of the tunnel lining has a great relationship with the operation speed of the train, and the size and increasing rate of stress increase with the increase of train speed. The relation between the stress of the lining structure and the train speed is summarized as follows in Table 2.

Tab. 2 - Relationship between the stress of lining structure and train speed

Maximum positive stress in X direction	$P=0.4661 * x^{2.027}$
Maximum negative stress in X direction	$P=-1.2515x^2+516.87x-86067$
Maximum positive stress in Y direction	$P=1.8432 * x^{2.027}$
Maximum negative stress in Y direction	$P=-4.9499x^2+2044.3x-340407$

The load spectrum of the tunnel lining structure due to the suspension under different

speed is shown in Table 3. The load should be considered in combination with the passage frequency of the tunnel when design the secondary lining. It is worth noting that the stress of the lining structure caused by the passing of the train is a cycle of tension, compression and tension, therefore, the calculated traffic frequency of the train should be 2 times that of actuality.

Tab. 3 - The load spectrum of the tunnel lining structure due to the suspension under different speed

<i>Train running speed (km/h)</i>	<i>Maximum positive stress (Pa)</i>	<i>Maximum negative stress (Pa)</i>
200	85596	-131679.016
250	133150	-134773.641
300	192234	-171765.75
350	263598	-235658.328
380	313027	-279730.906
400	348901	-311536.75

5. CONCLUSION

Due to the compressibility of air and limited internal space in tunnels, the high-speed trains will induce a series of tunnel aerodynamic effect when going through, the trains and the tunnel structures and various ancillary facilities will be influenced by aerodynamic load. The paper takes a tunnel on Qinhuangdao-Shenyang Railway as an example, and the force of lining structure is studied by numerical simulation. The conclusions are as follows:

- (1) The compression wave will be generalized when high-speed trains going through the tunnels, the bolt anchored catenary will be affected by aerodynamic loads because they will become an obstacle when the compression wave moves forward. Being fixed by the affiliated facilities, the load will finally deliver to the tunnel lining structures.
- (2) The numerical simulation shows that the force imposed on the lining structures by affiliated facilities under the aerodynamic loads stress is mainly on Y direction, and the stress of the lining structure caused by the passing of the train is a cycle of tension, compression and tension.
- (3) When the train speed is 400 km/h, the stress of X direction is 88215 Pa, while Y- direction stress is 348901 Pa. with no consideration of aerodynamic load when designing the lining structures is obviously unreasonable.
- (4) The maximum normal stress of tunnel lining with train speed according to the power law, and maximum normal stress with train speed according to quadratic function relation;
- (5) Considering about the safety of the actual operation of the train and the complexity of the treatment of the tunnel structure disease, this paper has some reference values for the design of the lining structures of the high railway tunnels.

REFERENCES

- [1] Miyachi T, Ozawa S, Iida M, et al. Propagation characteristics of tunnel compression waves with multiple peaks in the waveform of the pressure gradient: Part 2: Theoretical and numerical analyses. Proceedings of the Institution of Mechanical Engineers Part F Journal of Rail & Rapid Transit, 2015, 35(2):220–235.
- [2] WOODS W A, POPE C W. Secondary Aerodynamic Effects in Rail Tunnels During Vehicle Entry// Proceedings of the Second International Symposium on the Aerodynamics and Ventilation of Vehicle

Tunnels. Cranfield: BHRA, Fluid Engineering, 1976:71-86.

- [3] Cross D, Hughes B, Ingham D, et al. A validated numerical investigation of the effects of high blockage ratio and train and tunnel length upon underground railway aerodynamics. *Journal of Wind Engineering & Industrial Aerodynamics*, 2015, 146(17):195-206.
- [4] LUO Jianjun. Aerodynamic Effect Induced by High-Speed Train Entering into Tunnel in High Altitude Area. *Journal of Southwest Jiaotong University*, 2016, (04):607-614.
- [5] LUO Jianjun. The Influences of Enlarged Sections and Ventilation Shafts on Pressure Waves in High-Speed Metro Tunnels. *Modern Tunnelling Technology*, 2016, (04):22-28.
- [6] LI Hongmei. Research on Distance between Tracks for Intercity Railway Based on Aerodynamics. *Railway Engineering*, 2016,(10):101-104.
- [7] CHENG Aijun, MA Weibin. Analysis of aerodynamics effect in changeable cross-section tunnel. *Railway Engineering*, 2016,(01):29-32.
- [8] ZHANG Fengyu, CHENG Shu. Development of wireless data acquisition system in real vehicle passing through tunnels during Aerodynamic tests. *Journal of Railway Science and Engineering*, 2016, (07):1401-1406.
- [9] POPE C W, GAWTHORPE R G, RICHARDS. An experimental investigation into the effect of train shape on the unsteady flows generated in tunnels// *The 4th International Symposium on the Aerodynamics and Ventilation of Vehicle Tunnels*. Cranfield Bedford England: BHRA, 1982. C2, 107-128.
- [10] SHI Cheng-hua, YANG Wei-chao, et al. Analysis of catenary's safety under train wind action in high-speed railway tunnel. *Journal of Central South University (NATURAL SCIENCE EDITION)*, 2012, (09):3652-3658.
- [11] SHI Cheng-hua, YANG Wei-chao, et al. Study on Aerodynamic Influence on Stability of Ditch Covers in High-speed Railway Tunnels. *Railway Transaction*, 2012,(01):103-108.
- [12] Briffaut M, Benboudjema F, D'Aloia L. Effect of fibres on early age cracking of concrete tunnel lining. Part I: Laboratory ring test. *Tunnelling & Underground Space Technology*, 2016, 59:215-220.
- [13] Briffaut M, Benboudjema F, D'Aloia L. Effect of fibres on early age cracking of concrete tunnel lining. Part II: Numerical simulations. *Tunnelling & Underground Space Technology*, 2016, 59:221-229.

INFLUENCE OF GLASS POWDER AND STEEL SLAG ON PROPERTIES OF CONCRETE: A REVIEW

Sajjad Ali¹, Zia ur Rahman¹, and Muhammad Kamran Khan²

1. Department of Civil Engineering, CECOS University of IT & Emerging Sciences Peshawar, Pakistan, email: ali.sd863@gmail.com, z.r.k891@gmail.com
2. Department of Transportation, National Institute of Transportation, National University of Sciences and Technology, Islamabad, Pakistan, email: kamran.tn17@nit.nust.edu.pk

ABSTRACT

To overcome the scarcity of natural resources as construction material and to reduce the hazards from industries, industrial wastes can play a very significant role. In this paper, the influence of glass powder and steel slag is reviewed. It is concluded that glass powder and steel slag can upset some portion of concrete thereby providing significant improvement in mechanical properties of concrete consequently reducing the environmental hazards from industries.

KEYWORDS

Concrete, glass powder, steel slag, mechanical properties

INTRODUCTION

Concrete is a mixture of cement, fine aggregate and coarse aggregate. Some chemical admixtures are also added to gain varied properties. According to a study 11 billion tons of concrete was consumed worldwide [1]. Concrete is the most important construction material but the production of cement is very energy consuming and is a major source of greenhouse gases [2]. The emission of greenhouse gas is approximately 7% from cement industry. Similarly due to rapid industrialization, the concrete industry is facing scarcity of natural resources as construction materials. The use of waste materials is the best possible alternative to overcome these problems. Much attention has been paid toward the use of waste materials in concrete.

Glass is one of the oldest man-made materials. According to a study 130 million tons of waste glass is produced in the world [3]. The use of glass powder in the concrete binds the aggregate together thereby increasing the strength of concrete. The particles of glass powder are very fine and act as a filler, resulting in lower porosity and improving the durability of concrete. Glass is amorphous in nature and contains large amount of silica. When the particle size is less than 75 μ m then they show pozzolanic properties [4]. The problem with the use of glass powder is its high content of silica, but according to studies, ground glass powder does not influence the alkali-silica reaction [5], [6].

To overcome the exploitation of natural resources and reduce the emission of CO₂, the use of steel slag in concrete can also play a vital role [7]. The production of steel yields 15-20% of steel slag [8]. Approximately 35% of steel slag is disposed as waste material [9]. In 2012, the worldwide production of steel slag was nearly 230 million tons. This disposed slag not only affecting agriculture and environment but also causes shortage of space for landfilling.

Extensive research work has been performed to replace the aggregates by steel slag and the results showed positive influence on concrete properties [10], [11], [12]. Some other researchers have also reported the beneficial role of slag on fire resistance of concrete [13][14]. Steel slag contain cementing properties due to high amount of silica and calcium, but due to low cooling process its hydration process is very low compared to normal cement [15]. Tsakiridis et al. [16] have utilized steel slag for production of Portland cement clinker. They concluded that 10% replacement of steel slag results no negative impact on quality of cement produced. Steel slag in fine form can be utilized as admixture for concrete [17].

EFFECTS OF GLASS POWDER ON PROPERTIES OF CONCRETE

Effect on workability

Raju and Kumar [18] studied the workability of concrete, replacing the cement with glass powder from 5% to 40%. The results indicated that increasing the content of glass powder, the workability decreased. Vandhiyan et al. [19] suggested the possible reasons for reduction in workability. According to their findings, the loss in workability may be due to angular particles and high surface area of glass powder. Topcu and Canbaz [20] studied the behaviour of waste glass in concrete. They concluded that the addition of waste glass marked no significant effect on the workability of concrete. The utilization of waste glass slightly reduced the workability of concrete. Pollery et al. [21] concluded that concrete made with waste glass require more water than ordinary concrete. Schwarz et al. [22] investigated the behaviour of plain and glass powder modified concrete. They reported increase in the workability as the content of glass powder was increased. The increase in the workability may be due to the non-absorbent nature of glass powder which leaves free water in the mixture. Castro and Brito [23] studied the workability of concrete containing glass as fine and coarse aggregate. They reported increase in the workability when glass was used as coarse aggregate but as fine aggregate, there was reduction in the workability.

Effect on compressive strength

Aliabdo et al. [1] studied the performance of concrete containing glass powder. They reported increase in the compressive strength up to 10% replacement of cement with glass powder. Beyond this level, no further improvement was observed in the compressive strength of concrete. Yu et al. [24] investigated the effect of glass powder in addition with steel slag on compressive strength of concrete. They concluded that the compressive strength of concrete increased as the age of concrete increased. They also investigated that the compressive strength become double when the water/cement ratio was decreased from 0.55 to 0.40. Patil and Sangle [25] studied the effect of particle size of glass powder on compressive strength of concrete. They concluded that for particle size less than 90 micron, the concrete compressive strength was higher as compared when particle size ranges between 90 and 150 micron. They proposed 20% replacement of cement with glass powder as the optimum value. Tuan et al. [26] used glass powder with sewage sludge in light weight concrete. They concluded that there was loss in the compressive strength. Terro [27] replaced fine and coarse aggregate with recycled glass and investigated the mechanical properties of concrete. He concluded that the compressive strength decreased up to 20% from its original strength as the temperature increased. Parghi and Alam [28] studied the properties of concrete with recycled glass powder. They concluded that compressive strength increased with age of concrete and percentage of recycled glass powder. The higher strength may be due to high content of silica and alumina dissolution which contribute to pozzolanic reaction. Lee et al. [29] studied the particle size as well as curing effect on concrete block containing fine glass powder. They concluded that compressive strength decreased as the particle size increased. There was almost 8.8% loss in compressive strength for 28 days at 25%

replacement level when particle sizes were greater than 2.38mm. When particle sizes were reduced to less than 600 μm , there was significant increase in compressive strength.

Effect on tensile strength

Madandoust and Ghavidal [32] studied the effect of glass powder with rice husk ash on splitting tensile of concrete for 7, 28, 42 and 90 days of curing. They concluded that the tensile strength increased with the age of concrete. They reported that the ratio of tensile strength of concrete containing glass powder with rice husk to tensile strength of normal concrete was 71% at 7 days and 97% at 90 days of curing condition. They further stated that this ratio could be affected by many factors like testing method, shape and size of coarse aggregate etc. Raghvendra [33] investigated in his research that replacement of cement with 20% glass powder and 40% foundry sand achieved higher tensile strength compared to ordinary concrete. Afshinnia and Rangaraju [31] concluded in their investigation that practice of glass powder as aggregate, increased the splitting tensile strength by 21% but when cement was replaced by glass powder there was 12% reduction in splitting tensile strength of 28 days curing. Aliabdo et al. [1] studied the tensile strength of concrete by replacing cement with glass powder. They reported large increase in the tensile strength which may be due to the enhancement in the properties of transition zone.

Effect on flexural strength

Jitendra and Saiji [34] concluded in their findings that up to 35% replacement of cement with glass powder, improvement was seen in flexural strength but the maximum value was attained at 20% replacement level. Similarly other researchers like Dali and Tande (2012) and Bhagyasri et al. (2016) have also proposed 20% of cement with glass powder as the optimum value for flexural strength of concrete. The study of Park et al. [30] showed that the addition of waste glass reduced the flexural strength of concrete. Raju and Kumar [18] studied the variation in flexural strength by replacing cement with glass powder. The results showed the highest strength of 27%, 20% and 17% compared to control mix at 7, 28 and 90 days at 20% replacement of cement by glass powder. Yu and Tao [24] concluded that the flexural strength increased with the age of concrete. Similarly when w/c ratio was reduced, large improvement was in the flexural strength for the same type of concrete.

Effect on modulus of elasticity

Madandoust and Ghavidal [32] studied the modulus of elasticity concrete containing glass powder. They concluded that modulus of elasticity increased as the concrete become older. The modulus of glass powder added concrete to normal concrete was 88% at 7 days and 97% at 90 days of age. They further stated that concrete containing glass powder and rice husk ash are less compact as compared to normal concrete which results in lower modulus elasticity of concrete, but for long term the modulus of elasticity increased. Yu and Tao [24] investigated the effect of water/cement of concrete containing glass powder in addition with slag. There was significant increase in modulus of elasticity of concrete when water/cement ratio was reduced.

Effect on alkali-silica reaction

Zheng [37] investigated the role of glass powder in controlling alkali-silica reaction in concrete. They concluded that the alkali concentration increased in the pores due to reaction of glass powder, fine glass grains induced alkali-silica reaction (ASR) expansion largely. This mitigation was due to the increase in alumina concentration in pores, which decrease the dissolution of reactive silica, hence controlling the alkali-silica reaction. Schwarz et al. [22] used flame emission spectroscopy and electrical conductivity and measured that small amount of alkalis

were released from glass powder into the pore solution. Cota et al. [38] measured the ASR expansion for 28 days, which varied from 0.011 to 0.427. They concluded that the largest expansion was measured for coarse glass particles.

EFFECT OF STEEL SLAG ON PROPERTIES OF CONCRETE

Effect on workability

Roslan et al. [39] studied the effect of steel slag along with steel sludge on workability of concrete at w/c ratio of 0.58. They concluded that as the steel slag content was increased, there was decrease in the workability. This decrease in workability may be due to rough surface of steel slag and steel sludge. Similarly they concluded that no segregation and bleeding were observed in placing and compacting the concrete. Netinger et al. [42] studied the increasing content of steel slag in the mixture and reported reduction in workability.

Effect on air content

Qasrawi [11] concluded from experiments that addition of steel slag increased the air content by 1.5-2 times the expected value for higher replacements of steel slag. These increases in the air content may be attributed to angular particle size of steel slag compared to natural aggregates. Netinger et al. [42] studied that the air content of reference concrete was 0.9% but increased to 2.8% due to addition of steel slag.

Effect on fresh concrete density

Khan et al. [40] investigated that the addition of steel slag increased the fresh density of control mix from 2400 kg/m³ to 2750 kg/m³. This is due to higher density of steel slag. Gonzalez-Oretga et al. [7] investigated concrete properties containing steel slag. They concluded that density of concrete steel slag was 25% higher than control mix. Huang et al. [41] studied the effect of steel slag on density of green artificial reef concrete. The density of artificial reef concrete was 2765 kg/m³, 15% higher than normal concrete density of 2400 kg/m³. The higher density may be attributed to higher the specific gravity of steel slag (3.39) compared to sand and gravel (2.4-2.9). This higher density may be effective against sea waves.

Effect on compressive strength

Gonzalez-Oretga et al. [7] studied the compressive strength of concrete containing steel slag. The results obtained for compressive strength were satisfying the minimum strength for 28 days of 30 MPa. The compressive strengths of concrete containing slag and control mix were ranging 45-50 MPa. There was 15% increase in strength between 28 days and 90 days. Anastasiou et al. [49] investigated the effects of steel slag with fly ash on compressive strength of concrete. The 28 days compressive strength was nearly equal to that of control mix. The highest strength of 58 MPa was obtained for 365 days, which was 17.5% more than control mix. Plankar et al. [46] studied the effects of steel slag as coarse aggregate on compressive strength of concrete. They observed loss in compressive strength when steel slag was added as coarse aggregate compared to control mix. This reduction may be due to coating of calcite on surface of aggregates which affects the bond between aggregates and paste [47]. Pang et al. [48] concluded from their investigation that compressive strength increased up to 20% by the addition of steel slag at 3, 7

and 28 days of curing. They also observed strength loss at curing age of 60 days. Qjang et al. [44] studied the mechanical properties of concrete at w/c ratio of 0.45 and 0.30. They concluded that compressive strength of concrete with 10% slag at 90 days and w/c of 0.45 was 2.4% higher than control mix. They concluded that compressive strength of high strength concrete is not much affected by addition of steel slag. The proposed 20% of cement replacement with steel slag the optimum value. Ghouleh et al. [45] investigated that contribution of steel slag as aggregate to compressive strength of concrete was similar to control mix. Qjang and Peiyu [43] observed that the early strength of reference concrete was higher than concrete having steel slag. After 7 days, the steel slag added concrete gets strength quicker than reference concrete. The 90 and 360 days strength of concrete with steel slag was higher than reference concrete.

Effect on tensile strength

Mengxiao et al. [50] compared the splitting tensile strength of concrete having fly ash and steel slag under temperature match curing condition. They investigated that the early age splitting tensile strength of concrete containing high volume of fly ash was higher than concrete with steel slag. The increase in later age splitting tensile strength of both type of concretes were nearly similar. Qasrawi [11] investigated that the use of steel slag increased the tensile strength of concrete. This enhancement could be attributed to angularity of steel slag which influences the interaction of cement matrix. San-Jose et al. [55] concluded that addition of steel slag obtained similar split tensile strength as that of control mix. They also investigated that there was high cohesion in concrete having steel slag showing good regularity in fracture behaviour than control mix. Sabapathy et al. [54] investigated the effect of steel slag as coarse aggregate on split tensile strength of concrete for 7 days and 28 days of curing. They observed that maximum tensile strength was obtained at 25% replacement of steel slag. Beyond this level, there was loss in split tensile strength which may be due to porosity of concrete due steel slag.

Effect on flexural strength

Roslan et al. [39] investigated in their findings that 20% of steel can be added to concrete without any fear of quality effect on flexural strength. Alizadeh et al. [53] investigated the flexural strength of concrete containing steel slag. The results showed that flexural strength of concrete having steel slag was higher than control mix. Netinger et al. [42] investigated the effect of temperature on flexural strength of concrete having steel slag. They observed that flexural strength of specimen having high amount of steel slag was highly affected by temperature beyond 873 K. The flexural strength decreased to zero beyond this temperature.

Effect on modulus of elasticity

Gonzalez et al. [7] investigated modulus of elasticity of steel slag added concrete for 90 days of curing. They concluded that modulus of elasticity of steel slag added concrete was 10% higher than control mix. This increase may be attributed to hardness of steel slag. Netinger et al. [42] studied the effect of temperature on concrete having steel slag as aggregate. They concluded that modulus of elasticity increased up to 373 K but beyond this there was decrease in modulus of elasticity. Increasing temperature beyond 873K, the modulus of elasticity of control mix was 31% and concrete having slag was 23% of its initial values. Khan et al. [40] concluded in their investigation that addition of steel slag increased the modulus of elasticity of concrete. This could

be attributed to high crushing strength of concrete (Airey et al., 2004) and its irregular surfaces which makes the bond stronger (Zhou et al., 1995).

Effect on fire resistance of concrete

Netinger et al. [42] analysed the temperature effects on concrete containing steel slag. They concluded that slag in combination with Portland cement could not provide satisfactory resistance of concrete against fire. As the coefficient of thermal expansion of slag is higher, which causes deterioration of contact between aggregate and cement paste.

CONCLUSION

- Glass powder shows good performance in concrete. The optimum value of glass powder in the concrete is 20%. Beyond this level reduction occurs in the mechanical properties of concrete. The air content improves as the glass powder content increases in the mixture. Similarly increase in the workability occurs with the addition of glass powder.
- Mechanical properties of concrete with steel slag are highly influenced by particle size of steel slag. Fine particles results good or similar mechanical properties compare to normal concrete. The increasing content of steel slag have adverse effects on properties of concrete, higher the content of steel slag lesser will be the results for mechanical properties compared to control mix.

REFERENCES

- [1] Aliabdo A. A., Elmoaty M. A. and Aboshama A. Y. *Utilization of waste glass powder in the production of cement and concrete*. Construction and Building Materials, 2016, 124: 866-877.
- [2] Imbabi M. S., Carrigan C. and Mckenna S. *Trends and developments in green cement a2nd concrete technology*. International Journal of Sustainable Built Environment. 2012.
- [3] Rashed A. M. *Recycled waste glass as fine aggregate replacement in cementitious materials based on Portland cement*. Construction and Building Materials, 2014, 72: 340-357.
- [4] Shao Y., Lefort T. and Moras S. *Studies on concrete containing ground waste glass*. Cement and Concrete Research 2000, 30: 91-100.
- [5] Jin W., Meyer C. and Baxter S. *Glasscrete- concrete with glass aggregates*. ACI Material Journal, 2000, 97 (2): 208-213.
- [6] Shayan A. and Xu A. *Value-added utilization of waste glass in concrete*. Cement and Concrete Research, 2004, 34: 81-89.
- [7] Gonzalez-Ortega M. A., Segura I., Cavalaro S.H.P. and Aguado A. *Radiological protection and mechanical properties of concrete with EAF steel slag*. Construction and Building Materials, 2014, 51: 432-438.
- [8] Hou X., Xu D., Xue B. and Li H. *Study on volume stability problems of cement caused by steel slag*. Journal of Building Materials, 2012, 10: 589-595.
- [9] Motz H. and Geiseler J. *Products of steel slags an opportunity to save natural resources*. Waste Management, 2001, 21: 285-293.
- [10] Dunster A. M. *Blast furnace slag and steel slag as aggregates: a review of their uses and applications in UK construction*. 3rd European Slag Conference-Proceedings. "Manufacturing and Processing of Iron and Steel Slags". Quarry Product Association, Keyworth, UK, 2002, 21-29.
- [11] Qasrawi H., Shalabi F. and Asi I. *Use of low CaO unprocessed steel slag in concrete as fine aggregate*. Construction and Building Materials, 2009, 23(2): 1118-1125.
- [12] Zelic J. *Properties of concrete pavement prepared with ferrochromium slag as concrete aggregate*. Cement and Concrete Research, 2005, 35(12): 234-02349.
- [13] Shoab M. M., Ahmad S. A. and Balaha M. M. *Effects of fire and cooling mode on the properties of slag mortar*. Cement and Concrete Research, 2001, 31(11): 1533-1538.

- [14] Yuksel I., Siddique R. and Ozkan O. *Influence of high temperature on the properties of concrete made with industrial by-products as fine aggregate replacement*. Construction and Building Materials, 2011, 25(2): 967-972.
- [15] Zhang T. S., Yu Q. J., Wei J. X. and Li J. X. *Investigation on mechanical properties, durability and micro-structural development of steel slag blended cements*. Journal of Thermal Analysis and Calorimetry, 2011, 110 (2): 633-639.
- [16] Tsakiridis P. E., Papadimitriou G. D., Tsvivilis S. and Koroneos C. *Utilization of steel slag for Portland cement clinker production*. Journal of Hazardous Materials, 2008, 152: 805-811.
- [17] Tiifekqi M., Demirbas A. and Genc H. *Evaluation of steel furnace slags as cement additive*. Cement and Concrete Research, 1997, 27 (11): 1713-1717.
- [18] Raju S. and Kumar P.R. *Effect of using glass powder in concrete*. International Journal of Innovative Research in Science, Engineering and Technology, 2014, 3 (5): 421-427.
- [19] Vandhiyan R., Ramkumar K. and Ramya R. *Experimental study on replacement of cement by glass powder*. International Journal of Engineering Research and Technology, 2013, 2(5).
- [20] Topcu I. B. and Canbaz M. *Properties of concrete containing waste glass*. Cement and Concrete Research, 2004, 34: 267-274.
- [21] Pollery C., Cramer S. M. and Cruz R. V. *Potential from using waste glass in Portland cement*. Journal of Materials in Civil Engineering, 1998, 10(4): 210-219.
- [22] Schwarz N., DuBois M. and Neithalath N. *Electrical conductivity based characterization of plain and coarse powder modified cement paste*. Cement and Concrete Research, 2007, 29: 656-666.
- [23] Castro S. D. and Brito J. D. *Evaluation of the durability of concrete made with crushed glass aggregates*. Journal of Cleaner Production, 2013, 41: 7-14.
- [24] Yu X. and Tao Z. *Performance of concrete made with steel slag and waste glass*. Construction and Building Materials, 2016, 114: 737-746.
- [25] Patil D. M. and Sangle K. *Experimental investigation of waste glass powder as partial replacement of cement in concrete*. International Journal of Advanced Technology in Civil Engineering, 2013, 2(1).
- [26] Tuan B. L., Hwang C. and Lin K. *Development of lightweight aggregate from sewage and waste glass powder for concrete*. Construction and Building Materials, 2013, 47: 334-339.
- [27] Terro M. J. *Properties of concrete made with recycled crushed glass at elevated temperature*. Building Environment, 2006, 41(5): 633-639.
- [28] Parghi A. and Alam M. S. *Physical and chemical properties of cementitious composites containing recycled glass powder (RGP) and styrene butadiene rubber (SBR)*. Construction and Building Materials, 2016, 104: 34-43.
- [29] Lee G., Poon C. S., Wong Y. L. and Ling T. C. *Effects of recycled glass aggregates on the properties of dry-mixed concrete blocks*. Construction and Building Materials, 2013, 38: 638-643.
- [30] Park S. B., Lee B. C. and Kim J. H. *Studies on mechanical properties of concrete containing waste glass aggregate*. Cement and Concrete Research, 2004, 34(12): 2181-2189.
- [31] Afshinnia K and Rangaraju P. R. *Impact of combined use of glass powder and crushed glass aggregate on selected properties of Portland cement concrete*. Construction and Building Materials, 2016, 117: 263-272.
- [32] Madandoust R. and Ghavidel R. *Mechanical properties of concrete containing waste glass powder and rice husk ash*. Biosystem Engineering, 2013, 116: 113-119.
- [33] Raghvendra K. and Virendra K. N. *Reuse of glass powder and industrial waste materials in concrete*. International Journal of Research in Engineering and Technology, 2015, 4(7).
- [34] Jitendra B. and Saoji A. C. *Experimental Investigation of waste glass powder as the partial replacement of cement in concrete production*. Conference on Advances in Engineering and Technology, 2014.
- [35] Dali J. S. and Tande S. N. *Performance of concrete containing mineral admixtures subjected to high temperature*. Conference on OurWorld in Concrete and Structure, Singapore, 2012, 37.
- [36] Bhagyasri T., Prabhavati U. and Vidya N. *Role of glass powder in mechanical strength of concrete*. Proceedings of IRF International Conference, 2016, 37.
- [37] Zheng K. *Pozzolanic reaction of glass powder and its role in controlling alkali-silica reaction*. Cement and Concrete Composites, 2016, 67: 30-38.
- [38] Cota P., Melo C. D. and Panzera T. H. *Mechanical properties and ASR evaluation of concrete tiles with waste aggregate*. Sustainable Cities and Society, 2015.

- [39] Roslan N. H., Ismail M., Abdul-Majid Z. and Muhammad B. *Performance of steel slag and steel sludge in concrete*. Construction and Building Materials, 2016, 104: 16-24.
- [40] Khan M. S. H., Castel A., Foster S. J. and Smith M. *Utilization of steel furnace slag coarse aggregate in a low calcium fly ash geopolymer concrete*. Cement and Concrete Research, 2016, 89: 220-229.
- [41] Huang X., Wang Z., Liu Y., Hu W. and Ni W. *On the use of blast furnace slag and steel slag in the preparation of green artificial reef concrete*. Construction and Buildings Materials, 2016, 112: 241-246.
- [42] Netinger I., Varevac D., Bjegovic D. and Moric D. *Effect of high temperature on properties of steel slag aggregate concrete*. Fire Safety Journal, 2013, 59: 1-7.
- [43] Qjang W. and Peiyu Y. *Influence of steel slag on mechanical properties and durability of concrete*. Construction and Building Materials, 2013, 47: 1414-1420.
- [44] Qjang W., Mengxiao S. and Jun Y. *Influence of classified steel slag with particle sizes smaller than 20 μm on the properties of cement and concrete*. Construction and Building Materials, 2016, 123: 601-610.
- [45] Ghoulah Z., Guthrie I. L. and Shao Y. *Production of carbonate aggregates using steel slag and carbon dioxide for carbon-negative concrete*. Journal of CO₂ Utilization, 2017, 18: 125-138.
- [46] Palankar N., Shankar A. U. and Mithum B. M. *Durability studies on eco-friendly concrete mixes incorporating steel slag as coarse aggregates*. Journal of Cleaner Production, 2016.
- [47] Forster S. W. *Significance of tests and properties of concrete and concrete making materials*. Chapter 13- Soundness, deleterious substances and coatings, STP169D. ASTM, 2006.
- [48] Pang B., Zhou Z. and Xu H. *Utilization of carbonated and granulated steel slag aggregate in concrete*. Construction and Building Materials, 2015, 84: 454-467.
- [49] Anastasiou E., Filikas K. G. and Stefanidou M. *Utilization of recycled aggregates in concrete with fly ash and steel slag*. Construction and Building Materials, 2014, 50: 154-161.
- [50] Mengxiao S., Qiang W. and Zhikai Z. *Comparison of the properties between high-volume fly ash concrete and high-volume steel slag concrete under temperature matching curing condition*. Construction and Building Materials, 2015, 98: 649-655.
- [51] Airey G. D., Collop A. C. and Thom N. H. *Mechanical performance of asphalt mixtures incorporating slag and glass aggregates*. 8th Conference on Asphalt Pavement for South Africa, Sun City, South Africa, 2004.
- [52] Zhou P., Lydon F. D. and Barr B. G. *Effects of coarse aggregate on elastic modulus and compressive strength of high performance concrete*. Cement and Concrete Research, 1995, 25: 177-186.
- [53] Alizadeh R., Chini M., Ghods P., Hoseini M., Montazer S. and Shekarchi M. *Utilization of electric arc furnace slag as aggregate in concrete*. Environmental Issue Tehran: CMI Report, 1996.
- [54] Sabapathy Y. K., Shankari N. S., Kumar A. Y. and Ravichandar D. *Experimental investigation of surface modified EOF steel slag as coarse aggregate in concrete*. Journal of King Saud University-Engineering Science, 2016.
- [55] San-Jose J. T., Vegas, Arribas I. and Marcos I. *The performance of steel-making slag concretes in the hardened state*. Materials and Design, 2014, 60: 612-619.

STUDY ON ANTI-CRACKING PERFORMANCE EVALUATION METHOD OF STEEL FIBER REINFORCED CERAMSITE CONCRETE (SFRCC) BASED ON PARTLY-RESTRAINED SHRINKAGE RING

Zhang Yi-fan

College of Environment and Civil Engineering, Chengdu University of Technology, Chengdu 610059, China

ABSTRACT

In the study of crack resistance of steel fiber reinforced concrete in steel fiber on concrete deformation ability and prevent the Angle of the micro cracks, and the lack of overall evaluation on the performance of steel fiber reinforced concrete crack. By tinder barrier-free restrain some experimental research on steel fiber ceramsite concrete shrinkage ring crack resistance, and use the test results within the definition of steel ring strain from expansion to contraction cut-off age for early and late ages, and the ages of the cut-off point for the early and the late steel fiber ceramsite concrete anti-cracking performance evaluation. The results show that the anti-cracking properties of the steel fiber ceramic concrete are improved with the increase of steel fiber content.

KEYWORDS

Alkali slag cement, No diaphragm shrinkage ring, Concrete structure, Evaluation of crack resistance

INTRODUCTION

The shrinkage cracking of high performance concrete is one of the problems frequently encountered in engineering. Shrinkage ring test, based on some constraints can be used to study regeneration powder admixture of concrete shrinkage cracking tendency, the influence of the research shows that some reasonable constraint shrinkage ring test to evaluate the ability of resisting shrinkage cracking of concrete [1]. Different scholars for related research was conducted on the crack resistance of steel fiber reinforced concrete, steel fiber can prevent the expansion of the internal micro cracks of concrete added, and increase the tensile strength of concrete, and then against the improvement of the performance of the crack [2-3]. In this paper, the anti-cracking performance of the regenerated aggregate concrete with different presenting degree can be evaluated by partial constraint shrinkage ring test [4]. Literature [5] proposed a quick evaluation method for the anti-crack performance of lightweight aggregate concrete with the restraint shrinkage ring.

This paper proposes a more simple part with partition with constraint shrinkage ring crack resistance of concrete fast evaluation method, and evaluation by the method caused by

autogenous shrinkage of steel fiber reinforced ceramists concrete anti-cracking performance of (SFRCC).

TEST

1. Raw Materials and Proportion

1: Cement: use Sichuan refined stone brand 42.5R regular Portland cement, apparent density 3050kg/m³, 28day compressive strength of 45 MPa.

2: Steel fiber: shear wave shape steel fiber produced by Zhejiang Haining Bonn metal products co., LTD.

3: Ceramic granule: adopt the ceramic pellet of Yichang, Yichang, Hubei.

4: Fine aggregate: the Kawjiang river sand with a fineness modulus of 2.5, the stacking density of 1481 kg/m³, the apparent density of 2590 kg/m³.

5: Water: use tap water in Chengdu area.

6: Water reducing agent: using twin-js polycarboxylic acid water reducing agent produced by Sichuan institute of building science, the water reducing rate is 15~18%. In this experiment, the ceramists presetting 1h was used in this experiment, and the design of the variation parameters with the steel fiber content was shown in Table 1. Test condition is based on air temperature is 25 °C, humidity is 86%.

Tab. 1 - Concrete mixture ratio [kg/m³]

Component Numbering	Cement (kg/m ³)	Sand (kg/m ³)	ceramsite (kg/m ³)	Water (kg/m ³)	Water reducing agent (kg/m ³)	Steel fiber volume rate Vf (%)
SF00	476	698	583	167	8	0
SF05	476	698	583	167	8	0.5
SF10	476	698	583	167	8	1
SF20	476	698	583	167	8	2

2. Test Method

2.1 Partial constraint shrinkage ring test device

Restrain some shrinkage ring test, some constraint shrinkage ring device is in the literature [5-6] research concrete crack resistance device, which on the basis of the original device is equipped with diaphragm in the concrete ring, this experiment adopts some constraints, remove the diaphragm shrinkage ring device. The purpose of the partition plate is to produce stress concentration and accelerate the appearance of concrete ring cracks in the partition. But due to the crack evaluation index (area method) to evaluate, the cracking of do not need to be visible to the naked eye[5], surrounded by a certain age crack coefficient is included in the area of internal micro cracks of concrete information [9]. This not only simplifies the device, but also can meet the requirements of rapid evaluation. The improved part constraint shrinkage ring device schematic diagram is shown in Figure 1, strain gauge sets, steel ring inside height 1/2, 1 (point 1) strain

gauge set with 2 (point 2) strain gauge is just right across the street at 180 °. The specific dimensions of the device are shown in Table 2.

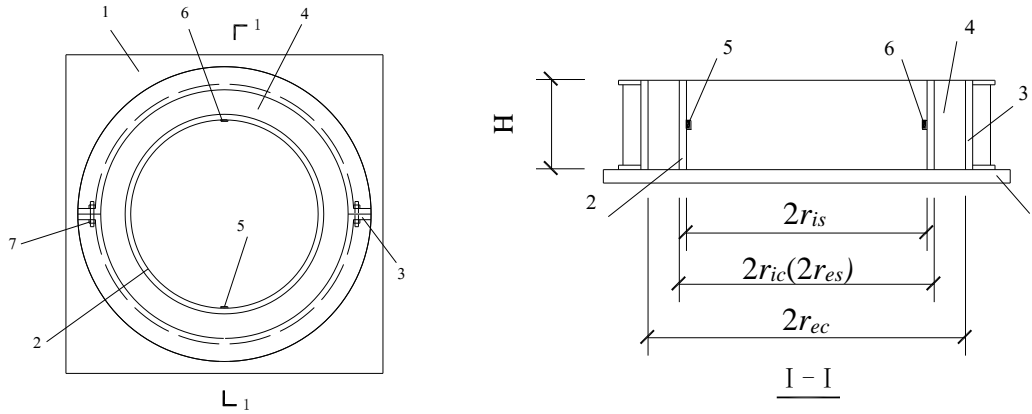


Fig.1 - No partition device schematic part shrinkage

Injection: 1- The tablet; 2- The steel ring; 3- The steel ring; 4- Concrete ring; 5- Strain gauge 1; 6- Strain gauge 2; 7- Bolts of fixed outer ring; $2r_{ec}$ - The outer diameter of the concrete ring; $2r_{ic}$ ($2r_{es}$)- Outer diameter of the inner diameter or inner ring of a concrete ring; $2r_{is}$ - Inner diameter of inner steel ring; H- The height of a concrete ring or steel ring.

Tab. 2 - The size of the ring test device is constrained by the constraint of the partition [mm]

$2r_{ec}$	$2r_{ic}$ ($2r_{es}$)	$2r_{is}$	H
395	315	299	100

2.2 The Test Results

In partial constraint shrinkage ring test, the development of the inner steel ring strain (ϵ_{st}) (the average of measurement point 1 and point 2) is shown in Figure 2.

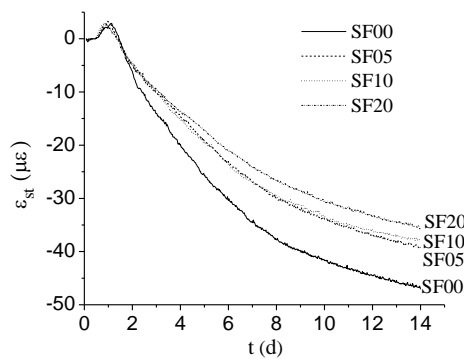


Fig.2 - Internal steel ring strain

3. Basic Mechanical Properties Test

Basic mechanical properties of concrete test according to the specification of ordinary concrete mechanics performance test method standard (GB50081-2002-T) [7], measurement of different steel fiber content of ceramsite concrete 1d., 2d, 3d, 5d, 7d and 14d and 28d compressive strength, splitting tensile strength. According to the standard of normal concrete long-term performance and endurance performance test method (GB/T 50082-2009) [8], the dt-15 moving-mode meter was used to measure the elastic modulus of sfr1d, 2d, 3d, 5d, 7d, 14d and 28d of SFRCC. The test results are shown in Tables 3-5.

Tab. 3 - Compressive strength [MPa]

Group number Age	SF00	SF05	SF10	SF20
1d	15.19	20.15	15.46	16.91
2d	22.01	26.39	23.15	24.52
3d	25.77	29.63	27.50	28.74
5d	29.90	33.07	32.37	33.43
7d	32.38	35.07	35.31	36.24
14d	36.58	38.38	40.39	41.04
28d	39.81	40.86	44.32	44.74

Tab. 4 - Splitting tensile strength [MPa]

Group number Age	SF00	SF05	SF10	SF20
1d	2.06	2.43	3.25	4.45
2d	2.33	2.75	3.54	4.67
3d	2.46	2.91	3.68	4.78
5d	2.59	3.06	3.81	4.87
7d	2.66	3.15	3.89	4.93
14d	2.77	3.28	4.01	5.01
28d	2.85	3.38	4.09	5.07

Tab. 5 - Dynamic modulus of elasticity [GPa]

Group number Age	SF00	SF05	SF10	SF20
1d	21.64	21.19	22.87	23.04
2d	23.77	23.53	25.05	25.19
3d	24.77	24.63	26.06	26.18
5d	25.74	25.72	27.07	27.17
7d	26.28	26.32	27.62	27.71
14d	27.13	27.28	28.50	28.57
28d	27.74	27.96	29.12	29.18

According to European standard [9], the use of 1 d, 28 d compressive strength, splitting tensile strength and elastic modulus formula of fitting, calculate the splitting tensile strength of each age, other smaller error between the theoretical value and the measured values is calculated [10]. The development of the tensile strength during the period of 14d of the ceramic concrete with different steel fiber content is shown in Figure 3.

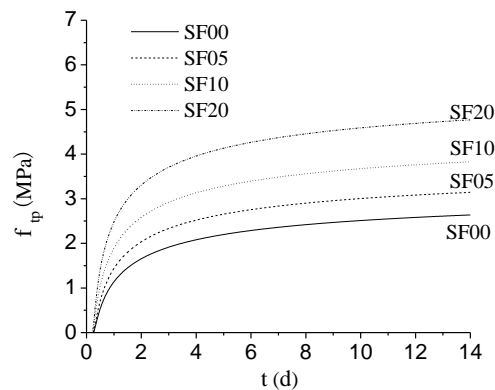


Fig. 3 - Splitting tensile strength at different ages

4. Evaluation of Crack Resistance

In the partial constraint shrinkage ring test, the equilibrium relation between the inner ring and the concrete ring is obtained, and the cyclic tension stress can be calculated by Equation (1) [5].

$$\sigma_c = \frac{h_{st}}{h_c} \sigma_s = \frac{E_{st} h_{st}}{h_c} \varepsilon_{st}(t) \quad (1)$$

In this paper, $\sigma_c(t)$ is the cyclic tensile stress of the concrete ring during the phase of the shrinkage ring in the circumferential ring test is restricted; $\sigma_s(t)$ is the circumferential stress of the

inner steel ring at the age of t ; E_{st} is the elastic modulus of inner steel ring (195GPa); h_{st} is the inner steel ring thickness (12mm); h_c is the thickness of the concrete ring (40mm), that is $(r_{ec} - r_{ic})$ or $(r_{ec} - r_{es})$.

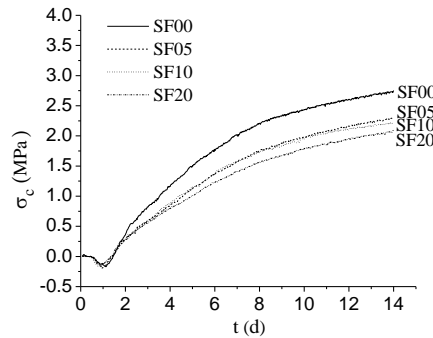


Fig. 4 - Relationship between concrete ring stress and age

ANALYSIS AND DISCUSSION

1. Evaluation Index of Crack Resistance

This paper presents a quick evaluation method for the crack resistance of concrete, There are two concepts of cracking coefficient $\zeta_t(t)$ and anti-crack evaluation index $A_{cr}(t)$ [5]. The cracking coefficient $\zeta_t(t)$ is the cyclic stress of concrete at the age of age with the tensile strength of concrete is corresponding $f_t(t)$ the ratio of tensile strength instead of the tensile strength is used in this paper, as shown in formula (2).

$$\zeta_t(t) = \frac{\sigma_c(t)}{f_t(t)} \quad (2)$$

Anti-crack evaluation index $A_{cr}(t)$ is the concrete cracking coefficient $\zeta_t(t)$ the integral of phase t, As shown in formula (3).

$$A_{cr}(t) = \int_0^t \frac{\sigma_c(t)}{f_t(t)} dt = \int_0^t \zeta_t(t) dt \quad (3)$$

The cracking coefficient of concrete $\zeta_t(t)$ with the diagram of relationship diagram of age t is shown in Figure 5 (In this case, the decrease of the coefficient of cracking coefficient due to temperature change is not considered)

According to formula (2), the cracking coefficient of SFRC can be obtained with the development rule of the age. As shown in Figure 5, the anti-crack evaluation index is obtained by formula (3) as shown in Table 6.

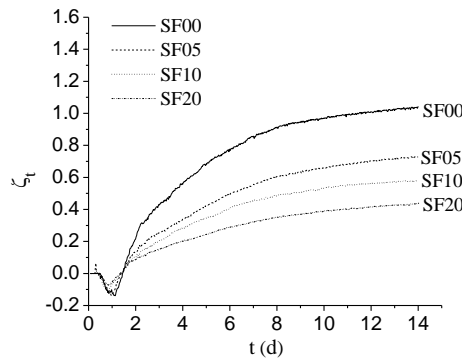


Fig. 5 - Relationship between cracking coefficient and age

Tab. 6 - Crack resistance evaluation index [d]

Group number	SF00	SF05	SF10	SF20
Early phase	-0.081	-0.063	-0.052	-0.034
Lately phase	9.88	6.56	5.30	3.87
Total	9.80	6.49	5.24	3.83

2. Anti-cracking performance evaluation method

Based on the literature [5] based on the anti-crack evaluation method based on partial constraint shrinkage ring test, the anti-cracking performance of SFRCC can be evaluated according to the following methods:

1. The anti-cracking performance of SFRC is better than that of SFRCC in the descending segment;
2. In the case of SFRCC for the cracking coefficient, the size of the anti-crack evaluation index $A_{cr}(14)$ of 14d phase is compared, and the larger the $A_{cr}(14)$ is, the better the anti-crack performance of the SFRCC;
3. For the cracking coefficient, the SFRCC is not reduced, and the size of the anti-crack evaluation indicator $A_{cr}(14)$ in 14d phase is compared, and the smaller $A_{cr}(14)$ is, the better the anti-crack performance of SFRCC;

The Figure 5 shows that SF00 SF05, SF10, cracking coefficient of SF20 group were only rise period, the Table 5 shows that SF20 $A_{cr}(14)$ minimally, followed by SF10, then SF05, SF00 group of $A_{cr}(14)$ is the largest, so the crack resistance order from good to bad SF20 > SF10 > SF05 > SF00. Therefore, the anti-cracking performance of SFRC increases with the increase of steel fiber content. This conclusion is confirmed by literature[4-5], indicating the correctness of the evaluation method.

3. Early and late crack resistance

The heat of the cement hydration reaction causes the concrete ring temperature to rise, the concrete ring heat transfers to the inner steel ring, so that the inner steel ring temperature also rises, then the inner steel ring expands. After the expansion of the concrete ring due to shrinkage and increase of elastic modulus, the concrete ring is strengthened by the contraction of the inner steel ring, resulting in the inner steel ring from expansion to contraction. For different types of concrete, the change of heat, elastic modulus and shrinkage of the water reaction are different, which can lead to different time points of internal steel ring strain from expansion to contraction. This time point is defined as the early and later boundary point of concrete, and the early and later boundary points of different steel fiber content are shown in Table 6. As can be seen from Table 7, the quantity of steel fiber has little effect on the age of dividing point.

Tab. 7 - The age of demarcation between early and late [d]

SF00	SF05	SF10	SF20
1.44	1.40	1.42	1.33

Put some constraints in Figure 5 the cracking coefficient of shrinkage ring test according to the early and late departure, get SFRCC law of development of early and late cracking coefficient along with age as shown in Figure 6, the corresponding crack evaluation index calculation results are shown in Table 6.

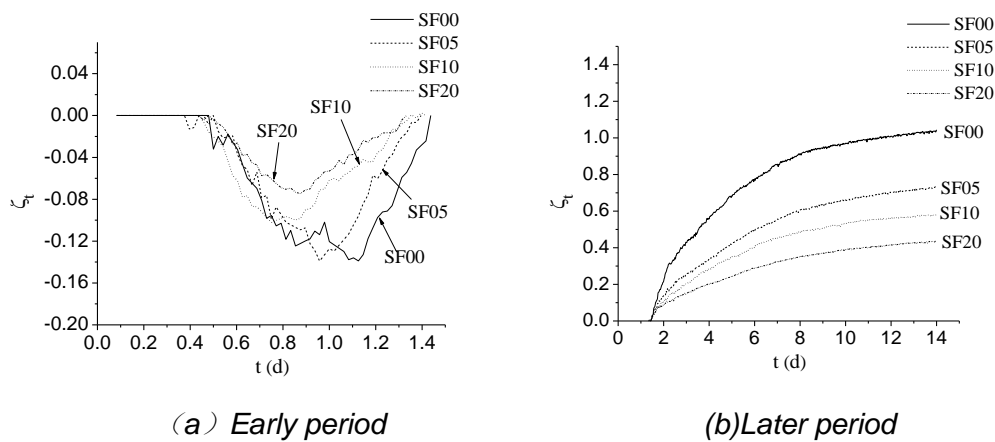


Fig. 6 - Relationship between cracking coefficient and age at early and late stages

The Figure 6, Table 6 shows that in some parts of the constraint shrinkage ring test, the early cracking of SFRCC coefficient $\zeta_t(t)$ and anti-crack evaluation index $A_{cr}(t)$ is negative, its value is less than the total 1%, negligible, so can be directly used in the late of anti-crack evaluation index to evaluate the anti-cracking performance of concrete. Late evaluation index with ceramsite concrete crack resistance of steel fiber content increase and decrease, so the late SFRCC crack resistance along with the increase of steel fiber content increased, the consistent with SFRCC overall cracking index evaluation result.

CONCLUSIONS

- (1) The constraint shrinkage ring experiment, exist in the steel ring strain from expansion to shrink, the moment the ages of the corresponding defined as the cut-off point of early and late ages, steel fiber content of steel fiber ceramsite concrete cut-off (SFRCC) age.
- (2) Based on the concept of partial constraint shrinkage loop test and cracking coefficient $\zeta_t(t)$ and cracking evaluation index $A_{cr}(t)$, the evaluation method of anti-cracking performance of SFRCC is given.
 - ① The anti-cracking performance of SFRCC is better than that of SFRCC in the descending segment;
 - ② The crack coefficient appears to be in the lower part of SFRCC, and the size of the anti-crack evaluation index $A_{cr}(14)$ in 14d phase is compared, and the larger the $A_{cr}(14)$ is, the better the anti-crack performance of the SFRCC;
 - ③ For the cracking coefficient of SFRCC, the size of the index $A_{cr}(14)$ of the anti-crack evaluation index of 14d phase was compared, and the $A_{cr}(14)$ was smaller, the better anti-crack performance of SFRCC is.
- (3) Early anti-crack evaluation indexes are small and can be ignored, and the anti-cracking performance of SFRCC can be correctly evaluated by using the anti-crack evaluation index and the total anti-crack evaluation index.
- (4) The anti-cracking performance of SFRCC increases with the increase of steel fiber content.

ACKNOWLEDGEMENTS

This study was supported by the National Natural Science Foundation of China (Grant Nos. 51479036). Our gratitude is also extended to reviewers for their efforts in reviewing the manuscript and their very encouraging, insightful and constructive comments.

REFERENCES

- [1] Gao Zhilou, Liu Xiaoyan, Zuo Junqing, (2012). " Study on shrinkage property of renewable powder concrete based on the ring test." Fly ash comprehensive utilization, 2:6-10. (in Chinses)
- [2] Sun qilin, Wang limin, Zhao chengquan, et al. (2005). "Test on anti-cracking performance of steel fiber reinforced concrete." Journal of Shandong Univercity of Technology (natural science edition), 19(3):21-26. (in Chinses)
- [3] Chen Wanxiang.(2013). "Reinforcing mechanism and anti-cracking performance analysis of steel fiber reinforced concrete. " Railway Engineering Cost Management, 28(3): 58-60.(in Chinese)
- [4] Ji T, Chen C Y, Chen Y Y.(2013). "Effect of moisture state of recycled fine aggregate on the cracking resistibility of concrete. " Construction and Building Materials, 44: 726-733.
- [5] Ji T, Zhang B, Chen Y, et al.(2014). "Evaluation method of cracking resistance of lightweight aggregate concrete. " Journal of Central South University, 21: 1607-1615.
- [6] Li S L.(2010). "Study on anti-cracking test method and evaluation system of cement-based materials." Fuzhou: Fuzhou Univercity. (in Chinses)
- [7] GB/T 50081—2002 Standard for test method of mechanical properties on ordinary concrete. Beijing: Standards Press of China,2003(in Chinses)
- [8] GB/T 50082—2009 Standard for test methods of long-term performance and durability of ordinary concrete. Beijing: Standards Press of China,2010(in Chinses)



- [9] Euro-International Concrete Committee. CEB-FIP Model Code 1990. Lausanne, 1993
- [10] Zhang B B.(2013). Early age tensile creep and anti-cracking performance evaluation method of steel fiber reinforced ceramsite concrete. Fuzhou: Fuzhou University. (in Chinses)

EXPERIMENTAL AND NUMERICAL INVESTIGATION OF BLASTING-INDUCED GROUND VIBRATION FROM TUNNEL UNDERCROSSING A VILLAGE

Fan Haobo^{1,2}, Yu Deqiang², Zhao Dongping¹, Lai Jinxing², Xie Yongli²

1. *China Railway Eryuan Engineering Group Co. Ltd, Chengdu, 610031, China.*
2. *Shaanxi Provincial Major Laboratory for Highway Bridge & Tunnel, Chang'an University, Xi'an, 710064, China*

ABSTRACT

To study the effect of blasting-induced vibration on ground buildings when tunnel undercrossing a village, a blasting vibration trial was carried out in Beizhuang tunnel in Henan Province, China. The safety blasting distance and reasonable explosive charge were pre-estimated according to empirical formula. The attenuation of ground vibration velocity was simulated using a 3D numerical model. Less explosive charge and longer distance to blasting source would result in lower ground vibration. When designed explosive charge was 54 kg, the safe distance was 42.26 m. While the distance between building and blasting source was about 37 m, the maximum explosive charge was 36.24 kg. The numerical results showed that the significantly horizontal affect region of blasting vibration was within 50 m to blasting source. Accordingly, effective vibration control is necessary to avoid disturbing human daily life during tunneling.

KEYWORDS

Tunnel undercrossing a village, In-situ test, FEM, blasting vibration, safe distance, reasonable explosive charge

1. INTRODUCTION

Various highway tunnels were constructed in China in last two decades to meet economy development and transportation function. For the purpose of economy and security, drilling and blasting are widely used in the construction of tunnel. Consequently, part of the explosive energy converts into seismic waves, which may cause somewhat damage to ground buildings [1, 2]. Gong et al. [3] suggested that a field blasting trial and vibration monitoring was necessary before tunnelling under buildings in a railway tunnel case study. Xia et al [4] and Li et al [5] studied the effects of tunnel blasting on surrounding rock and the lining systems of adjacent existing tunnels, respectively, and proposed some possible schemes of vibration control to ensure the safety of the

existing tunnels. Singh [6] conducted field investigations for several coal mines in India to analyse the effect of blasting on adjacent coal mines. Umit [7] investigated the ground vibration induced by blasting during the construction of the Istanbul Kadıköy–Kartal metro tunnel, and the particle velocities and frequency values of all blast events were evaluated according to Turkish Environmental Regulation [8]. In order to comprehensively understand the dynamic responses of tunnel and building to blasting vibration, numerical model was introduced to precisely analysis of in-situ data.

Jiang et al. [9], Zhu et al. [10] and Xu et al. [11] established a 3D nonlinear constitutive model to investigate the variation of internal force and settlement during the tunnel excavation, respectively. Tian and Li [12] introduced a numerical simulation in a different model to analyse the dynamic responses of building to ground shock induced by an explosion in tunnel. Numerous experiments have established to study response of building to blasting waves induced by the explosion in tunnel [13-15]. The optimal scheme of blasting explosive in new tunnel construction was argued by Wang et al [16] and Shao et al. [17, 18] in a numerical model using ANSYS/LS-DYNA program. However, little research has been carried out to discuss the blasting-induced ground vibration in tunnelling under cross a village. In this work, the blasting-induced ground vibration when tunnelling under cross a village was in-situ tested and numerical studied in Beizhuang tunnel in Henan province, China. The safety distance of blasting construction was evaluated by using the empirical formula [20-23]. The designed explosive charge of the shallow area was also optimized according to the safety distance. Significantly affect region of blasting vibration was obtained through the numerical experimental. The research results have provided guidance for the blasting excavation of Beizhuang tunnel, also guaranteed the safety of ground buildings.

2. TEST SITE DESCRIPTIONS

The Beizhuang tunnel undercrossed Beizhuang village, in Gongyi, China (Figures 1 and 2). The length of the left line is about 2505 m, and its range is ZK20+130-ZK22+635. While the length of the right line is 2530 m, and its range is YK20+085-YK22+615. The width and the height of the tunnel are 10.75 m and 7.10 m, respectively. The surrounding rock of the tunnel is mainly weathered limestone. The range of undercrossing section is K20+400-K20+900, and the depth of the tunnel is 37-55 m. The Beizhuang village was densely built, and most of the buildings were masonry structure and fragile to vibration.

The tunnel was constructed by bench method, and its surrounding rock belongs to grade IV. Given the cost of construction, especially in terms of time and security, the drilling and controlled blasting method was adopted when tunnelling, and the tunnelling footage is from 1.0 m to 1.2 m.

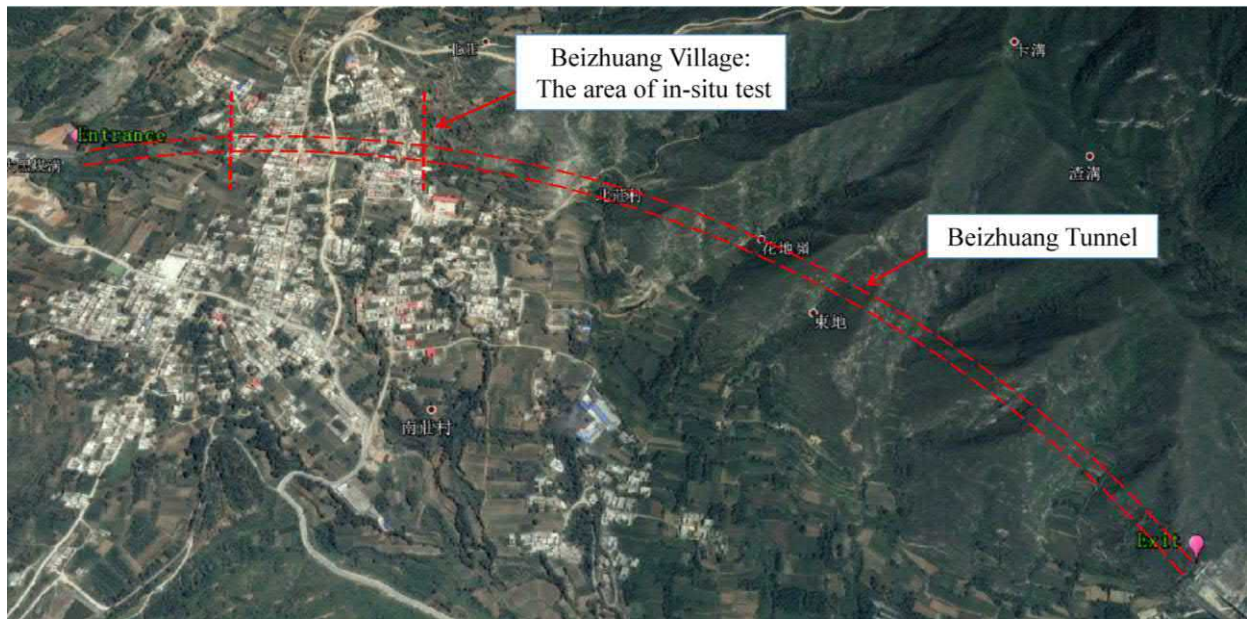


Fig. 1 - The Beizhuang tunnel

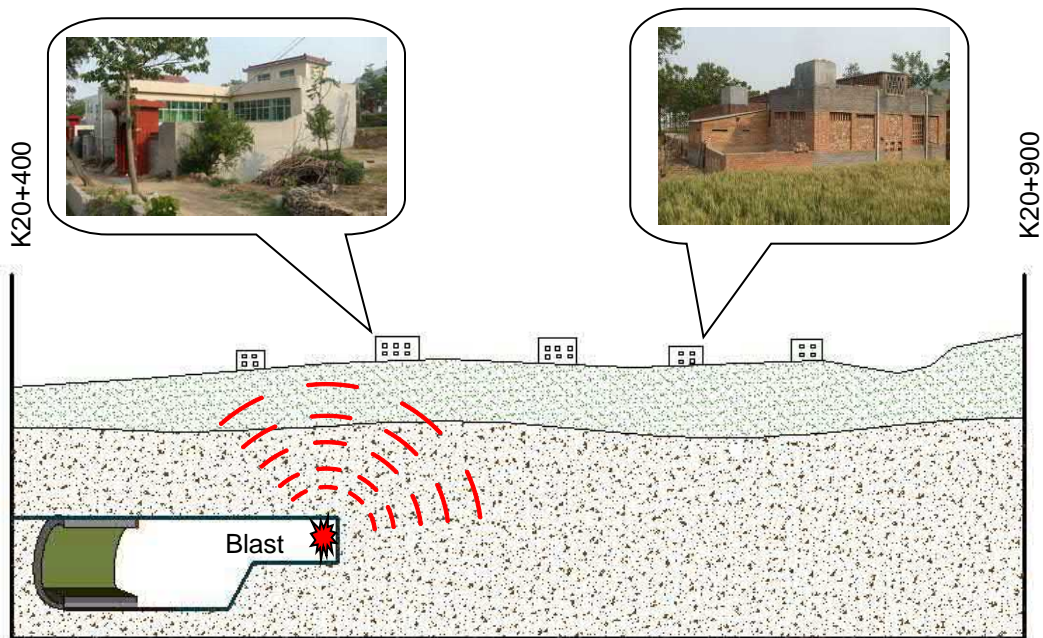


Fig. 2 - The profile diagram of tunnel undercross Beizhuang village

3. IN-SITU TEST

3.1. Test scheme

The section of the tunnel beneath Beizhuang village was subjected to short footage and weak blasting. Vibration data was acquired by REFTEK130B seismograph (US), the sensor was GURALP (UK). Sensor was installed to test point by gypsum, if the test point is on the hard rock, just fixed it on rock surface, in case of weathered rock, the weathered layer should be removed and then build concrete pier for fixing.

To obtain the ground vibration velocity, 5 testing points were placed along centre lines of the tunnel. The layout diagram of test points was shown in Figure 3.

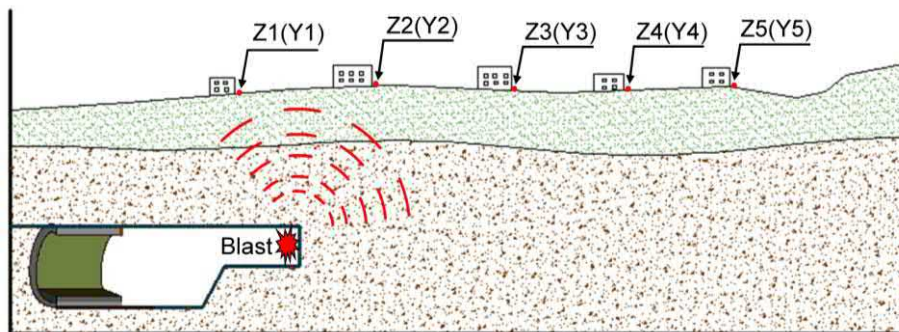


Fig. 3 - The layout diagram of test points for blasting vibration

To study the influence of tunnel blasting on buildings, the blasting test was carried out at ZK20+470 and YK20+510 in main tunnel and ZK20+400 and YK20+415 in pedestrian cross hole, respectively. Test points were placed from section ZK20+472 to YK20+510, with space of 25-55 m. The explosive charge for blasting was 54 kg for main tunnel and 9 kg for pedestrian cross hole. The distance between test the point and the blasting point along left line and right line of tunnel was shown in Tables 1 and 2, respectively.

Tab. 1 - The distance between testing point and blasting point along left line of tunnel

Test points	Z1	Z2	Z3	Z4	Z5
Location	ZK20+472	ZK20+507	ZK20+532	ZK20+562	ZK20+617
Horizontal distance away from the blasting point(main tunnel ZK20+470)/m	2	37	62	92	147
Spatial distance away from the blasting point (main tunnel ZK20+470)/m	44.9	60.2	80.5	107.0	157.6
Spatial distance away from the blasting point (pedestrian cross hole ZK20+400)/m	85.5	117.2	141.0	170.8	224.1

Tab. 2: The distance between test point and blasting point along right line of tunnel

Test points	Y1	Y2	Y3	Y4	Y5
Location	YK20+510	YK20+535	YK20+565	YK20+595	YK20+645
Horizontal distance away from the blasting point (main tunnel YK20+510)/m	0	25	55	85	135
Spatial distance away from the blasting point (main tunnel YK20+510)/m	44.9	51.6	72.6	98.2	144.3
Spatial distance away from the blasting point (pedestrian cross hole YK20+415)/m	102.2	129.4	157.9	187.1	236.3

3.2. Analysis of blasting vibration velocity

The high frequency part of the blasting seismic wave was wholly absorbed by the soil, while the low frequency part could propagate for a long distance [24-27]. The maximum ground vibration velocity was calculated according to the maximum amplitude of horizontal wave. The peak particle velocity (PPV) at each test point in main tunnel was shown in Table 3, and the PPV at each test point in pedestrian cross hole was shown in Table 4. The attenuation of vibration velocity on ground surface due to blasting in main tunnel and pedestrian cross hole were shown in Figures 4 and 5.

Tab. 3 - The PPV at each test point in main tunnel

Testing point	Explosive charge (kg)	Horizontal distance (m)	Spatial distance (m)	V_{max} (cm/s)	Testing point	Explosive charge (kg)	Horizontal distance (m)	Spatial distance (m)	V_{max} (cm/s)
Z1	54	2	44.9	1.366	Y1	54	0	44.9	1.313
Z2	54	37	60.2	1.021	Y2	54	25	51.6	1.174
Z3	54	62	80.5	0.852	Y3	54	55	72.6	0.64
Z4	54	92	107.0	0.426	Y4	54	85	98.2	0.388
Z5	54	147	157.6	0.142	Y5	54	135	144.3	0.088

Tab. 4 - The PPV at each test point in pedestrian cross hole

Testing point	Explosive charge (kg)	Horizontal distance (m)	Spatial distance (m)	V_{max} (cm/s)	Testing point	Explosive charge (kg)	Horizontal distance (m)	Spatial distance (m)	V_{max} (cm/s)
Z1	9	72	85.5	0.508	Y1	9	90	102.2	0.561
Z2	9	107	117.2	0.388	Y2	9	120	129.4	0.459
Z3	9	132	141.0	0.412	Y3	9	150	157.9	0.388
Z4	9	162	170.8	0.223	Y4	9	180	187.1	0.132
Z5	9	217	224.1	0.034	Y5	9	230	236.3	0.028

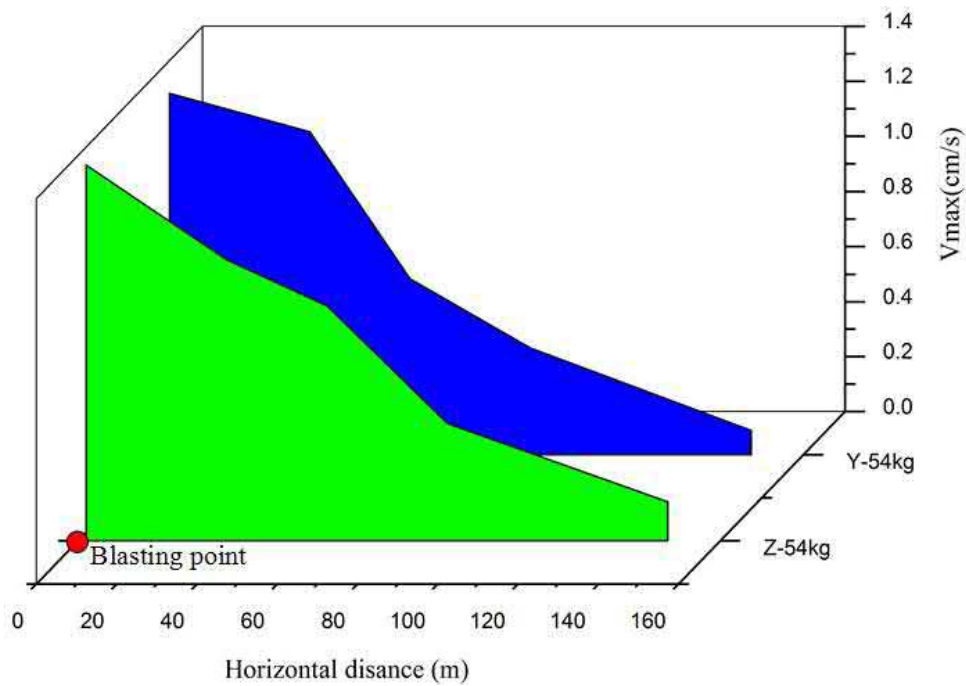


Fig. 4 - Attenuation of vibration velocity on ground surface due to blasting in main tunnel

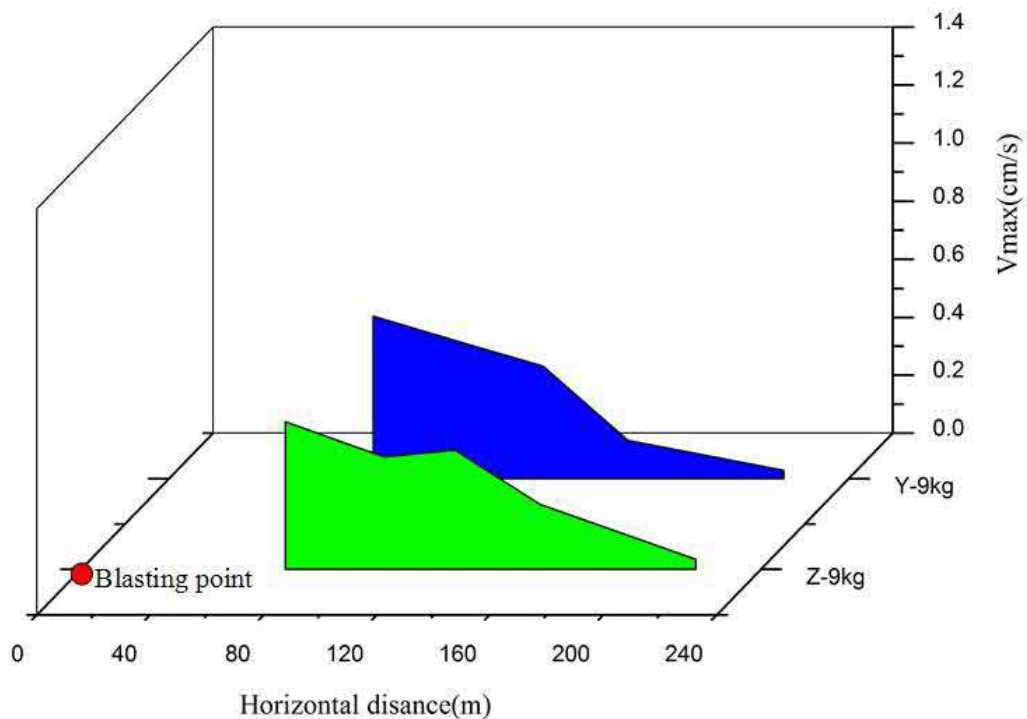


Fig. 5 - Attenuation of vibration velocity on ground surface due to blasting in pedestrian cross hole

It is obvious that less explosive charge and longer distance to blasting source could greatly slower vibration velocity on ground (Tables 3 and 4). When explosive charge is 54 kg, the maximum ground vibration velocity of left tunnel attenuated from $V_{\max} = 1.366$ cm/s (Z1) to $V_{\max} = 0.142$ cm/s (Z5), and that of the right tunnel attenuated from $V_{\max} = 1.313$ cm/s (Y1) to $V_{\max} = 0.088$ cm/s (Y5). When explosive charge was 9 kg, the maximum ground vibration velocity of left tunnel attenuated from $V_{\max} = 0.508$ cm/s (Z1) to $V_{\max} = 0.034$ cm/s (Z5), and that of the right tunnel attenuated from $V_{\max} = 0.561$ cm/s (Y1) to $V_{\max} = 0.028$ cm/s (Y5).

As the Figure 4 shows that the vibration velocity on ground surface due to blasting construction attenuates faster within the horizontal range of 50m. It is observed from Figures 4 and 5 that the vibration velocity due to blasting construction in pedestrian cross hole is far less than that in main tunnel, which is mainly associated with the decrease of explosive charge and increase in distance to blasting point.

The buildings above Beizhuang tunnel were defined to sustain blasting vibration velocity of 2.0 -2.5 cm/s, within the range of 10 Hz of frequency [28]. The maximum ground vibration velocity was 1.366 cm/s, so the ground buildings were safe when the designed explosive charge was approximate 54 kg.

3.3. Prediction of safe distance and reasonable explosive charge

Except for explosive charge and distance to blasting source, propagation of seismic wave was also influenced by charge measures, detonation mode and stratum characteristic. However, only the empirical formula (1) was commonly applied in engineering field [20-23]:

$$v = K(Q^{1/3} / R)^{\alpha} \quad (1)$$

Where v is the PPV; Q is maximum explosive charge of each blasting; R is the distance of test point to blasting source; K and α are the factors to reflect the influence of non-primary factors, which could be determined by regression analysis of in-situ test data.

Millisecond detonation was adopted in the blasting of Beizhuang tunnel, the explosive charge $Q=54$ kg. Formula (2) was obtained when substitute vibration velocity at each test point and the distance to blasting source into formula (1):

$$\begin{aligned} v_1 &= K(Q^{1/3} / R_1)^{\alpha} \\ v_2 &= K(Q^{1/3} / R_2)^{\alpha} \\ &\dots\dots \\ v_n &= K(Q^{1/3} / R_n)^{\alpha} \end{aligned} \quad (2)$$

Then $K = 250$, $\alpha = 2.0$ were got from formula (2).

Then, the safety distance for blasting and reasonable explosive charge for Beizhuang tunnel could be got by formula (1) and the maximum tolerant vibration velocity.

a. Prediction of safety distance for blasting in Beizhuang Tunnel

When the designed explosive charge Q_{\max} and maximum tolerant vibration velocity v_{\max} are given, the safety distance is:

$$R_{\min} = Q_{\max}^{1/3} (K / v_{\max})^{1/\alpha} \quad (3)$$

The designed explosive charge of Beizhuang Tunnel is 54 kg and the maximum tolerant vibration velocity defined in literature [28] is 2.0 cm/s, so the safe distance could be obtained from the formula (3):

$$R_{\min} = 42.26 \text{ m}$$

b. Prediction of reasonable explosive charge for Beizhuang Tunnel

When the allowable designed vibration velocity v_{\max} and the distance between ground surface and blasting source R are given, the allowable maximum explosive charge is:

$$Q_{\max} = R^3 (v / K)^{3/\alpha} \quad (4)$$

If the designed explosive charge $Q_{\max} = 54 \text{ kg}$ is adopted, the safety distance for blasting is 42.26 m according to the above discussion. While the depth of the section of Beizhuang tunnel is 37-50 m, and the distance between some of buildings and blasting point is shorter than the defined safe distance, so the designed explosive charge should be cut down in shallow part. The calculation was carried out according to the minimum depth ($R = 37 \text{ m}$) of the tunnel, so the explosive charge Q_{opt} could be gained from formula (4):

$$Q_{\text{opt}} = 36.24 \text{ kg}$$

4. NUMERICAL INVESTIGATION

It was very difficult to obtain complete field data due to various limitations in-situ, in that case, a 3D numerical model was set up in MIDAS/GTS [29] to comprehensively analysis the ground vibration velocity induced by blasting in the right tunnel of Beizhuang tunnel.

4.1. Numerical model

The model was built according to in-situ engineering conditions. The tunnel was one centred circle section with net width of 10.75 m and net height of 7.10 m, the building size was 10×10×6 m (L×W×H), and bottom size of the model was 40×180 m (L×W). The model height referred to the depth of the section from YK20+500 to YK20+680 of the Tunnel, was 44-53 m. The surrounding rock was subject to Mohr-Coulomb yield criteria, with surface spring built on its surrounding. The simulated explosive charge was about 54 kg. Parameters of the model were shown in Table 5.

Tab. 5: Parameters of the model

Materials Category	Modulus of elasticity E (MPa)	Poisson's ratio μ	Bulk density γ (kN/m ³)	Cohesive force C (kPa)	Friction angle φ (°)
Weathered limestone	19	0.29	24	1500	40
Building	25	0.18	28	0	0

4.2. Analysis of ground vibration velocity

Since section YK20+510 was right above the blasting point in the tunnel, the influence of blasting vibration on ground was significant. The testing point on this section was selected as the typical section to obtain the waveform chart of three-component blasting vibration velocity (Figure 6). In order to facilitate analysis, it is defined that X was the direction normal to axial line of tunnel, namely, transverse direction; Y was the direction along axial line of tunnel, namely longitudinal direction; Z was the direction normal to ground surface, namely vertical direction.

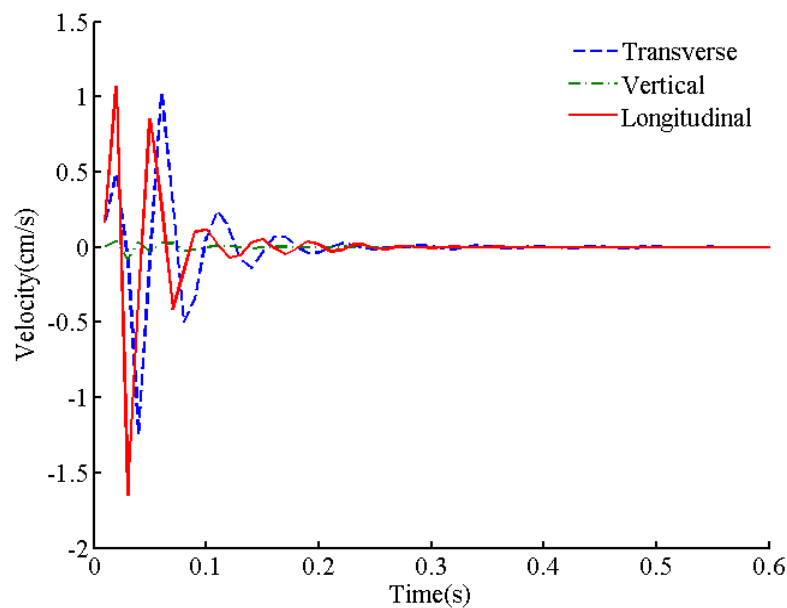
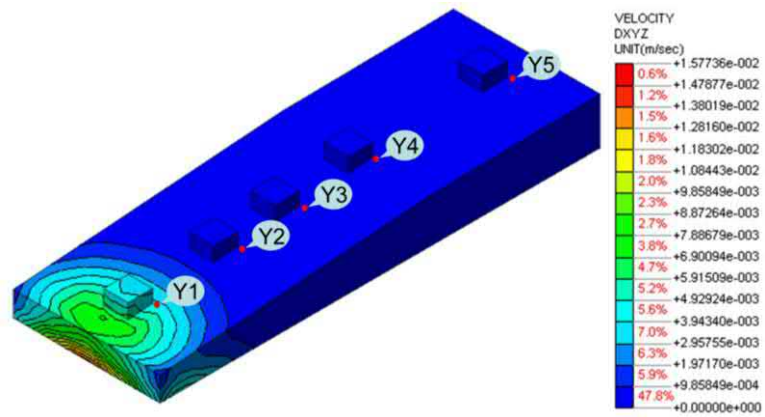
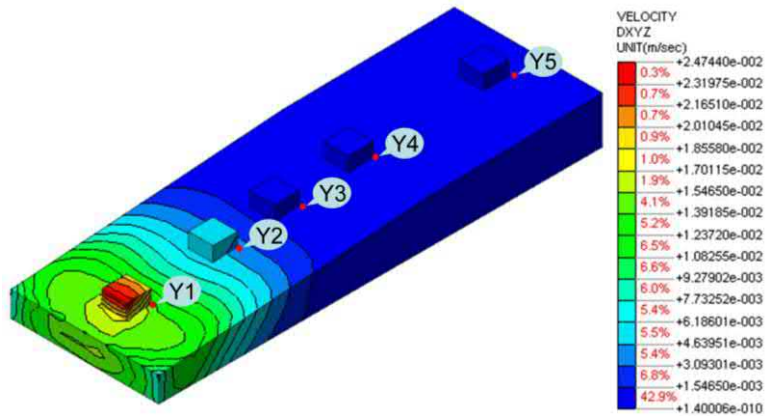


Fig. 6 - The typical waveform ($Y=0m$)

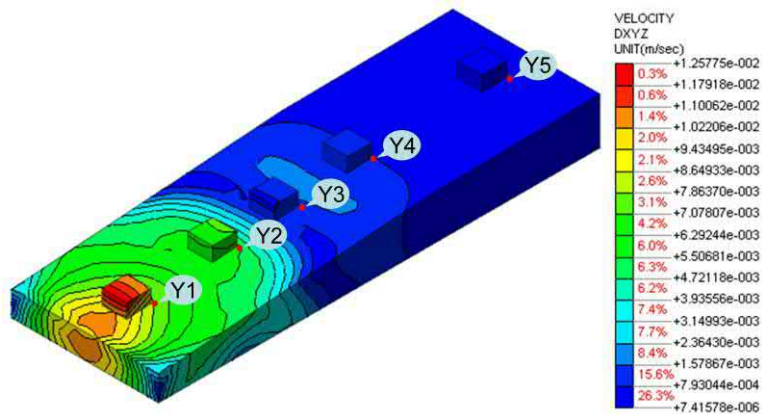
As shown in Figure 6, the vibration velocities along X direction and Y direction were much higher than that of Z direction, and the maximum vibration velocity at $Y=0$ m is 1.67 cm/s. The vibration velocity attenuated faster within the first 100 ms after blasting. The velocity nephograms of ground with time were shown in Figure 7.



(a) $t=10\text{ ms}$

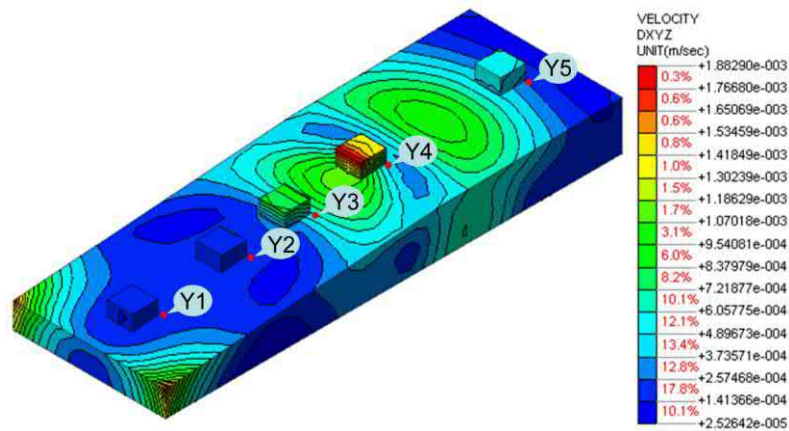


(b) $t=20\text{ ms}$



(c) $t=40\text{ ms}$

Fig. 7 - Velocity nephograms of ground with time



(d) $t=80\text{ ms}$

Fig. 7 - Velocity nephograms of ground with time

Figure 7 clearly displays the distribution of ground vibration velocity within 10 ms, 20 ms, 40 ms and 80 ms after blasting. When $t = 10\text{ ms}$, vibration is only generated around blasting source. The maximum vibration velocity takes place at the point of $Y=0\text{ m}$ and the PPV on the ground is less than that of the top of building. The seismic wave propagates in strata and attenuated gradually with the increase of time. When $t=80\text{ ms}$, the seismic wave propagates to the point of $Y=135\text{ m}$, and the corresponding PPV of this point is 0.068 cm/s , however, the PPV of the point $Y=0\text{ m}$ attenuates to 0 cm/s at the same time.

4.3. Comparative analysis of test results and simulation results

In order to analyse the distance-dependent attenuation of the ground vibration velocity, a comparative study between simulation results and test results was conducted using the ground PPV along the axial direction (Y direction) of tunnel. The attenuation of the ground vibration velocity vs. horizontal distance was shown in Figure 8.

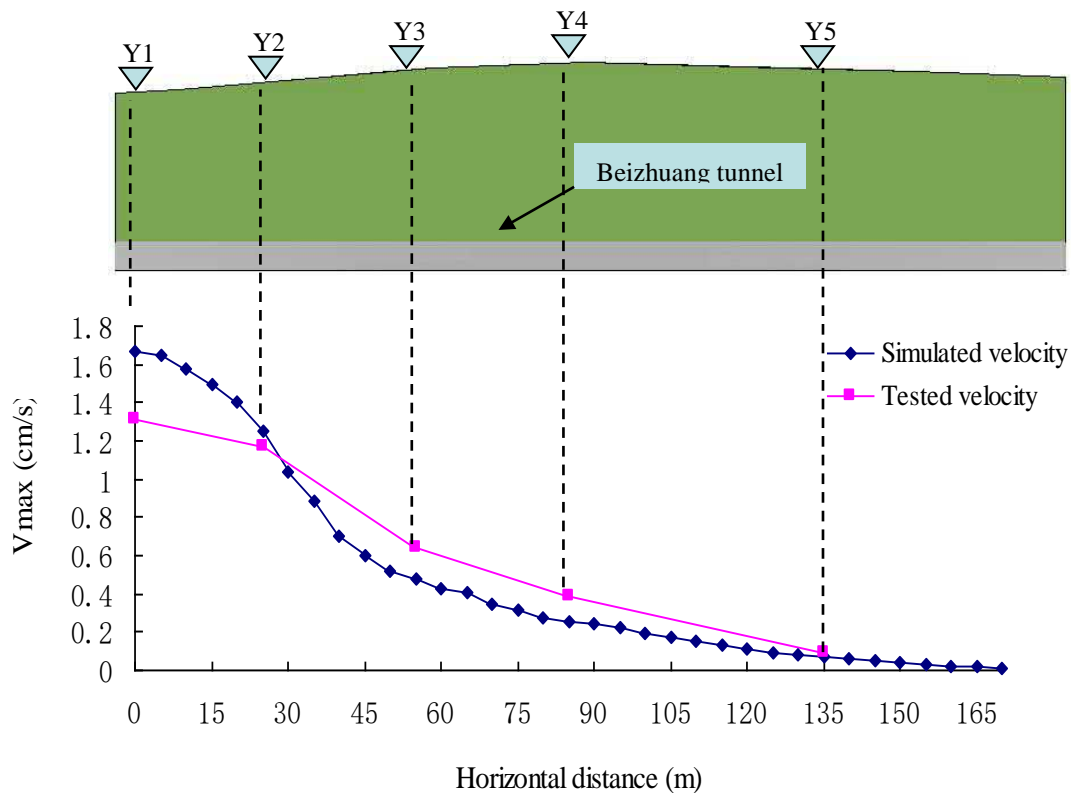


Fig. 8 - Attenuation of the ground vibration velocity vs. horizontal distance

The simulation curve indicates that the farther the distance to blasting source, the smaller the ground vibration velocity. When horizontal distance is $Y=50$ m, the maximum ground vibration velocity is 0.52 cm/s, which is only one third of that of $Y=0$ m. After the point of $Y=50$ m, the attenuation of ground vibration velocity is slowed. Since the soil was supposed to be uniform and continuous in numerical calculations, the simulation results were fairly ideal. Therefore, the ground vibration velocity in numerical calculations is slightly higher than that of in-situ test within 30 m horizontally, and it attenuates quickly. The main attenuation area of ground vibration velocity is within 50 m (Figures 7 and 8), so buildings within this area should be protected during blasting construction.

5. CONCLUSIONS

For the purpose of safety and economy, it is quite essential to determine the safe distance and design a reasonable explosive charge in tunnelling under cross a village. Experimental and numerical results about Beizhuang tunnel are as following:

(1) The blasting induced ground vibration velocity is closely associated with explosive charge and distance to blasting source. Less explosive charge and longer distance to blasting source lead to lower ground vibration velocity and less damage to ground building.

(2) When the explosive charge is around 54 kg, the maximum PPV is 1.366 cm/s, which is lower than the maximum vibration velocity allowed for building in masonry structure.

(3) When the distance between building and blasting source is more than 42.26 m, the explosive charge of 54 kg is relatively safe. While the blasting point is 37 m to building, the maximum explosive charge is 36.24 kg.

(4) With the increase of horizontal distance to blasting source, the ground vibration velocity attenuates rapidly. The main attenuation area for ground vibration velocity is within 50 m horizontal to the blasting source, which is also the significant affect region of blasting vibration.

ACKNOWLEDGMENTS

This work is partially supported by Industrial research project of Science and Technology of Shaanxi Province (No.2015GY185) and the Special Fund for Basic Scientific Research of Central Colleges of Chang'an University (No.CHD2012JC072). The authors also gratefully acknowledge the helpful comments and suggestions of the reviewers, which have improved the presentation.

REFERENCES

- [1] Kuzu C., 2008. The mitigation of the vibration effects caused by tunnel blasts in urban areas: a case study in Istanbul. *Environmental Geology*, 54, 1075-1080.
- [2] Zhu J.H., 2007. The safety evaluation of the close building under the tunnel blasting vibration. *Chinese Journal of Explosives & Propellants*, 30, 78-79.
- [3] Gong L., Qiu W.G., Gao X.Q., 2006. Controlled blasting experimental research of railway tunnel under through buildings closely. *Rock and Soil Mechanics*, 27, 1089-1092.
- [4] Xia X., Li H.B., Li J.C., Liu B., Yu C., 2013. A case study on rock damage prediction and control method for underground tunnels subjected to adjacent excavation blasting. *Tunnelling and Underground Space Technology*, 35, 1-7.
- [5] Li X.H., Long Y., Ji C., Zhong M.S., Zhao H.B., 2013. Study on the vibration effect on operation subway induced by blasting of an adjacent cross tunnel and the reducing vibration techniques. *Journal of Vibroengineering*, 15, 1454-1462.
- [6] Singh P.K., 2002. Blast vibration damage to underground coal mines from adjacent open-pit blasting. *International Journal of Rock Mechanics and Mining Sciences*, 39, 959-973.
- [7] Umit Ozer., 2008. Environmental impacts of ground vibration induced by blasting at different rock units on the Kadikoy-Kartal metro tunnel. *Engineering Geology*, 100, 82-90.
- [8] Khandelwal M., Singh T.N., 2007. Evaluation of blast-induced ground vibration predictors. *Soil Dynamics and Earthquake Engineering*, 27, 116-125.
- [9] Jiang X.L., Jia Y., Zhao B.J., Wang T., 2008. Analysis of influence of metro tunnel construction on adjacent buildings. *Rock and Soil Mechanics*, 29, 3047-3052.
- [10] Zhu G.Q., Lin Z., Zhu Y.C., Yang C., 2012. Research on influences of in-situ tunnel extension project on adjacent buildings. *Rock and Soil Mechanics*, 33, 251-256.

- [11] Xu J., Gu Y.L., Kang J.M., 2005. Study on interaction of tunnel and upper structure. *Rock and Soil Mechanics*, 26, 889-892.
- [12] Tian L., Li Z.X., 2008. Dynamic response analysis of a building structure subjected to ground shock from a tunnel explosion. *International Journal of Impact Engineering*, 35, 1164-1178.
- [13] Tian L., Li Z.X., 2004. Dynamic responses of sliding base isolated buildings subjected to shock wave of underground explosion. *Explos Shock Waves*, 24, 16-23.
- [14] Mostaghel N., Davis T., 1997. Representations of Coulomb friction for dynamic analysis. *Earthquake Engineering and Structural Dynamics*, 26, 541-548.
- [15] Fan J., Tang J.X., 2001. Dynamic characteristics and earthquake response analysis of structures supported on slide-limited friction base isolation system. *Jianzhu Jiegou Xuebao & Journal of Building Structures*, 22, 20.
- [16] Wang X.Y., Shao Z.S., Qiao R.J., 2013. Study on the dynamic responses of blasting vibration on undercrossing railway tunnel with small distance. *Chinese Journal of Applied Mechanics*, 30, 527-532.
- [17] Shao Z.S., Li P.P., Wang X.Y., 2014. Study on the blasting vibration control of tunnel with small distance. *Chinese Journal of Applied Mechanics*, 31, 230-235.
- [18] Shao Z.S., Qiao R.J., Wang X.Y., 2012. Numerical Investigation into Effect of Free Surface on the Response of Blasting Induced Vibration. *Chinese Journal of Underground Space and Engineering*, 8, 1052-1058.
- [19] Yao Q., Yang X.G., Li H.T., 2014. Residential comfort assessment due to blasting vibration. *Journal of Vibroengineering*, 16, 674-684.
- [20] GB6722-86., 1986 Chinese Code for Blasting Safety Standards. China Standard Publishing Company, Beijing.
- [21] Xie Q.M., Xia Y.Y., Li X.P., 2003. Study on blasting vibration control of creep mass slope of longtan hydropower station. *Chinese Journal of Rock Mechanics and Engineering*, 22, 1929-1932.
- [22] LÜ T., Shi Y.Q., Huang C., Li H.B., Xia X., Zhou Q.C., Li J.R., 2007. Study on attenuation parameters of blasting vibration by nonlinear regression analysis. *Rock and Soil Mechanics*, 28, 1871-1878.
- [23] Wu T., Peng L.M., Zhai X.D., 2009. Monitoring and Safety Evaluation of Construction Blasting for Metro Tunnels Underpassing Densely Populated Areas. *Modern Tunnelling Technology*, 46, 48-52.
- [24] Xue W.J., Wang L.B., Druta C., 2014. Monitoring the Speed, Configurations, and Weight of Vehicles Using An In-Situ Wireless Sensing Network. *IEEE Transactions on Intelligent Transportation Systems* 2014. doi: 10.1109/TITS.2014.2364186.
- [25] Yao Y., He C., 2009. Analysis of Blasting Vibration Response of Parallel Set Small Clear-distance Tunnels and Blasting Control Measures. *Rock and Soil Mechanics*, 30, 2815-2822.
- [26] Nateghi R., 2011. Prediction of Gound Vibration Level Induced by Blasting at Different Rock Units. *International Journal of Rock Mechanics and Mining Sciences*, 48, 899-908.
- [27] Xue Y.G., Li S.C., Zhang D.F., 2014. Vibration characteristics in subway operation and environmental responses of ancient buildings. *Polish Journal of Environmental Studies*, 23, 231-241.
- [28] GB6722-2003., 1999. Chinese Code for Blasting Safety Standards. China Standard Publishing Company, Beijing.
- [29] MIDAS GTS. 2009. User supports web page. < http://gts.midasit.co.kr/Tech_default/default.asp>.

PROGRESSIVE COLLAPSE ANALYSIS OF 2-D RC FRAMES USING AEM

Osama El-Mahdy¹, El-Sayed El-Kasaby², Hala Abusafa², Amr El-Gama²

1. *Department of Civil Engineering, Faculty of Engineering at Shoubra, Benha University, Shoubra, Cairo, Egypt*
2. *Department of Civil Engineering, Benha Faculty of Engineering, Benha University, Benha, Egypt, amr.ali@bhit.bu.edu.eg, engamrramadan@yahoo.com*

ABSTRACT

Numerical simulation of a progressive collapse of structures using computer has a very actual apprehension for structural engineers due to their interest in structures veracity estimation. This simulation helps engineers to develop methods for increasing or decreasing the progressive failure. Finite Element Method (FEM) is the most computer simulation analysis currently used to perform a structural vulnerability assessment. Unfortunately, FEM is not able to automatically analyze a structure after element separation and collision which has a great effect on a structure's performance during collapse. For instances, a bombing load can cause damage to a main supporting column in a structure, which will cause debris flying at a very high velocity from the damaged column. This debris can cause another local failure in another column upon impact and lead to the progressive collapse of the whole structure. A new simulation technique, which was developed in 1995 as part of Tagel-Din's doctoral research, called Applied Element Method (AEM) can simulate the structure's behaviour from zero loading until collapse, through the elastic phase, opening and propagation of cracks, yielding of reinforcement bars and separation and collision of elements. This method is used in Extreme Loading for Structures software (ELS) by Applied Science International (ASI). In the current paper, a brief description of the AEM is given. Also, numerical modelling based on two experimental studies available in the literature conducted by Ahmadi et al. [1] and Yi et al. [2] are generated using ELS. These models are used to confirm the capability of AEM in simulation the progressive collapse behaviour of structures. Also, the models are utilized to examine and measure the structural resisting mechanisms of reinforced concrete structures against progressive collapse. The obtained numerical results indicated that, ELS can accurately model all structural behaviour stages up to collapse. A better agreement between the experimental and numerical results is observed. Moreover, the results obtained with ELS indicated an enhanced agreement with other software packages such as; OpenSees, Ansys, Abacus, and MSC Marc.

KEYWORDS

Progressive collapse, Reinforced concrete frames, Applied element method, Extreme loading for structures, Displacement control

1. INTRODUCTION

The prevention of progressive collapse lies primarily in the appropriate and effective analysis of the structures having high potential to progressivity. To minimize the progressive collapse risks, the structural system of the building should be able to bear the removal of one or more structural elements and redistribute their loads on the neighbouring elements, so that disproportionate collapse would not take place.

Many definitions for progressive collapse phenomenon are given in buildings codes and standards such as ASCE 7-05 [3] and GSA [4]. Other definitions can be found in the related literature such as Nair [5] and Ellingwood & Dusenberry [6].

Progressive collapse of a building could be caused by man-made accidental extreme loadings such as car accident, explosion of gas or steam services system, or an aircraft crash. The failure of the structural member can be also due to intentional loading that aims the structure failure like using a bomb in a criminal or structure demolition. Another cause for the structural component loss is natural hazards like hurricanes, tornados, floods, fires, or earthquakes. Mistakes in design and construction or overload due to change of use or structural modifications can also lead to structurally significant abnormal loadings.

Because of such collapses, many international structural codes and standards started to consider the progressive collapse resistance that help owners, developers, and engineers in designing building facilities for withstanding progressive collapse effect. These codes and standards differ in dealing with the progressive collapse in different ways such as the definition of progressive collapse, the used load combination, consideration of lateral load, approaches for progressive collapse threshold, and acceptance criteria. Among the codes that discussed the issue of progressive collapse are the Interagency Security Design Committee (ISC) [7], the British standards (BS 5950-1) [8], the General Services Administration (GSA) published in 2003 [4], and the Unified Facilities Criteria (UFC) by Department of Defense, USA published in 2005 and 2009 [9]. However, regardless of the level of protection of the building, progressive collapse prevention should be achieved to allow for timely evacuation of the tenant to save lives.

Design codes use direct and indirect design methods for protection against progressive collapse. The indirect design method prevents progressive collapse by providing a minimum level of strength, continuity and ductility of the structure. The direct design method explicitly considers resistance to progressive collapse during the design process. ASCE7-05 [3] has proposed specific local resistance (SLR) and alternative load path (ALP) methods for direct designs. SLR requires that the building, or parts of the building, provide sufficient strength to resist load. In this method, the strength and ductility of critical elements can be determined during the design process. On the other hand, ALP allows local failure of structural members; however, it prevents extensive structural failure by providing an alternative load path. When a structural member fails, the energy stored in the damaged structural members is released and causes additional loading on the other structural members, which changes the load transmission paths. If the adjacent structural member has enough capacity and ductility to bear the additional load, the structural system forms an ALP to transfer the load. This method analyses the building under the effect of one or more structural elements removal. The major advantage of this method is that it is independent of the cause of failure and analysis can be applied to any threat for collapse of an element. In conventional methods of design, only the flexural mechanism is considered as an ALP, and compression arch action (CAA) and catenary action (CA) are beyond the scope of the design codes. CAA is a mechanism of resistance to vertical loads through the development of axial compressive force in beams. Development of this axial force requires the restriction of longitudinal deflection of beams by other members of the frame. CA is resistant to vertical loads through the development of tensile force in the horizontal members. Development of tensile force in beams requires a large deformation in the beam and the ability to create longitudinal restriction to balance this force.

Computer simulation is an important tool in determining the performance of structures in extreme loading conditions. The numerical methods used in structural analysis can be classified into two categories. In the first category, the model is based on continuum material equations. On the other hand, the second category can be defined using discrete element techniques, such as the extended distinct element method (EDEM). The finite element method (FEM) is the most common example for the first category, with the division of the domain into finite elements with the respective material properties. The FEM yields good results for structural analysis before collapse, even if one considers non-linear materials and geometry. However, if the structure's behaviour advances to a discrete state, because of crack opening and propagation, the FEM loses its efficiency. Discrete element techniques which allow the mechanical interaction between elements and can simulate the cracking process more easily when compared to FEM, depending on the size, shape and arrangement of the elements. Despite its advantages, in small displacement analysis, the EDEM is less accurate than the FEM and the analysis time is quite large for a reasonable number of elements that simulate real problems.

To overcome the EDEM's drawbacks, Tagel-Din and Meguro developed the Applied Element Method (AEM) which is adopting the discrete cracking approach. The major advantage of the AEM is its capacity to simulate different collapse modes of structures and the structure's behaviour from zero loading until collapse, including the elastic phase, opening and propagation of cracks, yielding of reinforcement bars and separation and collision of elements. However, the computation time required to simulate large structures' behaviour from zero loading until collapse might become very large due to the necessity of small time increments, to ensure numerical stability (Meguro and Tagel-Din [10-12] and Tagel-Din and Meguro [13-15]).

In this regard, one of the main advantages of the applied element technique is its capability of modelling, with high accuracy, both continuum and discrete phases of structural response. Figure 1 compares the performance of this method with respect to finite element techniques in terms of accuracy in a wide range of modelling capabilities.

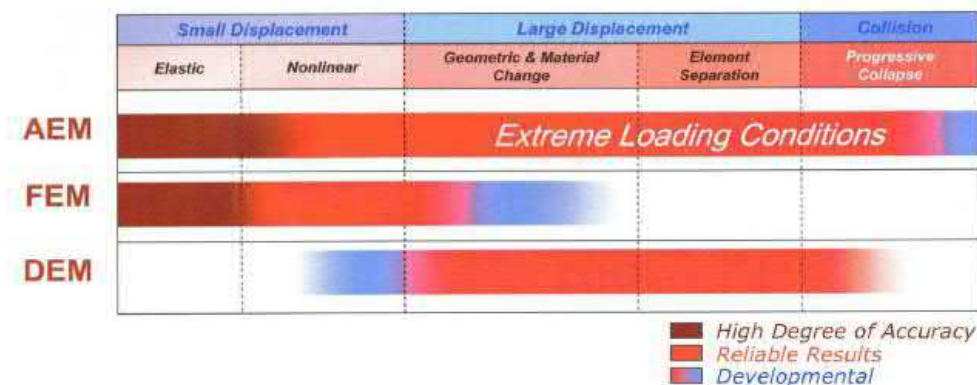


Fig. 1 - Analysis domain of AEM (ASI [16])

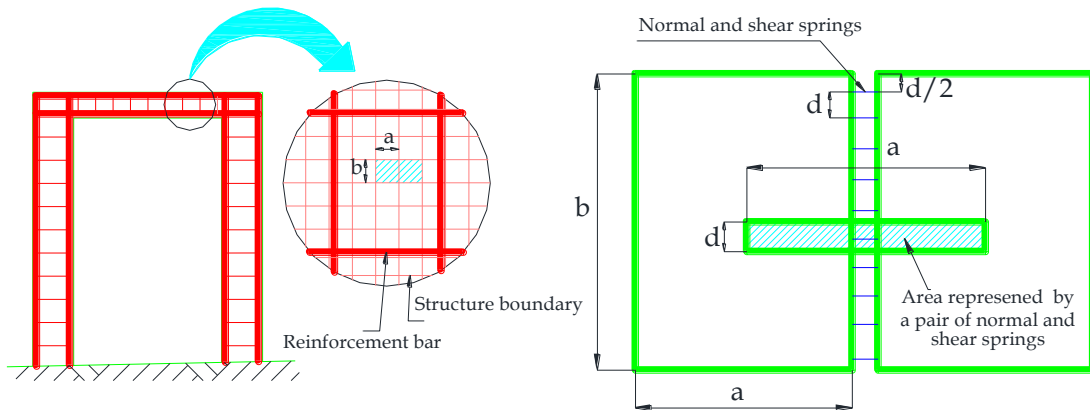
2. OBJECTIVE

The objective of this paper is to verify the capability of AEM in simulating the progressive collapse of two-dimensional reinforced concrete frames. Two experimental studies conducted by Ahmadi et al. [1] and Yi et al. [2] are modelled using the Extreme Loading for Structures (ELS) software. The obtained results are compared with those measured in the experimental works and predicated using other software package such as OpenSees, Ansys, Abacus and MSC Marc. Furthermore, the presented analytical model will lead to investigate and quantify the structural resisting mechanisms of reinforced concrete structures against progressive collapse.

3. BRIEF DESCRIPTION OF THE APPLIED ELEMENT METHOD (AEM)

The Applied Element Method (AEM) has been developed by Tagel-Din and Meguro [13] to create a link between the advantages of finite element method for continuum mechanics and discrete element method for discrete mechanics. Since then, the method was applied and verified for; elastic analysis, reinforced concrete structures subjected to cyclic loads and buckling and post-buckling behaviour (Meguro and Tagel-Din, [10-12]). Also, AEM was applied for crack initiation and propagation, estimation of failure loads of reinforced concrete structures, non-linear dynamic analysis of structures subjected to collisions and severe earthquakes (Tagel-Din and Meguro [13, 29 & 50]), fault-rupture propagation (Ramancharle et al. [17]), non-linear behaviour of brick structures (Mayorca and Meguro [18]) and blast analysis (Asprone et al. [19] and Coffield & Adeli [20]).

In the AEM, the structure is discretized into series of virtually relatively small rigid elements, with special shape and determined dimensions connected together along their faces through a set of three non-linear contact springs (one normal spring and two shear springs), which represent the continuity between elements and reflect the properties of the material characteristics used (concrete and reinforcement bars), and that is differ from the connectivity in FEM where the elements are connected by nodes, as shown in Figure 2. The springs located at contact points represent stresses, strains and deformations of a certain portion.



(a) Element generation for AEM (b) Spring distribution and area of influence of each pair of springs

Fig. 2 - Modelling in AEM (Meguro and Tagel-Din [10])

Each single element has six degrees of freedom; three for translations and three for rotations. Relative translational or rotational displacements between two neighbouring elements cause stresses in the springs located at their common face as shown in Figure 3.

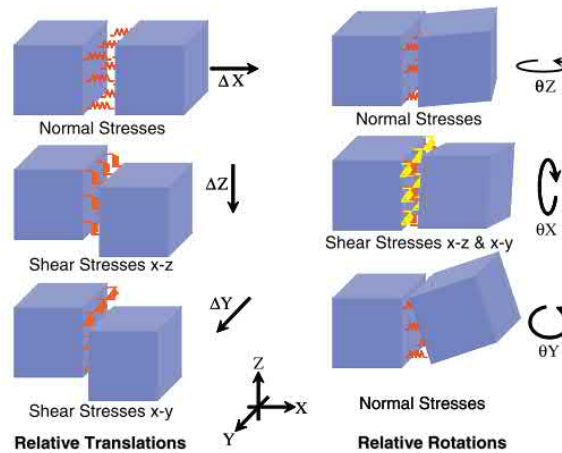


Fig. 3 - Stresses in springs due to elements' relative displacements (*Applied Science International* [21])

The AEM is a stiffness-based method, in which the stiffness of each pair of normal and shear springs connecting the element centerlines of an area ($d \times t$) with the length of “ a ” is calculated using Equations 1 and 2 (Meguro and Tagel-Din [10])

$$K_n = \left(\frac{E \times d \times t}{a} \right) \quad (1)$$

$$K_s = \left(\frac{G \times d \times t}{a} \right) \quad (2)$$

where, K_n is the stiffness of normal spring; K_s is the stiffness of the shear spring; d is the distance between the springs; t is the element thickness; a is the length of the representative area; and E & G are the Young's modulus and the shear modulus of the material, respectively.

Additionally, one must consider the element rotation, which is resisted by shear and normal springs. It is possible to calculate the theoretical rotational stiffness K_r from normal springs as follows:

$$K_r = \int_{-b/2}^{b/2} \frac{Et}{b} Z^2 = \frac{Etb^2}{12} \quad (3)$$

where, b the element's height and Z the spring's distance to the element centroid as represented in Figure 4. Therefore, it is possible to obtain the element's rotational stiffness as the sum of each spring's rotational stiffness, which leads to (Meguro and Tagel-Din [10]):

$$K_r = \frac{Etb^2}{4n^3} \sum_{i=1}^n \left(i - \frac{1}{2} \right)^2 \quad (4)$$

where $2n$ is the number of springs and i the spring number.

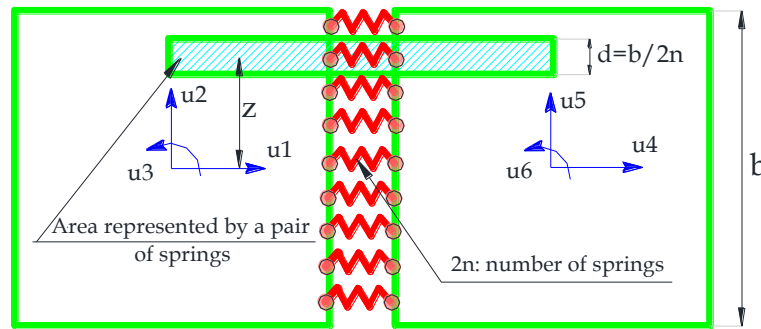


Fig. 4 - Normal springs for rotational stiffness (Meguro and Tagel-Din [10])

In the reinforced concrete model, two types of springs are used namely; matrix springs for concrete, and reinforcement springs for steel bars, as shown in Figure 5. Reinforcement springs can be set at the exact location of the steel bars so that all reinforcement details and amounts can be easily considered. In the case of the reinforcement spring, the representative area ($d \times t$) is replaced by the reinforcement bar area.

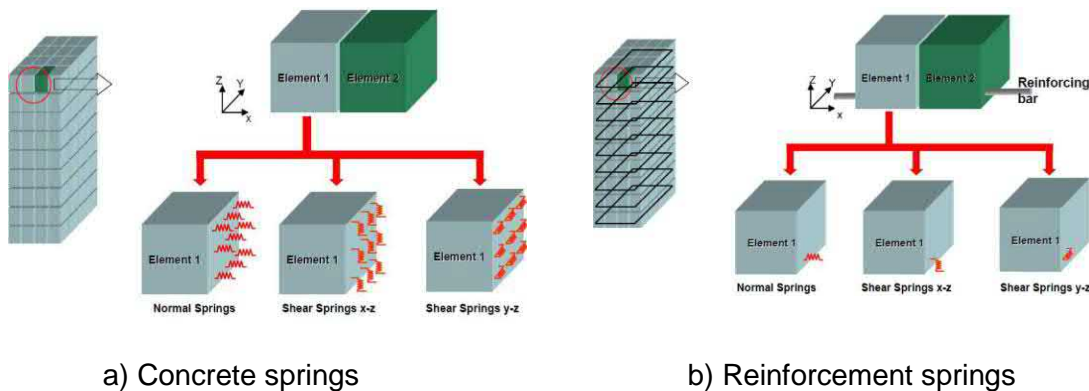


Fig. 5 - Concrete and reinforcement springs (Applied Science International [21])

In reinforced concrete structure, the matrix springs are cut or removed when the average tensile strain between two adjacent faces reaches the value of the separation strain, specified in the material properties of the model, and the element behaves as separate bodies for the rest of the analysis. Similarly, the reinforcement springs are cut off if the normal stress is equal or greater than the ultimate stress specified for this material or when the concrete spring cut even if the reinforcement springs have compression forces.

Although the reinforcement spring and the neighbouring concrete spring have the same strain, relative displacements can occur between reinforcement bars and the surrounding concrete, due to the assumption that the failure of concrete springs occurs prior to the failure of reinforcement springs (Applied Science International [21]).

In two-dimensional model, each element has three degrees of freedom and the size of the element stiffness matrix is (6 x 6). The element stiffness matrix is determined based on the relative coordinates between the location of the contact points and the element centerline and on the spring stiffness, as shown in Figure 6. On the other hand, in three-dimensional model, every element has six degrees of freedom. Therefore, a (12x12) stiffness matrix is generated (Meguro and Tagel-Din [11]). The element stiffness matrix depends on the spring material and status, for example, it considers whether the spring is for steel or concrete. In case of concrete, it considers

whether the spring is already cracked or reached compressive failure criteria. In case of steel, it also follows the constitutive stress-strain relations. These elements matrices are assembled at the structural master stiffness matrix.

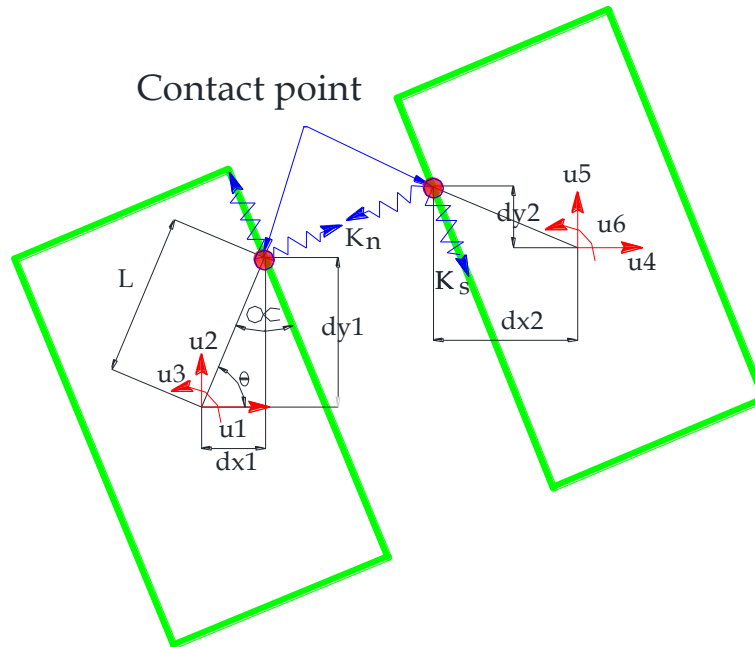


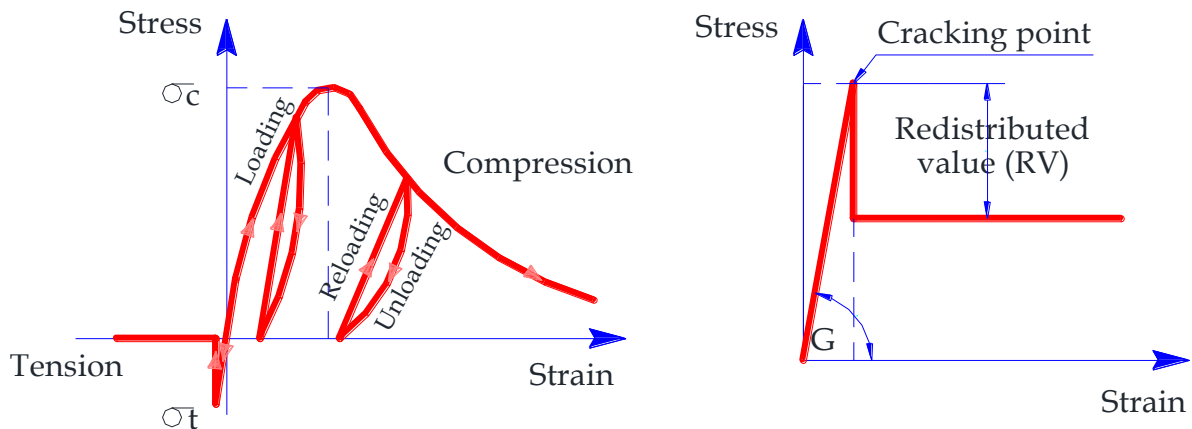
Fig. 6 - Element shape, contact point and DOF (Meguro and Tagel-Din [11])

In the AEM, fully non-linear path-dependent constitutive models are adopted for concrete and reinforcement bars as shown in Figure 7. The Maekawa compression model, an elasto-plastic and fracture model, is utilized for concrete in compression (Okamura and Maekawa [22]). While for concrete in tension, a linear stress-strain relationship is used until reaching the cracking point, then the stresses drop to zero. The residual stresses are then redistributed in the next loading step by applying the redistributed force values in the reverse direction. Also, the relationship between the shear stress and shear strain is assumed to be linear until the cracking of the concrete and the level of drop of shear stresses depends on the aggregate interlock and friction at the crack surface.

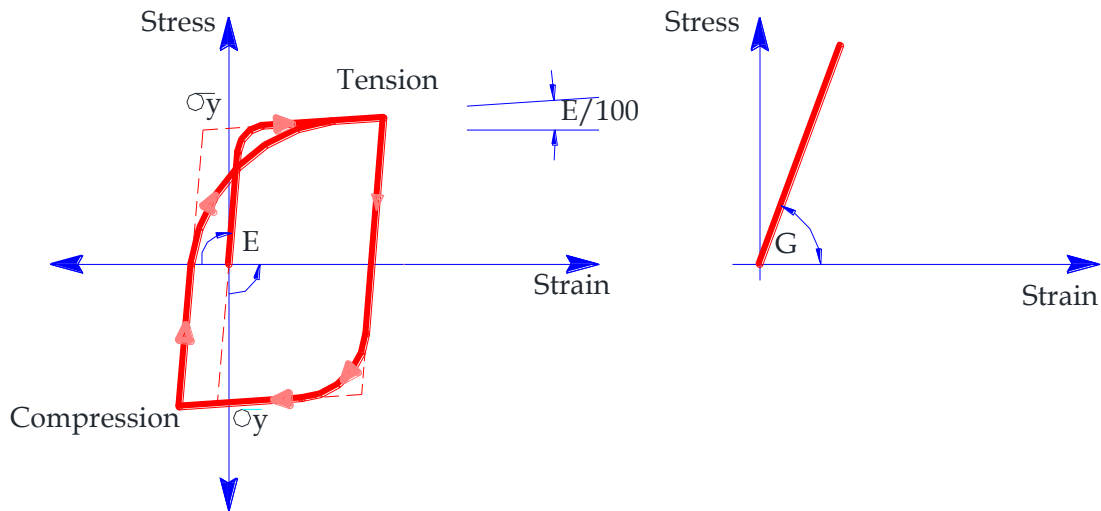
The transverse reinforcement confines the concrete and increases compressive strength. To consider the biaxial confinement effects in compression zones, Kupfer biaxial failure function is adopted. A modified compressive strength, f_{ceq} , is calculated as a function of the principal stress components (σ_1 and σ_2) and the compression stress f_c as follows (Kupfer et al. [23]):

$$f_{ceq} = \frac{1 + 3.65(\sigma_1/\sigma_2)}{[1 + \sigma_1/\sigma_2]^2} f_c \quad (5)$$

This indicates that the compressive resistance associated with each spring is variable and depends mainly on the stress situation at the spring location.



(a) Tension, compression and shear models for concrete [22]



(b) Reinforcement under axial and shear stresses [24]

Fig. 7 - Constitutive models for concrete and steel

For reinforcement bars, the model presented by Ristic et al. [24] is adopted. The stiffness of the steel spring after yielding is set to 1% of the initial spring stiffness. The tangent stiffness of reinforcement is calculated based on the strain from the reinforcement spring, loading status (either loading or unloading) and the previous history of steel spring which controls the Bauschinger's effect. The main advantage of this model is that it can consider easily the effects of partial unloading and Bauschinger's effect without any additional complications to the analysis. It should be emphasized that, some other failure phenomena like buckling of reinforcement and spalling of concrete cover, are not considered in the analysis yet.

To account for large displacements, the following modification to Equation 6 is introduced (Meguro and Tagel-Din [12]):

$$K\Delta u = \Delta f + R_M + R_G \tag{6}$$

where K is the non-linear stiffness matrix, Δu the incremental displacement vector, Δf the incremental load vector, R_G is the residual load vector due to geometric changes in structure during loading and R_M is the residual load vector due to cracking or incompatibility between spring stress and the corresponding strain.

The equilibrium equations represent a linear system of equations for each step. The solution of the equilibrium equations is commonly solved using Cholesky upper-lower decomposition. Separated elements may collide with other elements. In that case, new springs are generated at the contact points of the collided elements.

Modelling a progressive collapse mechanism should begin with the whole of structure elements then, specify the structural elements that will be instantaneously removed. However, most programs are incapable of analysing the change in their geometry and stiffness matrices. A more advanced software package was developed using the theory of AEM. This software is called Extreme Loading for Structures (ELS), and will be used in this paper.

4. VALIDATION OF AEM USING ELS SOFTWARE

Literature has shown that AEM gives good estimations for large displacements of structures undergoing collapse (Galal and El-Sawy [25], Meguro and Tagel-Din [10 & 11], Sasani [26], Wibowo et al. [27], Tagel-Din and Rahman [28], Tagel-Din and Meguro [15 & 29], Salem [30], Tagel-Din [31], Meguro and Tagel-Din [32], Park et al. [33], Helmy et al. [34 - 36], Salem and Helmy [37], Salem et al. [38 & 39], Lupoae and Bucur [40], Lupoae et al. [41] and El-Mahdy et al. [42]).

Experimental tests conducted by Ahmadi et al. [1] and Yi et al. [2] are modelled using ELS (v. 2.3) software to validate the AEM. However, sensitivity analysis for mesh, springs, loading steps, and calibration of the constitutive models should be done firstly.

4.1 Sensitivity analysis

A mesh sensitivity analysis is performed for the experimental works to study the effect of element size and the number of connecting springs between elements. The experiments are analysed using three increasingly smaller-sized elements (approximately cubic shapes with edges of 100, 50 and 25 mm). Additionally, for each different element size, two models are considered, using 5 and 10 connecting springs for each pair of adjacent element faces. The convergence is considered achieved when the changes in the load-displacement result from one analysis to the next are too small to be visually noticeable. As shown in Figures 8 and 9, the estimation for load-displacement is achieved for a mesh of edge of 50 mm and 5 connecting springs between element faces and therefore, this combination is considered an appropriate mesh and used for the tests reported in this paper. A similar analysis is performed to calibrate the loading increment on model. Load-displacement curves are obtained using 0.10, 0.50, 1.00, 1.50, 2.00 mm loading steps and no noticeable differences were obtained between the resulting capacity curves. So, for all experiments, a step of 1.00 mm is used.

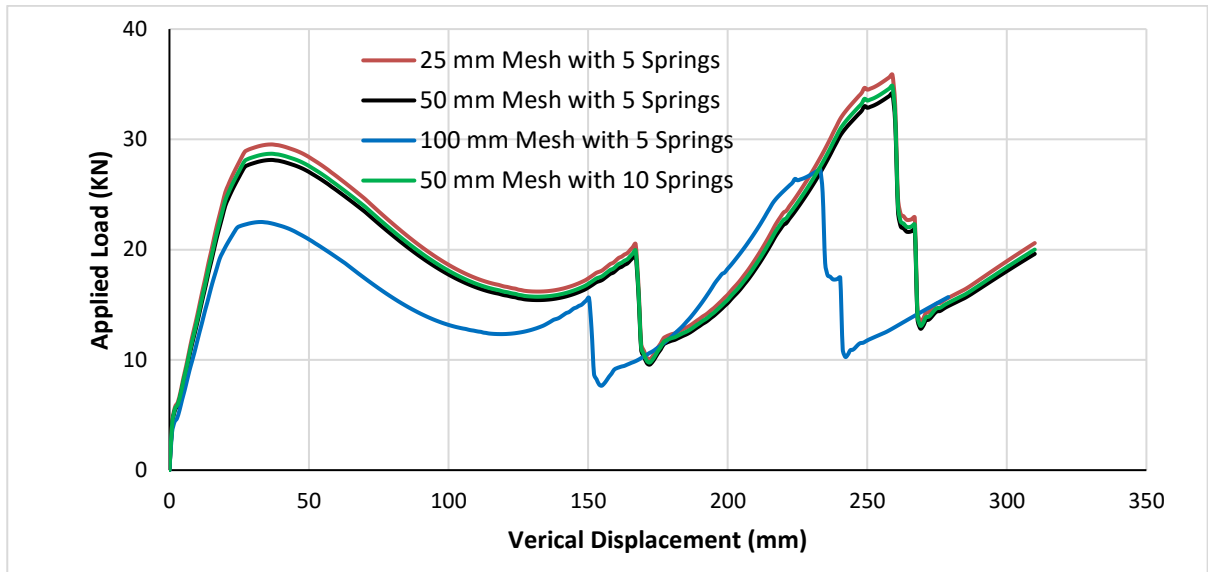


Fig. 8 - Effect of element size and the number of connecting springs between elements for Experimental work by Ahmadi et al. [1]

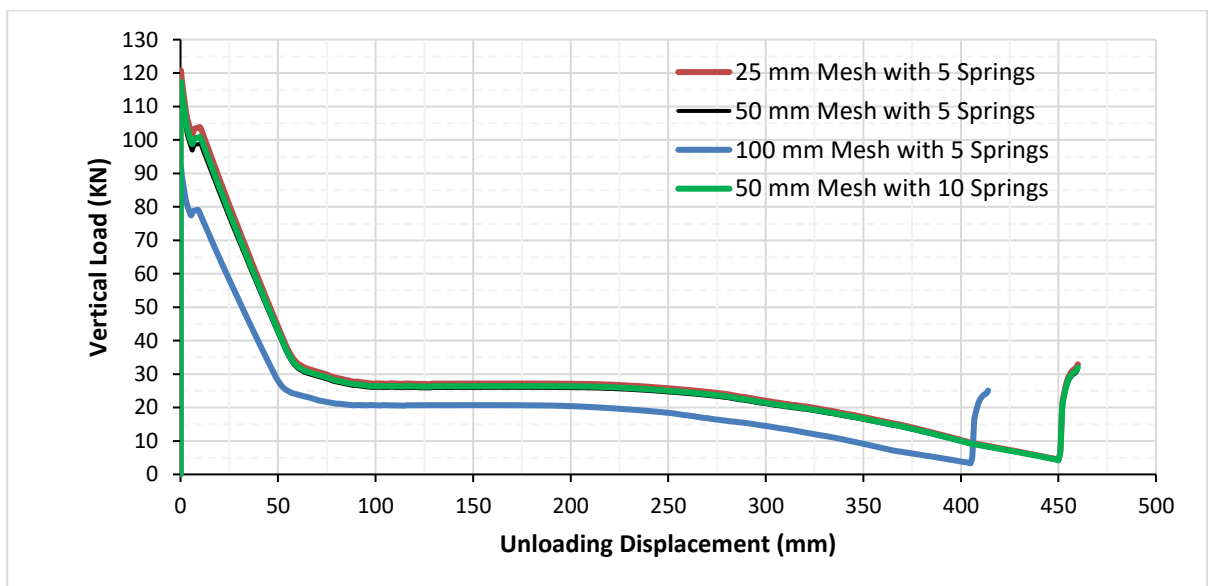


Fig. 9 Effect of element size and the number of connecting springs between elements for Experimental work by Yi et al. [2]

4.2 Calibration of the constitutive models

4.2.1 Steel

Due to lack of information for steel stress-strain curves in the experiments, the material characterization under tensile tests were simulated numerically and used to calibrate the parameters defining the Ristic constitutive model of steel (Ristic et al. [24]). The mechanical properties presented in each experimental were used, considering Young's modulus and shear modulus presented in each experimental and a post yield stiffness factor of 0.01.

4.2.2 Concrete

The characteristic compressive strength (f_{ck}), the modulus of elasticity (E_c) and the tensile strength of the concrete (f_{ct}) were calculated from its compressive strength according to Equations. 7 to 9 (FIP Model Code [43]). The concrete shear modulus is taken as $E/2(1+\nu)$ and a Poisson ratio (ν) of 0.2 is considered.

$$f_{ck} = f_c - 8 \text{ (MPa)} \quad (7)$$

$$E_c = 21.5 \left(\frac{f_c}{10} \right)^{1/3} \text{ (GPa)} \quad (8)$$

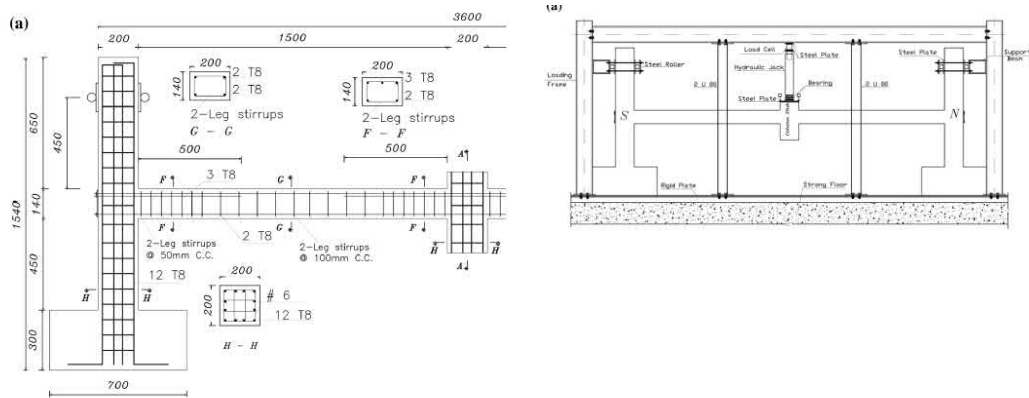
$$f_{ct} = 0.3(f_{ck})^{2/3} \text{ (MPa)} \quad (9)$$

Another important parameter characterizing the material constitutive models in ELS is the separation strain. This parameter defines the strain value in the springs located between two neighbouring elements at which the elements are considered to be physically separated. According to the ELS Modelling Manual (ASI [21]), for reinforced concrete elements, the separation strain should be higher than the ultimate tensile strain of the reinforcement bar.

4.3 Experimental work by Ahmadi et al. [1]

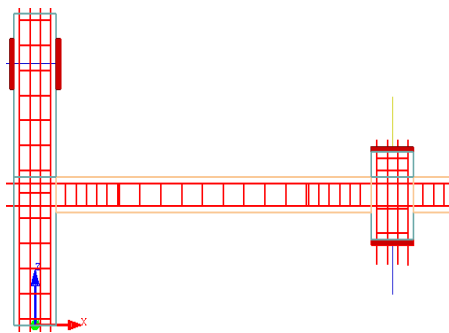
4.3.1 Experiment description

Ahmadi et al. [1], performed an experimental and numerical evaluation using the OpenSees open-source platform as part of a research program to examine progressive collapse of structures under column removal scenario at Iran University of Science and Technology (IUST). The aim of this work was to investigate the alternative load paths and resistance mechanisms in scaled sub-assembly and to compare the differences between the results of full-scale and scaled specimens. The full-scale assembly was selected from a 10-story office building which was designed based on an intermediate moment frame (IMF) system. The building was analysed based on the dead, live, and earthquake loads defined in ASCE7-05 [3] and designed based on ACI 318R-02 [44]. The specimen included two single-bay beams, one middle joint (a middle column stub), and two end columns with foundations to behave as two-dimensional specimen. The specimen was fastened to a displacement control point loaded (a monotonic vertical load) above the middle column stub to simulate the progressive collapse of the frame. The test continued until complete failure of the specimen. During testing, alternative load paths, mechanism of formation and development of cracks, corresponding displacements and strains at predefined points and sections were measured and the formation of resistance mechanisms and failure modes were recorded. The dimensions, reinforcement details of the specimen components, and test setup are shown in Figure 10. Furthermore, measured material properties are given in Tables (1 and 2). The researchers found that, load-displacement curve, mechanism of formation and development of cracks and failure mode of the scaled specimen had good agreement with the full-scale assembly. Also, they found that macro-model can provide a good estimation of collapse behaviour of RC sub-assembly under the middle column removal scenario.

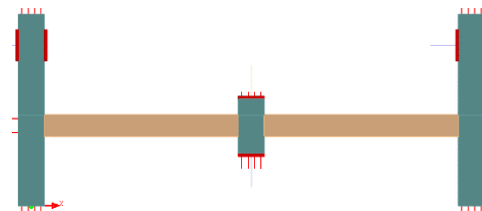


(a) Dimensions and reinforcement for the specimen (half part only) [1]

(b) Test setup [1]



(c) Modelling in ELS (half part only)



(d) Modelling in ELS

Fig. 10 - Specimen details and numerical modeling

Tab.1 - Concrete material properties (Ahmadi et al. [1])

Property	Young's Modulus (MPa)	Shear Modulus (MPa)	Tensile Stress (MPa)	Average Compressive stress (MPa)	Specific Weight (Kg/m ³)	Ultimate Strain
Concrete	2.610E4	1.0210E4	1.5	26	2500	0.20

Tab. 2 - Reinforcement material properties (Ahmadi et al. [1])

Property	Young's Modulus (MPa)	Shear Modulus (MPa)	Tensile and Compressive Yield Stress (MPa)	Ultimate Stress (MPa)	Specific Weight (Kg/m ³)	Ultimate Strain
T8	2.010E5	8.010E4	530	650	7840	0.16

4.3.2 Modelling and simulating

In the present paper, the tested specimen is modelled using ELS. Meshing division and reinforcement details similar to experimental work are shown in Figure 10. Also, Figure 10 shows the two steel rollers that are used to connect the tops of the columns of the main frame as reported in the experiment work to prevent the horizontal movement of the columns. Vertical movements of

the columns are not restricted. Also, a 10mm-thick steel plate is fastened above the middle joint to make the load uniformly distributed on the columns. The top and bottom longitudinal bars in beam are anchored with a mechanical anchor to simulate continuity in external beam column joints, as it is in the full-scale specimen.

As reported in the experiment, the numerical simulation of the gradual failure of the middle column stub is performed in a displacement controlled manner as follows; the self-weight of the structural components applied first with all columns support are fixed. Then, a vertical static displacement of the node above column stub is increased gradually to simulate the column failure and the support for this column stub only becomes free. The loading increment is thus defined as 1.0 mm per step (310 steps).

4.3.3 Results and discussions

Figure 11 shows a comparison of crack pattern due to vertical displacement of middle joint equal to 170 mm for scaled specimen (just before rebar fracture) with that obtained from numerical model in the same step. Figure 12 compares the final crack patterns for scaled specimen and the numerical model in ELS. It should be noted that, Figures 11 and 12 indicate that ELS has a great capability to simulate the cracking pattern at each stage.

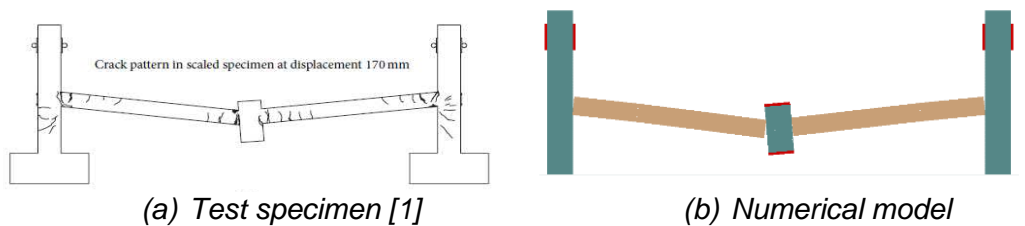


Fig. 11 Crack pattern in scaled specimen at 170 mm vertical displacements of middle Joint

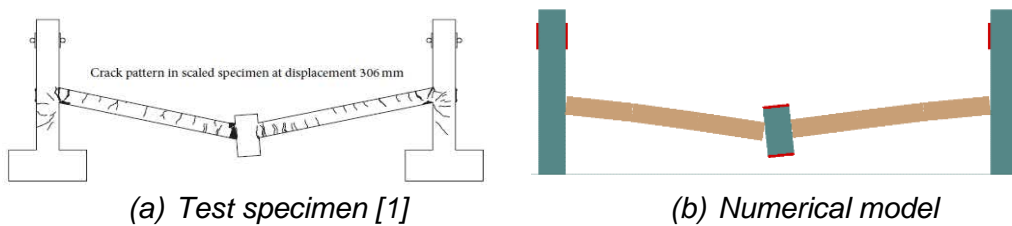


Fig. 12 - Comparison of crack pattern in scaled specimen at the end of test

Similarly, Figure 13 shows images of the bottom rebar fractures at the middle joint interface for both of scaled specimen and ELS. Figures 14 and 15 show images of the top rebar fractures at the side of south column interface for both scaled specimen and ELS. From these figures, it can be concluded that, ELS is capable to simulate rebar fractures very well.



Fig. 13 - Fracture of bottom bars at middle joint

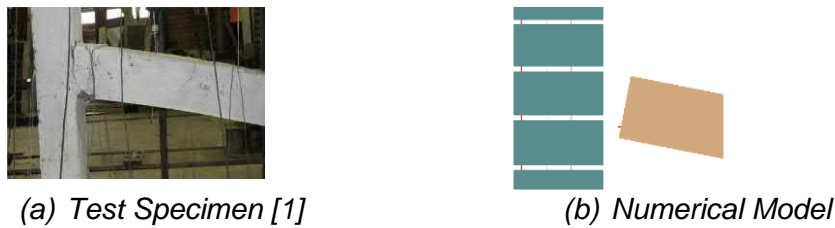


Fig. 14 - Crack pattern at south end

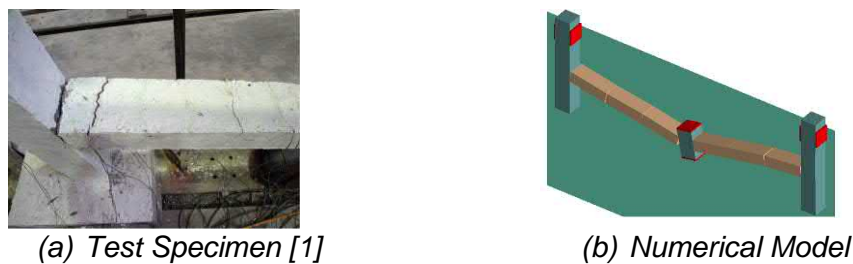


Fig. 15 - Crack pattern at south end

The load-displacement curves from experimental test, OpenSees numerical model, and ELS numerical model are shown in Figure 16. The three mechanisms that resist progressive collapse; flexural action, compressive arch action (CAA) and catenary action (CA) have occurred. As the lower and upper reinforcement at the middle and end joints are yielded quickly during the initial loading steps. Thus, plastic hinges in the beam are created which show that flexural action had reached its capacity at a vertical displacement of 48.3 mm (50 mm in experiment), which is close to half of the beam depth. The load reaches an initial peak of 27.9 KN (28.1 KN in experiment). This point corresponds to the compressive arch action (CAA) capacity of the beams and it can be noticed that, there is no separation point between flexural action and compressive arch action because the compressive arch action is developed at the beginning of the loading in axially restrained members. With additional increments in the vertical displacement, the vertical load started to decrease, and continued to do so until a vertical displacement of 133 mm (135 mm in experiment), which corresponded to a vertical load of 15.5 KN (20.9 KN in experiment) which is approximately equal to the beam depth. Beyond this point, the development of tensile force in the beams leads to increased vertical load capacity. This point is considered as the initiation of increasing the capacity due to catenary action (CA) mechanism of the in-plane frame. Increasing displacement up to 167 mm (170 mm in experiment), increased the vertical load resulting in the first fracture in the lower longitudinal bar in the beam which caused a sudden drop in the load from 20.46 KN to 9.7 KN (22.4 KN to 12.9 KN in experiment). The first rebar fracture occurred at the location of the main crack in the south beam at the interface with the middle column stub. With increasing the displacement, the load started to increase again until the fracture of second bottom bar occurred at displacement of 238 mm (230 mm in experiment) and load value of 33 KN (25.7 KN in experiment). Applying load was stopped with the fracture of one of the beam top bars at the south beam column connection at displacement of 265.5 mm (306 mm in experiment) and load value of 35.5 KN (38.2 KN in experiment), which attained a maximum for CA capacity. Also, it can be observed that there is a large difference in displacement between the stage of bottom bar fracture (at the middle joint) and top bar fracture (at the ends). This can be related to the formation of plastic hinges at the middle joint, which caused large deflections at that stage.

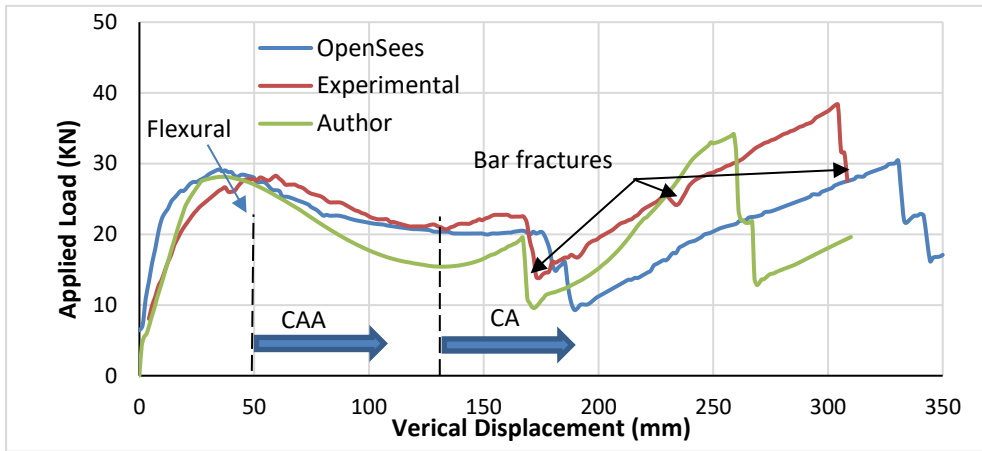


Fig. 16 - Numerical and experimental vertical load-deflection curves

Horizontal displacements of end columns at the beam mid heights which change from inward to outward direction at the vertical displacement of 171 mm (182 mm in experiment) are shown in Figure 17. Also, it can be observed the same behaviour in Figure 18, that shows beam axial force versus vertical displacement of middle joint. The beam axial compression force increased up to vertical displacement of 50 mm and then it started to decrease. In vertical displacement of 171 mm (182 mm in experiment), beam axial force changed from compression to tension and this was evident for development of tensile force in the beams of sub-assembly. This point is considered as the initiation of increasing capacity due to CA mechanism.

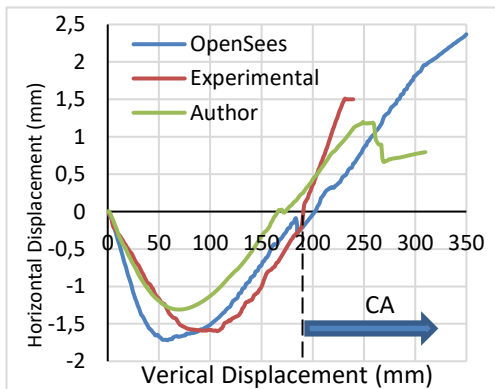


Fig. 17 - Horizontal displacement of end columns versus vertical displacement of center column

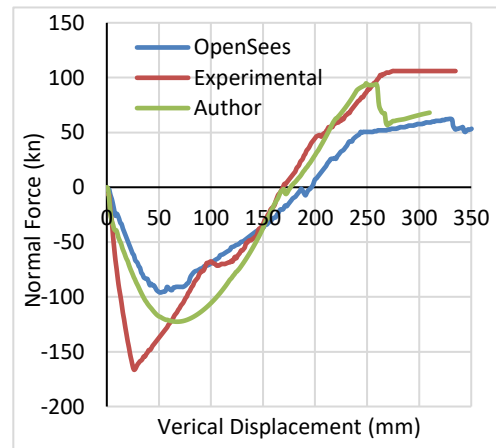


Fig. 18 - Axial force in beam

Strain results at mid span for top and bottom bars are shown in Figures 19 and 20. Generally, the development of strains in the numerical model is the same with experimental scaled specimen. However, the absolute value of strains cannot be modelled because of discrepancies of material properties and stress concentrations in the experimental program. Consequently, it can be concluded that, experimental and numerical results have better agreement especially before the fracture of bars.

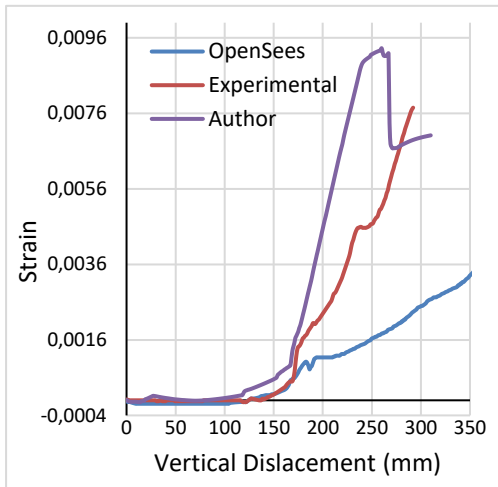


Fig. 19 - Strain in top reinforcing bar at mid-span of the beam

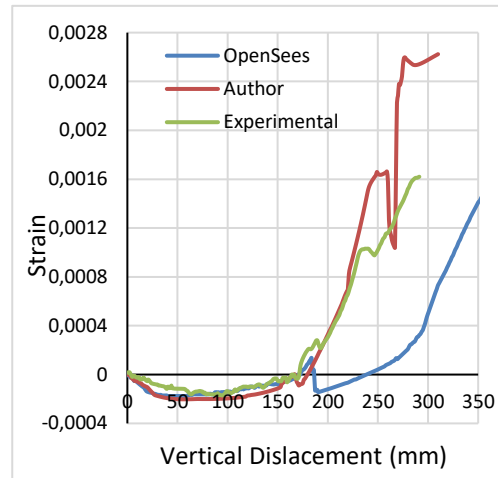


Fig. 20 - Strain in bottom reinforcing bar at mid-span of the beam.

From the above discussion, it should be noted that the numerical model shows better agreement for both vertical and horizontal displacement of the sub-assembly during collapse. Therefore, it is confirmed that AEM can be reliably used to study the progressive collapse of reinforced concrete frames. Furthermore, the results obtained from ELS are even better than those obtained by Ahmedi et al. [1] using OpenSees program.

4.4 Experiment work by Yi et al. [2]

4.4.1 Experiment description

Yi et al. [2] carried out a static experimental study of a three-storey RC frame structure to investigate progressive failure due to the loss of a lower storey column. In their experiment, it was observed that after the plastic mechanism has formed, the concrete strain in the compression zone at the beam ends reached its ultimate compressive strain, and the compressive steel bars are gradually subjected to tension with increasing displacement. For the experimental test, a one-third scale model representing the lower three-story of the original frame from the eight-story RC building was constructed as shown in Figure 21. The dimensions and the reinforcement details of the structural components are shown in Figure 21. Also, the measured material properties are given in Tables 3 and 4.

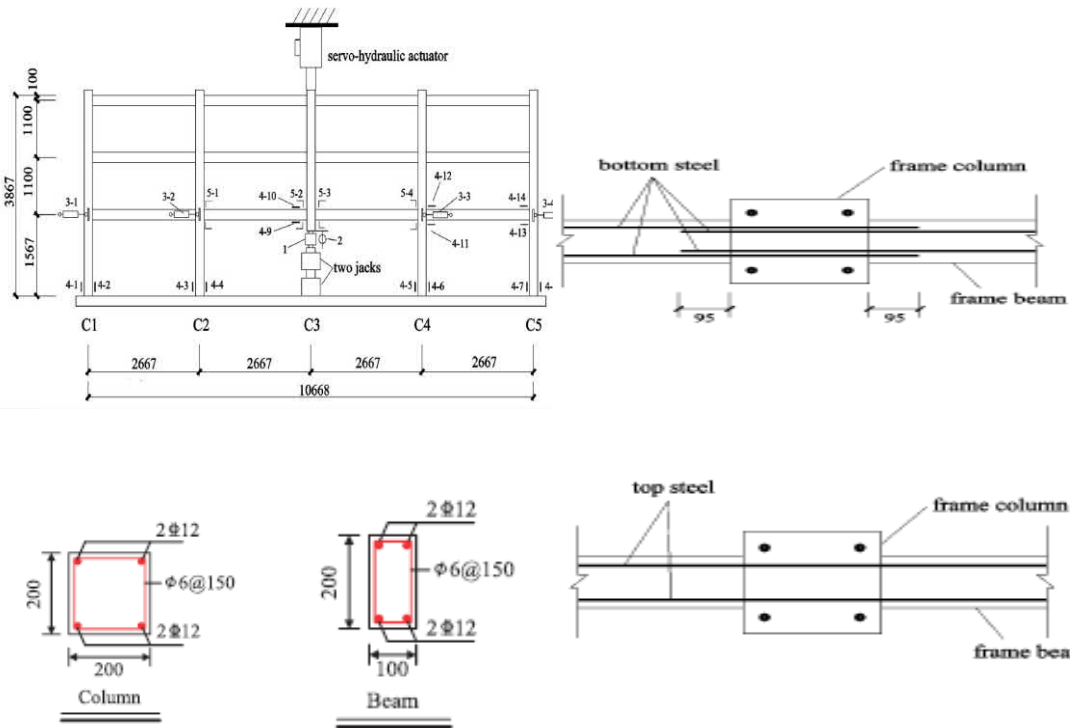


Fig. 21 - Specimen details (Yi et al. [2])

Tab. 3 - Concrete material properties (Yi et al. [2])

Property	Young's Modulus (MPa)	Shear Modulus (MPa)	Tensile Stress (MPa)	Cubic Compressive Stress (MPa)	Specific Weight (Kg/m ³)	Ultimate Strain
Concrete	2.70E4	1.1287E4	1.57	25	2500	0.30

Tab. 4 - Reinforcement material properties (Yi et al. [2])

Property	Young's Modulus (MPa)	Shear Modulus (MPa)	Tensile Yield Stress (MPa)	Compressive Yield Stress (MPa)	Specific Weight (Kg/m ³)	Ultimate Strain
Longitudinal RFT (HRB400)	2.01 E5	0.79 E5	416	416	7840	0.275
Lateral RFT (HPB235)	2.01 E5	079 E5	370	370	7840	0.325

4.4.2 Numerical modelling

Numerical model, mesh division, and reinforcement details similar to experiment are shown in Figure 22.

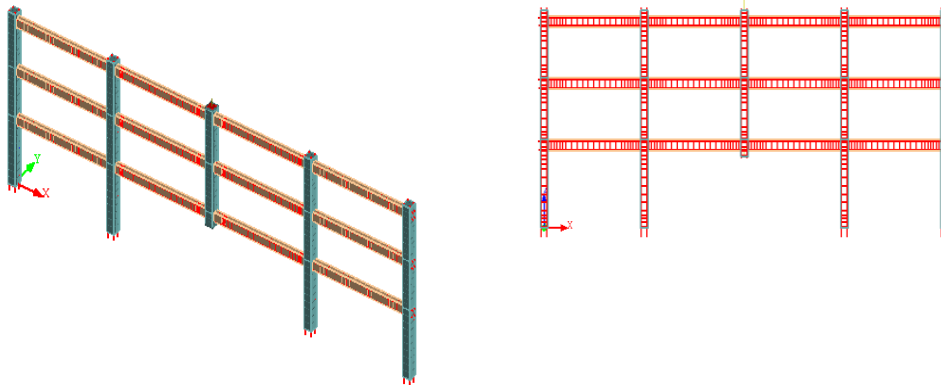


Fig. 22 - ELS Numerical model and reinforcement details

The numerical simulation of the gradual failure of the first-storey middle column is performed in a displacement controlled manner as follows; the self-weight of the structural components applied first then a vertical load of 109 KN is applied incrementally on the top of the middle column, the node associated to the failed column was fixed. After that, a vertical static displacement of this node is increased gradually to simulate the column failure. The loading increment is thus defined as 1.0 mm per step for all models (460 steps).

4.4.3 Results and discussion

It can be noted from Figure 23 that at a vertical displacement less than 5 mm, the elastic stage ended with the cracking of the frame beams. Then, increasing displacement to less than 25 mm, the elasto-plastic stage finishes in point with the yielding of the steel bars from the ends of the beams adjacent to the middle column indicating the formation of the plastic hinge mechanism. After that, increasing the displacement to 140 mm the plastic stage ended where, as in the experiment, large plastic rotations at beams ends and severe concrete crushing are observed in the numerical simulation. After this point the tension cracks in concrete penetrate the compressive zone which means that catenary action stage starts to appear, in which the general resisting mechanism changes from compression bending in beams to tension-bending. Therefore, in this stage the beams are acting mainly as ties. Finally, with increasing the displacement to 450 mm (similar with 456 mm from the experiment), the bottom rebar of the first-storey beam adjacent to the middle column is ruptured. The location of the ruptured rebar from the experiment and the numerical model are illustrated in Figure 24.

Moreover, Figure 23 shows the three stages of mechanism of progressive collapse as first, the adjacent frames are pushed and move outward, second the adjacent frames start being pulled inside, and finally the adjacent frames are pulled inside but the axial force in beams changes to tension. This is happened when the vertical displacement at the column removed point measures 140 mm indicating the formation of the catenary mechanism. Furthermore, comparison of the vertical resisting force versus vertical displacement of the central column obtained in this study with the results obtained by other researchers is shown in Figure 23. This comparison indicated that, the present work simulation is more efficient than other researchers even some of them use the same software and others use different software packages such as; OpenSees, Ansys, Abacus, and MSC Marc.

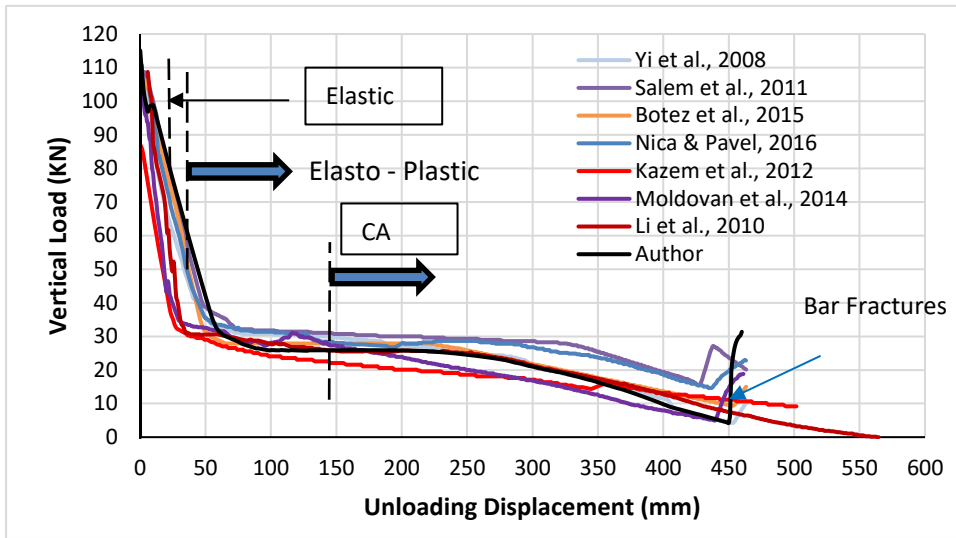
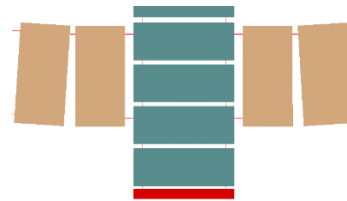


Fig. 23 - Comparison of load-deflection curves



(a) Test specimen (Yi et al. [2])



(b) ELS Model

Fig. 24 - Fracture of bottom bars at middle joint

Figures 25 and 26 present the variation of the vertical and horizontal displacements of sections 3-1 (see Figure 21) obtained from both experimental and numerical work. Also, Figure 27 shows the better simulation for the final deformation of the frame in ELS model with that in the experiment.

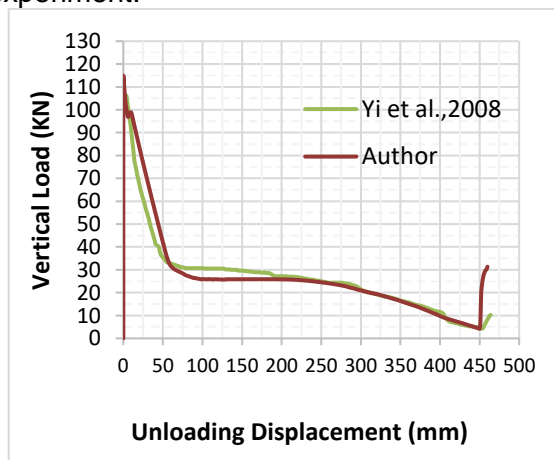


Fig. 25 - Vertical load-deflection results

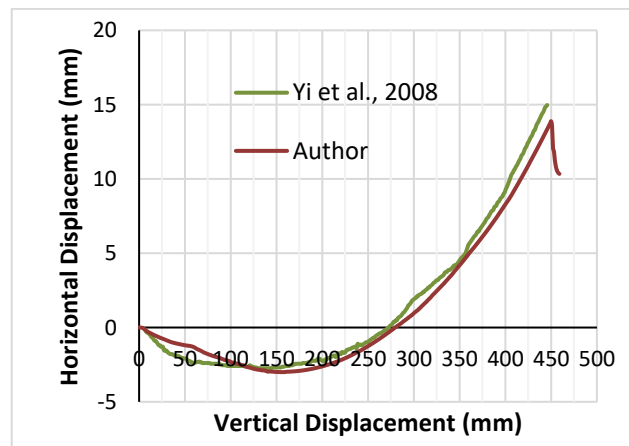
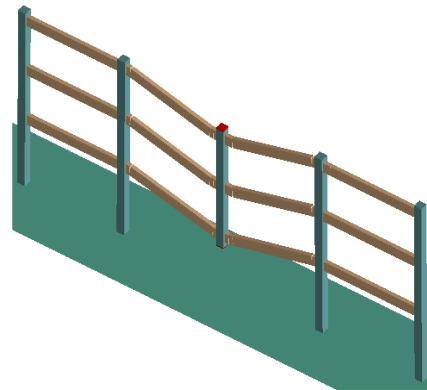


Fig. 26 - Horizontal displacement of end columns versus vertical displacement of center column



(a) Test specimen (Yi et al. [1])



(b) ELS model

Fig. 27 - Frame final deformation

5. CONCLUSION

In this study, a numerical investigation is conducted using ELS software (Extreme Loading for Structures) which is based on the Applied Element Method (AEM) based on an experimental data of the two experimental studies conducted by Ahmadi et al. [1] and Yi et al. [2]. The numerical modelling results are compared with those obtained from experiments as well as other software packages such as OpenSees, Ansys, Abacus and MSC Marc. The main findings in this study can be summarized as follows:

1. The applied element method is an efficient tool for analysis of progressive collapse of reinforced concrete structures.
2. The numerical results obtained using ELS show a better agreement with experimental results.
3. ELS has a great capability to simulate both the crack pattern in each stage and rebar fractures.
4. There is no separation point between flexural action and compressive arch action because the compressive arch action developed at the beginning of the loading in axially restrained members.
5. The transition point from compressive arch action to catenary action occurred only when axial loads changed from a compression force to a tension force.
6. The ELS software could be utilized in further progressive collapse analyses.
7. The developed numerical model is regarded a valid and economical alternative to experiments for prediction of the progressive collapse of reinforced concrete structures.

ACKNOWLEDGEMENTS

The authors acknowledge *Benha University* for its effort to provide us with all scientific papers and references needed to complete this research. Also, the authors would like to thank Eng. *Mahmoud Abbas*, Teaching Assistant, *Civil Engineering Department, Faculty of Engineering at Shoubra, Benha University* for support in modelling by ELS.

REFERENCES

- [1] Ahmadi, R., Rashidian, O., Abbasnia, R., Mohajeri Nav, F. and Yousefi, N., "Experimental and Numerical Evaluation of Progressive Collapse Behavior in Scaled RC Beam–Column Sub-Assemblage", *Shock and Vibration*, doi:10.1155/2016/3748435, 2016.
- [2] Yi, W.J., He, Q.F., Xiao Y., Kunnath, S.K., "Experimental Study on Progressive Collapse-Resistant Behavior of Reinforced Concrete Frame Structures", *ACI Struct J*, 105(4):433-439, 2008.
- [3] American Society of Civil Engineers (ASCE), "Minimum Design Loads for Buildings and Other Structures (SEI/ASCE 7/05).", Reston Va., USA, 2005.
- [4] General Service Administration, GSA, "Progressive Collapse Analysis and Design Guidelines for New Federal Office Buildings and Major Modernization Projects"; Washington DC, 2003.
- [5] Nair R.S., "Preventing Disproportionate Collapse," *Journal of Performance of Constructed Facilities* ASCE, vol. 20(4), pp. 309–314, 2006.
- [6] Ellingwood, B. R. and Dusenberry D. O., "Building Design for Abnormal Loads and Progressive Collapse", *Computer-Aided Civil and Infrastructure Engineering*, 20:194– 205, 2005.
- [7] Interagency Security Design Committee (ISC), "Criteria for New Federal Office Buildings and Major Reorganization Projects", 2001.
- [8] Structural Use of Steelwork in Building, Part 1: Code of Practice for Design - Rolled and Welded Sections, British Standards Institute, (BS 5950-1), 2000.
- [9] Department of Defense, DoD, "Design of Buildings to Resist Progressive Collapse", Unified Facilities Criteria (UFC, 4-023-03). USA; 2005 & 2009.
- [10] Meguro, K. and Tagel-Din, H., "Applied Element Method for Structural Analysis: Theory and Application for Linear Materials", *Structural Engineering Earthquake Engineering, International Journal of the Japan Society of Civil Engineers (JSCE)* 17(1):21s–35s, 2000.
- [11] Meguro, K. and Tagel-Din, H., "Applied Element Simulation of RC Structures Under Cyclic Loading", *Journal of Structural Engineering*, 127(11):1295–1305, 2001.
- [12] Meguro, K. and Tagel-Din, H., "Applied Element Method Used for Large Displacement Structural Analysis", *Journal of Natural Disaster Science*, 24(1):25–34, 2002.
- [13] Tagel-Din, H. and Meguro, K., "Applied Element Simulation for Collapse Analysis of Structures", *Bulletin of Earthquake Resistant Structure Research Centre, IIS, University of Tokyo*, pp. 113–123, 1999.
- [14] Tagel-Din, H. and Meguro, K., "Analysis of a Small-Scale RC Building Subjected to Shaking Table Tests Using Applied Element Method", *Proceedings of the 12th World Conference on Earthquake Engineering, New Zealand*, pp. 1–8, 2000a.
- [15] Tagel-Din, H. and Meguro, K., "Applied Element Method for Dynamic Large Deformation Analysis of Structures", *Structural Engineering Earthquake Engineering*, 17(2):215s–224s, 2000b.
- [16] Applied Science International, Durham, NC, "Extreme Loading for Structures - Theoretical Manual", 2013.
- [17] Ramancharla, P.K., Tagel-Din, H. and Meguro, K., "Dynamic Modeling of Dip-slip faults for Studying Ground Surface Deformation Using Applied Element Method", *13th World Conference on Earthquake Engineering*, 2004.
- [18] Mayorca, P. and Meguro, K., "Modeling Masonry Structures Using the Applied Element Method", *Seisankenkkyu*, 55(6):581–584, 2003.
- [19] Asprone, D., Nanni, A., Salem, H. and Tagel-Din, H., "Applied Element Method Analysis of Porous GFRP Barrier Subjected to Blast", *Advances in Structural Engineering*, 13(1):153–170, 2010.
- [20] Coffield, A. and Adeli, H., "An Investigation of the Effectiveness of the Framing Systems in Steel Structures Subjected to Blast Loading", *Journal of Civil Engineering and Management*, 20(6):767–777, 2014.
- [21] Applied Science International, Durham, NC, "Extreme Loading for Structures V3.1 - Modeling Manual", April 2010.
- [22] Okamura, H. and Maekawa, K., "Nonlinear Analysis and Constitutive Models of Reinforced Concrete", Gihodo Co. Ltd., Tokyo, 1991.
- [23] Kupfer, H., Hilsdorf, H.K. and Rusch, H. "Behavior of Concrete under Biaxial Stresses", *Proceeding of ACI Journal*, volume 66-8., 656-666, 1969.

- [24] Ristic, D., Yamada, Y. and Iemura, H., "Stress-Strain Based Modeling of Hysteretic Structures Under Earthquake Induced Bending and Varying Axial Loads", Research Report No. 86-ST-01. Kyoto (Japan): School of Civil Engineering. Kyoto University, 1986.
- [25] Galal K and El-Sawy T., "Effect of Retrofit Strategies on Mitigating Progressive Collapse of Steel Frame Structures", *J Construct Steel Res* 2010;66(4):520–31.
- [26] Sasani, M., "Response of a Reinforced Concrete Infilled-Frame Structure to Removal of Two Adjacent Columns", *Engineering Structures*, 30, 2478-2491, 2008.
- [27] Wibowo, H., Reshotkina, S. S. and Lau, D. T., "Modelling Progressive Collapse of RC Bridges During Earthquakes", CSCE Annual General Conference May 27-30 2009 St. John's, NL, Canada.
- [28] Tagel-Din, H. and Rahman, N., "Extreme Loading: Breaks Through Finite Element Barriers", *Struct Eng* 2004;5(6):32–40.
- [29] Tagel-Din, H. and Meguro, K., "Applied Element Method for Simulation of Nonlinear Materials: Theory and Application for RC structures", *Struct Eng Earthquake Eng Int J Jpn Soc Civil Eng (JSCE)* 2000;17(2):123s–48s.
- [30] Salem H., "Computer-Aided Design of Framed Reinforced Concrete Structures Subjected to Flood Scouring", *Journal of American Science*, 7, 191-200, 2011.
- [31] Tagel-Din, H., "Collision of Structures During Earthquakes", *Proceedings of the 12th European Conference on Earthquake Engineering*, 2002, London, UK.
- [32] Meguro, K. and Tagel-Din, H., "AEM Used for Large Displacement Structure Analysis", *Journal of Natural Disaster Science*, 2003, 24 (1), 25-34.
- [33] Park H, Suk C. and Kim, S., "Collapse Modeling of RC Structures using the Applied Element Method", *Journal of Korean Society for Roc Mechanics, Tunnel & Underground Space*, 2009, 19 (1), 43-51.
- [34] Helmy, H., Salem, H. and Tageldin, H., "Numerical Simulation of Charlotte Coliseum Demolition using the Applied Element Method", *USNCCM-10 conference-Ohio-USA*, 2009.
- [35] Helmy, H., Salem, H. and Mourad, S., "Progressive Collapse Assessment of Framed Reinforced Concrete Structures According to UFC Guidelines for Alternative Path Method", *Engineering Structures*, 2012, 42, 127–141.
- [36] Helmy, H., Salem, H. and Mourad, S., "Computer-Aided Assessment of Progressive Collapse of Reinforced Concrete Structures According to GSA Code", *Journal of Performance of Constructed Facilities*, ASCE, October 2013.
- [37] Salem, H. and Helmy, H., "Numerical Investigation of Collapse of the Minnesota I-35W Bridge", *Engineering Structures*, 2014, 59, 635–6.
- [38] Salem, H. M., El-Fouly, A. K. and Tagel-Din, H. S., "Toward An Economic Design of Reinforced Concrete Structures Against Progressive Collapse", *Engineering Structures*, 33, 3341-3350, 2011.
- [39] Salem, H., Mohssen, S., Kosa, K., and Hosoda, A., "Collapse Analysis of Utatsu Ohashi Bridge Damaged by Tohoku Tsunami using Applied Element Method", *Journal of Advanced Concrete Technology*, 2014, Vol. 12(10), 388-402.
- [40] Lupoae, M. and Bucur, C., "Use of Applied Element Method to Simulate the Collapse of a Building", *SISOM 2009 and Session of the Commission of Acoustics*, Bucharest 28-29 May.
- [41] Lupoae, M., Baciuc, C., Constantin, D. and Puscau, H., "Aspects Concerning Progressive Collapse of a Reinforced Concrete Frame Structure with Infill Walls", *Proceedings of the World Congress on Engineering*, WCE 2011. London, U.K.
- [42] El-Mahdy, O., El-Kasaby, E., Abusafa, H., and El-Gamal, A., "Application of AEM in Progressive Collapse Dynamics Analysis of R.C. Structures", *The Civil Engineering Journal (CEJ)*, Stavebni Obzor, Faculty of Civil Engineering, CTU in Prague, Czech Republic, October 2017
- [43] MC2010, FIP, "Model Code for Concrete Structures", Ernst & Sohn.
- [44] ACI 318-02, "Building Code Requirements for Structural Concrete and Commentary", American Concrete Institute, 2002.
- [45] Botez M., Bredean L., Ioani A., "Improving the Accuracy of Progressive Collapse Risk Assessment: Efficiency and Contribution of Supplementary Progressive Collapse Resisting Mechanisms", *ComputStruct*; DOI: 0.1016/j.compstruc.2015.11.002.

- [46] Nica, G.B. and Pavel, F., "Numerical Analysis of the Collapse of a RC Frame", Mathematical Modelling in Civil Engineering Journal, Vol. 12-No. 4, pp.22 - 35, 2016
- [47] Moldovan, T.S., Marchiş, A.G. and Ioani, A.M., "Progressive Collapse Analysis of an Old RC Structure Subjected to Extreme Loading", International Scientific Conference, People, Buildings and Environment 2014, Kroměříž, Czech Republic, pp. 316-327, ISSN: 1805-6784.
- [48] Li, Y., Lu, X., Guan H. and Ye, L., "An Improved Tie Force Method for Progressive Collapse Resistance Design of Reinforced Concrete Frame Structures", EngStruct, 33:2931-2942, 2011.
- [49] Kazem, A., Kazem, H. and Monavari, B., "Effect of Progressive Collapse in Reinforced Concrete Structures with Irregularity in Height", 15 WCEE, Lisboa, 2012.
- [50] Tagel-Din, H. and Meguro, K., "Nonlinear Simulation of RC Structures Using Applied Element Method", Structural Engineering Earthquake Engineering, 17(2):137s–147s, 2000c.

FAULT-RELATED INSTABILITY PROBLEMS OF TUNNELS - THE HOST ROCK SLIP CRITERION AND CHARACTERISTICS OF THE TUNNELING-INDUCED SHEAR DISPLACEMENTS

Jian-guo Liu, Xiao-jun Zhou, Qing-hua Xiao and Wei Zhao

Key Laboratory of Transportation Tunnel Engineering of Ministry of Education, School of Civil Engineering, Southwest Jiaotong University, Chengdu, 610031, China, email: xqh_bp@163.com

ABSTRACT

As one of the fault-related instability problems of tunnels, rock slip along fault plane is closely related to the shear strength of a fault, and usually causes irrecoverable and sometimes catastrophic engineering problems. In this paper, based on continuum assumption and Coulomb-slip failure, a criterion to evaluate rock slip along the fault plane was proposed for a circular tunnel in rock masses containing a fault. A mathematical equation that describes the relationship between required shear strength of a fault and horizontal stress ratio, fault spatial extension and location was established. From the equation, the influences of the important parameters on the required shear strength of a fault was analysed after a numerical validation was performed. Besides, the effects of fault spatial extension and location on the tunnelling-induced shear displacements were characterized through numerical models. Characteristics of the tunnelling-induced shear displacements at the excavation wall indicated that fault location with respect to the tunnel dominates the nonuniform rock deformations at excavation wall, and larger fault dip angles could lead to larger shear displacements in some specific pair cases. The presented investigation provides both a deeper insight into the instability problems of tunnels related to a fault and a guideline for tunnel support design.

KEYWORDS

Tunnel, Fault-related instability problem, Rock slip criterion, Fault shear strength, Tunnelling-induced shear displacement

INTRODUCTION

Fault is quite common in all types of hard rock masses, which affects the mechanical properties of rock mass greatly. Many failures or instability problems of tunnels reported are related to the nearby fault presence [1-4]. And the instability of host rock around tunnel usually led to irrecoverable and catastrophic results. Fault-related instability of underground openings are often presented as rock slide along the fault plane, the downfall of blocks, wedges cut by faults or minor joints inward the cavern[5-7]. Among these types of instability, rock slide along the fault plane is a severe problem that can cause irrecoverable failure and may be a severe threat on long-term stability

of underground openings [1,4,8,9]. A better understanding of this problem is therefore highly required and urgent in the determination of support design for tunnels. Typical structural failure of a tunnel caused by the rock slip is presented in Figure 1.

Attempts have been made to assess the fault-related problems by empirical or semi-quantitative methods such as rock mass classification [10] and limit equilibrium approach with the aids of stereographic projection and blocky theory [11, 12]. Numerical models and physical model tests were used more often as specific academic or engineering problems could be assessed much easier that many parameters could be taken into consideration. When tunnelling in hard rock containing faults, uneven rock pressures usually cause asymmetrical stress distribution in tunnel support [13 - 16], which is not favourable and even resulted in failure as the support is designed to be symmetrical. And rock failure or the uneven rock pressures acting on support are usually due to nonuniform rock deformations [17, 18], or shear behaviours of rock along the fault plane more precisely [7, 19].



Fig. 1 - Liner failure caused by rock slide along fault [7]

Shear behaviour of rock, also characterized as rock slip along the fault plane, is a typical response to insufficient shear strength of a fault. And in the researches of Yeung et al. [20], Hao et al. [21] and Wang et al. [22], the shear strengths of faults or joints were pointed out to have a dominant influence on the stability of rock. Furthermore, the appearance of rock slip did not seem to be just only dependent on the fault shear strength. More detailed analysis that considered some other important parameters of horizontal stress ratio, fault dip and fault location were performed too [22 - 24]. The consideration of other parameters revealed that, for a given fault shear strength, the stability of rock could not be determined when other parameters were not specified, and the required fault shear strength to keep rock stability showed dependency on stress ratios, fault dips and fault locations.

Given this background, the fault-related instability problems of tunnels need further investigation. Firstly, the spatial extension and location of a fault with respect to the tunnel needs to be characterized more precisely to enable the theoretical analysis of the problems. Secondly, the required fault shear strength is highly dependent on the stress ratio, fault dips and locations, and then the relationships among these parameters need to be addressed clearly. Besides, the

tunnelling-induced shear displacements at excavation wall resulting from relative insufficient fault shear strength were unfavourable to tunnel support. So the effects of the important parameters of horizontal stress ratio, spatial extension and location of a fault and shear strength of a fault on the tunnelling-induced shear displacements should be investigated.

In the present research, the fault spatial extension and location with respect to a tunnel were mathematically characterized firstly, which enabled the stress analysis of rock along the fault plane. And then based on continuum assumption [25], the elastic mechanics solution of rock along the fault plane was carried out. A criterion for circularly tunnelling in hard rock containing a fault that followed Coulomb-slip failure was proposed, which mathematically described the relationship between the required fault shear strength and fault spatial extension, fault spatial location and ground horizontal stress ratio. The required fault shear strength to prevent rock slip (named lower frictional angle of fault θ_{lim} when no cohesion was considered), was proposed and validated with numerical models. The effects of fault spatial extension and location and horizontal stress ratio on the lower frictional angle of fault θ_{lim} were analysed, which revealed the influences of a fault on the stability problems of tunnels. In addition, the effects of fault spatial extension and location on the tunnelling-induced shear displacements at excavation wall were characterized through numerical models. The attempts of this paper provided a deeper insight into the instability problems of underground openings related to fault slip.

THE CRITERION OF ROCK SLIP ALONG A FAULT

Stress analysis on the fault plane

A circular tunnel is selected in this research to simplify the stress analysis. The spatial geometric relationship between the fault and tunnel is illustrated in Figure 2. As the axial size of tunnel is much greater than the radial one, this problem can be simplified as a plain strain problem in the yoz plane. For a deeply buried tunnel, the tunnel radius r_0 is much smaller than the depth h , thus the model can be simplified as a problem of stress concentration around a small hole in infinite domain, as presented in Figure 3.

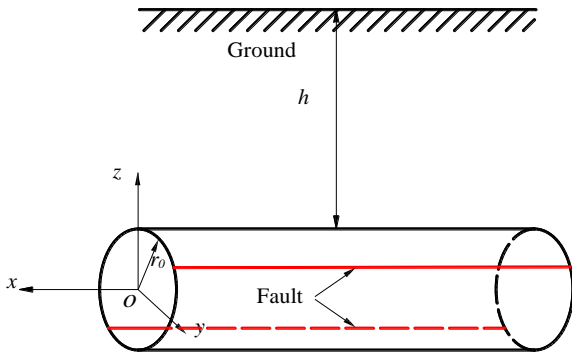


Fig. 2 - Spatial relationship between tunnel and fault

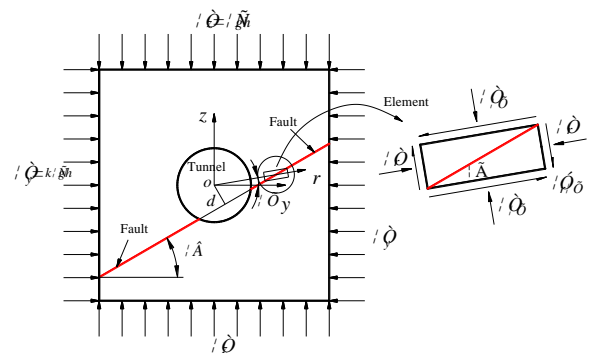


Fig. 3 - Simplified model for plane strain problem

As shown in Figure 3, a circular tunnel is excavated in infinite elastic medium which contains a fault, and the spatial extension and location of the fault could be characterized by dip angle of fault β and the distance between the fault plane and circular tunnel center d . And special assumptions are made as follows:

- (1) In the initial geostress field, the rock did not slide and the fault did not change the distribution of the initial stress;
- (2) The secondary stress distribution due to the excavation of tunnel is the same as that in rock mass without a fault prior to rock slip.
- (3) No tectonic stress field is considered.

According to the spatial relationship between fault plane and tunnel, for a fault going through the right bottom below the tunnel center, the relationship of fault dip angle β and γ in a polar coordinate system could be expressed as follows:

$$\sin \gamma = d / r = \sin(\beta - \varphi) \tag{1}$$

where γ is the angle between polar radius and fault plane, φ is the polar angle in the coordinate system. When only self-weight of rock mass is considered, the initial geostress can be expressed as:

$$\begin{aligned} \sigma_z &= \rho gh \\ \sigma_x = \sigma_y &= \mu / (1 - \mu) \rho gh = k \rho gh \end{aligned} \tag{2}$$

where ρ and μ are the density and Poisson's ratio of rock mass, respectively. And k is the horizontal stress ratio.

When a circular tunnel with a radius of r_0 is excavated, the secondary stress distribution in the rock mass containing a fault with a dip angle of β through the right bottom of a circular tunnel (), originally due to Kirsch [26], are:

$$\begin{aligned}
 \sigma_r &= \sigma_z / 2 \times [(1 - \alpha^2)(1 + k) - (1 - 4\alpha^2 + 3\alpha^4)(1 - k) \cos(2\beta - 2\gamma)] \\
 \sigma_\varphi &= \sigma_z / 2 \times [(1 + \alpha^2)(1 + k) + (1 + 3\alpha^4)(1 - k) \cos(2\beta - 2\gamma)] \\
 \tau_{r\varphi} &= \sigma_z / 2 \times [(1 - k) \times (1 + 2\alpha^2 - 3\alpha^4) \times \sin(2\beta - 2\gamma)]
 \end{aligned} \tag{3}$$

where $\alpha = r_0 / r$, and r is the coordinates in a polar coordinate system. For tunnels with D shape or horse-shoe shape, the stress can be analysed with complex valuable system.

An element contains the fault is derived to conduct stress analysis as shown in Figure 3, and the normal and shear stress components on the fault plane calculated based on the assumption (2), are given by:

$$\begin{aligned}
 \sigma_n &= (\sigma_\varphi + \sigma_r) / 2 + (\sigma_\varphi - \sigma_r) / 2 \times \cos 2\gamma - \tau_{r\varphi} \times \sin 2\gamma \\
 \tau &= (\sigma_\varphi - \sigma_r) / 2 \times \sin 2\gamma + \tau_{r\varphi} \times \cos 2\gamma
 \end{aligned} \tag{4}$$

Analysis of lower limit frictional angle of a fault

Prior to rock slip along the fault plane, according to Coulomb-slip criterion, the stress state must satisfy the following equation:

$$\tau \leq \sigma_n \tan \theta + c \tag{5}$$

where θ and c are the frictional angle and cohesion of the fault, respectively. And by substituting Equation 4 into Equation 5, the following equation is led to:

$$\begin{aligned}
 \tan \theta \geq \{ &[-\alpha^2(1 + k) - (1 - 2\alpha^2 + 3\alpha^4)(1 - k) \times \cos(2\beta - 2\gamma)] \times \sin 2\gamma + (1 + k)(1 + 2\alpha^2 - 3\alpha^4) \times \\
 &\sin(2\beta - 2\gamma) \times \cos 2\gamma\} / \{ (1 + k) - 2\alpha^2 \times (1 - k) \times \cos(2\beta - 2\gamma) + [-\alpha^2(1 + k) - (1 - 2\alpha^2 + 3\alpha^4) \times \\
 &(1 - k) \times \cos(2\beta - 2\gamma)] \times \cos 2\gamma - (1 + k)(1 + 2\alpha^2 - 3\alpha^4) \times \sin(2\beta - 2\gamma) \times \sin 2\gamma \}
 \end{aligned} \tag{6}$$

Where $\sin 2\gamma = 2\alpha d / r_0 \times \sqrt{1 - (\alpha d / r_0)^2}$ and $\cos 2\gamma = 1 - 2(\alpha d / r_0)^2$. Equation 6 denotes the criterion to evaluate whether rock would slide along the fault or not, and it is a local criterion, and not for the rock along the whole fault. For deep hard rock engineering, the fault cohesion was always assigned to be zero [21,27]. And for a simplified analysis, cohesion of fault is not considered ($c=0$) in Equation 6.

By setting the left part in Equation 6 equal to the right one, the local lower limit frictional angle of the fault θ_{lim} , which is the local minimum of fault shear strength that prevents host rock of tunnel from sliding along the fault plane, is obtained with no cohesion considered. And for the prevention of rock slip along the whole fault plane, the shear strength of fault should be no less than maximum value of θ_{lim} , and then the max lower frictional angle of fault θ_{max} is determined as $\theta_{max} = \max \{ \theta_{lim} \}$.

According to Equation 6, θ_{lim} is dependent on the horizontal stress ratio k , dip angle of fault β and the distance between the fault plane and circular tunnel center d . It should be noted that rock slip criterion along fault is proposed for the right half of a fault extending at the right bottom of circular tunnel, and for the left part, similar analysis can be performed by transforming the coordinates in the same way.

Numerical validation

To validate the proposed slip criterion of host rock and lower frictional angle θ_{max} , a numerical model is established where vertical stress $\sigma_z = 4\text{MPa}$, horizontal stress ratio $k=0.5$, tunnel radius $r_0 = 5\text{m}$, fault dip angle $\beta=30^\circ$, and distance between the fault plane and circular tunnel center $d=1\text{m}$. By substituting the parameters of the example into Equation 6, the local lower limit frictional angle of fault along the fault plane is calculated and shown in Figure 4.

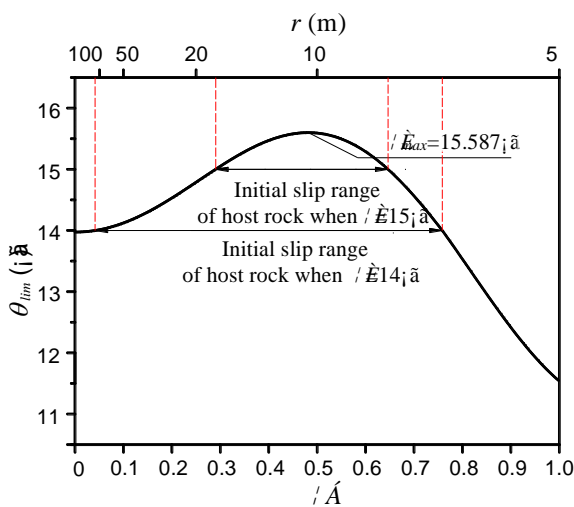


Fig. 4 - Variation of lower limit frictional angle of fault along fault plane

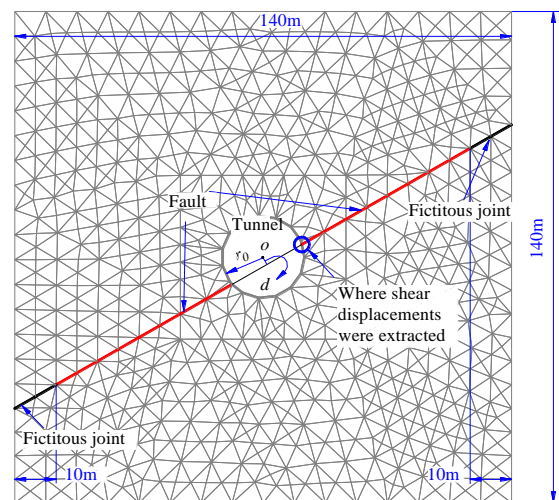


Fig. 5 - Generation of numerical model

Figure 4 illustrated the lower limit frictional angle of fault along the fault plane, which increases firstly and then decreases from excavation wall to infinite in this case. And it can be seen that, θ_{max} is located at where $\alpha \approx 0.48$ in this case, which means that, to maintain the stress distribution at where $\alpha \approx 0.48$, the frictional angle of the fault θ should be no less than 15.587° . Besides, the initial slip ranges of host rock with different frictional angle of fault were presented in Figure 4. For example, when frictional angle of fault $\theta=14.0^\circ$ and $\theta=15.0^\circ$, the initial slip ranges of host rock are 6.59m~118.17m and 7.74m~17.23m from tunnel center, respectively.

Numerical modelling strategies

The numerical model to validate the criterion proposed is based on the Universal Distinct Element Code (UDEC) [28]. UDEC is a program developed to solve fault-related problems in discontinuous rock system. Large deformation of rock along the fault is allowed and the properties of fault are quite convenient to be changed in this program. With many kinds of built-in constitutive models of fault, UDEC is suitable for the verification of the criterion proposed in Equation 6. In the modelling process, the Coulomb slip model was adopted. In UDEC, if

$$|\tau_s| \leq \sigma_n \tan \theta + c = \tau_{max} \quad (7)$$

Where τ_s is the shear stress on the fault plane; θ is the frictional angle; σ_n is the normal stress; and c is the cohesion of fault. Then, the shear displacement can be described as:

$$\Delta u_s^e = \Delta \tau_s / k_s \quad (8)$$

where Δu_s^e is the elastic component of incremental shear displacement; and k_s is the constant shear stiffness. Or, if

$$|\tau_s| \geq \tau_{max} \quad (9)$$

then

$$\tau_s = \text{sign}(\Delta u_s) \tau_{max} \quad (10)$$

where Δu_s is the total incremental shear displacement.

From Equation 7 to 10, it can be concluded that prior to rock slip along the fault plane, the total shear displacement of rock along the fault is the elastic constant component. And once rock has already slid, the shear displacement is enlarged. Thus, the criterion presented in Equation 6 can be verified by the derivations and comparisons of shear displacements of nodes along the fault in the numerical model.

In the numerical model, rock was assumed to be elastic medium and fault followed Coulomb-slip criterion. Properties of rock mass were taken from the research of Jiang et al. [27], and properties of fault were evaluated under the constant normal stress conditions [29, 30]. In order to prevent the fault from opening, tensile strength of the fault was set at a relatively high value up to 10GPa. Properties of rock mass and fault are presented in Table 1 and Table 2.

Tab. 1 - Properties of rock masses

Density ρ (kg/m ³)	Young's modulus E (GPa)	Poisson's ratio μ
2.5	3.03	0.17

Tab. 2 - Properties of the fault

Normal stiffness k_n (GPa/m)	Shear stiffness k_s (GPa/m)	Cohesion c (MPa)	Frictional angle θ (°)	Tensile strength σ_{ten} (GPa)
20	0.8	0	Varies	10

Stress boundaries were applied to the model, and horizontal stress ratio k was simulated by inputting different horizontal stress while vertical stress remained constant. A circular tunnel of $r_0 = 5m$ was excavated in the rock mass, and in order to eliminate the boundary effect, size of model was set at 140m×140m. Besides, fictitious joint segments were generated near the boundary of model to stabilize the boundary [31], with 10m-long projection on the horizontal axis. The numerical model was generated as shown in Figure 5. The frictional angle of fault θ put into the numerical model was in a narrow range near the maximum lower limit frictional angle θ_{max} .

Shear displacements along the fault plane

The shear displacements of nodes along the fault plane D_s in the 7 cases are presented in Figure 6. For cases with $\theta / \theta_{max} \geq 1.00$, the displacement curves are almost the same, which means that the shear displacements of the same node are constant and from elastic shear behaviour according to Equation 7 and 8. While for cases with $\theta / \theta_{max} < 1.00$, the shear displacement curves increases gradually within the middle range, which means that the host rock has slid already and stepped into the plastic shear stage according to Equations 9 and 10. It could be summarized that, when the frictional angle of the fault is larger than θ_{max} , the stress distribution of host rock could be maintained and rock slip along fault plane is prevented, otherwise the rock slip occurs.

Also in Figure 6, when $\theta / \theta_{max} = 0.96 \rightarrow \theta = 14.96^\circ$, the simulated rock slip range is $r \approx 7m \sim 33m$, which shows a great disparity compared to that in Figure 4. This difference could be attributed to the stress redistribution effect: when $|\tau_s| \geq \tau_{max}$ for a fault element, part of τ_s would be transferred to neighbouring elements, causing the shear failure of the neighbouring elements, and then the slip range of host rock is enlarged.

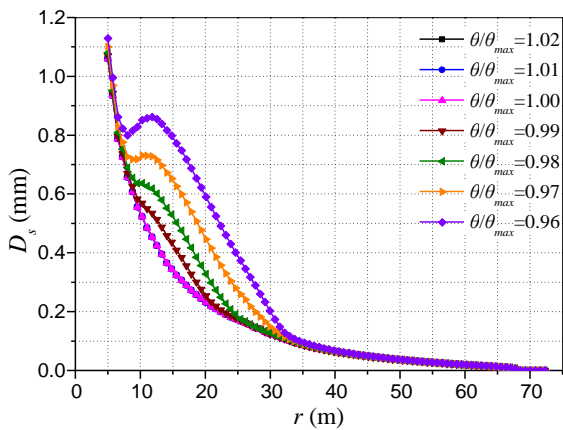


Fig. 6 - Shear displacements of rock along fault plane

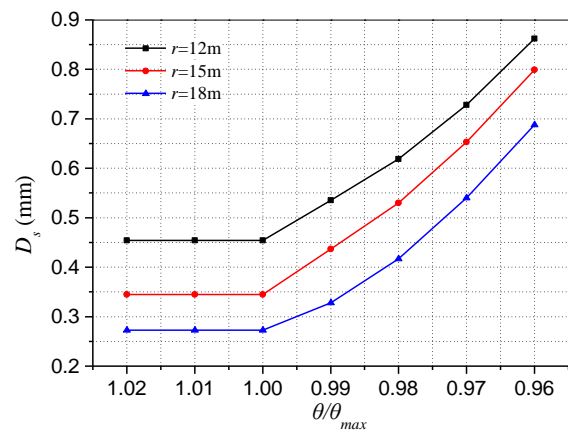


Fig. 7 - Local shear displacements with different frictional angles of fault

The shear displacements of nodes at where $r=12\text{m}$, $r=15\text{m}$ and $r=18\text{m}$ in the 7 cases are presented in Figure 7, which donates sensitivity of the rock shear behaviour to the fault shear strength. With frictional angle decreased, the shear displacements of nodes kept constant when $\theta/\theta_{max} \geq 1.00$, and increased when $\theta/\theta_{max} < 1.00$, which validated the proposed rock slip criterion in an intuitive way.

ADDRESSING THE IMPORTANT PARAMETERS RELATED TO ROCK-SLIP INSTABILITY PROBLEMS

It is found in Equation 6 that, the lower limit frictional angle of a fault to maintain rock stability related to rock slip along fault plane when tunnelling in hard rock is determined by 3 parameters, including the horizontal stress ratio k , dip angle of the fault β and the distance between the fault plane and circular tunnel center d . To obtain a more comprehensive understanding of the effects of these parameters, a parametric analysis was conducted. The tunnel radius r_0 and vertical stress σ_z were set at 5m and 4MPa, respectively.

The effects of fault dip angle

It can be seen in Figure 8 that to keep host rock from sliding at excavation wall, the same lower limit frictional angle θ_{lim} is required with different dip angle of the fault. And for different dip angle β , θ_{lim} along the fault plane show different tendency: when fault spatially extends with a very small β , θ_{lim} increases all the way from infinite field to the excavation wall (e.g. $\beta=10^\circ$), while for $30^\circ < \beta < 80^\circ$, θ_{lim} increases firstly and then decreases in the same range. And in the far field (about

$\alpha < 0.1$), the lower limit frictional angle θ_{lim} shows a great disparity with different fault dips and changes little along the fault plane, which can be explained that the stress distribution far away from tunnel is much less disturbed by excavation, and the required shear strength of fault (θ_{lim}) is mainly determined by the initial stress field. The relation between dip angle and lower frictional angle of fault strongly suggests that fault with dip angle in the vicinity of 60° may be identified to be the most unfavourable to the stability problems of tunnels in terms of the rock slip along fault.

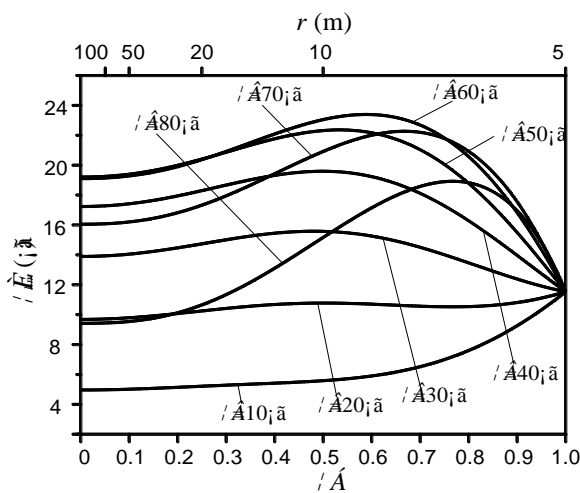


Fig. 8: Lower limit friction angle θ_{lim} along fault plane with different β ($k=0.5, d=1m$)

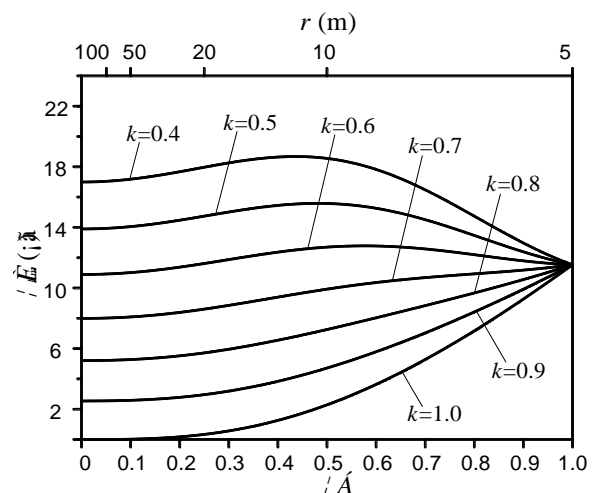


Fig. 9: Lower limit friction angle along fault plane θ_{lim} with different k ($\beta=30^\circ, d=1m$)

The effects of horizontal stress ratio

It has been found that the rock slip was very sensitive to the horizontal stress ratio k of ground [21], and the input fault shear strength had to be set significant large to reach model equilibrium. By nature, the rock slip along fault is caused by relative insufficient fault shear strength which is also closely related to stress ratio. Therefore, the effects of horizontal stress ratio on the lower limit frictional angle should be investigated.

The lower limit frictional angle of fault in the far field is strongly dependent on horizontal stress ratio as presented in Figure 9, and it increases with the decrease of horizontal stress ratio from 1.0 to 0.4 in detail. From all the cases, it can be summarized that with horizontal stress ratio closer to 1.0, higher stability of host rock related to fault could be expected.

The relation between lower limit angle and horizontal stress ratio in Figure 9 is similar to that of Figure 8, which is: the lower limit frictional angle is strongly dependent on horizontal stress ratio in the far field (α approaches 0), while that of fault at excavation wall are the same in each figure. According to the relations presented in Figure 8 and Figure 9, it suggests that, the lower limit frictional angle of fault to keep host rock from sliding at excavation wall seems independent of horizontal stress ratio and fault dip angle. However, it should be noted that, rock slip along fault plane is dependent on the shear strength of the whole fault, and the rock near excavation wall is in a loose

state somehow. Given this comprehension, horizontal stress ratio and fault dip angle are also critical for the instability problem of underground excavation related to fault.

The effects of fault spatial location

Stress redistribution induced by excavation is significant around the tunnel, which means that the stress components on the fault plane near excavation wall are strongly affected. And thus the stress components along the fault plane near the excavation wall should be different with different fault spatial location with respect to the tunnel, which might lead to changes of the required shear strength of fault θ_{lim} .

As presented in Figure 10, with different fault spatial locations, θ_{lim} approaches the same value of 13.90° when α approaches 0, and it suggests that in the far field, the stress components of on fault plane is not affected by fault location with respect to tunnel. While when α approaches 1 (near the excavation wall), θ_{lim} changes significantly with different d (e.g. $\theta_{lim, d=0.1m} \approx 1.2^\circ$ and $\theta_{lim, d=2m} \approx 23.5^\circ$). And this is remarkable evidence that the instability problems of tunnels in terms of rock slip in the vicinity of excavation wall are dominated by the distance between fault plane and tunnel center.

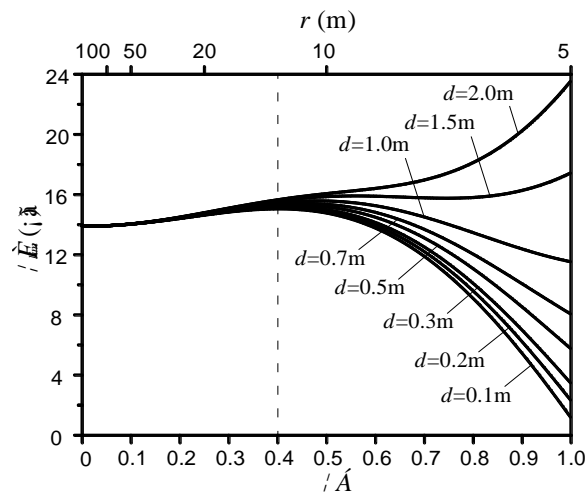


Fig. 10 - Lower limit friction angle along fault plane θ_{lim} with different d ($\beta=30^\circ, k=0.5$)

CHARACTERISTICS OF SHEAR DISPLACEMENTS INDUCED BY TUNNELING

Once rock slip along the fault plane appears, the tunnel support might be subjected to significant nonuniform rock deformation which would result in unfavourable load on support. By taking this into consideration, the tunnelling-induced nonuniform rock deformation related to fault is characterized by using numerical simulations.

The numerical analysis was focused on the parameters of fault dip angle, horizontal stress ratio and the distance between fault plane and circular tunnel center. Another important parameter was the shear strength of fault (for fault in hard rock, the cohesion could be neglected). To stabilize the rock slip far away from excavation wall along fault plane, the frictional angle of fault should be larger than a certain value (called θ_{ini} , short for the initial required frictional angle of a fault) which could be calculated by Equation 6 with $\alpha = 0$. Given this understanding, the frictional angle of the fault in the numerical analysis should be not less than θ_{ini} .

In the numerical cases, prior to tunnel excavation, the model was applied to ground stress at boundaries to reach equilibrium and to produce the in situ stress field. As the proposed criterion was based on elasticity assumption, the models were assumed to be elastic media (other properties of rock and fault are listed in Table 1 and Table 2. In the initial stress equilibrium process, the frictional angle of the fault was the main parameter that affects the equilibrium of the whole system with specified stress boundary conditions and spatial extension and location of a fault. After model equilibrium was reached, the tunnel was excavated in one step and the model was solved for a following equilibrium.

Shear displacements induced by tunnelling related to fault shear strength

It is obvious that the tunnelling-induced shear displacements are determined by the shear strength of a fault. The fault frictional angle might be larger than θ_{max} , or in the range of θ_{ini} to θ_{max} , or less than θ_{ini} , when in-situ combinations of ground horizontal stress ratio and fault spatial extension and location (i.e. fault dip angle and the distance between fault plane and tunnel center) are specified. To analyse the tunnelling-induced shear displacements, the input θ should not exceed θ_{max} . The frictional angle of the fault θ was reduced from θ_{max} to θ_{ini} with an interval of $2\% \times (\theta_{max} - \theta_{ini})$. The variations of shear displacements D_s at excavation wall (as located in Figure 5) induced by tunnelling are summarized in Figure 11.

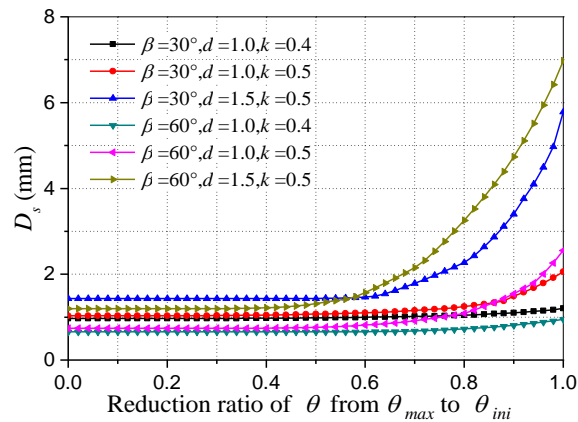


Fig. 11 - Shear displacements at excavation wall varying with gradual reduction of fault shear strength for different combinations of horizontal stress ratio and fault spatial extension and location

It could be seen in Figure 11 that, the shear displacements at excavation wall with different combinations of horizontal stress ratio and fault spatial extension and location show similar tendency. With gradually reduction of the input frictional angle of the fault, tunnelling-induced shear displacements increase only when the reduction ratios exceed about 0.4, and this phenomenon might be attributed to a stress redistribution process that, part of shear stress of slip-failure zones were transferred to nearby zones, and then the distinguishable rock slip was delayed. For cases in Figure 11 with larger distances between fault plane and tunnel center, tunnelling-induced shear displacements are much larger than that of other cases when fault frictional angles are reduced to θ_{ini} .

The effects of fault dip angle

To reveal the effects of fault dip angle or horizontal stress of ground on the tunnelling-induced shear displacement at excavation wall, other important parameters in the numerical models should be given fixed values. As discussed before, the input frictional angle of fault should be in the range of from θ_{ini} to θ_{max} . And for remarkable shear displacements from the numerical models, the input shear strength of the fault should better to be set at θ_{ini} according to Figure 11. The relationship between the initial required frictional angle θ_{ini} and horizontal stress ratio and fault dip angle graphically presented in Figure 12, however, shows that for a fixed dip angle of fault, there is no identical θ_{ini} could be approached when stress ratio changes. And this is a sign that analysing the effects of stress ratios on the tunnelling-induced shear displacement was hard to be performed. On the other hand, for a fixed stress ratio, there is identical a θ_{ini} that could be approached, which indicates that the analysis on the effect of fault dip angle on the tunnelling-induced shear displacement is practicable. 5 combinations of horizontal stress ratios and dip angles of faults are

presented in Figure 13 to demonstrate case pairs in the analysis on the effect of dip angle. And the case conditions of each combination were set with identical stress ratio and input frictional angle of fault.

The fault dip angle is a main parameter that characterizing the spatial extension of a fault, which has a dominant influence on the ground stress distribution. And the rock deformations may show some different characteristics when tunnelling. Figure 14 demonstrates the shear displacements induced by tunnelling with different fault dip angles while other parameters in the models are fixed. It's clearly seen that, fault dips have remarkable influences on the tunnelling-induced shear displacements in each dip pairs. It also could be found that, the shear displacements in each pair of numerical models with larger dip angles are larger than that of models with smaller dip angles. And when the dip angles in each pair are getting closer, the differences of shear displacements get smaller.

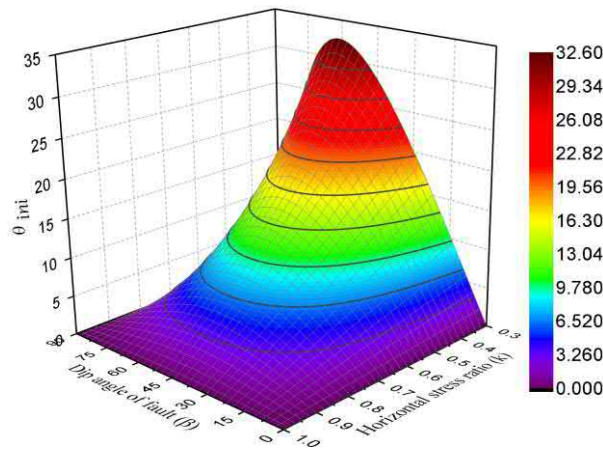


Fig. 12 - Variation of the initial required frictional angle of fault θ_{ini} with stress ratio of ground and dip angle of fault

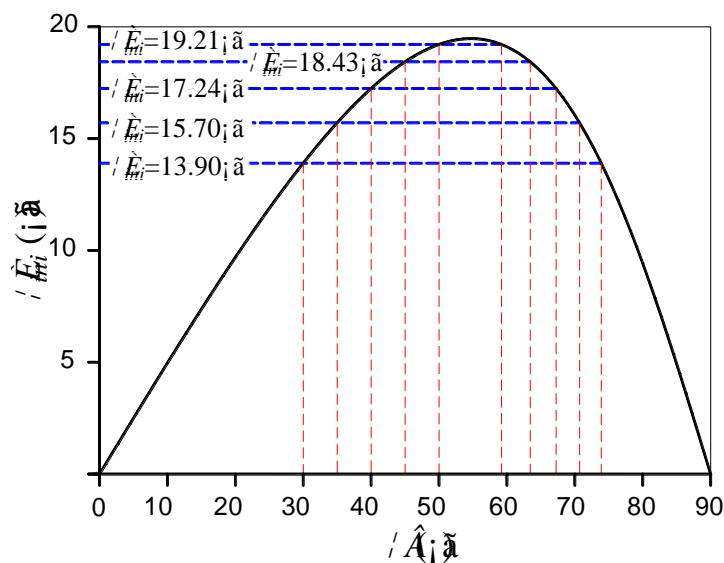


Fig. 13 - Variation of the initial required frictional angle of fault θ_{ini} with dip angle of fault ($k = 0.5$)

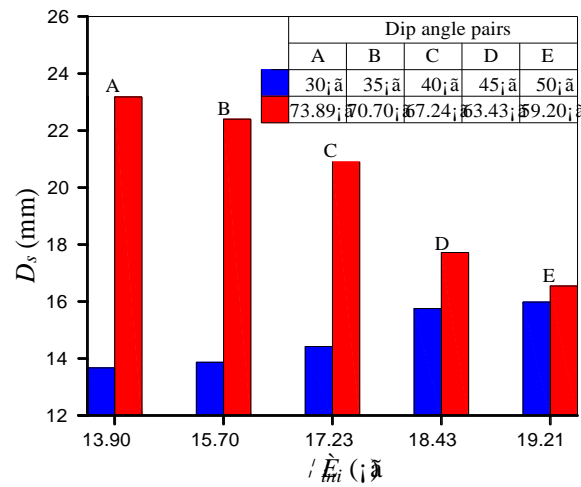


Fig. 14 - Relationship between tunnelling-induced shear displacements and different fault dip angle pairs ($k = 0.5, d = 2.0\text{m}$)

It should be noted that, the effects of fault dip on the tunnelling-induced shear displacements D_s was investigated just for individual dip angle pairs that determined the same θ_{ini} as the input frictional angle of a fault. And no relationship of shear displacements varying with continuous variation of fault dip angle was investigated. However, it still could be concluded that, larger fault dip angle ($\beta > 55^\circ$ for specified stress ratio and spatial extension of a fault, according to Figure 13) is not favourable to the stability of host rock of tunnel related to fault when compared to the corresponding smaller one.

The effects of fault location

The distance between tunnel center and fault plane d in detail, is an important parameter that characterizes the fault relative spatial location. As has been discussed before, only the lower frictional angle of a fault near the excavation wall was strongly affected by d (Figure 10). Then, the effect of d on the shear displacements could be investigated by giving fixed fault dip angles and horizontal stress ratios.

Results of the four cases with d increased from 0m to 3m presented in Figure 15 show similar tendencies, which could be described as: further the fault plane is away from tunnel center (no larger than the tunnel radius), larger shear displacement D_s induced by tunnelling at excavation wall could be expected. And the relationship of shear displacement varying with d indicates that, when tunnelling in faulted hard rock, fault location with respect to tunnel has a dominant influence on the stability of rock near where fault intersecting with tunnel.

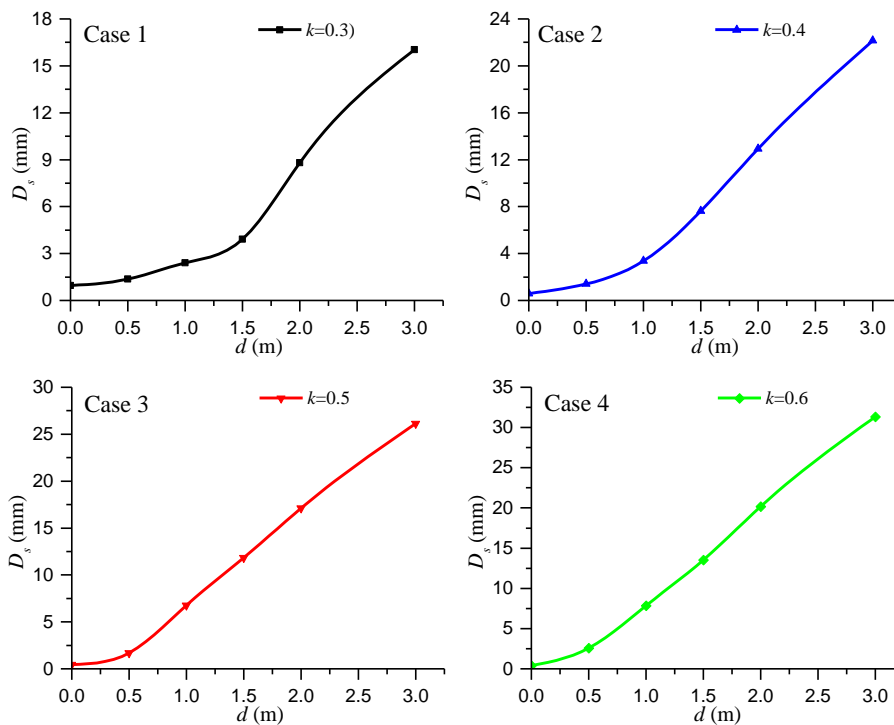


Fig. 15 - The relationship of shear displacements varying with d ($\beta=50^\circ$)

The 4 cases are modelled with different horizontal stress ratio and it seems that, larger stress ratio results in larger shear displacement. However, this apparent phenomenon could be explained by Figure 9 that, with a stress ratio closer to 1, the θ_{ini} input into the numerical model is smaller and resulting in larger shear displacements.

CONCLUSIONS

Based on continuum assumption and Coulomb-slip criterion, analysis of stress on the fault plane was carried out, and then a criterion to evaluate rock slip along the fault for a circular tunnel, which was excavated in rock mass containing a fault was proposed. The proposed criterion was validated through numerical models. By mathematically describing the proposed rock slip criterion, the “lower limit frictional angle of a fault” parameter was put forward, which was the required shear strength of local part of a fault to prevent rock slip. The main advantage of the proposed criterion is that the potential rock slip along a fault around a circular tunnel could be evaluated by simple calculations and comparisons. By theoretical analysis and numerical explorations, deeper insight into the fault-related instability problems of tunnels is provided, which could be summarized as below:

The fault shear strength was proved to be the main parameter that controlled the stability of rock mass around the tunnel, when compared to required shear strength (the lower limit frictional angle of a fault). The required shear strength of a fault is determined by horizontal stress ratio of ground and the spatial extension and location of a fault, and the analysis of these important parameters' influences on the lower frictional angle of a fault suggested that the rock slip instability near the excavation wall was strongly dependent on the fault spatial location. And this phenomenon was also demonstrated by the effect of fault location on the tunnelling-induced shear displacements near the excavation wall, as larger shear displacement appeared with larger distance between tunnel center and fault plane.

Fault dip in relation to the tunnel was proved to be an important parameter, which the required shear strength of the fault is dependent on. It is demonstrated that, the rock slip stability along the whole fault was influenced by the fault dip. Besides, the tunnelling-induced shear displacement at excavation wall with greater fault dip angle ($0^\circ < \beta < 90^\circ$) was larger than that of the smaller corresponding fault dip with which the other parameters of the numerical models could be set as the same values.

The effect of ground stress ratio also showed great influence on the stability problem of tunnels in faulted rock masses. With the stress ratio closer to hydrostatic stress state, the required shear strength of a fault is much smaller in the far field. Meanwhile, the required shear strength of a fault near the excavation wall is affected by the ground stress ratio much less, as it is mainly determined by fault location.

Generally, the present research is based on elastic mechanics, and thus no plastic behaviour of rock could be considered, which might be the main limitation of this research. And if the plastic behaviour of rock could be taken into consideration, further explorations of the fault-related instability problems of tunnels could be more comprehensive and useful.

ACKNOWLEDGEMENTS

This paper was sponsored by the National Natural Science Foundation of China (Grant No. 51378436). The authors wanted to express thanks to the foundation.

REFERENCES

- [1] Bruneau G., Tyler D., Hadjigeorgiou J, Potvin Y., 2003. Influence of faulting on a mine shaft—a case study: part I—Background and instrumentation. *International Journal of Rock Mechanics and Mining Sciences*, vol. 40: 95-111
- [2] Meng L., Li T., Jiang Y., Wang R, Li Y., 2013. Characteristics and mechanisms of large deformation in the Zhegu mountain tunnel on the Sichuan–Tibet highway. *Tunnelling and Underground Space Technology*, vol. 37: 157-164
- [3] Kun M., Onargan T., 2013. Influence of the fault zone in shallow tunneling: A case study of Izmir Metro Tunnel. *Tunnelling and Underground Space Technology*, vol. 33: 34-45
- [4] Suorineni F., Tannant D., Kaiser P., 1999. Determination of fault-related sloughage in open stopes. *International Journal of Rock Mechanics and Mining Sciences*, vol. 36: 891-906
- [5] Brekke T.L., Howard T.R., 1972. Stability problems caused by seams and faults. *International Journal of Rock Mechanics & Mining Sciences & Geomechanics Abstracts*, vol. 12: 95
- [6] Nagelhout A.C.G., Roest J.P.A., 1997. Investigating fault slip in a model of an underground gas storage facility. *International Journal of Rock Mechanics & Mining Sciences*, vol. 34: 212.e211–212.e214
- [7] Li D., Xia B.W, Hao C., Bai S.W., 2009. Research on stability of tunnel in anisotropic layered rockmass with low inclination angle bedding by model test. *Rock & Soil Mechanics*, vol. 30: 1933-1938
- [8] Brekke T.L., Howard T.R., 1974. Functional classification of gouge materials from seams and faults in relation to stability problems in underground openings : 65F, 18T, 84R. US BUR. MINES, TECHNICAL REPORT, 1973. *International Journal of Rock Mechanics & Mining Sciences & Geomechanics Abstracts*, vol. 11: 62-62
- [9] Moretto, O., 1993. A case history in Argentina – rock mechanics for the underground works in the pumping storage development of Rio Grande No. 1 *Comprehensive Rock Engineering*, vol. 5. Pergamon Press, Oxford
- [10] Barton N., Lien R., Lunde J. (1974) Engineering classification of rock masses for the design of tunnel support. *Rock Mechanics*, vol. 6: 189-236
- [11] Brady, B.H.G., Brown, E.T., 1993. *Rock Mechanics for Underground Mining*, second ed. Chapman & Hall, London
- [12] Goodman, R.E., Shi, G.H., 1985. *Block Theory and its Application to Rock Engineering*. Prentice-Hall, Englewood Cliffs, NJ. p. 338
- [13] Sun X.L., Wang H.Z., 2006. 3D FEM analysis of horizontal jet grouting prelining in a tunnel under

asymmetric loads. *Tunnelling & Underground Space Technology*, vol. 21: 366-367

- [14] Xiao J.Z., Dai F.C., Wei Y.Q., Min H., Xu C., Tu X.B., Wang M.L., 2014. Cracking mechanism of secondary lining for a shallow and asymmetrically-loaded tunnel in loose deposits. *Tunnelling & Underground Space Technology*, vol. 43: 232-240
- [15] Zhou X.J., Gao Y., Li Z.L., 2006. Experimental study on the uneven rock pressure and its distribution applied on a tunnel embedded in geologically bedding strata. *Modern Tunnelling Technology*, vol. 41: 12-21
- [16] Huang F., Zhu H., Xu Q., Cai Y., Zhuang X., 2013. The effect of weak interlayer on the failure pattern of rock mass around tunnel – Scaled model tests and numerical analysis. *Tunnelling and Underground Space Technology, incorporating Trenchless Technology Research*, vol. 35: 207-218
- [17] Zhu Z.Q., Qian S., Mei S.H., Zhang Z.R., 2009. Improved ubiquitous-joint model and its application to underground engineering in layered rock masses. *Rock & Soil Mechanics*, vol. 30: 3115-3121+3132
- [18] Bhasin R., Hoeg K., 1998. Parametric study for a large cavern in jointed rock using a distinct element model (UDEC—BB). *International Journal of Rock Mechanics & Mining Sciences*, vol. 35: 17-29
- [19] Jeon S., Kim J., Seo Y., Hong C., 2004. Effect of a fault and weak plane on the stability of a tunnel in rock—a scaled model test and numerical analysis. *International Journal of Rock Mechanics & Mining Sciences*, vol. 41: 658-663
- [20] Yeung M.R., Leong L.L., 1997. Effects of joint attributes on tunnel stability. *International Journal of Rock Mechanics & Mining Sciences*, vol. 34: 348.e341–348.e318
- [21] Hao Y.H., Azzam R., 2005. The plastic zones and displacements around underground openings in rock masses containing a fault. *Tunnelling & Underground Space Technology*, vol. 20: 49-61
- [22] Wang X., Kulatilake P.H.S.W., Song W.D., 2012. Stability investigations around a mine tunnel through three-dimensional discontinuum and continuum stress analyses. *Tunnelling and Underground Space Technology, incorporating Trenchless Technology Research*, vol. 32: 98-112
- [23] Jia P., Tang C.A., 2008. Numerical study on failure mechanism of tunnel in jointed rock mass. *Tunnelling & Underground Space Technology, Incorporating Trenchless Technology Research*, vol. 23: 500-507
- [24] Zhang Z., Chen F., Li N., Swoboda G., Liu N., 2017. Influence of fault on the surrounding rock stability of a tunnel: Location and thickness. *Tunnelling and Underground Space Technology, incorporating Trenchless Technology Research*, vol. 61:1-11
- [25] Xu D.P., Feng X.T., Cui Y.J., Jiang Q., 2015. Use of the equivalent continuum approach to model the behavior of a rock mass containing an interlayer shear weakness zone in an underground cavern excavation. *Tunnelling and Underground Space Technology*, vol. 47: 35-51
- [26] Kirsch E.G., 1898. Die Theorie der Elastizität und die Bedürfnisse der Festigkeitslehre. *Z VDI. Zeitschrift Des Vereines Deutscher Ingenieure*, vol 42:797-807
- [27] Jiang Y., Tanabashi Y., Li B., Xiao J., 2006. Influence of geometrical distribution of rock joints on deformational behavior of underground opening. *Tunnelling and Underground Space Technology, incorporating Trenchless Technology Research*, vol. 21: 485-491
- [28] Itasca Consulting Group Inc., 2004. UDEC (Universal Distinct Element Code), Version 4.0, User Manual. Itasca Consulting Group Minneapolis, MN, USA
- [29] Jiang Y., Nakagawa M., Esaki T., 2010. Quantitative evaluation of mechanical properties of the natural rock joints for analyzing behavior of structures in discontinuous rock masses. In: *Proceedings of JSCE*, vol. 624: 231-243
- [30] Jiang Y., Xiao J., Tanabashi Y., Mizokami T., 2004. Development of an automated servo-controlled direct shear apparatus applying a constant normal stiffness condition. *International Journal of Rock Mechanics & Mining Sciences*, vol. 41: 275-286
- [31] Kulatilake P.H.S.W., Ucpirti H., Wang S., Radberg G., Stephansson O., 1992. Use of the distinct element method to perform stress analysis in rock with non-persistent joints and to study the effect of joint geometry parameters on the strength and deformability of rock masses. *Rock Mechanics & Rock Engineering*, vol. 25: 253-274

DESIGN OF AN ACTIVE LOW FREQUENCY VIBRATION ISOLATION SYSTEM FOR ATOM INTERFEROMETRY BY USING SLIDING MODE CONTROL

*Dong-Yun Luo, Bing Cheng, Bin Wu, Xiao-Long Wang, and Qiang Lin**

Center for Optics and Optoelectronics Research, College of Science, Zhejiang University of Technology, Hangzhou, China, email: g20158028@xs.ustb.edu.cn

ABSTRACT

Active vibration isolation is gaining increased attention in the ultra-high precision application of atom interferometry to effectively treat the unavoidable ground vibration. In this system, a digital control subsystem is used to process and feedback the vibration measured by a seismometer. A voice coil actuator is used to control and cancel the motion of a commercial passive vibration isolation platform. The system level simulation model is established by Simulink software, The simulation results demonstrate the asymptotic stability of the system and the robustness of the control algorithm. Compared with the conventional lead-lag compensation type controller, the algorithm adopted uses sliding mode control, taking advantage of its easy computer implementation and its robust high performance properties. With the feedback path closed, the system acts like a spring system with a natural resonance frequency of 0.02 Hz. The vibration noise in the vertical direction is about 20 times reduced during 0.1 and 2 Hz, The experimental results verify that the isolator has significant vibration isolation performance, and it is very suitable for applications in high precision gravity measurement.

KEYWORDS

Active vibration isolation, Low frequency vibration, Sliding control, Atom interferometry

INTRODUCTION

Ultra-low frequency vibration isolation has valuable applications in precision instruments such as laser interferometers, atomic force microscope, electron-beam microscopes and so on. Similarly, in our precision atom interferometry measurements which have been one of the best items of equipment to measure gravitational acceleration g . Any change in the relative paths of the two Raman beams due to vibrations will be seen as a spurious interferometer phase shift and noise in the measurement. This phase noise directly couples into the interferometer phase and completely washes out the interferometer fringes for longer pulse separations if not addressed¹. For example, in the 5m atom interferometer(AI), the free evolution time T , can reach 0.8Hz greatly influences the experiment. Therefore, to suppress the low frequency noise primarily caused by the vibration of a retro-reflecting mirror mounted at the bottom of our AI. To prevent the interferometer fringes from washing out, vibrations have to be reduced to a level where the resulting phase shifts are much smaller than 1 rad. Appropriate vibration isolation of the retro-reflecting mirror is crucial for achieving clean atom interferometer fringes at long pulse separation. Constructing a vibration isolation platform capable of delivering sufficient performance has been the main task of this work and is described extensively in the paper.

Chu's team first constructed a system that isolates a key element of our experimental setup from vertical motions of the ground and the surrounding apparatus [1]. The system combines the

passive isolation of mechanical springs and an optical table floating on compressed air with an active system that measures the acceleration of the mass to be isolated and feeds back to a solenoid actuator to cancel this motion [2]. With the feedback path closed, the system acts like a spring-mass system with a natural resonance frequency of 0.033 Hz. The acceleration error signal is reduced from 0.1 to 20 Hz. Freier simplified the structure of his active vibration isolation lowering the effective resonance frequency from 0:5 Hz to 0:025 Hz by exerting an additional force to the payload mass and suppressed the vibrational noise from about 0.03 to 5 Hz by a factor of up to 200. The vibration of the power spectral density stays on a roughly constant value of $1 \times 10^{-7} g / \sqrt{\text{Hz}}$ between 0:03 Hz and 0.5 Hz³. The accuracy of the existing setup has been improved significantly from $3 \times 10^{-6} g$ to $5 \times 10^{-8} g$. Tang suppress the vertical vibration (0.1–10 Hz) measured by the in-loop seismometer is reduced by an additional factor of up to 500 on the basis of a passive vibration isolation platform.

The teams above mentioned used programs to measure the open-loop frequency response and to graphically set the parameters for the feedback lead–lag compensation filters. They got the highest possible feedback gain of the system with enough phase margin by adjusting the parameters of the feedback filters which is designed by using a combination of lag compensators. The combination of lag compensators contains multiple tuning parameters. For the sake of initial turn-on spike in Ref. [3]. The gain of feedback loop set to the designed value must be slowly increased to its final value over a period of about 3 mins [3]. To deal with these drawback, sliding control strategy which has the advantage of a simple structure, model-free, higher computation efficiency ability and few tuning parameters. We have designed and implemented an active system that combines relatively short mechanical springs with an electronic feedback loop to produce an almost critically damped spring-mass system with an effective resonance frequency of 0.02 Hz by using sliding mode control, thus significantly reducing the effect of harmful vibrations at frequencies from 0.05 to 10Hz [4-5].

THEORY

(1) Vibration Noise

The acceleration of the retro-reflector is indistinguishable for the gravimeter which can measure the gravitational acceleration by the equivalent principle. So the vibration noise has been is the largest noise source of the atomic interferometer, the effect of vibration noise suppression determines the performance of gravity acceleration measurement [6]. The sensitivity of the vibration acceleration function can be expressed as $g_a(t)$:

$$g_a(t) = 2 \lim_{\delta_a \rightarrow 0} \frac{\delta P_a(\delta_a, t)}{\delta_a} \quad (1)$$

Where δ_a is an infinitesimal disturbance, $g_s(t)$ is the sensitivity function of the gravimeter, the relationship between $g_a(t)$ and $g_s(t)$ can be expressed as:

$$g_s(t) = \frac{d^2 g_a(t)}{k_{eff} dt^2} \quad (2)$$

Where k_{eff} is Raman wave number. The relationship between the vibration acceleration transfer function $H_a(w)$ and the interferometer transfer function $H_\phi(w)$ can be expressed as:

$$|H_a(w)|^2 = \frac{k_{eff}^2}{w^4} |H_\phi(w)|^2 \quad (3)$$

Assume that the power spectral densities of the vibration displacement and the vibration acceleration respectively are $S_z(w)$ and $S_a(w)$, the power spectral density of the phase $S_\phi(w)$ can be expressed as:

$$S_\phi(w) = |k_{eff}|^2 S_z(w) = \frac{|k_{eff}|^2}{w^4} S_a(w) \tag{4}$$

The rms (root mean square) value of the total phase of the interferometer can be expressed as:

$$(\sigma_\phi^{rms})^2 = \int_0^\infty |H_\phi(w)|^2 S_\phi(w) dw \tag{5}$$

The acceleration transfer function is a low-pass filter effect, the filter cut off rate is $1/(2T)$. With the experimental parameters $T = 70ms$ and $\tau = 4\mu s$, $H_a(f)$ can be expressed as:

$$H(f) = \frac{4}{1 - (4\tau f)^2} \sin(\pi(T + 2\tau)f) (\sin(\pi T f) + 4\tau f \cos(\pi(T + 2\tau)f)) \tag{6}$$

From Figure 1 we can see low frequency vibration has more weight coefficient than high frequency vibration. The surrounding vehicle movement, construction activities around our laboratory have a great impact on interferometer [7-8]. The function of gravity acceleration g measured by interferometer can be expressed as:

$$g = \frac{1}{k_{eff} T^2} \Delta\phi \tag{7}$$

where $\Delta\phi$ is the phase of the interferometer. In order to assess the effect of vibration on the phase, we have mounted retro-reflector mirror on passive isolation platform and measured noise power spectrum which can calculate the contribution of vibration noise under different T.

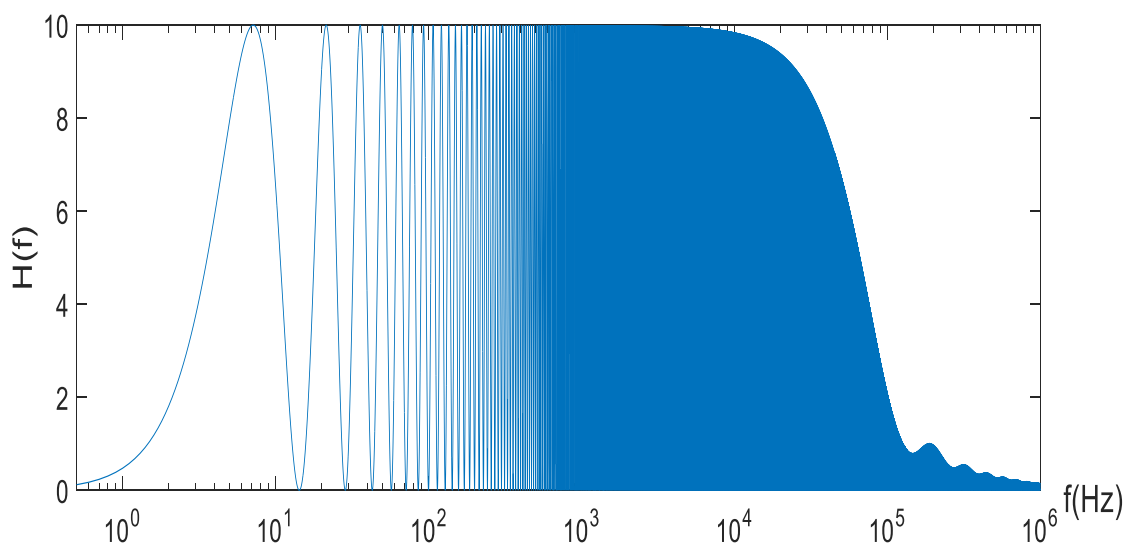


Fig.1 - Weight function curve of influence of Phase Noise on Interferometer Phase

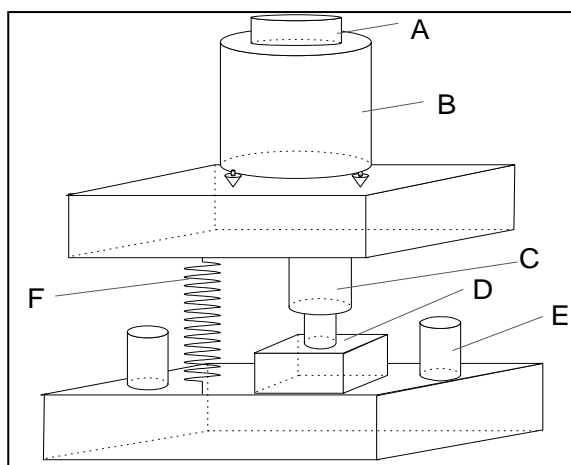
Tab. 1 - Contribution of vibration noise under different T

T (ms)	phase of the interferometer (mrad)
40	18.2
50	25.0
60	32.5
70	42.2

(2) Mechanical system

A typical schematic diagram of active vibration isolation is shown in Figure 2. Motion from the ground passing through the spring and damping system drives the mass. A sensor detects the motion of the mass and feedback it to an actuator to generate an equal force in the opposite direction to cancel the motion of the mass [9].

The mechanical setup is based on a commercial passive isolation platform. (25BM-4, Minus K Technology, Inglewood, CA, USA). It has a net payload of 4.5 kg to 10 kg and is easily transportable with dimensions of approx. 31×31×11.7cm and a weight of 9 kg. By employing patented mechanism using negative stiffness elements, it provides vibration isolation in 3 spatial directions with a low vertical resonance frequency of 0.5 Hz and a horizontal resonance frequency of 1.5 Hz. It is clear that passive vibration isolators can only isolate against ground motions at frequencies above 0.7Hz. There is no effect for vibration below 0.5 Hz. A broadband and sensitive commercial seismometer (CMG-3ESP) is installed on the top of the passive isolator [10-11]. The seismometer is a triaxial sensor, and can directly measure the velocity of the platform caused by ground vibration. It can measure very low frequency velocity from 0.017 to 50 Hz with sensitivity of $2040V / ms^{-2}$ and a noise level lower than $10^{-9} g / \sqrt{Hz}$, The maximum peak-to-peak value of the differential output voltage of the seismometer is $\pm 10V$ [12-15]. The voltage signal from the seismometer is collected by a FPGA based data acquisition and processing card (NI-9223, National Instruments Corporation, Austin, TX, USA) which is 16-bit resolution.



(a)

(b)

Fig.2 - (a) and (b) Mechanical setup of our active VIS. (A) mirror, (B) seismometer, (C) voice coil motor, (D) translation stage, (E) counter weight, (F) passive vibration isolation platform

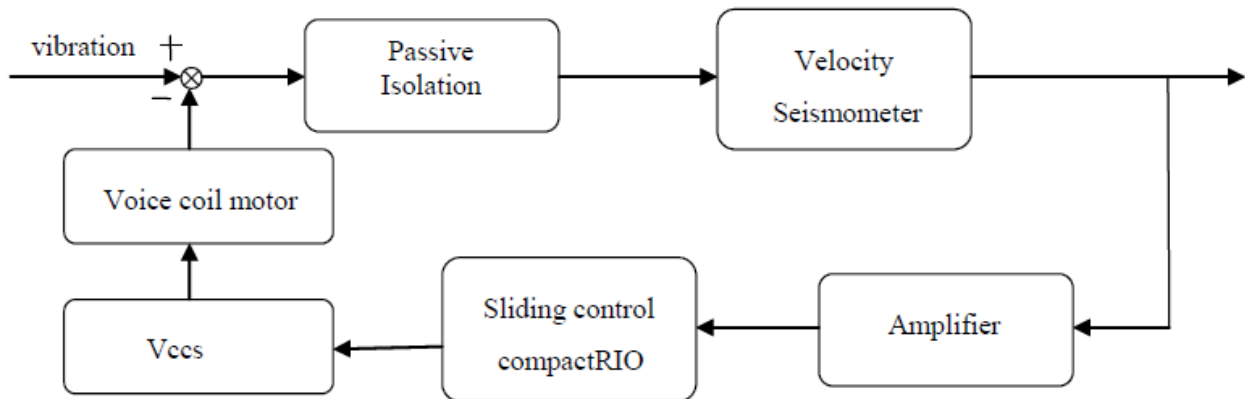


Fig.3 - Diagram of the feedback loop

The acquisition and processing card can only resolve the vibration velocity signal of $1.5 \times 10^{-7} \text{ m/s}$, but vibration speed goal is $6.28 \times 10^{-8} \text{ m/s}$, so the velocity signals from the sensor are amplified by independent low-noise amplifiers (AD624) which pin programmable gains of 1, 200, 500 and 1000 can be provided on the chip. We used a National Instruments compactRIO Real-Time Computer System (NI cRIO9031, National Instruments Corporation, Austin, TX, USA) with an FPGA backplane to perform the sliding mode control. All programs were written in NI LabVIEW 2016, The system is controlled remotely via LabVIEW which allows easy access from the main control computer of the atom interferometer. The program running on the FPGA chip and a control and monitoring program implemented on a 1.33GHz CPU which is also part of the cRIO system. The driven current for the voice-coil comes directly from a voltage controlled-current-source (VCCS). The VCCS can provide a current of 500 mA with 5 V driving voltage. The frequency response of the VCCS will limit the bandwidth of the feedback loop. The corner frequency of the VCCS circuits is larger than 100 Hz, while the demand for our feedback loop is only 50 Hz, thus the bandwidth is large enough. Due to size restrictions inside the vertical vibration isolator, small actuators (LA12-17, BEI Technologies, San Marcos, CA, USA) manufactured with a diameter of 30.48mm and a mid-stroke length of 43.18mm were chosen. Because the clearance on each side of voice coil actuator is 0.38 mm, the coil side is mounted on a two-dimensional translation stage, which is used to adjust the space between the coil and magnet [16-18]. The magnet side is mounted on an aluminum plate as shown in Figure 2. A copper coil and magnets of voice-coil type actuators, each comprised of a copper coil and magnet, are used to provide feedback forces. The force constant is 7.46 N/A, which is obtained by measuring the excited acceleration under a constant driving current. Diagram of the feedback loop is shown in Figure 3.

A mass m whose motion x we wish to decouple from any motion of the ground y is suspended from a spring with linear spring constant k and damping factor c (Figure 1). By analyzing the system we get a well known linear 2nd order dynamic equation with constant coefficients [19-21]:

$$\ddot{x} + 2\xi_0\omega_0(\dot{x} - \dot{y}) + \omega_0^2(x - y) = \frac{F}{x} \tag{8}$$

Where $\omega_0 = \sqrt{k/m}$ is the intrinsic resonance frequency, $\xi_0 = c/2m\omega_0$ is the intrinsic damping constant, $F = -2mH\dot{x}$, H is the adjustable gain factor of feedback force magnitude. The transfer function of this active system is obtained by Laplace transformation to both sides of Equation 6:

$$\frac{\dot{x}}{\dot{y}} = \frac{2\xi_0\omega_0(i\omega) + \omega_0^2}{(i\omega)^2 + 2\omega_0(\xi_0 + H)(i\omega) + \omega_0^2} \quad (9)$$

Equation 8 shows that with the increase in feedback gain H which lower the effective resonance frequency and thus increase the range over which the system tends to isolate motions of the ground from motions of the mass [22-23].

We use signal generator ((DGU1022, RIGOL Corporation, Beijing, China) to produce the frequency swept slowly from 0.03 to 300 Hz to make sure that the data acquisition (DAQ) card obtains enough velocity response data of the platform to calculate its transmissibility. From Figure 4 and Figure 5 we can calculate that $\omega_0 = 2\pi \times 0.7 = 4.396$ and $\xi_0 = 0.1$.

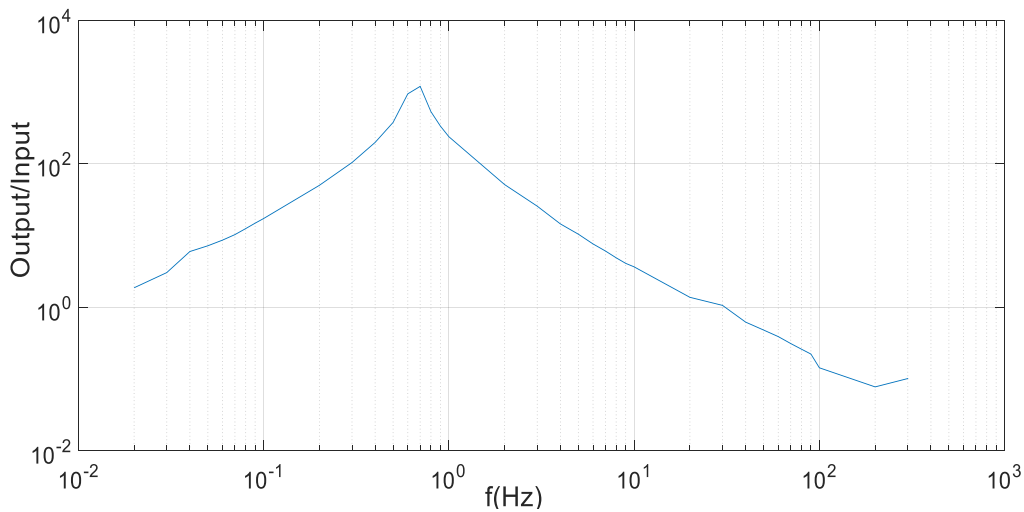


Fig. 4 - Magnitude bode plot of open loop

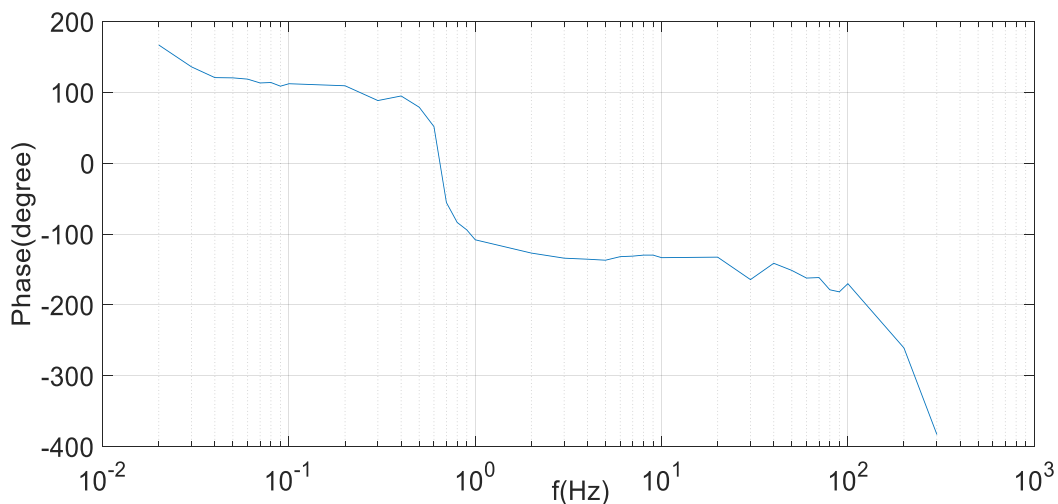


Fig. 5 - Phase bode plot of open loop

SLIDING MODE CONTROL ALGORITHM

(1) Controller Design

From Equation 9 we can deduce active vibration isolation system mathematical model:

$$\ddot{x} + a\dot{x} + lx + bu + d = 0 \quad (10)$$

Where $a = 2\xi_0\omega_0$, $l = \omega_0^2$, $b = -\frac{1}{m}$, $d = -2\xi_0\omega_0\dot{y} - \omega_0^2 y$, $F = ku$, u is sliding controller output voltage, d is external disturbance, d is coefficient between the force of voice coil motor and controller output voltage [24-26].

Sliding surface can be designed as:

$$s(t) = ce(t) + \dot{e}(t) \quad (11)$$

Where $c > 0$, meet Hurwitz condition. Error and its derivative can be expressed as:

$$e(t) = x_d - x \quad (12)$$

$$\dot{e}(t) = \dot{x}_d - \dot{x} \quad (13)$$

Where $x_d = 0$ is the setpoint of the vibration displacement, $\dot{x}_d = 0$ is the setpoint of the vibration velocity, thus:

$$\dot{s}(t) = c\dot{e}(t) + \ddot{e}(t) = c(\dot{x}_d - \dot{x}) + (\ddot{x}_d - \ddot{x}) \quad (14)$$

Substituting Equation (10) into Equation (14), the following can be achieved:

$$\dot{s}(t) = c(-\dot{x}) + (-a\dot{x} - cx - bu - d) = -(c+a)\dot{x} - cx - bu - d \quad (15)$$

Index approaching law can be designed as:

$$\dot{s}(t) = -\varepsilon \operatorname{sgn}(s) - ks \quad (16)$$

Where $\varepsilon > 0, k > 0$.

Equation 15 and Equation 16 can be achieved: $-(c+a)\dot{x} - cx - bu - d = -\varepsilon \operatorname{sgn}(s) - ks$
 $\operatorname{sgn}(s)$ can be described as:

$$\text{Where } \operatorname{sgn}(s) = \begin{cases} 1 & x > 0 \\ 0 & x = 0 \\ -1 & x < 0 \end{cases}$$

Sliding mode control law can be expressed as:

$$u = \frac{1}{b} [-(c+a)\dot{x} - cx + \varepsilon \operatorname{sgn}(s) + ks - d] \quad (17)$$

Obviously, disturbance d is unknown, The above control law can not be achieved, we used disturbance bound to design control law in order to solve this problem [27-28].

Sliding mode control law can be designed as:

$$\dot{s}(t) = c(-\dot{x}) + (-a\dot{x} - cx - bu - d) = -(c+a)\dot{x} - cx - bu - d \quad (18)$$

Where d_c is positive real number related to disturbance d bound.

Substituting Equation 18 into Equation 15 , the following can be achieved:

$$u = \frac{1}{b} [-(c + a)\dot{x} - cx + \varepsilon \operatorname{sgn}(s) + ks - d_c] \quad (19)$$

The stability of the control system is ensured by selecting d_c , satisfy the sliding mode arrival condition, assume:

$$d_L \leq d \leq d_U \quad (20)$$

Where d_L and d_U are disturbance bound.

$$d_c = d_2 - d_1 \operatorname{sgn} s \quad (21)$$

Where $d_1 = \frac{d_U - d_L}{2}$ and $d_2 = \frac{d_U + d_L}{2}$

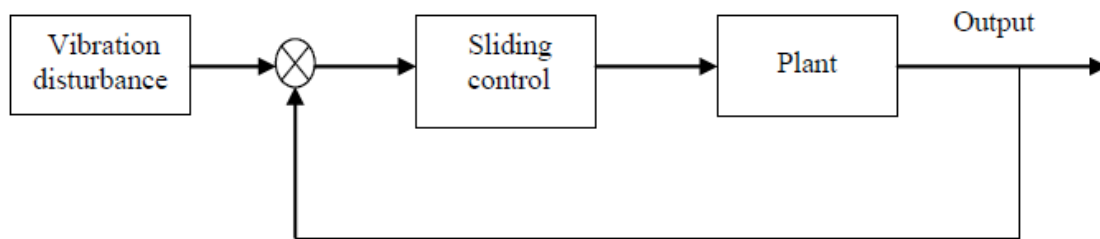


Fig. 6 - Diagram of the Sliding control

(2) Simulation

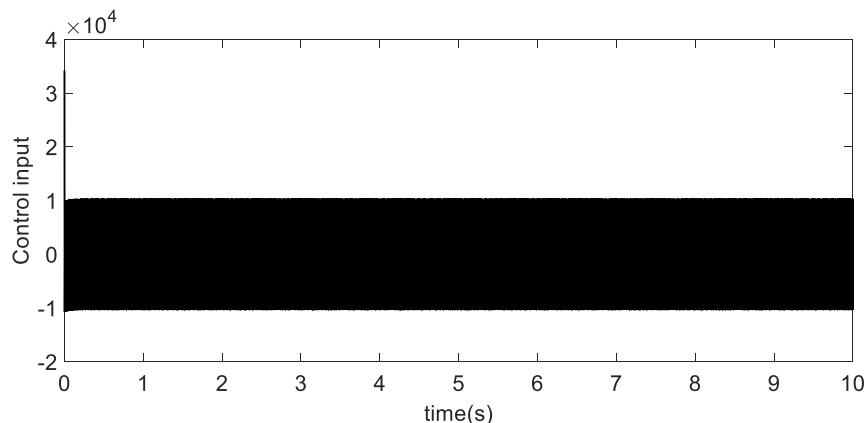


Fig. 7 - Sliding controller output

Figure 7 shows the control input for sliding controller. As can be seen, the control input of sliding controller shows continuous fluctuations. This is because the rule bank changes with each sampling point, and the continuous switching back and forth produces this chattering. By injecting a sinusoidal signal into the system (Figure 8), one can also observe that the control is effective in suppressing vibrations. Acceleration in z is reduced from 1 to 10^{-6} . Overall, the sliding controller is better than the lead-lag controller; it has better vibration isolation effect.

Tab 2. - Values of control parameters used in Sliding control

Symbol	Description	Properties	Unit
ω_0	natural resonance frequency	4.396	rad...
ξ_0	natural damping constant	0.1	N/(m/s)
m	Weight of load	10	Kg
c	Sliding surface coefficient	15	
d_U	Upper bound	26	
d_L	Lower bound	-26	
ε	exponential approach law coefficient	1000	
k	exponential approach law coefficient	1000	

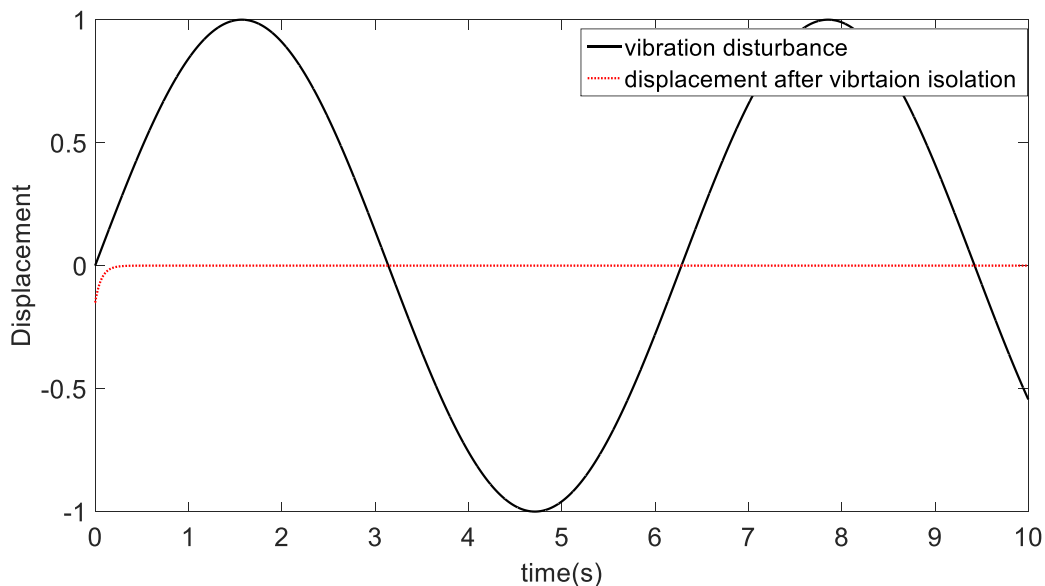


Fig. 8 - Vibration isolation simulation results of sliding controller

(3) Experiment Results

The performances of our active vibration isolation are shown in Figure 9. Figure 9 shows that the vibrational noise around 0.8 Hz has been suppressed by up to 300 times when the feedback is turned on with in loop measurement. The actual bandwidth of in-loop measurement was 0.08–10 Hz, which matched the theoretical prediction. Maximum vibration suppression is higher than 300 at the intrinsic resonant frequency of the passive system, and the vibration of 0.08–0.1 Hz was reduced by a factor of 3, while the vibration of 0.1–3 Hz was reduced by a factor of more than 50.

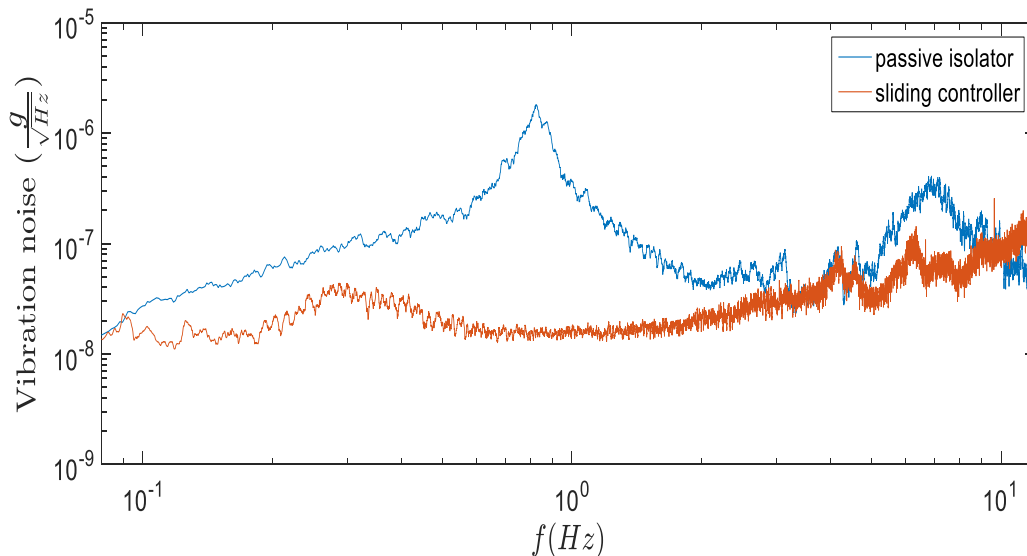


Fig. 9 - The performance of our active vibration isolation

The interference fringe of $T = 60$ ms is obtained by varying the chirp rate, which is displayed in Figure 11. The phase measurement of the fringe is obtained with a sinusoidal fit of the experimental data. The total interrogation time is optimized to 120ms and repetition rate is 2.2 Hz. The number of total points is 57 and each point is obtained as an average of four times; one full fringe period corresponds to 102 s.

CONCLUSIONS

We have implemented this active vertical vibration isolation system, by comparing the error signal reduction of our single-stage vertical vibration isolation system with the reported isolation of with the lowest effective resonance frequency. Maximum vibration suppression is higher than 300 at the intrinsic resonant frequency of the passive system, and the vibration of 0.08–0.1 Hz was reduced by a factor of 3, while the vibration of 0.1–3 Hz was reduced by a factor of more than 50. Despite a short total interrogation time of 120 ms, a sensitivity of $1.0 \times 10^{-7} g / \sqrt{\text{Hz}}$ and a resolution of $5.7 \times 10^{-9} g$ within 1000 s integration time were achieved. The long-term gravity data of 128 h were measured and they are in good agreement with the standard tidal model. In addition, a seismic wave of about 1h has been recorded by our atomic gravimeter.

ACKNOWLEDGEMENTS

This study was supported by the National Natural Science Foundation of China (Grant Nos. 61475139) and National Basic Research Program of China (973 Program-2013CB329501). Our gratitude is also extended to reviewers for their efforts in reviewing the manuscript and their very encouraging, insightful and constructive comments.

REFERENCES

- [1] Hensley, J. M., et al. (1999). "Active low frequency vertical vibration isolation." *Review of Scientific Instruments*, 70(6): 2735-2741.
- [2] Zhou, M. K., et al. (2015). "Note: A three-dimension active vibration isolator for precision atom gravimeters." *Review of Scientific Instruments*, 86(4): 046-108.

- [3] Tang, B., et al. (2014). "A programmable broadband low frequency active vibration isolation system for atom interferometry." *Review of Scientific Instruments*, 85(9): 093-109.
- [4] Wang wen-chao., et al.(2010)."Design and Matlab simulation of an ultra-low frequency vibration-isolating system for atom interferometers." *Chinese Journal of Quantum Electronics*, 27(3): 367-372.
- [5] Tjepkema, D., et al. (2012)."Sensor fusion for active vibration isolation in precision equipment." *Journal of Sound and Vibration*,331(4): 735-749.
- [6] Boulandet, R., et al. (2016)."A sensorless method for measuring the point mobility of mechanical structures." *Journal of Sound and Vibration*, 378: 14-27.
- [7] Tang, B., et al.(2014). "A programmable broadband low frequency active vibration isolation system for atom interferometry." *Review of Scientific Instruments*, 85(9): 093-109.
- [8] Fu, J., et al. (2016)."Model-free fuzzy control of a magnetorheological elastomer vibration isolation system: analysis and experimental evaluation." *Smart Materials and Structures*, 25(3): 035030.
- [9] Ahmad Mazlan, A. Z. and Z.Mohd Ripin (2017). "The effective frequency range of an active suspended handle based on the saturation effects of a piezo stack actuator." *Journal of Vibration and Control*, 23(5): 752-769.
- [10] Aloufi, B., et al. (2016)."Modeling and design of a high-performance hybrid actuator." *Smart Materials and Structures*, 25(12): 125004.
- [11] Liang, J. W., et al. (2013)."Active suppression of pneumatic vibration isolators using adaptive sliding controller with self-tuning fuzzy compensation." *Journal of Vibration and Control*, 21(2): 246-259.
- [12] Yen, J.-Y., et al. (2005)."Active vibration isolation of a large stroke scanning probe microscope by using discrete sliding mode control." *Sensors and Actuators A: Physical*, 121(1): 243-250.
- [13] Li, B., et al.(2014). "Dynamic modeling and control for a five-dimensional hybrid vibration isolator based on a position/orientation decoupled parallel mechanism." *Journal of Vibration and Control* ,22(15): 3368-3383.
- [14] Hogsberg, J. and M. L. Brodersen (2014). "Hybrid viscous damper with filtered integral force feedback control." *Journal of Vibration and Control* 22(6): 1645-1656.
- [15] Xia, Z., et al. (2016). "Non-linear dynamic analysis of double-layer semi-active vibration isolation systems using revised Bingham model." *Journal of Low Frequency Noise, Vibration and Active Control* ,35(1): 17-24.
- [16] Li, G., et al.(2014). "Ultra-low frequency vertical vibration isolator based on LaCoste spring linkage." *Review of Scientific Instruments*, 85(10): 104502.
- [17] Kim, M. H., et al. (2016)."Design and Control of a 6-DOF Active Vibration Isolation System Using a Halbach Magnet Array." *IEEE/ASME Transactions on Mechatronics* 21(4): 2185-2196.
- [18] Van de Ridder, L., et al. (2016)."Coriolis mass-flow meter with integrated multi-DOF active vibration isolation." *Mechatronics* 36: 167-179.
- [19] Chen, H. Y., et al. (2013)."Active pneumatic vibration control by using pressure and velocity measurements and adaptive fuzzy sliding-mode controller." *Sensors (Basel)*, 13(7): 8431-8444.
- [20] Persson, P., et al. (2016)."Numerical study of reduction in ground vibrations by using barriers." *Engineering Structures* ,115: 18-27.
- [21] Stabile, A., et al.(2017). "Design and verification of a negative resistance electromagnetic shunt damper for spacecraft micro-vibration." *Journal of Sound and Vibration*, 386: 38-49.
- [22] Plattenburg, J., et al. (2016). "A new analytical model for vibration of a cylindrical shell and cardboard liner with focus on interfacial distributed damping." *Mechanical Systems and Signal Processing*, 75: 176-195.
- [23] Sang, H., et al.(2016). "A fuzzy neural network sliding mode controller for vibration suppression in robotically assisted minimally invasive surgery." *Int J Med Robot*, 12(4): 670-679.
- [24] Ning, D., et al. (2016). "Active control of an innovative seat suspension system with acceleration measurement based friction estimation." *Journal of Sound and Vibration*, 384: 28-44.
- [25] Le, T. D.and K. K.Ahn (2013)."Fuzzy sliding mode controller of a pneumatic active isolating system using negative stiffness structure." *Journal of Mechanical Science and Technology*, 26(12): 3873-3884.
- [26] Ouyang, H., et al. (2016). "Load vibration reduction in rotary cranes using robust two-degree-of-freedom control approach." *Advances in Mechanical Engineering*,8(3): 168781401664181.



- [27] Tourajizadeh, H. and S.Zare (2016). "Robust and optimal control of shimmy vibration in aircraft nose landing gear." *Aerospace Science and Technology*, 50: 1-14.
- [28] Oliveira, F., et al.(2015). "A comparative study of semi-active control strategies for base isolated buildings." *Earthquake Engineering and Engineering Vibration*, 14(3): 487-502

INPUT DATA OF BURNING WOOD FOR CFD MODELLING USING SMALL-SCALE EXPERIMENTS

Petr Hejtmánek¹, Libor Ševčík² and Kamila Cábová³

1. *Czech Technical University, Faculty of Civil Engineering, Department of Building Structures, Thákurova 2077/7, Prague, Czech Republic; hejtmpet@fsv.cvut.cz*
2. *Technical Institute of Fire Protection in Prague. Písková 42, Prague 4 – Modřany, Czech Republic; libor.sevcik@tupo.izscr.cz*
3. *Czech Technical University, Faculty of Civil Engineering, Department of Steel and Timber Structures, Thákurova 2077/7, Prague, Czech Republic; kamila.cabova@fsv.cvut.cz*

ABSTRACT

The paper presents an option how to acquire simplified input data for modelling of burning wood in CFD programmes. The option lies in combination of data from small- and molecular-scale experiments in order to describe the material as a one-reaction material property. Such virtual material would spread fire, develop the fire according to surrounding environment and it could be extinguished without using complex reaction molecular description. Series of experiments including elemental analysis, thermogravimetric analysis and difference thermal analysis, and combustion analysis were performed. Then the FDS model of burning pine wood in a cone calorimeter was built. In the model where those values were used. The model was validated to HRR (Heat Release Rate) from the real cone calorimeter experiment. The results show that for the purpose of CFD modelling the effective heat of combustion, which is one of the basic material property for fire modelling affecting the total intensity of burning, should be used. Using the net heat of combustion in the model leads to higher values of HRR in comparison to the real experiment data. Considering all the results shown in this paper, it was shown that it is possible to simulate burning of wood using the extrapolated data obtained in small-size experiments.

KEYWORDS

Combustion of wood, Pine, FDS, Cone calorimeter, FTCH, Small-size experiment

INTRODUCTION

Computer based modelling of a fire is the one of the progressive methods in fire safety engineering. This approach, used in performance-based design, brings new possibilities to fire safety design of the buildings, which would not be allowed to build according current prescriptive approach or they would require many fire safety appliances and the costs would be inadequate. Computer modelling is a powerful tool, however, it is still a tool only and it comes with several problems or disadvantages. Except others, the method needs a detailed and precise description of input parameters. The numerical solution also takes a lot of time and it demands a lot of computing power.

For pyrolysis and combustion modelling, fire-technical characteristics (FTCH) are the most important input parameters and its obtaining is not an easy task. This task has been a subject of research for many years. Input data for numerical modelling in terms of material pyrolysis properties are introduced in [1]. If we want to model the real-size environment, there are several attitudes, how FTCH can be obtained:

- The most precise values can be acquired from **large-scale experiments**. There is no problem with power and dimensions scaling during a full-scale experiment, on the other hand, it is time and money consuming and it might not match every model application. General characteristic (the “final” characteristics respectively) can be obtained.
- **Intermediate- or small-scale experiments** are much cheaper and it is possible to run series of them to obtain mean values. But there is a question, whether the values are size independent or whether the FTCH must be modified when used on a bigger model object. Again, the “final” characteristics can be obtained.
- Completely different attitude is used with **molecular-scale experiments**. Such experiments give very good knowledge about decay and pyrolysis and those values are size-independent. On the other hand, it is not the final FTCH and the modelling software has to compute the reaction with given data in every cell in every time step and it protracts the computation. This method, as it will be mentioned lower, is almost impossible to run in real-scale building applications.

This paper deals with an optimizing the input phase of fire modelling and it analyses the possibility of using combination of small- and molecular-scale experiments to obtain the “final” characteristics. The goal of the research is to acquire data that can be simplified to a CFD code as a one-reaction material property: so it would be able to simulate heat effect of the wood without direct description of HRR and without need of combustion parameters and setting the reaction, so it can be extinguished, for example.

Series of experiments were performed and then the FDS model of cone calorimeter was built where those values were used. The model was verified comparing the model HRR with the data from the real cone calorimeter experiment. All the experiments were performed with pine wood.

METHODS

For the numerical modelling purpose, the Fire Dynamics Simulator (FDS) was chosen. It is a solver based on finite volume calculation methods called Computational Fluid Dynamics (CFD). This open source software was first released in 2000. The solver itself does not have any user interface. The creation of a model required a knowledge of special FDS language code. For the purpose of preparation of the FDS model the commercial software (e.g. Pyrosim) can also be used. In this paper the basic FDS version 6.1.2 was used.

As well as there are several methods of obtaining FTCH, there are two methods, how to describe the pyrolysis and combustion in modelling software, namely FDS: Firstly, it is possible to use the “final” characteristics, such as HRR, on the object. This method does not require any additional computational time, on the other hand, directly entered HRR cannot react on the environmental changes (for example extinguishing effect of sprinklers). And secondly, it is possible to enter the complex pyrolysis data from molecular-scale experiments and model the pyrolysis and combustion. Because the combustion conditions are revised and computed in every cell and in every time step, it respects the environment, but it is vastly time-consuming. The FDS model, which is described in this paper, covers a relatively small computational space. In the space there are applied as many of elementary attributes as possible in order to calculate temperature analysis of pine wood with high level of accuracy. First of all, the geometry of the model was built. After that heating conditions of the model as well as the material properties were determined.

COMPOSITION OF WOOD AND BURNING OF WOOD

The main goal of conducted small-scale experiments was to determine as many elementary attributes as possible. For the simulation purpose it is necessary to define a proper pyrolysis model which contains the material properties and the reaction of combustion solids. Both of these attributes contribute to burning process of solids in the FDS.

Material properties define the speed and intensity of reaction which the material undergoes during the heating. After building up a geometry and defining the heating condition of the model it is necessary to determine composition of the materials. Wood is highly complex biopolymer material. Biopolymer substances, often in literature described as the main building elements of the wood, cover 90–97 %. Cellulose and hemicellulose stands for approximately 70 % of this main substance. Approximately 30 % of total mass consists of substance called lignin. The other substances are described as accompanying substances, e.g. waxes, tannins, minerals etc. [2]. For modelling purposes, it is ideal to define as many substances as possible in one material.

Every substance in wood has its own function and exhibits unique behaviour during the heating. In a microscopic level the wood is created by the cell walls. Function of the main elements can be likened to concrete. Basic structural component which creates a frame of the cell is cellulose. In concrete analogy it can be compared to aggregates. Hemicelluloses is often likened to a cementing material, which holds the frames together. There are many different types of hemicelluloses. Some of them are very flammable and some of them are not. In general, it can be said that hemicelluloses are greatly contributing to fire development. The last major substance is lignin. It can be likened to an accompanying substance in concrete analogy which is surrounding and strengthening the cells [3]. Lignin consists of mutually connected benzene rings. In other words, it is created mostly from incombustible carbon. From the fire engineering point of view, the very interesting fact is that lignin contributes to the creation of protecting char layer greatly during the heating process.

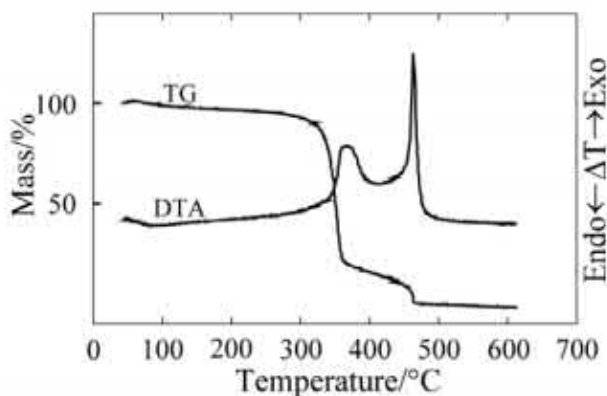


Fig. 1 - Thermal analysis of cellulose in air [4]

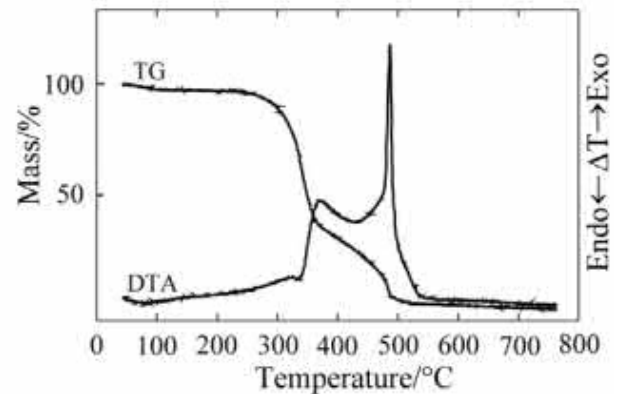


Fig. 2 - Thermal analysis of wood in air [4]

Despite of “inflammable” lignin the wood is still considered as combustible material because it contains high amount of extremely flammable cellulose. Figures 1 and 2 describe the data from thermogravimetric analysis (TGA). The TG curve shows the function of mass loss of cellulose and wood exposed to elevated temperature. As shown, fire behaviour of the cellulose in TGA is very similar to the wood behaviour. The differential thermal analysis (DTA) curve is the first derivation of the TG curve. It describes the momentary speed of mass loss reaction with elevated temperature.

When cellulose was tested (Figure 1), the first mass loss is found around 100 °C and it can be connected with evaporation of bound water, where about 10 % of original mass was lost. First

exothermic peak is found at temperature around 350 °C (around 70 % of mass loss). This thermal degradation is associated to oxidation of cellulose into laevoglucosan, water carbon monoxide and carbon dioxide. The last peak around 450 °C (around 10 % of mass loss) represents breaking carbon-carbon bonds [5, 6]. Although the wood contains many different kinds of substances, it depends mostly on the combustion of cellulose and the main mass loss and energy release is found around 350 °C, when cellulose is decomposed. This finding is used further in FDS modelling, where the wood is viewed as single-component single-reaction material with water in the form of moisture.

MATERIAL PROPERTIES BASED ON EXPERIMENTS

It is necessary to assign detailed material properties to all obstacles in the FDS model. Required data were obtained by performing an elemental analysis of pine wood. The sample material was grinded to a very fine powder in a laboratory of fuel analysis at University of Chemistry and Technology in Prague (UCT). The sample used for an experiment was thoroughly chosen as it was required not to have any defects such as knags etc.

After grinding the sample, the humidity test was performed. The result was 7,76 % of the mass. The heat of combustion test was the next small-scale experiment performed in the laboratory. Data obtained from this experiment belong to the main FTCH which affects the total burning intensity in the model. Performed experiment provided the heat of combustion value of 16,94 MJ·kg⁻¹. This value is very similar to the one specified in the Czech technical standard ČSN 73 0824 [7]. The value of the heat of combustion of the pine wood equals here to 17,00 MJ·kg⁻¹. However, this value cannot be used for model purposes as it does not correspond to a real situation. The measured value is so called “net heat of combustion” and can be achieved only in laboratory conditions when all the sample materials including the carbon rests and other products of burning are burned down. In real situation as well as during the cone calorimetry test a great amount of energy stays unused. This type of heat reaction is called “effective heat of combustion”. This value depends on the process of heating of the material and it can be obtained by performing cone calorimetry experiment. The effective heat of combustion value obtained from cone calorimeter was 11,41 MJ·kg⁻¹. Heat flow used in this experiment was 35 kW·m⁻². The model simulation was performed twice – using net heat of combustion value and value of effective heat of combustion.

Tab. 1 - Entered heat of combustion to the model

Heat of combustion			
Type of experiment	TÚPO Cone Calorimeter 35 kW·m ⁻²	UCT Prague Bomb Calorimeter IKA C200	ČSN Standard value [7]
Value [MJ·kg ⁻¹]	11,41	16,94	17,00

The other part of the grinded sample was conserved and sent to the laboratory for performing elemental analysis. This experiment covers all the combustible sulphur – both organic and inorganic – as well as organic and inorganic carbon. Analysis is performed with a very small amount of the sample. Maximum weighted amount for the Elementar Vario apparatus is 5 mg. The results of this analysis are shown in the Table 2.

Tab. 2 - Results of elemental analysis

Sample	Amount (mg)	% N	% C	% S	% H
E 1 - CVUT	3,114	-	47,400	-	6,477
E 2 - CVUT	4,047	-	47,340	-	6,508
E 3 - CVUT	4,149	-	47,250	-	6,551

Results show that there is neither nitrogen nor sulphur in any form in the sample material. Content of hydrogen is variable depending on the humidity of sample material. The average value of hydrogen is 6,512 %. Carbon is highly represented in the wood as it is the main unit of all wood components (e.g. cellulose). Average carbon content is 47,330 %. The rest is oxygen. Content of this element is 46,158 %. Data obtained during elemental analysis were used for checking the chemical formula of pine wood which can be found in literature. Chemical formula of pine wood is $CH_{1,7}O_{0,83}$ [8]. Ratio between the pine wood mass and water moisture was specified to 92,2:7,8. Specific heat capacity, conductivity and density were specified for both of them [8].

Tab. 3 - Material properties

	Density [$kg \cdot m^{-3}$]	Specific heat capacity [$kJ \cdot kg^{-1} \cdot K^{-1}$]	Thermal conductivity [$W \cdot m^{-1} \cdot K^{-1}$]
Water	1000	4,18	0,6
Pine wood	520	2,5	0,2
Char layer	200	1,6	1

Determination of the appropriate thermal response was essential for creating the pyrolysis model. FDS solver is sufficient with the final products of combustion in material section, resp. in this section the percentage of material that is transformed to both non-combustible rest and to gas is specified.

In the model as well as in the real situation the solid material is not burnt. After heating above certain temperature, the material is degraded with heat without the access of oxygen (pyrolysis). Material structure is changed in this process. The carbon bonds in main material component are disrupted. Cellulose macromolecules are shortened and during this process flammable substance are produced. A good example is an unstable compound of laevoglucosan. Gas and solid ratio is essential for model situation as it determines the amount of fuel which is then changed to thermal energy and therefore to HRR. The gas and solid ratio was found by simple experiment which was performed in the Technical Institute of Fire Protection in Prague (TÚPO). The sample was weighted, completely burnt down and then weighted again. There were two samples examined in the test. Results are shown in the following Table 4.

Tab. 4 - Weight of samples before and after burning

	Unit	Experiment nr. 1	Experiment nr. 2
Weight of sample	g	21,7	18,92
Weight of residue	g	3,32	2,71
Weight difference	g	18,38	16,21

Weight difference was 84,7 %. This measurement was also a part of experiment called Analysis of Combustion Products which is described in the other part of this article.

Thermogravimetric analysis

Except the final products of pyrolysis, it is necessary to define the process of the reaction. In other words, to define the temperature and reaction rate when the material is transformed. These variables can be defined with coefficient based on Arrhenius equation. This equation describes the relationship between the reaction temperature and the reaction rate. Generally, the higher the temperature is, the higher the reaction rate is. These variables can be used in FDS code in two ways.

The first way covers the direct use of both variables in the code. They can be calculated from the following formulas [8]:

$$E_{i,1} = \frac{e r_{p,i}}{Y_{s,i}(0)} \frac{R T_{p,i}^2}{\dot{T}} \quad ; \quad A_{i,1} = \frac{e r_{p,i}}{Y_{s,i}(0)} e^{E/RT_{p,i}} \quad (1); (2)$$

where $r_{p,i}/Y_{s,i}(0)$ is the reference rate of reaction, the R factor expresses the molar gas constant and $T_{p,i}$ stands for the reference temperature of chemical reaction.

All the unknown variables can be found out during the thermogravimetric analysis (TGA) experiment. Parameter \dot{T} describes the rising rate of temperature in the furnace.

Another way of defining the kinetic parameters is a straight assigning of the above mentioned parameters from TGA. FDS solver is able to calculate these kinetic parameters. This data should be given for each pyrolysis reaction. Each material in FDS can undergo only one reaction. If there are two materials defined (pine wood and water), two pairs of kinetic parameters have to be defined in FDS. Results of thermogravimetric analysis, which was carried out with TG-DTA thermal analyser Setaram Setsys Evolution in Laboratory of Thermal-Gravimetric Analysis (TGA), UCT Prague, are shown in the following graph.

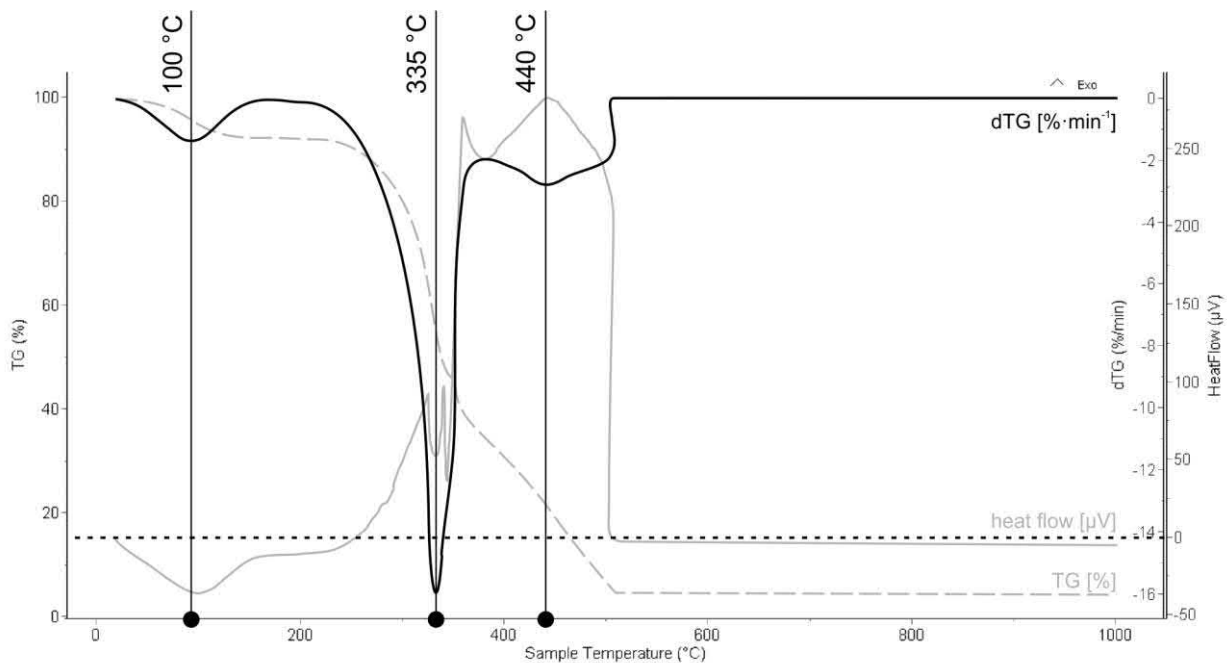


Fig. 3 - TGA data of pine wood

The dashed curve represents the decrease of weight of the tested sample. The decrease of weight depends on the temperature rise. The rise was $5 \text{ K} \cdot \text{min}^{-1}$ (\dot{T}). The black full curve represents the rate of weight decrease depending on the temperature. The grey full curve represents the heat flow produced by the material during the experiment. From the results of thermogravimetric analysis it is possible to identify how many reactions the material undergoes during heating. The decrease of curve means a reaction. When the temperature reaches $100 \text{ }^\circ\text{C}$, the material undergoes the first reaction dehydration – evaporation of unbound water. Another reaction comes at $335 \text{ }^\circ\text{C}$ (another curve decrease), which represents the cellulose and other wood components degradation. The third decrease comes at $440 \text{ }^\circ\text{C}$ and this is the final degradation of lignin. Reference temperatures ($T_{p,i}$) used in FDS model are $100 \text{ }^\circ\text{C}$ for water and $335 \text{ }^\circ\text{C}$ for pine wood. Material consists of two components and so the temperature $442 \text{ }^\circ\text{C}$ was not used in the FDS model. Also the intensity of

reaction is very important. This can also be read from the graph. This value can be found at the top of the curve. Water reaction intensity is $0,00033 \text{ s}^{-1}$, pine wood reaction intensity $0,00267 \text{ s}^{-1}$ and charring reaction intensity is $0,00036 \text{ s}^{-1}$.

REACTION OF COMBUSTION BASED ON EXPERIMENTS

Although wood combustion might look like one complex process in the real life situation, it is actually a mixture of two processes: pyrolysis and combustion. Pyrolysis is the process of solid state decomposition to various gases; combustion, on the other hand, is burning of those flammable gases. In the FDS, those two processes must be distinguished and separately entered. In presented proposal, the pyrolysis is described with stoichiometric equation with values of both reactants and products. To get this equation, it is necessary to explicitly define the chemical reaction of combustion. This equation determines the combustion intensity of the elements that has been created during the combustion process.

Analysis of combustion products

The chemical reaction of combustion which is essential for accurate modelling cannot be made without the knowledge of stoichiometry ratios of combustion products. The analysis to determine the stoichiometry ratio was held in TÚPO.

For the experiment, the smoke chamber which corresponds to the requirements of ISO 5659-2 [10] was used. There were two test samples of pine wood. The smoke chamber is completely airtight and its total volume is 509 litres of air. The cone calorimeter is placed inside this chamber. Its total possible heat flux output is 50 kWm^{-2} . Principle of the experiment is following: the heat flux from the cone emitter falls on the surface of the sample. Due to high amount of thermal radiation the sample completely burns out. The products of combustion are caught in the smoke chamber. After creating the maximum concentration of combustion products, the analysis is performed. Results of the analysis of combustion products are shown in the Table 5.

Tab. 5 - Results of analysis of combustion products

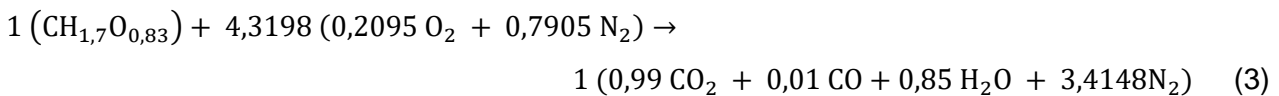
Compound	$\text{mg} \cdot \text{g}_{\text{sample}}^{-1}$	Percentage [%]
CO	12,3	0,8706
NO	0,2	0,0142
CO ₂	1400	99,0898
NO ₂	0,02	0,0014
SO ₂	0,1	0,0071
VOC*	0,24	0,0170

* VOC (Volatile Organic Compounds).

The carbon dioxide (CO₂) was the most produced compound. Other compounds are represented in a small amount of the whole combustion products. The second most represented compound was carbon monoxide (CO). Other inorganics components in fumes are insignificant. In spite of elemental analysis, there were also detected products based on sulphur in the sample in smoke chamber. However, the amount of sulphur dioxide is minimal and it does not have to be included in the CFD code. Moreover, this difference, or error respectively, may be probably at the side of the elemental analysis due to used procedure and measurement errors.

Equation of burning

Chemical equation can be divided into three parts. Firstly, it is the reactants (pine) itself. Chemical equation of the pine wood is $CH_{1,7}O_{0,83}$ [8]. Burning is the reaction of reactant with air. There is roughly 79,05 % of nitrogen (N_2) and 20,95 % of oxygen (O_2). Other components of air can be neglected. The last part of the equation is the product of combustion. Due to the ratio known from the Analysis of combustion products it was further worked with only two most represented compounds carbon dioxide and carbon monoxide (CO_2 , CO). During combustion there is also the leakage of water vapour. It is necessary to enter the stoichiometry of combustion products as well as quantification of chemical equation into FDS. The balance equation of combustion which is used in the FDS is following:



Heat of reaction, heat of combustion

Together with the balance equation which defines the process of combustion, it is necessary to determine an amount of heat released during the exothermic reaction. This parameter is defined by the heat of combustion. The total amount of heat that needs to be added to the system in order to cause exothermic reaction has to be defined as well. This parameter directly influences the time of ignition in the model and it is called the heat of reaction. It is possible to calculate the heat of reaction from the following picture.

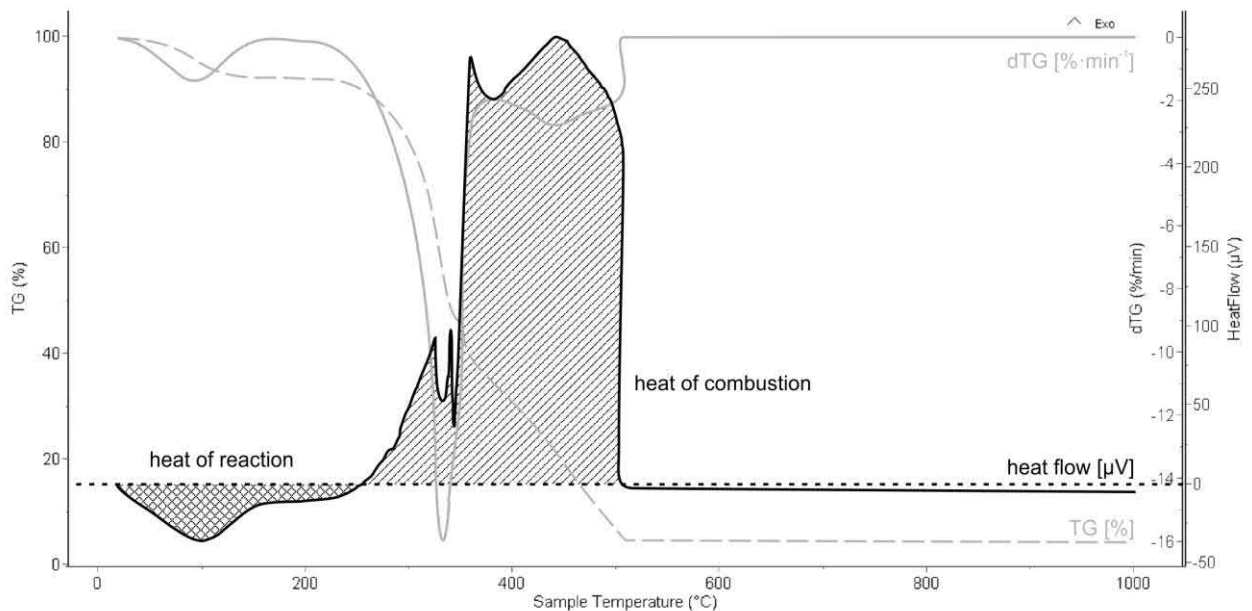


Fig. 4 - Graphical difference between the heat of reaction and the heat of combustion (pine)

From the ratio of areas below and above the curve of heat flow, the heat of reaction has been calculated. Boundary conditions were determined by interface between endothermic reaction and the exothermic one. The reaction is exothermic if the curve is rising.

FDS MODELLING AND COMPARISON OF RESULTS

From all performed experiments, simplified burning of wood setup for FDS was prepared [9]. As mentioned before, both processes (pyrolysis and combustion) and other related entities had to be entered.

Firstly, a material properties of sample were defined. The pine SURF line of the FDS code was due to moisture composed from pine and water in ratio 93:7. Water MATL line was copied from validated examples and it was used only to remove heat as it would be in the real situation. Pine MATL line is a little bit more complicated and used material properties such as density, specific heat or conductivity either from analyses or from literature.

Then, on the same line, the pyrolysis was described forcing the pine to decompose in one reaction into one solid product, char, and one gaseous product, namely pyrolyzate. Char residue covers 15,3 % of the material corresponding results from analysis of combustion products. The reaction is started at reference temperature of 355 °C (main peak of DTA). Other values describing TGA-DTA experiment, reference rate (0,00267 s⁻¹) and heating rate (5 K·min⁻¹) were also entered. Last input in the pine MATL line was heat of reaction (1047 J·g⁻¹), which was computed from the ratio between assumed heat of reaction and heat of combustion acquired from TGA-DTA (see Figure 4) and from the value of effective heat of combustion.

The gaseous pyrolyzate then undergoes the combustion reaction defined in the REAC line and the stoichiometric equation set from combustion analysis (described in the previous chapter) was used. The agents of reaction were PYROLYZATE, AIR and PRODUCTS only, and compositions of those agents were defined in particular SPEC lines as lumped components. In the AIR, only oxygen (0,2095) and nitrogen (0,7905) were defined. Volume fractions of PRODUCTS correspond the chemical combustion analysis results (see Table 5).

For the purpose of numerical modelling a simplified model of cone calorimeter was created. Only parts that were necessary for measuring of HRR were modelled – the conical emitter and the tested item. For both parts a very fine mesh is used. Dimensions of one cell are 10 mm x 10 mm x 10 mm. Coarser part of the model has dimensions of cells of 20 mm x 20 mm x 40 mm. In the coarser mesh there is a part of hood used for catching the combustion products. Total number of cells does not exceed 4 736. The model simulates thermal conditions in real cone calorimeter, heat flux of 35 kW·m⁻² hits the element of size 10 cm x 10 cm x 1 cm. All boundaries of the model space were defined as OPEN, except the exhausting hood in the upper part. The surface of the hood was modelled as a thin steel plate.

The cone of the calorimeter was entered as a set of obstructions that create a pyramidal object. It was made of solid obstructions representing both the steel hood and the source of radiation. The radiation was entered as VENTs with TMP_FRONT = 1553 °C. This temperature is slightly higher than in the real cone calorimeter at TÚPO (around 1400 °C), because VENTs were put only on the bottom surface in the simplified model. The temperature was therefore raised to ensure the required heat flux on the sample surface.

The calculation was performed twice, each with a different heat of combustion (see Table). The Model 1 uses the net heat of combustion (16,94 MJ·kg⁻¹) and the Model 2 includes a value of the effective heat of combustion (11,41 MJ·kg⁻¹). Both models are compared and validated to the experimental measurements.

Values of the heat of combustion are very different. The heat of combustion together with the heat of reaction are the most important FTCH. Both values have significant effect on final HRR process of the material for their indication of the energy amount used in endothermic reaction and produced in exothermic reaction.

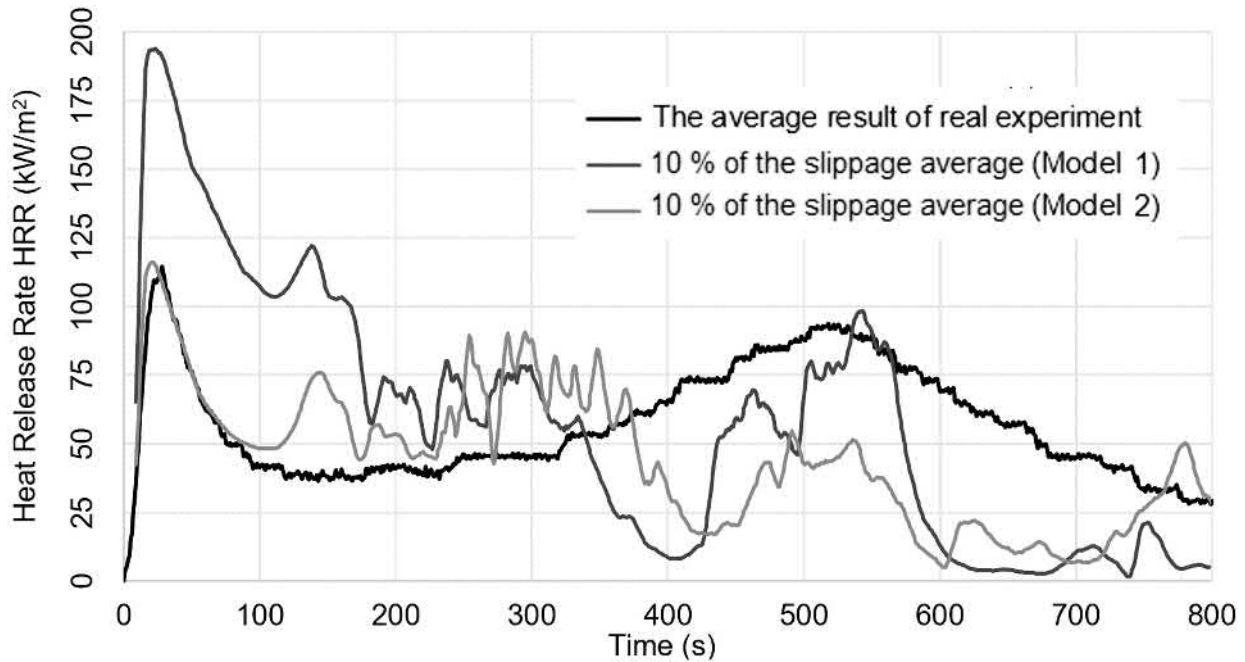


Fig. 5 - Comparison of results

The graph shows the development of HRR in time. The black curve represents the real experiment. There are two peaks. Following Table 6 shows a comparison of real experiment data and data from the model.

Tab. 6 - Comparison of the experimental results and results from the model

		Experiment 35 kWm ⁻²	Model 1	Model 2
Ignition	[s]	90	170	180
	[°C]	440	408	402
1. peak HRR	[s]	28	22	24
	[kW·m ⁻²]	114,59	195,44	120,00
2. peak HRR	[s]	518	Not observed	295
	[kW·m ⁻²]	89,0	Not observed	93,7

The Model 2, which uses effective heat of combustion, is closer to the real experimental data. In both cases the ignition comes at the third minute of the simulation. The difference between this and a real cone calorimeter experiment (90 seconds) is due to the fact of using a spark for easier ignition of the element. In the real experiment, the time of ignition was measured while in the model situation the time of auto ignition was observed. The final peak of HRR in the Model 2 corresponds quite accurately to the real experiment data. In contrast, the Model 1, which uses the net heat of combustion, shows higher values in comparison to the real cone calorimeter experiment.

The difference between these two curves is mainly due to the different ways of burning off the model and the real situation. The first peak, which was very accurately simulated, occurs during the thermal decomposition of the central part of the element. After burning out of the middle section flame moves to the outer parts where the pyrolysis was already held before. Burning off all the outer parts at once creates the second peak.

There is a significant charred part in the middle of the sample. This already degraded part is surrounded by flames burning the outer parts of this sample. As explained above, this is the situation when model does not correspond to the real experiment. There is no gradual expansion of the flame on the element surface. The flame moves randomly on the model – at the first one corner burns and then the other. Fluctuations in HRR values are therefore caused by an incorrect flame spread on the surface of the sample.

CONCLUSION

The goal was to create very simple model of wood burning using results from cheap and fast small-scale experiments that could be used in the CFD modelling programmes such as FDS. Purpose of research is to obtain a virtual material that would spread fire, develop the fire according to surrounding environment and that could be extinguished without using complex reaction molecular description. Small-scale experiments that were conducted were: elemental analysis, thermogravimetric analysis and difference thermal analysis, and combustion analysis.

In this paper, pine wood was used as the tested sample. The aim of the model was to compare HRR values to the real standard fire-technical experiment in the cone calorimeter. In the model the first peak of burning was achieved very accurately. Further development of HRR is different than HRR from the real experiment because of the difference in fire spread on the element's surface. Though, maximum HRR values are similar to the real ones.

It was verified that for the purpose of modelling the effective heat of combustion, which is one of the basic FTCH affecting the total intensity of burning, should be used. Using the net heat of combustion in the model leads to higher values of HRR in comparison to the real experiment data.

There are several things that can be improved in this model. Primarily it is necessary to work on flame spread on the surface of the material. It is also possible to upgrade the description of reaction in the pyrolysis model using coefficient from Arrhenius equation. More wood components can also be defined. The sample element would not consist only of water (as moisture) and pine wood mass but also of lignin, cellulose, hemicellulose and water. For definition of the chemical reaction of burning for all these substances, it would be necessary to perform a number of other small-size experiments (thermogravimetric analysis) that should provide more information about their behaviour during heating.

Considering all the results shown in this paper, it was shown that when adjusting the model as mentioned above, it can be possible to simulate burning of wood using the extrapolated data obtained in small-size experiments.

An adjusting of the model can be a further option in continuing in this work thus appear. Another very important thing is also using the effective heat of combustion in fire engineering practice. This could be certainly used in determining the standoff distances from the buildings, especially from wooden structures and wooden facades. These types of buildings are significantly disadvantaged because of the use of the net heat of combustion.

ACKNOWLEDGEMENTS

The work was supported by project n. 16-18448S, Grant Agency of the Czech Republic. Special acknowledgements go to Ing. Milan Růžička from TÚPO, Ing. David Bouška and Ing. Jakub Havlín, both from UCT.

REFERENCES

- [1] KIM, Mihyun Esther, Dembsey Nicholas. Engineering guide for estimating material pyrolysis for fire modelling. Worcester Polytechnic Institute, 2012.
- [2] GANDELOVÁ, Libuše, Petr HORÁČEK a Jarmila ŠLEZINGEROVÁ. Nauka o dřevě. Vyd. 2. Brno: Mendelova zemědělská a lesnická univerzita, 2002. ISBN 8071575771.
- [3] HIGUCHI, Takayoshi. Biosynthesis and biodegradation of wood components. Orlando: Academic Press, 1985. ISBN 0123478804.
- [4] GAO, Ming, Caiyun SUN and Kai ZHU. Thermal degradation of wood treated with guanidine compounds in air: Flammability study. Journal of Thermal Analysis and Calorimetry [online]. 2004, vol. 75, no. 1, s. 221-232. ISSN 1388-6150.
- [5] AGGARWALL, P. and D. DOLLIMORE. A thermal analysis investigation of partially hydrolyzed starch. Thermochemica Acta, 319, 17-25, 1998.
- [6] SHEN, Dekui, Xiao RUI, Gu SAI and Huiyan ZHANG. The Overview of Thermal Decomposition of Cellulose in Lignocellulosic Biomass. Cellulose-Biomass Conversion. InTech. 2013. ISBN 978-953-51-1172-6
- [7] ČSN 73 0824. *Požární bezpečnost staveb - Výchřevnost hořlavých látek*. Praha: Úřad pro technickou normalizaci, metrologii a státní zkušebnictví, 1992.
- [8] BABRAUSKAS, Vytenis. *SFPE handbook of fire protection engineering* [online]. Sage Publications, Inc, 2016. 164 s. ISBN 0734-9041.
- [9] MCGRATTAN, K. et al. Fire Dynamics Simulator User's Guide. Sixth Edition. NIST - National Institute of Standards and Technology, VTT - Technical Research Centre of Finland. Also available: <http://firemodels.github.io/fds-smv/>
- [10] ISO 5659-2. *Plastics -- Smoke generation -- Part 2: Determination of optical density by a single-chamber test*. Geneva: International Organization for Standardization. 2017.

RELATIONSHIP BETWEEN FOAMING BEHAVIOR AND SURFACE ENERGY OF ASPHALT BINDER

Jian-ping Xu^{1,2}, Kai Zhang³ and Yao-ting Zhu³

1. *College of Traffic and Transportation, Chongqing Jiaotong University, Chongqing, No. 66 university avenue, nankiang district, China; 318661112@qq.com*
2. *Jiangxi Provincial Expressway Investment Group Co.Ltd, Nanchang, No. 367 chaoyang road, China*
3. *Department of Road and Material, Jiangxi Transportation Institute, Nanchang, No. 809 sands avenue, China; kaizhang@whut.edu.cn, 12322756@qq.com*

ABSTRACT

To solve the problem of insufficiency in microscopic performance of foamed asphalt binder, surface energy theory was utilized to analyze the foaming behavior and wettability of asphalt binder. Based on the surface energy theory, the Wilhelmy plate method and universal sorption device method were employed to measure the surface energy components of asphalt binders and aggregates, respectively. Combined with the traditional evaluation indicator for foamed asphalt, the relationship between the foaming property and surface energy of asphalt binder was analyzed. According to the surface energy components, the wettability of asphalt binder to aggregate was calculated to verify the performance of foamed asphalt mixture. Results indicate that the foaming behavior of asphalt will be influenced by surface energy, which will increase with the decline of surface energy. In addition, the surface energy of asphalt binder significantly influences the wettability of asphalt binder to aggregates. Meanwhile, there is an inversely proportional relationship between surface energy of asphalt binder and wettability. Therefore, it can be demonstrated that surface energy is a good indicator which can be used to evaluate the foaming behavior of the asphalt binder. And it is suggested to choose the asphalt binder with lower surface energy in the process of design of foamed asphalt mixture.

KEYWORDS

Foamed asphalt mixture, Surface energy theory, Foaming behavior, Surface energy, Wettability

INTRODUCTION

As a stabilizer and regenerative, foamed asphalt has extremely wide applicability. In many countries, foamed asphalt technology has been used for road substrate materials (including recycled asphalt mixture). Foamed asphalt for cold recycling technology can not only solve the stacking problem of asphalt recycling material (RAP), which is conducive to protecting the environment and saving energy, but also has less impact on the environment in the construction process [1~2]. In the application process of foamed asphalt technology, the foaming property of the asphalt binder directly influences on the performance of the foamed asphalt mixture [3]. A good foaming performance can obviously improve the mechanics and road performance of cold recycled asphalt mixture [4~5]. Therefore, it is necessary to carry out in-depth research and analysis on the foaming performance of asphalt in the study of cold recycled asphalt pavement.

At present, the characteristics of foamed asphalt can be characterized by the expansion rate (ER) and half-life (HL), which can be mainly affected by many factors [6~7]. Meanwhile, many researches have been conducted for foaming property of asphalt at home and abroad. Brennen et al. studied the influence of water content and temperature on expansion rate and half-life [8]. Maccarone et al. used the additive agent to improve the foaming performance of foamed asphalt [9]. Yang et al. discussed the effect of viscosity on the performance of asphalt foaming in terms of main indicators of asphalt [10]. It can be seen that researches on the performance of asphalt foaming mainly focused on the external influencing factors, such as temperature, water content, additive, without the in-depth conducting of microscopic performance analysis. In addition, based on the macroscopic nature of asphalt binder, a few researches have shown that foaming performance mainly depends on the components of asphalt binder [11~13]. However, different categories of asphalt have different internal components, so that it is hard to accurately judge advantages and disadvantages of asphalt foaming in terms of the main technical indexes of asphalt [14~15]. Based on the foaming mechanism of asphalt, the foaming process is a kind of surface physical chemistry which can mainly divided into four consecutive stages including cooling, expansion, film-formation and metastability. These series of surface physical chemistry are the keys to promote the foaming of asphalt binder. Meanwhile, grasping the foam stability of asphalt is an effective way to improve the foaming property of asphalt and road performance of foamed asphalt mixture. In addition, how to use surface energy of the asphalt binder to evaluate the performance of foamed asphalt mixture is another key issue in this study.

As the basis of surface physical chemistry theory, surface energy theory is widely used in many important fields, which can well explain the physical chemistry on surface or interface of materials [16~17]. Meanwhile, the property of surface expansion and contraction of materials can be accurately characterized through surface energy which is a subsistent contraction force on the surface of a material. Therefore, the purpose of this paper is to utilize the surface energy theory to analyze the relationship between the foaming performance and surface energy of asphalt binder, with reasonably forecasting the foaming performance of asphalt binder through conducting foaming test and Wilhelmy plate method. Finally, the wettability of asphalt binder to aggregate was used to verify the performance of foamed asphalt mixture based on the relationship between the foaming performance and surface energy of asphalt binder.

FOAMING PERFORMANCE OF ASPHALT

Materials

In this study, 4 kinds of representative asphalt binders were used to manufacture foamed asphalt. According to standard test methods of bitumen and bituminous mixtures for highway engineering [18], the main indexes of asphalt were measured, as shown in Table 1.

Tab. 1 - Results of indexes test

Type	KLMY-70	Guo Chuang AH-70	SHELL-70	China Offshore AH-70	Requirement
Penetration (100g, 5s, 25°C) (0.1mm)	69.6	66	66.7	70.5	60-80
Ductility(5 cm/min, 5°C)(cm)	156	125	161	120	≥100
Softening Point (°C)	48.9	47.5	49.5	47.1	≥46

Theoretical limit for the water content

The influence of water on the foamed asphalt cold recycled pavement can be divided into two aspects: the effect on the foaming performance of asphalt; and the effect on the performance of foamed asphalt mixture. Firstly, the foaming process of asphalt is a series of physical reactions, including the following process:

- Thermal exchange occurs on the surface of hot asphalt and cold moisture droplets, accompanied by evaporation of water vapor.
- The steam bubbles are pressed into the continuous phase of the asphalt under a certain pressure to form asphalt foam.
- During the rapid expansion of the foam, the surface tension of the asphalt film is resisted with the vapor pressure. As the foam expands, the vapor pressure decreases gradually until it forms a balance with the surface tension. But if the steam bubble expands beyond the tensile limit of the asphalt during this process, the foam will burst.
- Due to the low thermal conductivity of asphalt and water, the asphalt foam can be maintained for several seconds, but the amount of bubbles formed during the foaming process is in a steady state and prone to burst.

Researches have shown that the increase of water content will reduce the HL and improve the ER [19~20], as shown in Figure 1. The limit of water content is decided by the intersection or the adjacent points of two curves to obtain the best foaming property.

Secondly, the limit of water content will significantly influence the performance of foamed asphalt mixture [21~22]. Excessive water content will affect the compaction effect and the strength of the mixture, so the appropriate amount of water must be determined during the mixing and compaction process to optimize the performance of the foamed asphalt mixture. As a medium, water provides a channel for the dispersion of foamed asphalt in aggregates. If the amount of water is too small, it will affect the uniform dispersion of the asphalt. If the water is too much, it will cause the debonding of asphalt from the surface of aggregates. Many researches have been conducted on the determination of the optimal water content for the foamed asphalt mixture [23]. Lee has studied the water content under different grades of foamed asphalt mixtures and found that there was an optimum water content for each mixture [24]. Meanwhile, the optimum water of mixture should be 65% to 85% of the corrected AASHTO optimum water content. Sakr has obtained the optimum water consumption formula (1) from the researches of different gradation asphalt mixture, with using the statistical methods [25].

$$MMC = 8.92 + 1.48OMC + 0.4PF - 0.39BC \quad (1)$$

Where MMC = the optimum water content; OMC = the corrected AASHTO optimum water content; PF = the mass fraction of fine aggregate; BC = asphalt content.

In addition, Wirtgen found the relationship between the optimum water content and the amount of water reduction, as shown in formula (2). For the purpose of optimum mixing, the water content can be calculated according to Equation (2). Subsequently, the quality of the water to be added is calculated according to Equation (3).

$$w_{add} = w_{OMC} - w_{moist} - w_{reduce} \quad (2)$$

$$m_{water} = \frac{w_{add}}{100} \times (m_{aggregate} + m_{cement}) \quad (3)$$

Where w_{add} = added water consumption in the aggregate; w_{OMC} = the optimum water content; w_{moist} = water content in the aggregate; w_{reduce} = reduction of water; m_{water} = mass of the water; $m_{aggregate}$ = dry mass of the aggregate; m_{cement} = quality of cement.

At present, few researches are aimed to address the optimum water content in foamed asphalt and its mixture [23]. There are no relevant conclusions according to the range of water content. Therefore, this paper will determine the optimum water content in the foamed asphalt and its mixture through the follow-up performance test.

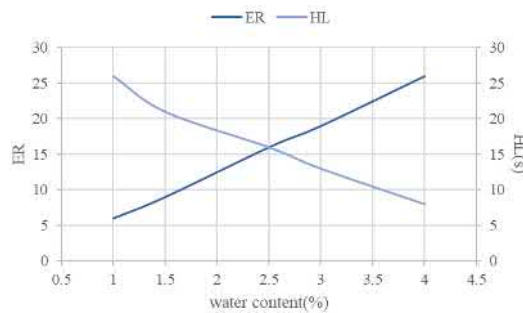


Fig. 1 - Determination method of water content for the best foaming property

Foaming test

According to the physical facilities of asphalt foaming applied in the engineering, the small equipment was employed in this study, called Wirtgen WLB 10S made in Germany, shown in Figure 2. During the process of foaming, the foaming temperature was 165°C and the water consumption was 2.5%. Meanwhile, the environment conditions such as temperature, relative humidity, water pressure, air pressure were controlled for 20 °C, 83%, 0.4 MPa and 0.55 MPa, respectively. The results of asphalt foaming tests were shown in Table 2.



(a) Asphalt foaming device



(b) Foamed asphalt

Fig. 2 - Foaming test

Tab. 2 - Results of asphalt foaming tests

Type							
KLMY-70		Guo Chuang AH-70		SHELL-70		China Offshore AH-70	
Expansion rate (%)	Half-life (s)	Expansion rate (%)	Half-life (s)	Expansion rate (%)	Half-life (s)	Expansion rate (%)	Half-life (s)
11.7	11.8	12.0	10.9	8.2	10.5	10.9	12.7

Generally, the ER and HL are used to evaluate the performance of foamed asphalt. On the one hand, the greater ER is in favor of sufficient contact and coating between foamed asphalt and aggregates. On the other hand, the longer HL can promote the mixing effect between foamed asphalt and aggregates. Generally speaking, the great expansion and long half-life can ensure good foaming property of asphalt [26~27]. Therefore, as seen in Table 2, under the same test conditions, the sequence of foaming performance for various types of asphalt was China Offshore AH-70> KLMY-70> Guo Chuang AH-70> SHELL-70.

SURFACE ENERGY THEORY

In a vacuum, there is a kind of force occurred on the material surface, which is used to balance the internal and external force, called surface energy and denoted by the Greek letter γ [28]. The surface energy of any material is mainly composed of two parts which respectively are the non-polar van der Waals component (LW) and polar acid-base component (AB), and can be represented by the formula (4):

$$\gamma = \gamma^{LW} + \gamma^{AB} = \gamma^{LW} + 2\sqrt{\gamma^+ \gamma^-} \quad (4)$$

Where γ^{LW} = Lifshitz-van der Waals component; γ^{AB} = acid-base component; γ^+ = Lewis acid component; γ^- = Lewis base component.

Simply put, the foaming of asphalt binder is mainly due to the steam bubble pressed into the continuous phase of asphalt under the certain condition, causing the asphalt foam. At the same time, the expansion of compressed vapor will lead to form a kind of asphalt film which takes advantage of its own surface energy to coat the bubble. In the process of expansion, the surface energy of asphalt film will resist to steam pressure until a state of balance, namely metastable state.

Researchers considered that the reason caused the collapse of asphalt foam in the process of expansion is a pressure difference [29]. A bubble has a nearly stable gas cell like a cellular structure, both sides of which are foam film. When three or more bubbles gather each other, the Plateau boundary is formed due to the curved asphalt film and concaving toward the gas cell. At the Plateau junction consisted of multiple bubbles, the greater curvature radius will create the pressure difference between the gas phase and the liquid phase, as shown in the Laplace equation:

$$\Delta p = \frac{2\gamma}{r} \quad (5)$$

Where r = curvature radius.

The pressure difference between the gas phase and the liquid phase will decrease with the increase of curvature radius of bubbles, therefore the hydraulic pressure in the Plateau junction is less than the place which has a small curvature. Subsequently, the liquid will flow from the place with a small curvature to the Plateau boundary with a great curvature. In addition, the pressure difference will increase with the increase of surface energy. Similarly, the increase of surface energy will promote the flow of asphalt film towards the Plateau boundary. If the asphalt film becomes thinner and reaches a certain extent, usually is from 5 to 10nm for thickness, the foam of asphalt binder will fracture, as shown in Figure 3.

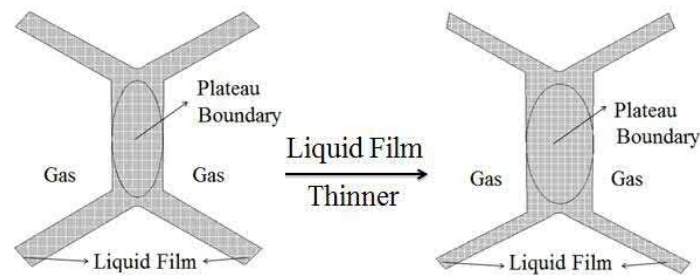


Fig. 3 - Micro structure of foamed asphalt binder

Generally, the increase of surface energy will force the fracture of asphalt foam, which is the disadvantage of property of foamed asphalt [16]. Therefore, it should be tried to choose the asphalt with lower surface energy during the preparation of foamed asphalt binder.

In addition, the better wetting property of asphalt to aggregate is more beneficial to promote the pavement performance of foamed asphalt mixture [30]. The formation of the wetting is a complex physical and chemical process. According to the surface energy theory, wettability refers to the ability of a material spreading on the surface of another material. For asphalt mixtures, a good wetting property of asphalt is favorable to wrap the aggregate and wet up the surface micro texture of aggregates, with improving the performance of asphalt mixtures. The appearance of the wetting mainly depends on the value of adhesion energy between foamed asphalt and aggregates and cohesion energy of foamed asphalt, respectively termed as W_{AB} and W_{BB} . Meanwhile, the wetting property of asphalt to aggregate can be expressed by formula (6) [31]:

$$R_s = W_{AB} - W_{BB} \tag{6}$$

Where R_s = wettability; W_{AB} = adhesion work between foamed asphalt and aggregates; W_{BB} = cohesion work of foamed asphalt.

The adhesion work is defined that when two materials are in touch with each other to form a new interface, the surface free energy of these materials will cause them to physically adhere to each other. Meanwhile, the work required to separate these two materials is defined as the adhesion work. Similarly, the cohesion energy occurs inside of the material. As a matter of fact, the adhesion energy and cohesion energy both are the results of molecular interaction, which can be described well by the surface energy theory. Finally, the adhesion work and cohesion work are explained by the formula (7) and (8), respectively [32].

$$W_{AB} = 2\sqrt{\gamma_A^{LW} \gamma_B^{LW}} + 2\sqrt{\gamma_A^+ \gamma_B^-} + 2\sqrt{\gamma_A^- \gamma_B^+} \tag{7}$$

$$W_{BB} = 2\gamma_B^{LW} + 4\sqrt{\gamma_B^+ \gamma_B^-} \tag{8}$$

Where γ_A^{LW} , γ_A^+ , and γ_A^- = surface energy components of aggregate; γ_B^{LW} , γ_B^+ , and γ_B^- = surface energy components of asphalt binder.

Generally speaking, when the cohesion work of asphalt is significantly greater than the adhesion between foamed asphalt and aggregates, the intermolecular forces in asphalt binder will be stronger than the acting force between asphalt and aggregate, leading to the reduction of the wetting property of asphalt to aggregate. However, when the cohesion work is significantly lower than the adhesion, good wetting effect will occur [33]. Subsequently, the performance of asphalt mixture will be improved obviously.

RELATIONSHIP BETWEEN THE FOAMING PERFORMANCE AND SURFACE ENERGY

Wilhelmy plate method

Based on Wilhelmy plate method, the automatic surface tensiometer was utilized to measure the surface energy components of asphalt binders, shown as in Figure 4. Based on kinetic force equilibrium, the Wilhelmy plate method can be described that when a glass slip uniformly coated with asphalt is immersed in a probe liquid solvent at a slow and constant speed of 20 μm/s, the stable and dynamic contact angle between the asphalt and the probe liquid is measured. Figure 5 shows the loading process of the glass slip. The following Equation (9) is used to calculate the contact angle from all the parameters that are determined during testing.

$$\cos \theta = \frac{\Delta F + V_{im}(\rho_L - \rho_{air}g)}{P_i \gamma_L} \quad (9)$$

Where ΔF = buoyancy difference between mass of a plate measured in air and partially immersed in a probe liquid; V_{im} = the volume immersed in the liquid; P_i = the perimeter of the bitumen coated plate surface; ρ_L = the density of the probe liquid; ρ_{air} = the air density; g = the local gravitational force; γ_L = the surface energy of the probe liquid.



Fig. 4 - Automatic surface tensiometer

Under the environment of 20 °C, place the glass slides coated with asphalt binder into the operating chamber and conduct the test, as shown in Figure 5. On the basis of the Young-Dupre and Good-van Oss-Chaudhury equation, the surface energy components of asphalt were obtained by using the following equation [34]:

$$\gamma_i(1 + \cos \theta) = 2\sqrt{\gamma_s^{LW} \gamma_i^{LW}} + 2\sqrt{\gamma_s^- \gamma_i^+} + 2\sqrt{\gamma_s^+ \gamma_i^-} \quad (10)$$

Where γ_s^{LW} 、 γ_s^+ 、 γ_s^- = three unknown components of surface energy; γ_i^{LW} 、 γ_i^+ 、 γ_i^- = surface energy components of probe liquid; γ_i = total surface energy of probe liquid; θ = the contact angle between the glass slip and the probe liquid.



(a) Asphalt sample

(b) Size measurement

(c) Measurement of contact angle

Fig. 5 - Wilhelmy plate method

Analysis of surface energy

To improve the test accuracy, four solvent liquids whose surface energies were known must be used to produce three simultaneous equations. Water, formamide, glycerin and ethanediol were used as probe liquid solvents, due to their relatively large surface energy, immiscibility with asphalt binder and differing surface energy components. The surface energy components of the four solvent liquids were listed in Table 3. According to the contact angles between the asphalt and the probe solvents, the surface energy components of the asphalt binders were calculated with Formula (7), shown as in Table 4. Figure 6 graphically illustrates the proportion of non-polar and polar component of surface energy.

Tab. 3 - Surface energies of solvents

Probe solvents	Surface energy components, (ergs/cm ²)				
	γ^{Total}	γ^{LW}	γ^+	γ^-	γ^{AB}
Distilled Water	72.8	21.8	25.5	25.5	51.0
Glycerin	64.0	34.0	3.92	57.4	30.0
Formamide	58.0	39.0	2.28	39.6	19.0
Ethanediol	48.0	29.0	1.92	47.0	19.0

Tab 4. Surface energy components of asphalt binders

Type	Surface energy components, (ergs/cm ²)					W^{BB}
	γ^{LW}	γ^+	γ^-	γ^{AB}	γ^{Total}	
KLMY-70	6.53	3.27	1.17	3.91	10.44	20.88
Guo Chuang AH-70	7.64	3.15	1.91	4.91	12.55	25.10
SHELL-70	12.17	2.19	0.79	2.63	14.80	29.60
China Offshore AH-70	6.71	4.50	0.64	3.39	10.10	20.20

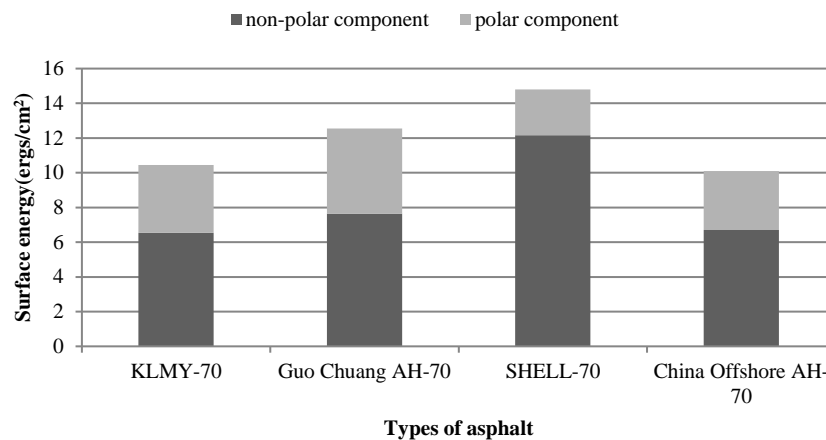


Fig. 6 - Surface energies of asphalt binders

Data in Figure 6 indicates that the order of the total surface energy of different asphalt binders is SHELL-70 > Guo Chuang AH-70 > KLMY-70 > China Offshore AH-70. The non-polar LW component of the total surface energy accounts for the largest proportion. Hence, the four materials present non-polar interaction on their surface. Moreover, according to the value of the polar acid and base composition, the surface of four kinds of asphalt mainly presents a polar base interaction, with showing acidic property in nature.

According to the influence of surface energy on foaming property of asphalt, it can be decided that the use of China Offshore AH-70 will improve the asphalt foaming and the mixing with aggregates, due to its lowest surface energy. Combined with the results of foaming test of asphalt, shown as in Table 2, the evaluation results for asphalt foaming property used surface energy theory have a good coincidence with the using of conventional method. It is reasonable to consider that the surface energy as a key index can be used to effectively evaluate the foaming property of the asphalt binder.

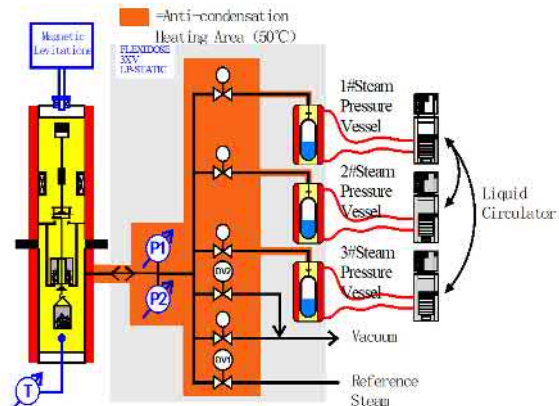
WETTABILITY OF FOAMED ASPHALT TO AGGREGATE

Measurement of surface energy components of aggregates

In this study, the surface energies of two kinds of aggregates were measured with the universal sorption device (USD) method by using the magnetic suspension weight analysis system, as shown in Figure 7. Similar to the calculation of surface energy components of the asphalt binder, the USD method utilized the gas adsorption characteristics of selected solvent, whose surface energy components were known, to indirectly measure the surface energy components of aggregates at 20 °C [35~36]. Table 5 shows the surface energy components of aggregates obtained in this study.



(a) Physical diagram



(b) Schematic diagram

Fig. 7 - Magnetic suspension weight analysis system

Tab. 5 - Surface energy components of aggregates

Type	Surface energy components, (ergs/cm ²)				
	γ^{LW}	γ^+	γ^-	γ^{AB}	γ^{Total}
Basalt	82.42	1.09	392.93	41.43	123.85
Granite	100.36	7.75	169.42	72.47	172.83

Analysis of wettability

Table 6 illustrates the adhesion work between asphalt binders and the selected aggregates. Subsequently, the wettability of asphalt binders to aggregates was calculated by using formula (3), shown as in Table 7. Figure 8 and 9 show the adhesion work between asphalt binders and aggregates and wettability of aggregates by asphalt binders, respectively.

Tab. 6 - Adhesion work between asphalt binders and the selected aggregates

Type	Adhesion work, (ergs/cm ²)			
	KLMY-70	Guo Chuang AH-70	SHELL-70	China Offshore AH-70
Basalt	120.38	123.44	118.43	132.80
Granite	104.30	109.28	107.37	111.58

Tab. 7 - Wettability Rs of asphalt to aggregates

Type	Wettability, (ergs/cm ²)			
	KLMY-70	Guo Chuang AH-70	SHELL-70	China Offshore AH-70
Basalt	99.50	98.34	88.83	112.6
Granite	83.42	84.18	77.77	91.39

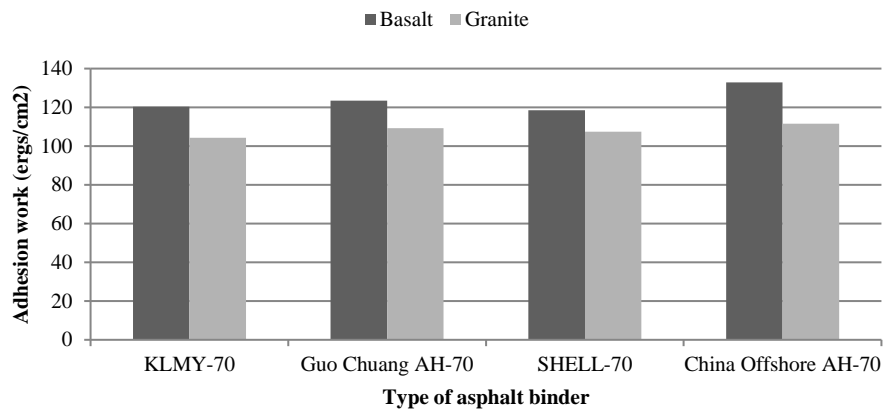


Fig. 8 - Adhesion work between asphalt binders and aggregates

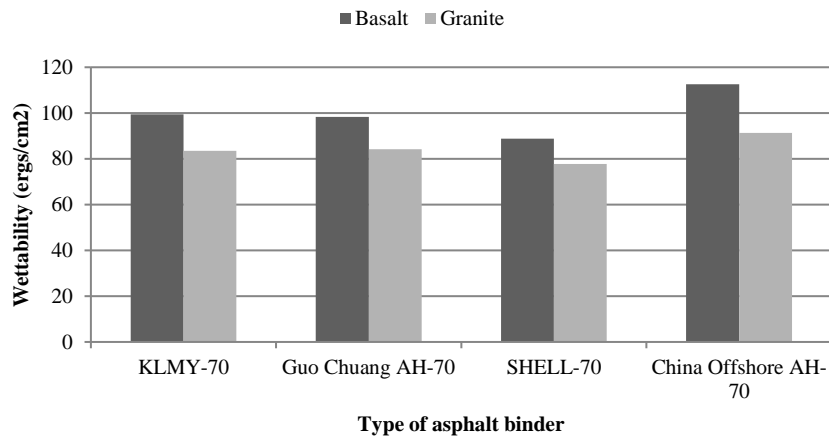


Fig. 9 - Wettability of aggregates by asphalt binders

As a very important factor in foamed asphalt mixture, the more positive the adhesive work, the better the bonding between asphalt binder and aggregate. It can be seen from the data in Figure 4 that compared with other asphalt binders, the asphalt binder of China Offshore AH-70 has greatest adhesion work with basalt. And compared with granite, the adhesion work between asphalt binders and basalt is greater. As noted above, good wettability is in favor of improving the pavement performance of foamed asphalt mixture. It can be observed from Figure 5 that the wettability of basalt by China Offshore AH-70 is greatest, which is the same as the results of adhesion work. The foamed asphalt mixture prepared by China Offshore AH-70 and basalt has the best performance in these combinations of mixtures.

Combined with the surface energies of asphalt binders, it is concluded that the lower the surface energy of asphalt binder, the better the foaming property of asphalt binder. During the process of calculation including adhesion work between asphalt binders and aggregates and cohesion work of asphalt binders, the lower surface energy facilitates the lower cohesion work of asphalt binder, which can improve the wettability of asphalt binder to aggregate. Therefore, for the foamed asphalt mixture, the surface energy of the asphalt binder not only can influence on the foaming property, but also has an impact on the wettability of asphalt binder to aggregate. In order to improve the foaming property of the asphalt binder and the pavement performance of foamed asphalt mixture, it should be suggested to choose the asphalt binder with the lower surface energy in the design process of foamed asphalt mixture.

CONCLUSIONS

This research focused on using a method to analyze the relationship between foaming behavior and surface energy of asphalt binder from a key point of view based on the influence of surface energy of asphalt binder on the foaming property and wettability of asphalt to aggregates. Based on the surface energy theory, the surface energy components of asphalt binders and aggregates were measured by utilized Wihelmy plate method and universal sorption device method, respectively. Subsequently, the surface energies of asphalt binders and wettability of asphalt binders to aggregates were calculated to evaluate and verify the property of foamed asphalt mixture, respectively.

The following conclusions can be drawn from the present research:

- Through mechanism analysis of foaming of the asphalt binder, it can be found that the surface energy will significantly influence the foaming property of asphalt. The lower the surface energy of selected asphalt binder, the greater the foaming property.
- Combining the expansion rate (ER) with the half-life (HL), it can be seen from the macroscopic perspective that the asphalt binder of China Offshore AH-70 has a greatest foaming property among four kinds of asphalt under the same experimental conditions.
- The calculation results of surface energies of asphalt binders demonstrate that the surface energy used to evaluate the foaming property has a good consistency with the indicators of expansion rate and half-life.
- Based on surface energy theory, surface energy as a good index can be used to effectively evaluate the foaming property of asphalt. Results of the traditional asphalt foaming test validated the results of the surface energy method.
- The surface energy of the asphalt binder significantly influences the wettability of asphalt binder to aggregate. Under a certain condition, there is an inversely proportional relationship between surface energy of the asphalt binder and wettability.
- To optimize the foaming behavior of asphalt binder and the pavement performance of foamed asphalt mixture, it is suggested to choose the asphalt binder with lower surface energy in the design process of foamed asphalt mixture.

This paper has a few limitations. The research is mainly based on surface energy theory to analyze the influence of surface energy on foaming behavior of asphalt and wettability of asphalt binder to aggregate. The performance test of mixture has not been conducted. In the future study, it is necessary to research the influence of surface energy of asphalt as well as the effects of water susceptibility and thereby the adhesion on the foamed asphalt mixture. In addition, a kind of approach based on the influence of surface energy method was developed to evaluate the asphalt foaming property and pavement performance of foamed asphalt mixture, which can provide the theoretical basis for the development of performance of foamed asphalt mixture.

ACKNOWLEDGEMENTS

The authors acknowledge the financial support of the National Natural Science Foundation of China (Project No. 51508246) and Jiangxi Provincial Science and Technology Support Program (Project No. 2013Y0005), which are sponsored by the National Natural Science Foundation of China and Transportation Department of Jiangxi Province, respectively.

STATEMENT

The authors declare that there is no conflict of interest regarding the publication of this paper.

REFERENCES

- [1] Ali, A., Abbas, A., Nazzal, M., Alhasan, A., Roy, A., Powers, D, 2013. Effect of Temperature Reduction, Foaming Water Content, and Aggregate Moisture Content on Performance of Foamed Warm Mix Asphalt. *Construction & Building Materials* 48(19): 1058-1066.
- [2] Babuin C., Palsat B., Clark E., Terness K., 2012. Falling Weight Deflectometer and Life Cycle Cost Analysis of A Major Urban Arterial Roadway Rehabilitated Using A Foamed Asphalt Stabilized Base: 57th Annual Conference of the Canadian Technical Asphalt Association, Vancouver, British Columbia.
- [3] Wozzuk A., Zofka A., Bandura L., Franus W., 2017. Effect of Zeolite Properties on Asphalt Foaming. *Construction & Building Materials* 139: 247-255.
- [4] Sunarjono S., 2012. Investigating Fatigue Performance on the Foamed Asphalt Specimens Generated Using Different Foam Properties. *Jurnal Transportasi* 12: 33-42.
- [5] Vaiana R., Luele T., Gallelli V., Tighe S.L., 2014. Warm Mix Asphalt by Water-Containing Methodology: A Laboratory Study on Workability Properties Versus Micro-Foaming Time. *Canadian Journal of Civil Engineering* 41(3): 183-190.
- [6] Ling T. Q., He L., Ma Y., 2009. A Cold Recycling Technique for Foamed Bitumen Mix. *Journal of Civil Architectural & Environmental Engineering* 31(1): 141-146.
- [7] He L., Wang Z., Ma Y., Ling T. Q., Huang X. M., 2010. Effect of Foaming Agent on Asphalt Foaming and Water Stability of Mixture. *Journal of Building Materials* 13: 198-202.
- [8] Fu P., Jones D, Harvey J. T., 2011. The Effects of Asphalt Binder and Granular Material Characteristics on Foamed Asphalt Mix Strength. *Construction & Building Materials* 25(2): 1093-1101.
- [9] Ozturk H. I., Kutay M. E., 2014. Effect of Foamed Binder Characteristics on Warm Mix Asphalt(Wma) Performance: 93th Transportation Research Board, Washington DC.
- [10] Yang H. R., He G. P., Han H. F., 2004. Effect of Bitumen Viscosity on Foamability. *Highway* 6: 107-112 .
- [11] Yan J., Zhu H., Zhang Z., Gao L., Charmot S. 2014. The Theoretical Analysis of the RAP Aged Asphalt Influence on the Performance of Asphalt Emulsion Cold Recycled Mixes. *Construction & Building Materials* 71(71): 444-450.
- [12] Minotra D., Veeraragavan A., Mallick R. B., 2015. Laboratory and Field Investigation of Mechanistic Properties of Foamed Asphalt Recycled Base Course Materials for High Volume Pavements in India. *Journal of Performance of Constructed Facilities*, 29(6): 1-7.
- [13] Khosravifar S., Schwartz C.W., Goulias D.G., 2013. Mechanistic Structural Properties of Foamed Asphalt Stabilised Base Materials. *International Journal of Pavement Engineering* 16 (1): 27-38.
- [14] Brennen M., Tia M., Altschaeffl A. G., Wood L. E., 1983. Laboratory Investigation of the Use of Foamed Asphalt for Recycled Bituminous Pavements. *Transportation Research Record* 911: 80-87.
- [15] Shi F. Z., Ma W. M., 2006. *Technical Manuals of Asphalt Pavement Regeneration*. Communication Press, Beijing, China.
- [16] Bhasin A., 2006. *Development of Methods to Quantify Bitumen-Aggregate Adhesion and Loss of Adhesion Due To Water*. College Station: Texas A&M University.
- [17] Cheng D., 2002. *Surface Free Energy of Asphalt-Aggregate System and Performance Analysis of Asphalt Concrete Based on Surface Free Energy*. College Station: Texas A&M University.
- [18] JTG E20-2011. 2011. *Standard Test Methods of Bitumen And Bituminous Mixtures for Highway Engineering*. Ministry of Transport, China, Beijing.
- [19] Li L., Chao Z., Nian W., Qiao W. H., 2013. Experimental Study on Foaming Characteristics of Foamed Asphalt. *Applied Mechanics & Materials* 363: 1507-1510.
- [20] Xu J. Z., Hao P. W., 2011. Research on the Evaluation Index and Optimization Design of Asphalt Foaming Characteristics. *Journal of Building Materials* 14(6): 776-780.

- [21] Yin F., Arambula E., Newcomb D. E., 2015. Effect of Water Content on Binder Foaming Characteristics and Foamed Mixture Properties. *Transportation Research Record Journal of the Transportation Research Board* 2506: 1-7.
- [22] Liu J. L., Wei L. Y., Zhang G. Q., 2011. The Study on Foaming Characteristics of Foamed Asphalt in Cold Recycling Technology. *Advanced Materials Research* 243: 4293-4296.
- [23] Li X. J., Zhi S. F., Ping Z. Y., 2008. Influence of Water Percentage on Performance of Foamed Bitumen Mixture. *Journal of Building Materials* 11(1): 64-69.
- [24] Lee D. Y., 1981. Treating Marginal Aggregates and Soils with Foamed Asphalt. *Association of Asphalt Paving Technologists* 50:211-250.
- [25] Sakr H. A., Manke P. G., 1985. Innovations In Oklahoma Foamix Design Procedures. *Transportation Research Record* 1034:26-34.
- [26] Hailesilassie B. W., Hugener M., Partl M. N., 2015. Influence of Foaming Water Content on Foam Asphalt Mixtures. *Construction & Building Materials* 85: 65-77.
- [27] Sunarjono S., 2013. Performance of Foamed Asphalt under Repeated Load Axial Test. *Procedia Engineering* 54: 698-710.
- [28] Abbas A. R., Ali A., 2011. Mechanical Properties of Warm Mix Asphalt Prepared Using Foamed Asphalt Binders. Akron: University of Akron.
- [29] Van Oss C. J., Giese R. F., 2007. Surface Modification of Clays and Related Materials. *Journal of Dispersion Science & Technology* 24(3-4): 363-376.
- [30] Li K. Y., 1998. *Physical Chemistry of Interface and Colloid*. Harbin Institute of Technology Press, Harbin, China.
- [31] Zhang K., Luo R., Zhang D. R., 2016. Wettability Analysis on Colored Resin Asphalt Binder Based on Surface Free Energy Theory. *China Journal of Highway and Transport* 29(5): 29-40.
- [32] Bhasin A., 2006. *Development of Methods to Quantify Bitumen-Aggregate Adhesion and Loss of Adhesion Due to Water*. College Station: Texas A & M University.
- [33] Good R. J., Van Oss C. J., 1991. *The Modern Theory of Contact Angles and the Hydrogen Bond Components of Surface Energies*. Plenum Press, New York.
- [34] Erbil H. Y., 2006. *Solid and Liquid Interfaces*. Blackwell Publishing, Oxford.
- [35] Arabani M., Hamed G. H., 2011. Using the Surface Free Energy Method to Evaluate the Effects of Polymeric Aggregate Treatment on Moisture Damage in Hot-Mix Asphalt. *Journal of Materials in Civil Engineering* 23(6): 802-811.
- [36] Lytton R. L., Masad E. A., Zollinger C., Bulut R., Little D.N., 2005. *Measurements of Surface Energy and Its Relationship to Moisture Damage*. College Station: Texas A & M University.

NUMERICAL SIMULATION OF ULTRASONIC DETECTION FOR CONCRETE STRUCTURE BASED ON EQUIVALENT OFFSET MIGRATION

Mingshun Hu^{1,2}, Juanjuan Li^{3}, Dongming Pan² and Shen Chen⁴*

1. *China University of Mining and Technology, Key Laboratory of Gas and Fire Control for Coal Mines, Xuzhou, China; dejekdm@163.com*
2. *China University of Mining and Technology, School of Resource and Geosciences, Xuzhou, China; pdm3816@163.com*
3. *China University of Mining and Technology, IoT Perception Mine Research Center, Xuzhou, China; lijuanjuan19850110@163.com*
4. *University of North Carolina at Charlotte, Department Civil of and Environmental Engineering. Charlotte, USA; schen12@uncc.edu*

ABSTRACT

Ultrasonic wave testing is a classic Non-destructive testing (NDT) method to detect, locate and monitor the crack/fracture in construction materials. However, it is still hard to examine those small abnormal bodies since effective reflected signal from abnormality is usually rather weak. In this paper, a new ultrasound imaging technique, equivalent offset migration (EOM), is studied to demonstrate the feasibility and applicability for detecting concrete cracks. Thus, a complex numerical model along with six small scale flaws was built, and then the ultrasonic wave propagation in concrete was modeled by high order finite difference approximation method. Numerical simulation indicates that 1) there exists a strong scattering phenomenon while ultrasound propagates in concrete with multiple small scatter flaws, and 2) EOM is capable of imaging small flaws in concrete with high resolution and accuracy.

KEYWORDS

Equivalent offset migration (EOM), Common scatter point (CSP) gather, Non-destructive testing (NDT), Ultrasonic wave; Concrete

INTRODUCTION

Concrete is a composite material consisting of a binding medium with two types of particles, normally gravel and sand. Defects, such as void, crack and delamination in concrete, affect construction structures severely. Therefore, NDT technique is necessary in structural health monitoring (SHM). Currently, three important methods (sonic, ultrasonic and impact echo test), are widely used in NDT of concrete structures [1-3]. The main reason for using ultrasonic wave to assess strength of concrete is that a direct link between Young's modulus and wave velocity in an elastic media is theoretically supported. Besides, empirical relations have been long recognized between strength and modulus.

Bogas et al. (2013) evaluated the compressive strength of a wide range of structural lightweight aggregate concrete mixtures by ultrasonic pulse velocity (UPV) method [4]. Dilek (2007) discussed the application of UPV in field detection of damage to concrete in service and field quality assessment of cast-in-place concrete and masonry under construction [5]. Mohammed et al. (2011) applied both UPV and rebound hammer tests to evaluate the rubbercrete [6]. Acciani et

al. (2010) studied the ultrasonic wave propagation in concrete structures with defects based on finite element simulations [7].

As regards ultrasound data processing, frequency compounding method has been applied to the ultrasonic signals in concrete [8]. Bilgehan (2011) compared artificial neural network and adaptive neuro-fuzzy inference system used in concrete compressive strength estimation [9]. Bui and Kodjo (2013) presented that Ultrasonic travel time shift is more sensitive when used in an indirect configuration of transmission instead of in a semi-direct configuration in evaluation of concrete distributed cracks [10].

Bancroft and Geiger (2011) introduced an alternative technique initially known as common scatter point (CSP) migration and now is named equivalent offset migration (EOM) [11-15]. This method was also applied in other relative fields due to its advantage in imaging scattered waves [16, 17]. In this paper, we use numerical simulation method to determine the feasibility and effectiveness of the application of EOM in improving the accuracy and resolution of detection for flaws within concrete structure by ultrasonic wave.

SCATTERING CHARACTERISTIC OF ULTRASONIC WAVE PROPAGATION IN CONCRETE

Since concrete is a strongly heterogeneous solid including aggregates, cracks and porosity, Ultrasonic wave propagation in this material consists of a complex mixture of multiple scattering, which results in a diffusive energy transport [18].

In terms of Huygens-Fresnel principle, every point to a luminous disturbance reaches becomes a source of a spherical wave. The sum of these secondary waves determines the form of the wave at any subsequent time. Therefore, the recorded data is the sum of the disturbance. As shown in Figure 1, when the scale of flaws in concrete structure is small, the incident ultrasonic wave would be strongly diffracted and generate scattering waves. Only if the interface of the flaw is smooth and long enough, deflection waves with strong energy could be generated.

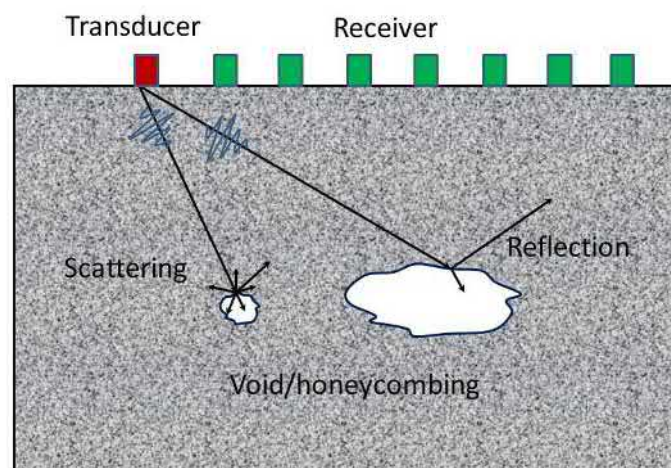


Fig. 1 - Schematic of scattered waves and reflection waves in heterogeneous concrete

In the case of the scale of the flaws being small and the concrete being highly inhomogeneous, impact echo testing method does not work. We placed transducers and sensors on the same surface which is similar to the surface geophysical exploration, and tried to apply a relatively new signal processing method in the detection of concrete structure with ultrasonic wave.

PRINCIPLE OF SCATTERED WAVE IMAGING

Double square-root (DSR) equation

Scattered wave imaging method is based on the concept of equivalent offset and CSP gather [11, 14]. We assumed that the concrete material is composed by a large number of single scatter points. Figure 2 shows the schematic of traveling path and time of scattered waves for a single scatter point. Initially, the ultrasonic waves travel from the source (transducer) to the scatter point within the concrete and then propagate backward to the receiver (sensor). Then, the receiver can record the information of the scatter point. As shown in Figure 2, MP is the middle point between the source (S) and receiver (R), and SP is the projection point of the scatter point to the observation surface. The total travel time of source-scatter point-receiver is

$$t = t_s + t_r \tag{1}$$

Where t_s is the travel time from the source to the scatter point and t_r is the travel time from the scatter point to the receiver, assuming the velocity of the acoustic wave is constant. In terms of the geometry in Figure 2, Equation 1 can be expanded as the following double square-root (DSR) equation:

$$t = \left[\frac{z_0^2 + (x+h)^2}{v^2} \right]^{\frac{1}{2}} + \left[\frac{z_0^2 + (x-h)^2}{v^2} \right]^{\frac{1}{2}} \tag{2}$$

In Equation (2), z_0 is the depth of the scatter point from the observation surface. x is the distance between MP and SP, and h is the half distance between the source (S) and receiver (R). However, the velocity of heterogeneous material is not constant. Hence, we use root-mean-square (RMS) velocity to replace the constant velocity in Equation (2) which can also be rewritten as:

$$t = \left[\left(\frac{t_0}{2} \right)^2 + \frac{(x+h)^2}{v_{rms}^2} \right]^{\frac{1}{2}} + \left[\left(\frac{t_0}{2} \right)^2 + \frac{(x-h)^2}{v_{rms}^2} \right]^{\frac{1}{2}} \tag{3}$$

Where t_0 is the vertical two-way travel time between SP and the scatter point, and v_{rms} is the RMS velocity at the position of scatter point.

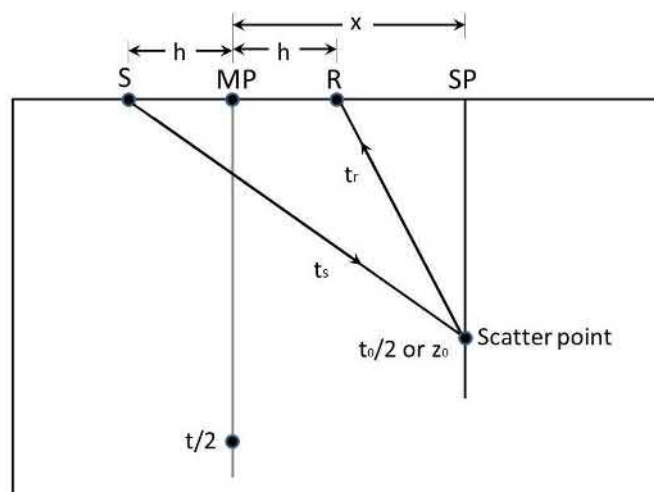


Fig. 2 - Schematic of traveling path and time of scattered waves for a single scatter point

In Figure 2, SP is the projection of scatter points to the observation surface. R is the receiver. S is the source. MP is the middle point between the source and the receiver point. t_0 is the vertical two-way travel time between point SP and scatter point. t_s is the travel time source and scatter point. t_r is the travel time between receiver and scatter point.

Equivalent offset

As shown in Figure 3, if the two-way travel time between the point E and the scatter point equals the travel time of source (S)-scatter point-receiver (R), namely $t = 2t_e = t_s + t_r$, we call the distance between point E and CSP equivalent offset. Therefore, we have the following equation:

$$t = 2t_e = 2 \left[\left(\frac{t_0}{2} \right)^2 + \frac{h_e^2}{v_{rms}^2} \right]^{\frac{1}{2}} \tag{4}$$

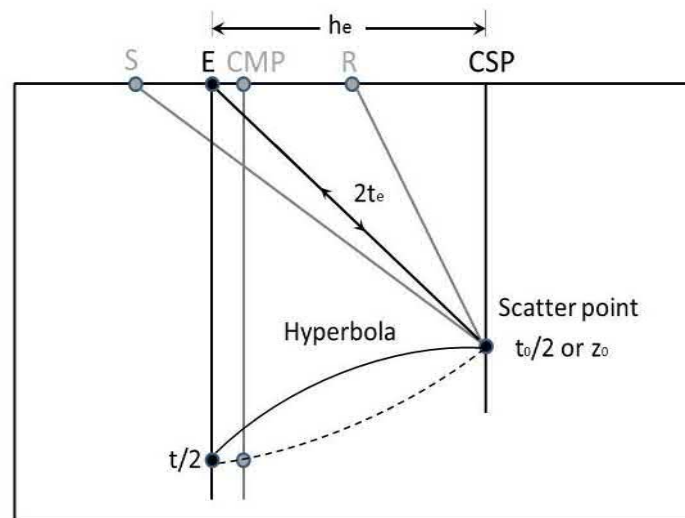


Fig. 3 - Schematic of equivalent offset

In Figure 3, CSP is the projection of scatter points to the observation surface. h_e the is equivalent offset, R is the receiver. S is the source. E is the combined equivalent source and receiver point. CMP is the middle point between source and receiver point. t_e is the travel time between point E and scatter point. t_s the is travel time source and scatter point. t_r the is travel time between the receiver and the scatter point.

Put Equation 3 into Equation 4, and then a new equation is derived as follows:

$$2 \left[\left(\frac{t_0}{2} \right)^2 + \frac{h_e^2}{v_{rms}^2} \right]^{\frac{1}{2}} = \left[\left(\frac{t_0}{2} \right)^2 + \frac{(x+h)^2}{v_{rms}^2} \right]^{\frac{1}{2}} + \left[\left(\frac{t_0}{2} \right)^2 + \frac{(x-h)^2}{v_{rms}^2} \right]^{\frac{1}{2}} \tag{5}$$

Equation 5 can be further simplified in Equation 6

$$h_e^2 = x^2 + h^2 - \left(\frac{2xh}{tv_{rms}} \right)^2 \tag{6}$$

Therefore, we notice that under the conception of equivalent offset, the DSR Equation 2 can be transformed to single square-root Equation 6. Based on Equation 4 and 6, the common

shot gathers can be projected into the domain of common scatter point (CSP) gathers.

Fowler (1997) validated that there are several different types of hyperbolas which can be simplified from DSR Equation 2 [19]. The method based on equivalent offset is a unique way to project all data into the CSP gathers without time shift. The CSP gather, based on equivalent offset, is actually a kind of equivalent zero-offset section. Thus, the CSP gather corresponding to the point CSP on observation surface contains all information about the scatter points under the same point SP shown in Figure 3.

Equivalent offset migration (EOM)

As discussed above, in terms of Equation 4 and 6, we can project each sample in common shot gathers into CSP gathers. The CSP gathers are equivalent zero-offset sections. Therefore, as shown in Figure 4, we can integrate along the hyperbolic scattered wave events to implement the scattered wave migration based on Kirchhoff diffraction theory.

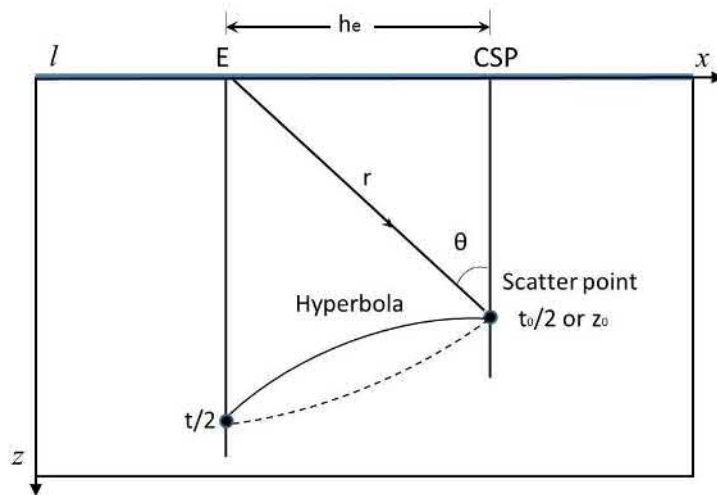


Fig.4 - Schematic of Kirchhoff integration in CSP gather

Two-dimensional Kirchhoff integration equation can be written as:

$$P(x, z; \tau) = \frac{1}{4\pi} \int_l \left\{ \frac{1}{r} \left[\frac{\partial P}{\partial z} \right] + \frac{\cos \theta}{r^2} |P| + \frac{\cos \theta}{vr} \left[\frac{\partial P}{\partial t} \right] \right\} dl \tag{7}$$

Where $P(x, y; t)$ is the acoustic wave pressure field which propagates at the velocity of $v(x, y)$, θ is the incident angle of wave, and l is the observation line, time relay $\tau = t - \frac{r}{v}$, $r = \sqrt{(h_e^2 + z_0^2)}$.

In Equation (7), the first term in the right integration is related to the gradient of pressure respect to z-direction. The second term in the right integration is called near-source term due to its attenuation by $1/r^2$. Therefore, these two terms are usually neglected in real migration due to their negligible contribution. The third term in the right integration is the basis of Kirchhoff integration migration whose discrete form is:

$$P_{out} = \frac{\Delta x}{4\pi} \sum_N \frac{\cos \theta}{vr} \frac{\partial}{\partial t} P_{in} \tag{8}$$

Where Δx is the space between two adjacent channels in CSP gathers. $P_{out} = P(x_{out}, z; \tau = 2z_0/v)$ is the migration output wavefield based on the input wavefield $P_{in} = P(x_{in}, z = 0; \tau = t - r/v)$. Thus, we can find that this method is essentially Kirchhoff integration scatter imaging, which is called equivalent offset migration (EOM) [14].

NUMERICAL SIMULATION

To validate the effectiveness of the scattered wave imaging method, here we designed a numerical concrete model with six flaws that forms a pentagon shape shown in Figure 5. The size of this concrete model is 300 mm × 450 mm with velocity 4000 m/s. And we set the size of each flaw quite small, and all of them are 6 mm × 6 mm with velocity of 2000 m/s. The reason of this design is to determine the capability of scattered wave imaging for small scale scatter point.

In this simulation, 19 sensors are used with equal space 25 mm on the top surface of the model, and 3 sources are located in the position $x = 0$ mm, 200 mm and 450 mm. High order finite difference approximation is used to investigate the ultrasonic wave propagation in this kind of heterogeneous concrete. We set the cell size 2 mm and use 150 kHz Ricker wavelet as source function.

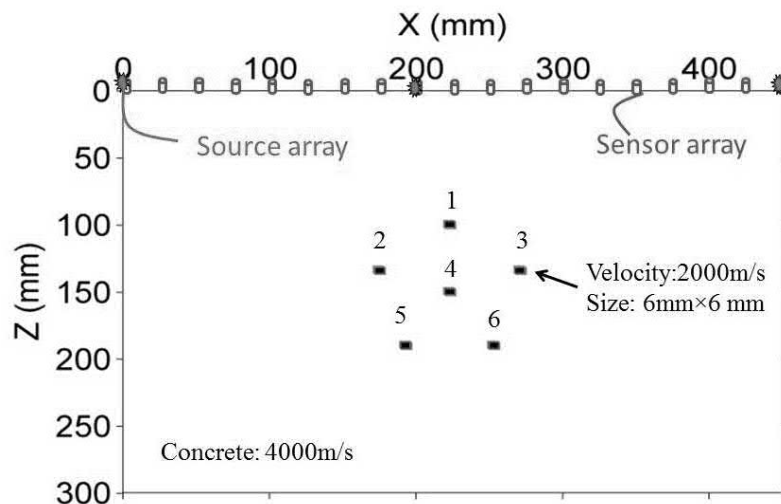


Fig. 5 - Numerical concrete model with small scale flaws

Figure 6 presents four snapshots recorded in the second shot. From these snapshots, we can notice that severe scattering waves are generated when the ultrasound hit these scatter points (flaws in small size). Each scatter point can generate new spherical wave as a new point source. All these new spherical waves later interference each other. Due to the strong scattering, the characteristic of wave field becomes quite complex. It is hard for conventional migration methods to image these small scatter points.

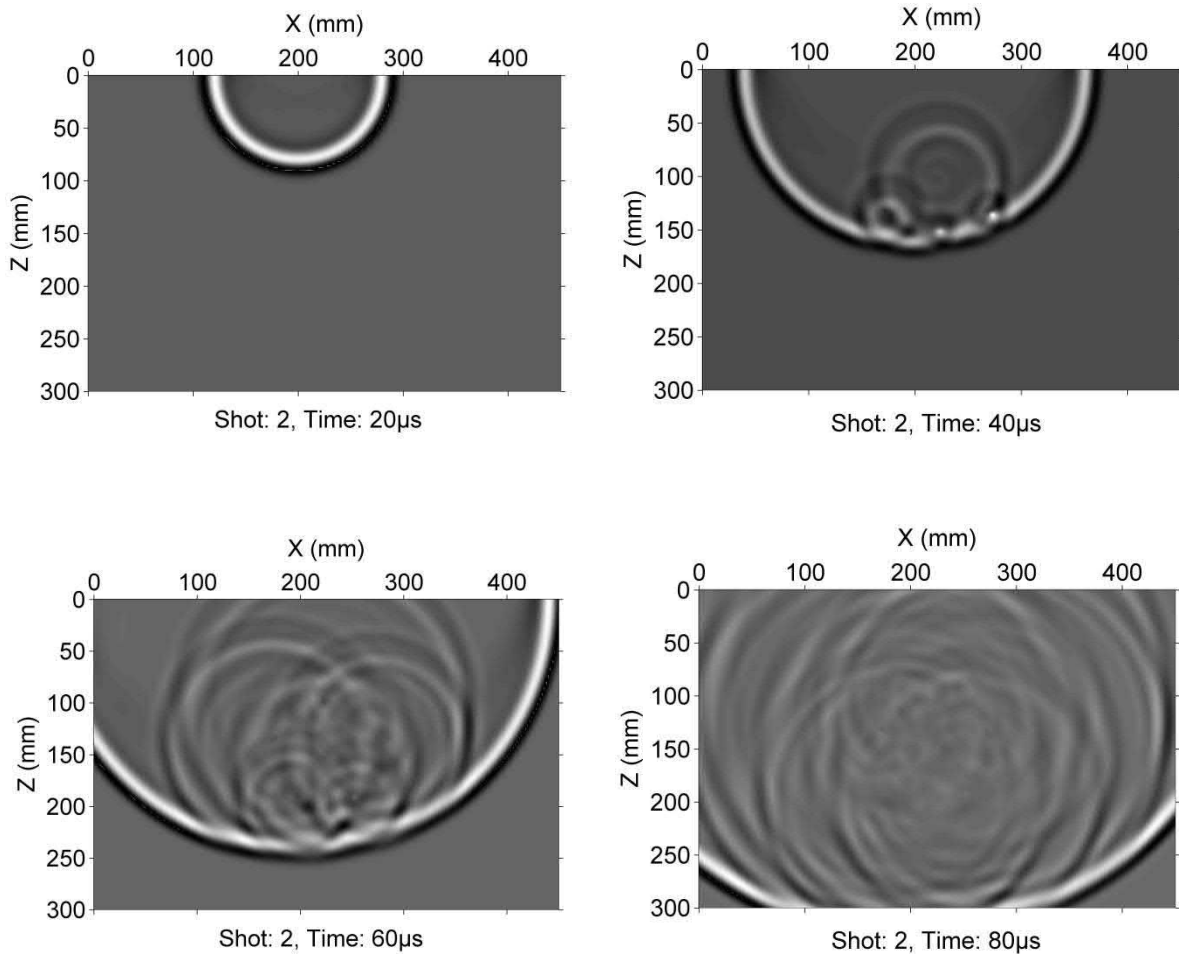


Fig.6 - Snapshot of second shot ($x = 200$ mm)

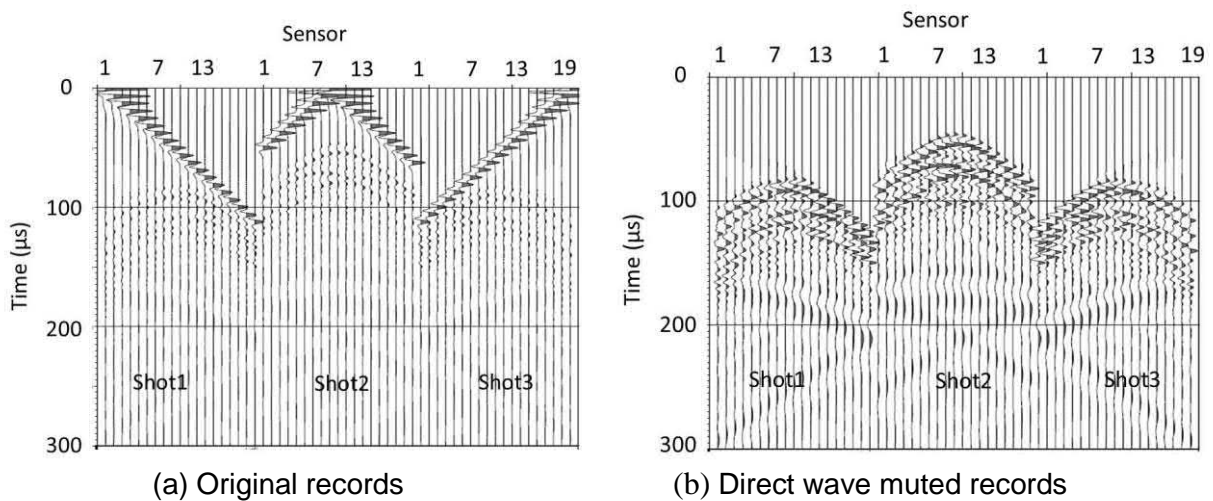


Fig.7 - Wave records

We can also find the same characteristic in wave records in Figure 7 (a) which is the original wave records. Due to the strong energy in direct waves (these waves propagate from source to receiver directly along the observation surface), the coda waves containing the

information of the inside structure of the concrete model present very low amplitude. It is not good to image the testing objects due to the interference of direct waves. Therefore, these direct waves should be muted before using scattered wave imaging. Figure 7 (b) is the wave record without direct waves.

Figure 8 is the imaging results by different migration methods. Figure 8 (a) is imaged by equivalent offset migration (EOM) and Figure 8 (b) by reverse time migration (RTM). RTM, a migration method based on wave equation, can get the best imaging result if the velocity of model is known. In other words, RTM is highly affected by the level of velocity analysis technique. However, in order to get the most accurate result and compare it with the imaging result by EOM, the imaging result in Figure 8 (b) is made by RTM with the velocity of model we created. Compared to Figure 8(b), the imaging result in Figure 8 (a) has apparent diffraction interference that is classic migration noise resulting from Kirchhoff integration migration. Additionally, the flaws, No. 5 and No. 6, are not as clear as other four flaws, especially flaw No. 1. The reason of this phenomenon is that the energy of the backward scattered waves from bottom flaws is not as strong as the energy of the waves from top flaws. In practice, we should improve the amplitude of the signal from the bottom structure by some energy compensation process, such as exponent gain and spherical compensation.

In addition, from the Equation (4), (6) and (8), velocity model is necessary for implementing EOM. As regards concrete detection by ultrasound, usually we can consider the velocity of ultrasound waves as a constant value. For this numerical case, the velocity we get is 3950 m/s which is a little less than the velocity of direct wave 4000 m/s. So we can see that EOM is not like RTM in the requirement of accuracy for analysis. That means EOM is quite applicable for real testing due to the difficulties in velocity analysis for real detection.

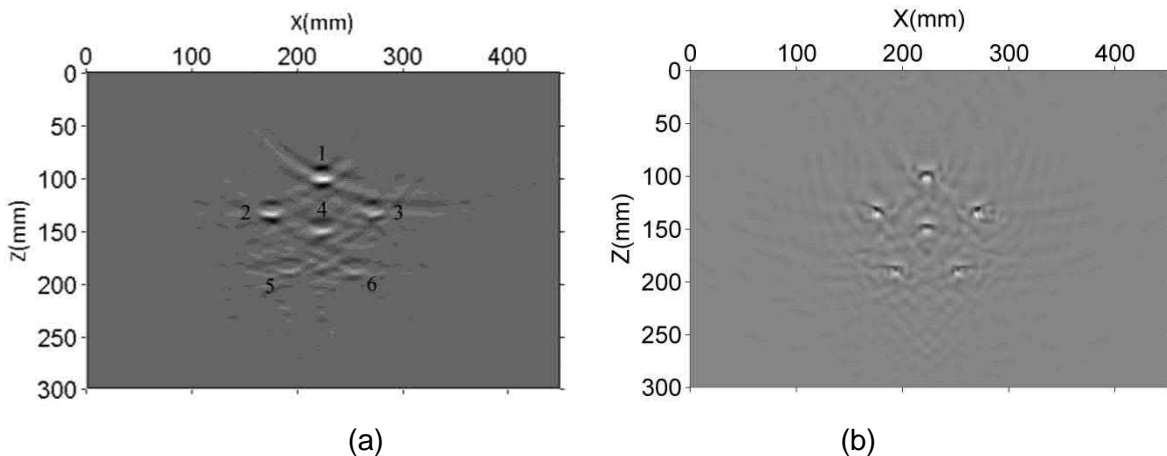


Fig. 8 - Imaging results of numerical model by EOM (a) and RTM (b)

RESULTS AND DISCUSSIONS

The above numerical simulation indicates that EOM is good at utilizing scattered waves to image very small scale structures. The main reason is that EOM is a pre-stack migration method based on the scattering wave theory. In terms of Equation (4) and (6), CSP gathers can be projected from original shot gathers under the conception of equivalent offset with the Huygens principle. CSP gathers is actually a type of equivalent zero-offset section, and we can easily apply Kirchhoff integration to image these scatter points (the whole testing object volume can be thought as the mixture composited by a large number of single scatter points). Due to the basic theory of EOM, it is suitable to apply EOM to detect the heterogeneous materials, such as concrete with different kinds of flaws and aggregates. It is also possible that EOM can be extended into other

fields of detection, such as metal plate damage evaluation.

CONCLUSIONS

This paper investigated the effectiveness of EOM applied in detecting concrete structures by ultrasonic waves. In terms of the conception of equivalent offset and Kirchhoff integration migration, we built a numerical concrete model, with six small scale flaws, to determine the applicability and feasibility of EOM for concrete structure detection by ultrasonic waves. The simulation result shows EOM is a great imaging method for detecting small scale concrete defects. However, some physical modelling tests should be carried out to evaluate it deeply in the future.

ACKNOWLEDGEMENTS

The authors are grateful for the financial support from Fundamental Research Funds for the Central Universities of China (2015QNB22, 2015XKMS036), Natural Science Foundation of Jiangsu Province (BK20160245), National key research and development program of China (2017YFC0804105) and A Project Funded by Priority Academic Program Development of Jiangsu Higher Education Institutions.

REFERENCES

- [1] Mccann D. M., Forde M. C., 2001. Review of NDT methods in the assessment of concrete and masonry structures. *NDT & E International*, 34(2): 71-84.
- [2] Aggelis D. G., et al., 2011. Longitudinal waves for evaluation of large concrete blocks after repair. *NDT & E International*, 44(1): 61-66.
- [3] De Belie N., et al., 2005. Ultrasound monitoring of the influence of different accelerating admixtures and cement types for shotcrete on setting and hardening behaviour. *Cement and Concrete Research*, 35(11): 2087-2094.
- [4] Bogas J. A., Gomes M. G., Gomes A., 2013. Compressive strength evaluation of structural lightweight concrete by non-destructive ultrasonic pulse velocity method. *Ultrasonics*, 53(5): 962-972.
- [5] Dilek U., 2007. Ultrasonic Pulse Velocity in Nondestructive Evaluation of Low Quality and Damaged Concrete and Masonry Construction. *Journal of Performance of Constructed Facilities*, 21(5): 337-344.
- [6] Mohammed B. S., Azmi N. J., Abdullahi M., 2011. Evaluation of rubbercrete based on ultrasonic pulse velocity and rebound hammer tests. *Construction and Building Materials*, 25(3): 1388-1397.
- [7] Acciani G., et al., 2010. Nondestructive evaluation of defects in concrete structures based on finite element simulations of ultrasonic wave propagation. *Nondestructive Testing & Evaluation*, 25(4): 289-315.
- [8] Ho K. S., et al., 2012. Application of frequency compounding to ultrasonic signals for the NDE of concrete. *AIP Conference Proceedings*, 1430(1): 1508-1515.
- [9] Bilgehan M., 2011. A comparative study for the concrete compressive strength estimation using neural network and neuro-fuzzy modelling approaches. *Nondestructive Testing & Evaluation*, 26(1): 35-55.
- [10] Bui D., et al., 2013. Evaluation of Concrete Distributed Cracks by Ultrasonic Travel Time Shift Under an External Mechanical Perturbation: Study of Indirect and Semi-direct Transmission Configurations. *Journal of Nondestructive Evaluation*, 32(1): 25-36.
- [11] Bancroft J. C., Geiger H. D., 1994. Equivalent offset CRP gathers. *SEG Technical Program Expanded Abstracts 1994*, 672-675.
- [12] Bancroft J. C., Xu Y., 1999. Equivalent offset migration for vertical receiver arrays. *SEG Technical Program Expanded Abstracts 1999*, 1279-1282.

- [13] Bednar J. B., 1999. A theoretical comparison of equivalent - offset migration and dip moveout - prestack imaging. *GEOPHYSICS*, 64(1): 191-196.
- [14] Bancroft J. C., Geiger H., Margrave G., 1998. The equivalent offset method of prestack time migration. *GEOPHYSICS*, 63(6): 2042-2053.
- [15] Khaniani H., Bancroft J. C., 2011. Enhancing the inversion of migration velocity by implementation of tilt effects on CSP data. *SEG Technical Program Expanded Abstracts 2011*, 3882-3886.
- [16] Hu M., Pan D., Li J., 2010. Numerical simulation scattered imaging in deep mines. *Appl Geophys*, 7(3): 272-282.
- [17] Zhang T. X., et al., 2009. Application of the equivalent offset migration method in acoustic log reflection imaging. *Appl Geophys*, 6(4): 303-310.
- [18] Schubert F., Marklein R., 2002. Numerical Computation of Ultrasonic Wave Propagation in Concrete Using the Elastodynamic Finite Integration Technique (EFIT). *IEEE Ultrasonics Symposium 2002*, 799-804.
- [19] Fowler P. J., 1997. A comparative overview of prestack time migration methods. *SEG Technical Program Expanded Abstracts 1997*, 1571-1574.

A MECHANISTIC-EMPIRICAL IMPACT ANALYSIS OF DIFFERENT TRUCK CONFIGURATIONS ON A JOINTED PLAIN CONCRETE PAVEMENT (JPCP)

Lubinda F. Walubita¹, Tito P. Nyamuhokya², Stefan A. Romanoschi³, Xiaodi Hu⁴ and Mena I. Souliman⁵

1. *The Texas A&M University System, College Station, TX 77843, USA; lfwalubita@tamu.edu*
2. *The Texas A&M University System, College Station, TX 77843, USA; tnyamuhokya@tti.tamu.edu*
3. *University of Texas at Arlington, Department of Civil Engineering, Arlington, Texas 76019, USA; romanoschi@uta.edu*
4. *Wuhan Institute of Technology, Transportation Research Center (TRC), Wuhan, China. huxiaodi625@hotmail.com*
5. *University of Texas at Tyler, Department of Civil Engineering, Tyler, Texas 75799, USA; msouliman@uttyler.edu*

ABSTRACT

Until the last decade, the 1993 American Association of State Highway and Transportation Officials (AASHTO) design guide has been traditionally used for the design of flexible and rigid pavements in the USA and some parts of the world. However, because of its inability to meet the new traffic and material challenges, a Mechanistic Empirical Pavement Design Guide (MEPDG) was introduced based on an NCHRP 1-37 A study conducted in 2004. This study used the MEPDG software and associated models to determine, through comparative truck damage analysis, the effects of nine different truck configurations on a 12 inch-jointed plain concrete pavement (JPCP). The study recorded truck damages at the end of each analysis period (40 years) and comparatively analyzed the relative pavement damage in terms of fatigue cracking, faulting, and surface roughness. The results indicated that the most critical damage to the concrete pavement was caused by truck cases with high and uneven load distribution and relatively smaller size axles group (e.g. tandem). Other key findings included the following; (1) increase in damage when the truckloads were shifted between the same size axles, (2) decrease in truck damage when the truckloads were shifted from tandem axle to quad axles, and (3) no change in truck damage when the axle spacing was increased between wheels of a quad axle.

KEYWORDS

Jointed Plain Concrete Pavement (JPCP), Mechanistic Empirical (ME), Axle loading, Fatigue Cracking, Faulting, Surface roughness, Trucks configurations

INTRODUCTION

Jointed plain concrete pavement is one of the common types of concrete pavements used in the USA. Concrete pavements, which are also known as rigid pavements, typically consist of a Portland cement concrete (PCC) surface layer supported by a sub-base or subgrade. The concrete pavements are categorized based on the type of joints constructed and use of steel reinforcement

[1]. Each of these pavement types has specific failure mechanisms, and each failure mechanism is caused by specific factors. Examples of such failure mechanisms include fatigue damage, faulting, and surface roughness of the concrete pavement. These failure mechanisms are usually caused by the following factors: heavy vehicle loading, climate, poor drainage, materials properties, and inadequate layer thicknesses [2]. Out of these factors, the impacts of heavy loaded vehicles constitute some of the major sources for concrete pavement damage [1].

The magnitude and configuration of vehicular loads together with the environment have a significant effect on the induced tensile stresses within the concrete pavement [3]. The impacts of heavy loaded vehicles subject the pavement to high stresses causing damage. However, not all trucks have the same damaging effects; their damage depends on vehicle speed, wheel loads, number and location of axles, load distribution, type of suspension, number of wheels, tire types, tire inflation pressure, etc. [1].

The proper estimation of truck damage is important for truck permit regulators since the fees and penalties applied to truck operators for using the roads are related to the distresses induced to the road network. Regulators must permit trucks and allocate costs to vehicle operators in accordance with the truck damage induced on the pavement. The proper evaluation of truck damage also helps the highway engineers to optimize pavement design and maintenance activities [4].

In the recent years, several studies have estimated the truck damage by computing the responses (stresses, strains, and deflections) of pavements under heavy vehicle loading using mechanistic approaches [5-11]. In this study, the Mechanistic Empirical Pavement Design Guide (MEPDG) was utilized to directly assess the cumulative damage to a concrete pavement. Among its many advantages, MEPDG can be used to analyze the pavement damage over a selected period (or design life) – an aspect that is very conducive for concrete pavement design and analysis [12].

OBJECTIVES

Given the above background, the primary objectives of this study are : (a) to use the MEPDG and its associated models to determine the failure magnitude of a Jointed Plain Concrete Pavement (JPCP) structure due to truck loading of various configurations and, (b) to compare the truck damage of each configuration based on the magnitude of the resulting damages. Specifically, the study aimed at evaluating the truck damage when:

- Truck axles (i.e., tandems, quads, etc.) are loaded unequally,
- Number of axles in a group of axles are increased or decreased (change of axle type),
- Axle spacing varies, and
- Individual axles of the same group (i.e., axles in a tandem group) share the load unequally.

METHODS

Concrete Pavements

Concrete pavements insignificantly deflect under loading because of the high stiffness that the PCC possess while constructing it to serve as a surface layer. The pavement structural layers are typically composed of a stiff PCC surface layer on top of a base or sub base layer (when used) as exemplified in Figure 1.



Fig. 1 - Typical Concrete Pavement Sections [13].

Depending on the type of construction, concrete pavements are classified as JPCP, jointed reinforced concrete pavement (JRCP), or continuously reinforced concrete pavement (CRCP). These are briefly discussed as follows:

Jointed Plain Concrete Pavement (JPCP): JPCP is the most widely used type of concrete pavement [15]. Its construction costs are lower than those of the other two types of concrete pavements. Instead of using costly steel reinforcements or meshes, the JPCP is designed with short joint spacing to control the development of transverse cracks (Figure 2). The joints relieve stresses in the concrete pavement and control the development of transverse shrinkage cracks. In most cases, the joints are provided with dowel bars spaced at 12 inch intervals. The typical size of slabs for JPCP is 12 to 15 ft wide by 15 to 20 ft long [13].

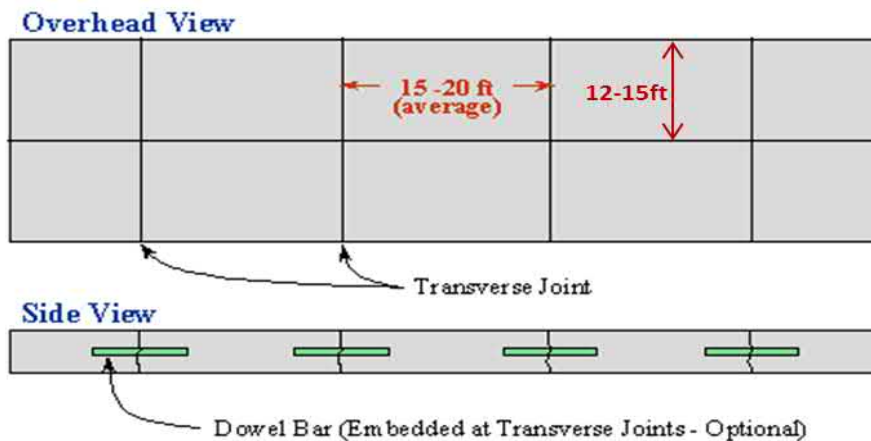


Fig. 2 - Jointed Plain Concrete Pavement [14].

Jointed Reinforced Concrete Pavement (JRCP): JRCP is comprised of a concrete surface layer with steel reinforcements and transverse joints to control cracks (Figure 3). The steel reinforcement in JRCP is in the form of a welded wire fabric mesh or deformed bars and does not increase the strength of the pavement but allow the use of longer joint spacing [15]. The mesh enhances the usage of longer joints since it holds transverse cracks tightly together [12]. The typical JRCP joint spacing varies from 25 to 50 ft [13]. However, under long-term performance, the longer joint spacing causes relatively early slabs cracking as compared to the other two types of concrete pavements. Because of such long-term performance problems, most states in the USA rarely use JRCP for highway pavements [13].

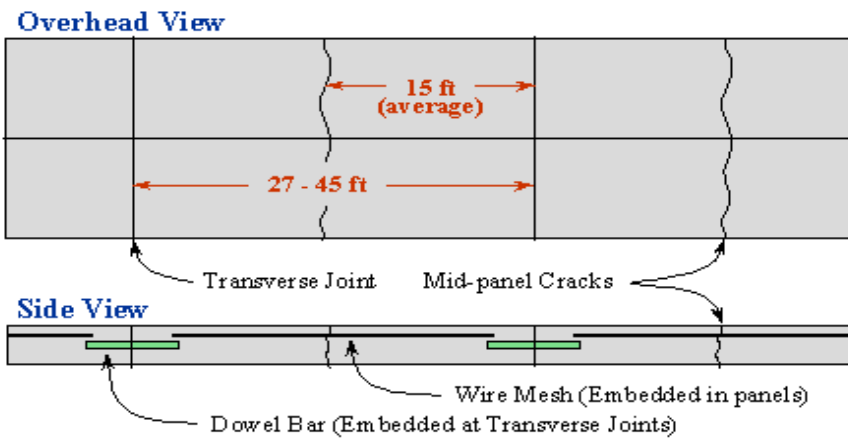


Fig. 3 - Jointed Reinforced Concrete Pavement [14].

Continuously Reinforced Concrete Pavement (CRCP): CRCP are constructed free of contraction/expansion joints (Figure 4). CRCP allows transverse cracks to occur but holds them tightly with steel reinforcements [12]. The transverse cracking behavior in CRCP depends on concrete properties (drying shrinkage, thermal properties, tensile strength, creep, and elastic modulus), reinforcing steel properties (bar diameter and coefficient of thermal expansion), and environmental conditions [16]. Typically, the reinforcement steels make up 0.6-0.7 percent of the concrete cross-sectional area [13]. Because of the joint-free design and reinforcements, the CRCP pavement thickness can be reduced. However, due to extensive use of reinforcements, its construction costs are higher than the other two types of concrete pavements.

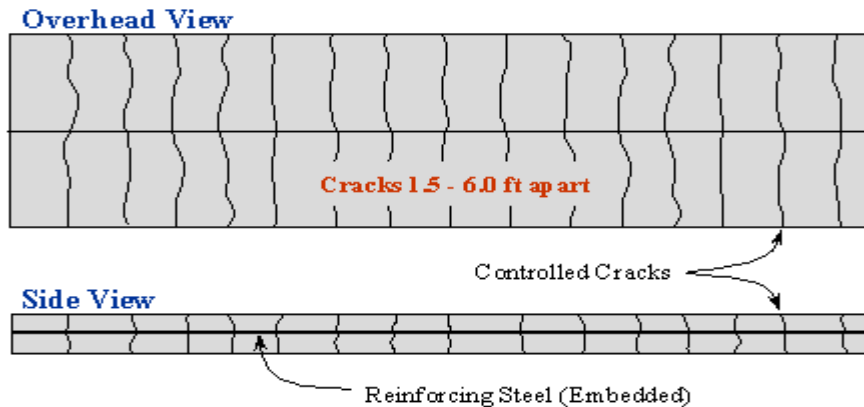


Fig. 4 - Continuously Reinforced Concrete Pavement [13].

Distresses in Concrete Pavements

Distresses in pavements refers to damage that hinders pavement performance. The extent and severity of the distresses are mainly due to the variation of the subgrade soil strength, pavement materials characteristics, traffic loading, environmental effects, construction quality, and aging effects (oxidation). For concrete pavements, the common distresses include spalling, faulting, joint seal damage, longitudinal cracks, transverse fatigue cracks, D-cracking, popouts, pumping, settlement, etc. In this study, only damage due to transverse fatigue cracking and faulting were used to compare the relative pavement damage from truck loading.

Transverse fatigue cracks

Transverse cracks develop on all concrete types, usually perpendicular to the pavement centerline. The width of the cracks developed may go up to 6mm [17]. The means by which the cracks develop differ from one type of concrete pavement to another. In JPCP, transverse cracks are caused by repeated traffic loading, drying shrinkage of the concrete, temperature variations, curling/warping, reflective cracking caused by existence of transverse cracking in the underlying layers and late, or inadequate transverse joint sawing. The transverse cracks may either start at the bottom or the top of the concrete slab depending upon the temperature and/or moisture gradients. When temperature and moisture gradients are negative (i.e., low temperature and less moisture at top of the concrete surface), the cracks initiates from top of the concrete slab, while bottom-up cracks develop when temperature and moisture gradients are positive (i.e., low temperature and less moisture at the bottom of the concrete slab) (Figure 5).

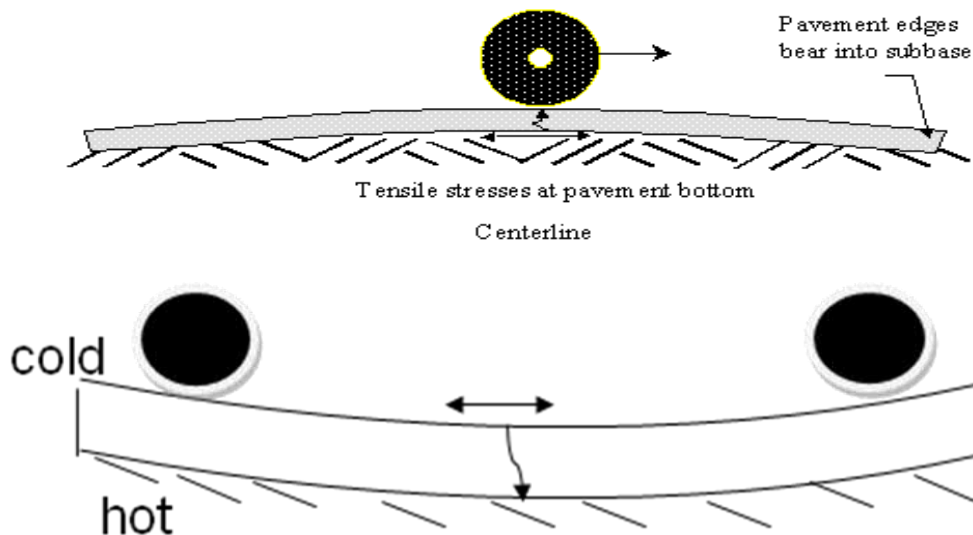


Fig. 5 - Transverse Cracks (a) Bottom Up Cracks, (b) Top Down Cracks.

Faulting

Faulting is recorded when a difference in elevation of concrete slab(s) across joints or cracks is observed (Figure 6). The major cause of faulting is heavy traffic loading and climatic variations. If dowels are used, dowel loosening and enlargement of dowel sockets also play a part in faulting. Pavements with poor drainage are more likely to develop faulting than those with good drainage. Also, erosion under joints due to poor subbase materials contributes to faulting. In fact, the progression of faulting is a function of subbase/base material; the poorer the subbase/base is the higher the faulting.

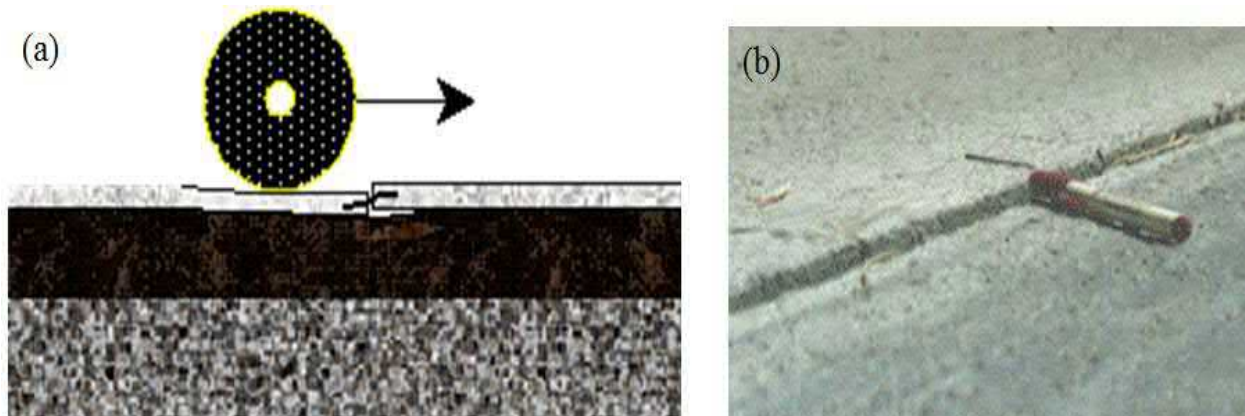


Fig. 6 - Joint Faulting (a) Cross-Section View (b) Photo Top View

Truck Configuration

The USA Department of Transportation and Federal Highway Administration (FHWA) classify vehicles into 13 groups. Classes 1 to 3 are light vehicles with two axles, while Classes 4 and higher are heavy vehicles with more than two axles. According to the FHWA, only vehicles in Classes 4 to 13 cause significant damage to pavements [17].

The FHWA classification of the trucks is based on the number of axles and trailer units. The other characteristics of trucks such as axle group type, suspension system, tire types, distance between axles of a given axle group, distance between centers of dual tires, tire inflation pressure, and loading capacities vary based on the vehicle's manufacturers [18]. This section will describe some characteristics of the trucks used in this study.

Truck cases: In order to easily identify the truck axle and load configurations used for the MEPDG analysis, this study classified the truck configuration into truck cases, namely L1, L2, L3, L4, L5, L6, L7, L8, and L9 as illustrated in Figure 7. Each of the truck cases is made up of one or more of the following axles: single axle single tire (SAST), single axle dual tire (SADT), tandem axle dual tire (TADT), tridem axle dual tire (TRADT), and quad axle dual tire (QADT); see the illustration in Figure 8 [18].

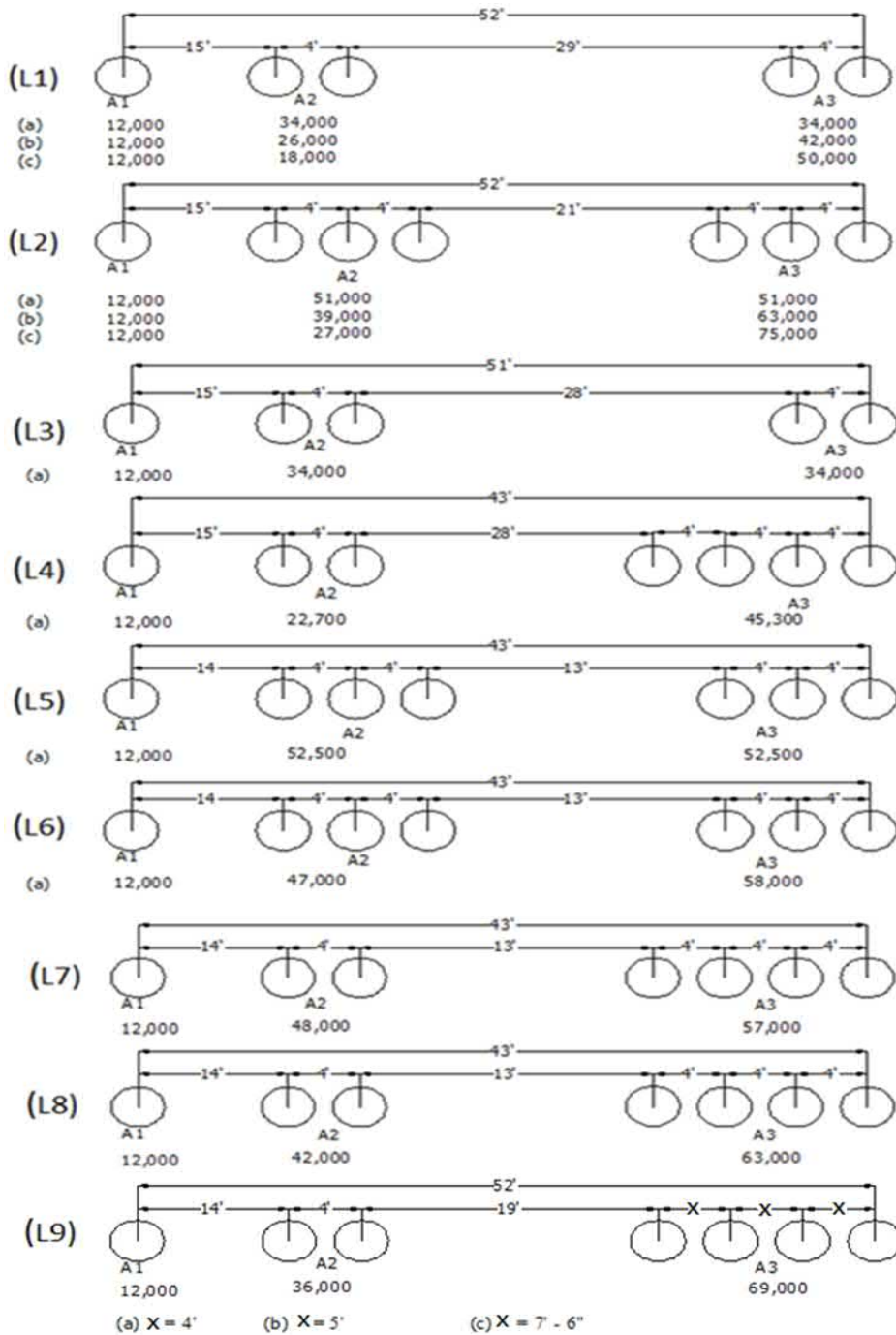


Fig. 7 - Truck Cases Used in the MEPDG Truck Damage Analysis.

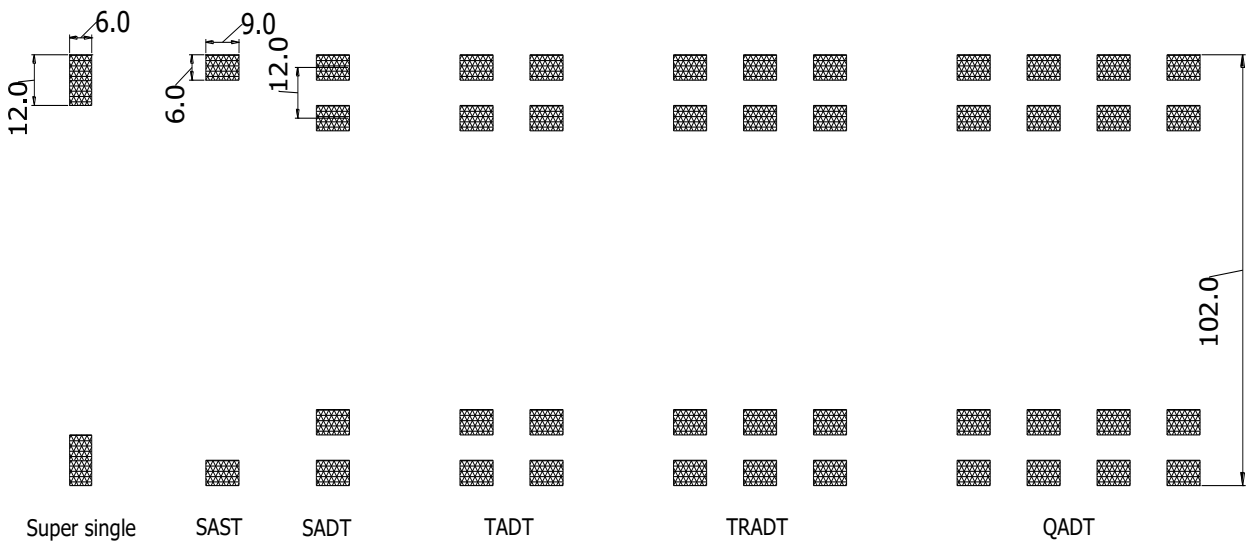


Fig. 8 - Truck Axle Types.

Distance between axles in a given axle group: This parameter also depends on the vehicle's manufacturer. All axles in truck cases L1 to L9 were spaced at a distance of 4 ft.

Axle width and space between centers of dual tires: Axle width refers to the distance from the center of dual tires of an axle to another center of dual tires of the same axle while the space between centers of dual tires mean the distance between centers of paired tires. Different researchers have been using different axle width and space between dual tires for their studies. While Kim et al. [19], for example, assumed these distances to be 75 inches and 13 inches, respectively. Hiller et al. [20] assumed them to be 74 inches and 13.5 inches, respectively. This study assumed the axle width and space between centers of the dual tires to be 84 inches and 12 inches, respectively [12].

Tire inflation pressure: The tire inflation pressure affects the contact area and stress when the tire is in contact with the pavement surface. According to Darestani et al. [21], the tire pressure of heavy trucks varies between 70 to 140 psi. However, the MEPDG software allows use of a tire inflation pressure of 120 psi only. Therefore, most designs and analyses are based on this value when using the MEPDG software.

Axle spacing: Different trucks may have different axle spacing. This parameter is inconsequential when analyzing bottom up crack damage of concrete pavements, but has significant effects when top down cracks are considered. Typically, the bottom part of pavements under reasonably spaced axles is under compressive stresses and thus, no bottom up cracks develop [22]. The axle spacing of the trucks used in this study is shown for the truck cases L1 to L9 in Figures 7 and 8.

Axle loads: This is the most important parameter required for pavement design and analysis. This study used the provided truck cases L1 to L9 loading in Figure 7.

MEPDG Analysis and Design Inputs

The inputs into the MEPDG software define the conditions under which the pavement is expected to perform. The MEPDG inputs also depend on the level of accuracy needed. Better results are expected when more data and a high level of accuracy are used within the analysis. The following is the sequence of MEPDG software inputs as used in this study:

- General data,
- Traffic,
- Climate, and
- Pavement structure

General data inputs

One of the required MEPDG general inputs is the design or expected life of the pavement. For JPCP, a design life of 40 years is typically adapted for high traffic volume pavements (i.e., > 15,000 Average Annual Daily Truck Traffic, AADTT) which was implemented during this study. Other general inputs used in this study are summarized in Table 1.

Tab. 1 - JPCP Performance Criteria.

Parameter	Criteria Range	Default Criteria	Assumed Reliability ⁽¹⁾
Initial IRI (in/mi)	0-200	63	-
Terminal IRI (in/mi)	0-300	172	90%
Mean joint faulting (in)	0-0.25	0.12	90%
Transverse cracking (% slabs cracked)	0-50	15	90%
(1) The assumed reliabilities are within the range of reliabilities values used for interstate highways [12].			
Legend: IRI = International Roughness Index			

Traffic inputs

Unlike the 1993 AASHTO Pavement Design Guide, which expresses traffic in terms of equivalent single axle loads (ESALs), the MEPDG requires a detailed estimate of all heavy vehicle axles that will travel on the pavement. Since the objective of this study was to assess and compare damages due to different truck configurations, each truck was analyzed separately, however the traffic volume was kept constant for all the cases studied. Traffic volume and the related parameters were arbitrarily selected from a range of default parameters in the MEPDG software. The MEPDG software allows an initial AADTT ranging from 100 to 25,000. This study used an AADTT of 24,000 on a two-lane pavement in the design direction to simulate high pavement damage. In addition, the study assigned the MEPDG recommended values of 55% and 90% as percentage of trucks in the design direction and design lane, respectively. Furthermore, the study used a minimum speed of 40 mph recommended for freeways. The speed was selected based on the theory that lower truck speed induces more damage to the pavement than relatively higher speeds.

Another set of traffic inputs required for the analysis included traffic monthly adjustment and growth factors, vehicle class distribution, hourly truck distribution and axle load distribution. This study used the MEPDG default values of 1.0 and 4% for traffic monthly adjustment and growth factors, respectively. Table 2, 3, and 4 show the vehicle class distribution, hourly truck distribution, and axle load distribution used in the analysis.

Tab. 2 - Vehicle Class Distributions.

Vehicle Class	MEPDG Default	Vehicle Distribution (%) for each Truck case								
		L1	L2	L3	L4	L5	L6	L7	L8	L9
4	1.8	0	0	0	0	0	0	0	0	0
5	24.6	0	0	0	0	0	0	0	0	0
6	7.6	0	0	0	0	0	0	0	0	0
7	0.5	0	0	0	0	0	0	0	0	0
8	5.0	0	0	0	0	0	0	0	0	0
9	31.3	100	0	100	0	0	0	0	0	0
10	9.8	0	100	0	100	100	100	100	100	100
11	0.8	0	0	0	0	0	0	0	0	0
12	3.3	0	0	0	0	0	0	0	0	0
13	15	0	0	0	0	0	0	0	0	0
Total	100	100	100	100	100	100	100	100	100	100

Tab.3 - Hourly Truck Traffic Distributions.

Time	% Hourly Distribution	Time	% Hourly Distribution
Midnight	2.3	Noon	5.9
1.00 am	2.3	1.00 pm	5.9
2.00 am	2.3	2.00 pm	5.9
3.00 am	2.3	3.00 pm	5.9
4.00 am	2.3	4.00 pm	4.6
5.00 am	2.3	5.00 pm	4.6
6.00 am	5.0	6.00 pm	4.6
7.00 am	5.0	7.00 pm	4.6
8.00 am	5.0	8.00 pm	3.1
9.00 am	5.0	9.00 pm	3.1
10.00 am	5.9	10.00 pm	3.1
11.00 am	5.9	11.00 pm	3.1

Tab. 4 - Monthly Axle Load Distribution Values for Truck Cases.

Truck Case	Single Axle		Tandem Axle		Tridem Axle		Quad Axle	
	Loads	%	Loads	%	Loads	%	Loads	%
L1a	12,000	100	34,000	100	0	0	0	0
L1b	12,000	100	26,000	50	0	0	0	0
			42,000	50	0	0	0	0
L1c	12,000	100	18,000	50	0	0	0	0
			50,000	50	0	0	0	0
L2a	12,000	100	0	0	51,000	100	0	0
L2b	12,000	100	0	0	39,000	50	0	0
					63,000	50	0	0
L2c	12,000	100	0	0	27,000	50	0	0
					75,000	50	0	0
L3	12,000	100	34,000	100	0	0	0	0
L4	12,000	100	22,000	100	0	0	45,000	100
L5	12,000	100	0	0	54,000	100	0	0
L6	12,000	100	0	0	48,000	50	0	0
					60,000	50	0	0
L7	12,000	100	48,000	100	0	0	57,000	100
L8	12,000	100	42,000	100	0	0	63,000	100
La	12,000	100	36,000	100	0	0	69,000	100
L9b	12,000	100	36,000	100	0	0	69,000	100
L9c	12,000	100	36,000	100	0	0	69,000	100



The development of the traffic inputs was completed by inserting parameters to define the axle load configuration and loading details used for calculating the responses and traffic volume. The traffic inputs used under this category were:

Mean wheel location: This is the distance between the external edge of the nearest truck wheel and the pavement edge marking. The value for mean wheel location may be derived from specific site data, statewide data, or the national average. This study used a default value of 18 inches.

Traffic wander standard deviation: This is the standard deviation of the lateral traffic wander. The input defines the average position of the axle from the point for predicting distresses and performance. The greater the wander value, the higher the fatigue life. The default wander standard deviation of 10 inches was used in this study.

Design lane width: This is the distance between two lane markings of the design lane. This distance may or may not be equal to the slab width. This study used a default value of 12 ft for the standard lane width.

Number of axle types per truck class: This requires an insertion of the average number of axles for each truck class (Class 4 to 13) and each axle type (single, tandem, tridem, and quad). The values for truck cases L1 to L9, as obtained from Figure 7, are shown in Table 5.

Tab. 5 - Number of Axles per Truck Class

Truck case	Single	Tandem	Tridem	Quad
L1	1	2	0	0
L2	1	0	2	0
L3	1	2	0	0
L4	1	1	0	1
L5	1	0	2	0
L6	1	0	2	0
L7	1	1	0	1
L8	1	1	0	1
L9	1	1	0	1

Axle configuration: This is a section where decision values regarding axle configurations are inserted in order to aid in the pavement response computations. The inputs used included:

- **Average axle width:** This is the width covering from one outside edge of an axle to the other side. The default value of 8.5ft was used for this study.
- **Dual tire spacing:** This is the center to center distance between dual tires. The default value of 12 inches was used for this study.
- **Axle spacing:** This is the average distance between two consecutive axles of an axle group (tandem, tridem, or quad). The schematic drawings of the truck configuration provided in Figures 7 and 8 specified the values used in this study.
- **Tire pressure:** Tire pressure input is needed for estimation of the tire print area. The MEPDG has a fixed tire pressure of 120 psi. Therefore, the study had no other choice than using this value for the MEPDG analyses.



Wheelbase: Wheelbase information is used in the process of determining top down fatigue cracking. The information defines how far the steering axle is located from the drive axle of the same truck, and to what percentage is the wheelbase characterized as either short, medium, or long. The input values are applicable for vehicle Class 8 and above. The values for wheelbase are in two categories, namely:

- *Average spacing:* The MEPDG default axle spacing are 12, 15, and 18 ft for short, medium, and long axles, respectively. In this study, truck case L1 to L4 had an average axle spacing of 15 ft, while truck cases L5 to L9 had average axle spacing of 14 ft.
- *Percentage of truck axle spacing type:* This percentage represents the proportion of trucks with short, medium, and long axle spacing in a vehicle class. The default values provided in the MEPDG are 33, 33, and 34% for short, medium, and long axles, respectively. This study used 100% medium spacing for each truck analyzed since each truck has only one wheelbase.

Climate

Climate is one the major components of the MEPDG design guide. Climatic conditions have significant effect on concrete pavement performance indices such as curling up and down. In the design and analysis of JPCP pavements, the temperature and moisture effects that matter most are:

- A combination of permanent built-in curling during construction and permanent warping due to differential shrinkage.
- Transient hourly negative and positive non-linear temperature differences caused by the heat of the sun.
- Transient hourly negative humidity during each month of the year.

The MEPDG recommends the usage of an available database from nearly 800 weather stations in the USA. Some of these stations have about 100 months of climatic data. However, the MEPDG requires at least 24 months of actual weather station data for computational purposes. The software tracks any weather station data when its latitude (degrees), longitude (degrees), and elevation (ft) are manually inserted or imported from saved weather files. Albany, New York weather station was used in the analysis of this study. The station location is 42.45° latitude and -73.48° longitude at an elevation of 281 ft above mean sea level.

Another important parameter is the *groundwater table depth*. This parameter plays a significant role in the overall accuracy of the pavement moisture content, and hence, equilibrium moduli values. The depth is measured from the pavement surface. The MEPDG allows the user to insert either an estimate of the annual average depth or seasonal average depth (i.e., depths for all four seasons of the year). This study estimated and used Albany, New York's yearly average groundwater table depth of 10 ft [23].

Pavement structure

This aspect mainly defines the pavements layer design features and properties. As discussed subsequently, the JPCP design features required in the MEPDG software are slab thickness, permanent curl/warp effective temperature difference, joint design, edge support, slab-base interface, and base erodibility.

Slab thickness: The thickness of a concrete pavement slab may vary from 6 to 15 inches. However, slab thicknesses of 9 to 12 inches are commonly used in the USA. This study adapted a thickness of 12 inches for all the pavement and traffic damage analyses.

Permanent curl/warp effective temperature difference: This represents the locked stresses in the concrete slab due to construction temperatures, shrinkage, creep, and the curing processes. This value is negative because the top surface is expected to be cooler than the bottom surface under the initial conditions. This study adapted a default “curl/warp temperature difference” of -10°F as recommended in the MEPDG design guide [12].

Joint design: Concrete pavement joints refer to predetermined cracks designed to relieve the stresses in the concrete. As discussed in the subsequent text, the design inputs include type of sealant, joint spacing, and dowel sizing and spacing.

- **Sealant type** – the sealant type is an input to predict spalling. In turn, spalling is used in the smoothness prediction model, but the MEPDG does not consider it as a direct effect on performance. The types of sealant available for MEPDG analysis are liquid, silicon, and preformed sealants. This study used the *silicon type* of sealant for all the analysis.
- **Joint spacing** – joint spacing has effects on the stresses developed in the JPCP and its construction cost. The spacing increases the stresses but reduces the cost. Typical joint spacing is between 15~20ft [13]. In this study, a joint spacing of 15 ft was used.
- **Dowel diameter and spacing** – dowel diameter and spacing are critical inputs for predicting joint faulting. The larger the dowel diameter and the smaller the dowel spacing, the lower the concrete bearing stress and joint faulting. Respectively, the typical dowel diameters and spacing are 1 to 1.75 inches and 12 inches, respectively [12]. This study used a dowel spacing of 12 inches and dowel diameter of 1.5 inches.

Edge support: The edge support inputs required by the MEPDG are tied concrete shoulders or widened slab, and long-term load transfer efficiency (LTE). Tied shoulders can significantly improve JPCP performance by reducing critical deflections and stresses along the edge. In this study, *tied concrete shoulders* with a long-term LTE of 70%, which lies between the values recommended for monolithically constructed tied shoulders, was used.

Slab-base interface: The structural contribution of a stabilized base under a cement concrete slab is significant if the base is fully bonded to the slab. However, the effects of environmental and traffic loading tend to weaken the bond over time. This study used a non-stabilized crushed stone base; thus, unbonded conditions were assumed throughout the JPCP design life.

Base erodibility: This input has significant effects on the initiation and development of pavement distresses. The MEPDG classifies the base types according to their erodibility behavior as follows:

- Class 1 – Extremely erosion resistant materials
- Class 2 – Very erosion resistant materials
- Class 3 – Erosion resistant materials
- Class 4 – Fairly erodible materials
- Class 5 – Very erodible materials

This study defined the used base materials as *Class 3 – erosion resistant* materials. This is the average class of erodibility property of material defined by the MEPDG guide.

Other essential parameters of structure inputs fall in the category of design layers and properties. The MEPDG software allows as many layers as practically possible to reflect and accommodate the actual various pavement structures in the field. The layer properties used in this study are shown in Table 6.

Tab. 6 - Pavement Design Layers and Properties.

Layer and Mix Properties	Layers			
	Layer – 1 (12 in)	Layer – 2 (12 in)	Layer – 3 (60 in)	Layer – 4 (Semi-infinite)
	Concrete slab surface	Crushed stone base	CH-subgrade	Weathered rock bed
Surface absorptive	0.85	N/A	N/A	N/A
Unit weight (pcf)	150			140
Poisson's Ratio	0.15	0.35	0.4	0.15
Coefficient of lateral pressure (k_o)		0.5	0.5	
Coefficient of thermal expansion (per °F x 10 ⁻⁶)	5.5	N/A	N/A	N/A
Thermal conductivity (BTU/hr-ft- °F)	1.25	N/A	N/A	N/A
Heat capacity (BTU/lb- °F)	0.28	N/A	N/A	N/A
Cement type	Type I	N/A	N/A	N/A
Cementitious material content (lb/yd ³)	600	N/A	N/A	N/A
Water/cement ratio	0.4	N/A	N/A	N/A
Aggregate type	Limestone	N/A	N/A	N/A
Ultimate shrinkage at 40% R.H (microstrains)	50	N/A	N/A	N/A
Time to develop 50% ultimate shrinkage (days)	35	N/A	N/A	N/A
Curing Method	Compound curing	N/A	N/A	N/A
28 days modulus of rupture (psi)	700	N/A	N/A	N/A
28 days elastic modulus (psi)	4,000,000	N/A	N/A	N/A
Resilient modulus (psi)		35,000	5,000	500,000

Legend: N/A = Not Applicable

RESULTS AND ANALYSIS

At first, the MEPDG analysis predicted the levels of both top-down and bottom-up fatigue cracking along with joint faulting. Then, the roughness of the pavement surface, expressed in terms of the International Roughness Index (IRI), was computed from the cracking and joint faulting data. Figures 9 to 11 show typical trends of the predicted damages from initial to the 40th year due to cracking, faulting, and roughness, respectively. There are three plots in each figure representing the estimated damages at 100% and 90% reliability and limit damage criteria. As described in the input section, this study used 90% reliability level. Based on the failure criteria adapted in this study (MEPDG default values), the pavement analytically failed by faulting and roughness. However, in this study, the failure criteria are inconsequential (as opposed to a design problem) since the MEPDG software was intentionally preset to complete the runs and not necessarily to limit the damages.

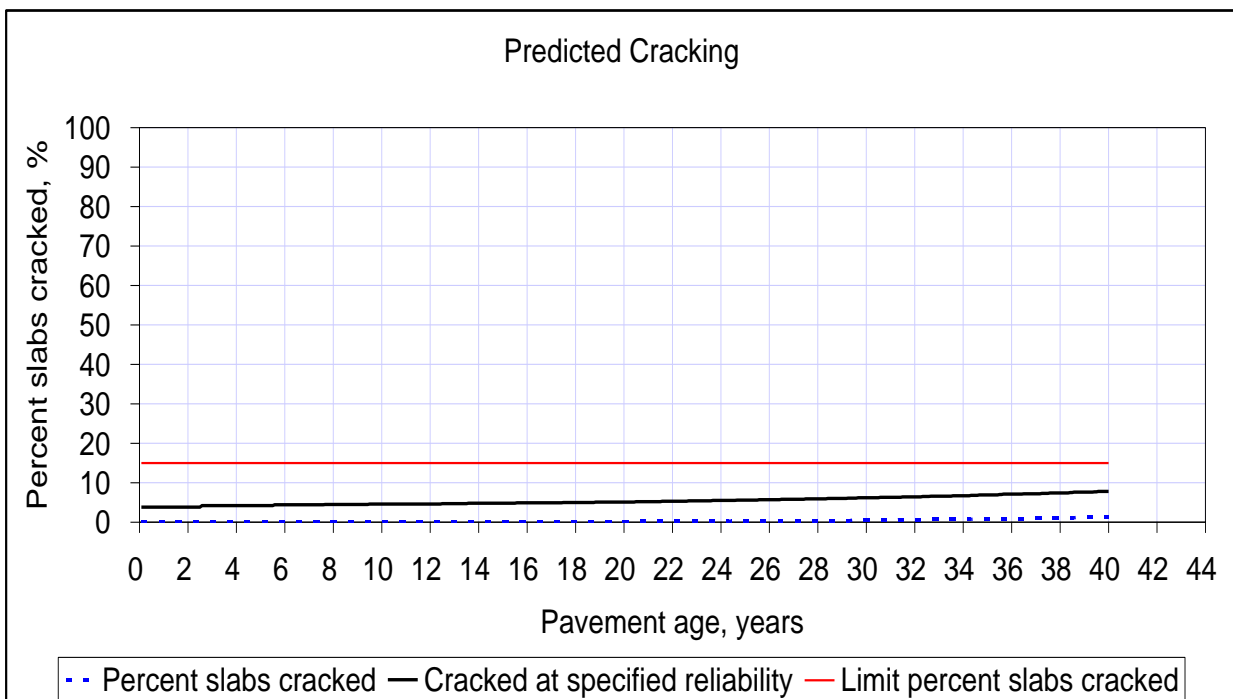


Fig. 9 - Typical % Slab Cracking Development as a function of Time.

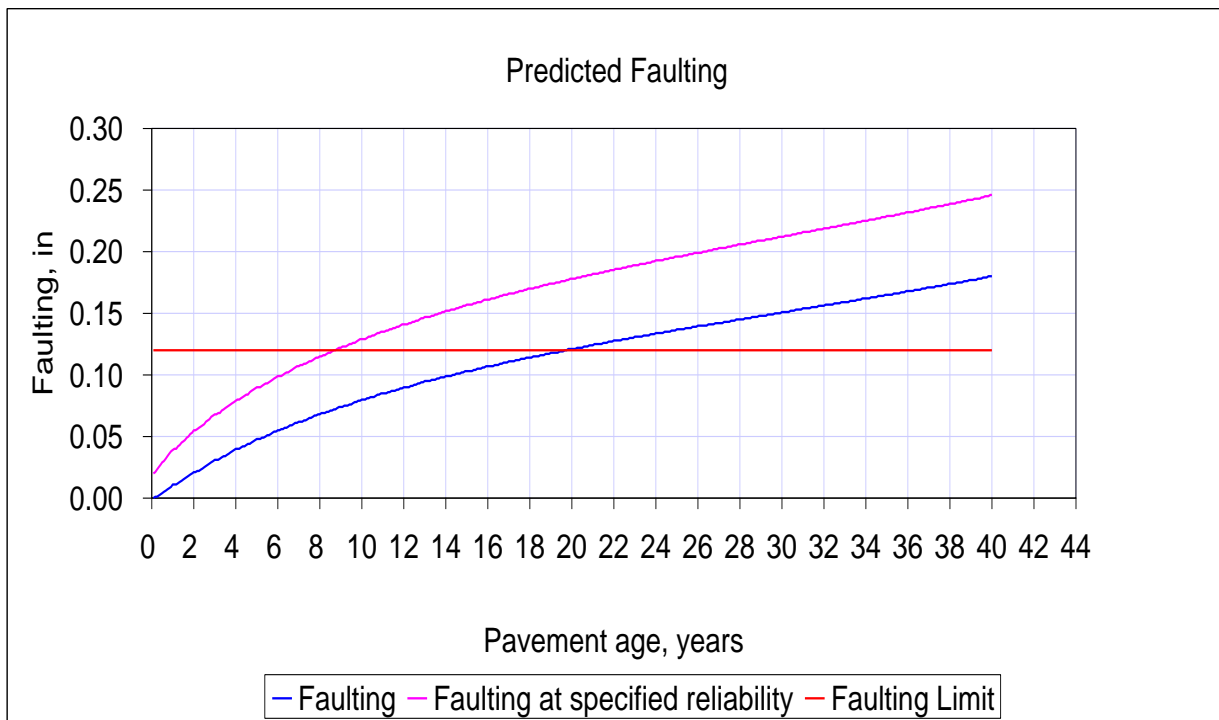


Fig. 10 - Typical Faulting Development as a function of Time.

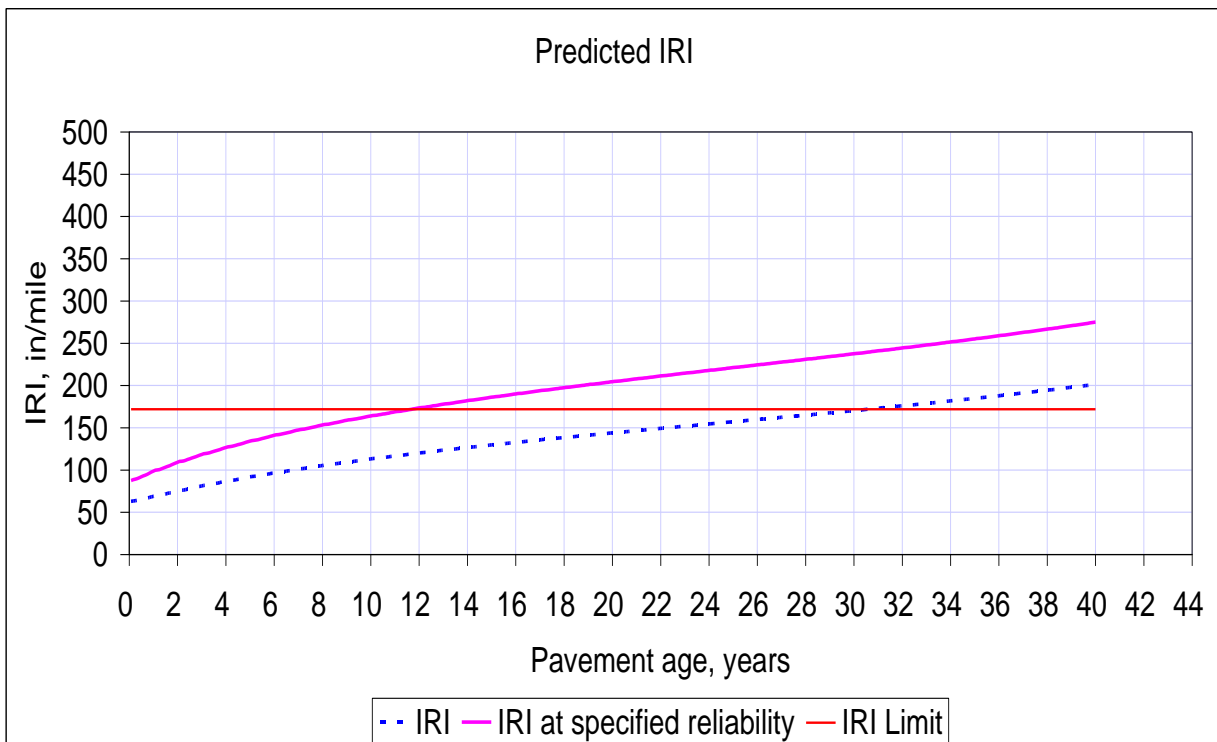


Fig. 11 - Typical IRI Development as a function of Time.

In addition, the study determined relative damages by dividing each truck damage to the damage developed under truck case L1a (the selected base truck). L1 was one of the simplest truck configuration analyzed in this study and was arbitrarily utilized as the base truck. The relative damage simplified the comparison of the truck damages. A summary of the MEPDG damage output and average truck damages are shown in Table 10 and Figure 12, respectively. The results show that truck case L7 was more detrimental to the JCPD pavement than any other truck case presented in this paper. The truck case L7 is composed of steering single, tandem, and quad axle on the trailer. Moreover, on its tandem axle it carries the most loads per wheel than any axle group analyzed, which presumably contributed to its detrimental damaging effects. Figure 12 also shows that the variations in the truck configuration have relatively small effect on the rate of change of faulting and roughness. Similarly, relatively smaller damages were observed for truck cases L4, L5, and L6. A combination of greater number of wheels per truck (larger axle groups) and lesser load distribution per wheel contributed to the relatively smaller damages from these truck cases.

Tab. 10 - Summary of the MEPDG Performance Output.

Truck Case	Bottom-Up Cracking		Top Down Cracking		Transverse Cracking (% Slab)		Faulting		IRI	
	Dam at Year 40	Relative Damage	Dam at Year 40	Relative Damage	Dam at Year 40	Relative Damage	Dam at Year 40	Relative Damage	Dam at Year 40	Relative Damage
L1a	0.0023	1	0.11	1	8.1	1.00	0.25	1.00	276	1.00
L1b	0.0073	3.17	0.14	1.23	9.2	1.14	0.25	1.00	275	1.00
L1c	0.0302	13.13	0.21	1.87	13.2	1.63	0.25	1.00	280	1.01
L2a	0.0026	1.13	0.21	1.87	12.1	1.49	0.25	1.00	279	1.01
L2b	0.0083	3.61	0.21	1.87	13	1.60	0.24	0.96	270	0.98
L2c	0.0339	14.74	0.21	1.87	12.5	1.54	0.25	1.00	280	1.01
L3	0.0023	1	0.11	1	8.5	1.05	0.24	0.96	275	1.00
L4	0.0001	0.04	0.02	0.18	5	0.62	0.22	0.88	260	0.94
L5	0.0043	1.87	0.02	0.21	5	0.62	0.26	1.04	278	1.01
L6	0.0062	2.7	0.02	0.21	5	0.62	0.26	1.04	282	1.02
L7	0.0218	9.48	0.21	1.88	25	3.09	0.28	1.12	305	1.11
L8	0.0072	3.13	0.26	2.36	15	1.85	0.28	1.12	299	1.08
L9a	0.0019	0.83	0.16	1.41	10	1.23	0.27	1.08	290	1.05
L9b	0.0019	0.83	0.16	1.41	10	1.23	0.27	1.08	295	1.07
L9c	0.0019	0.83	0.16	1.41	10	1.23	0.27	1.08	295	1.07

Dam = damage

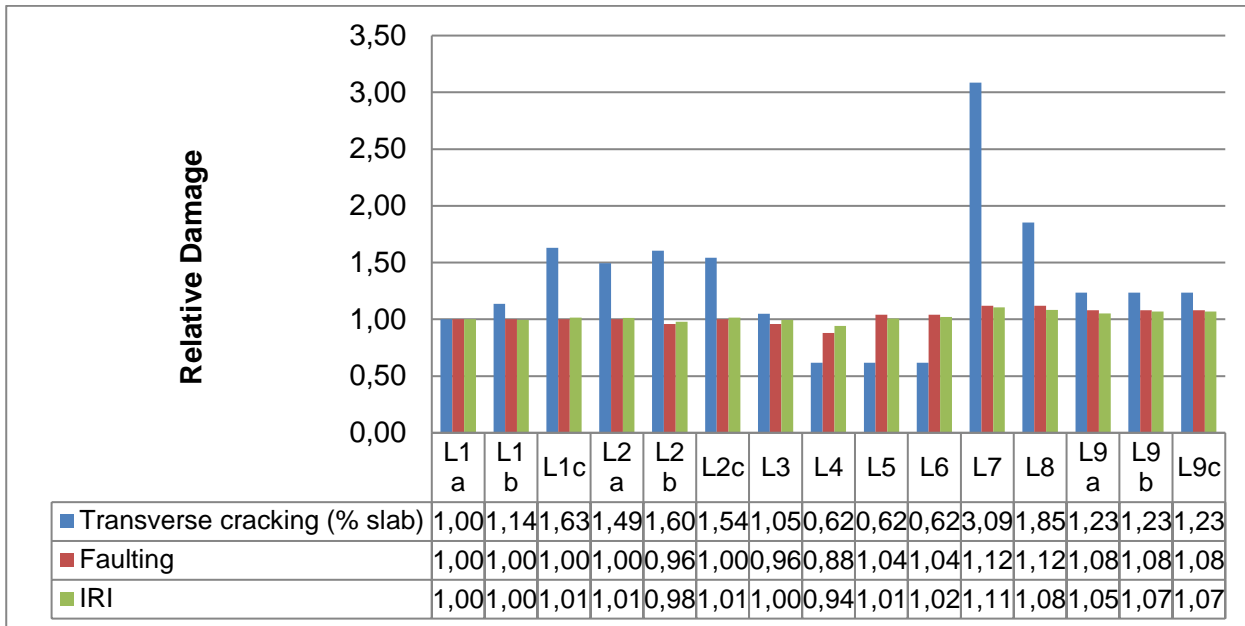


Fig. 12 - Transverse Cracking, Faulting, and IRI Damages for All Truck Cases.

Furthermore, the study analyzed the effects on JPCP due to load shifting and changes in the space between the axle groups. These aspects are discussed in the subsequent text.

Effects of load shifting (equal sized axles)

Figures 13 and 14 present the MEPDG damage analysis results for trucks L1 (tandem to tandem axles load shifting) and L2 (tridem to tridem axles load shifting), respectively. The results indicate that shifting of the loads increases damage for all the types of JPCP cracking that were assessed. By contrast, faulting and roughness were negligibly affected by shifting the load. Of all the damages under this category, bottom up cracking had the highest rate of increase of damage. In addition, the study observed slightly higher damages due to truck case L2 (tridem wheels) than truck case L1 (tandem wheels) even though each wheel of the truck cases carried the same weight. For example, truck cases L1a and L2a all have 17,000bs per wheel.

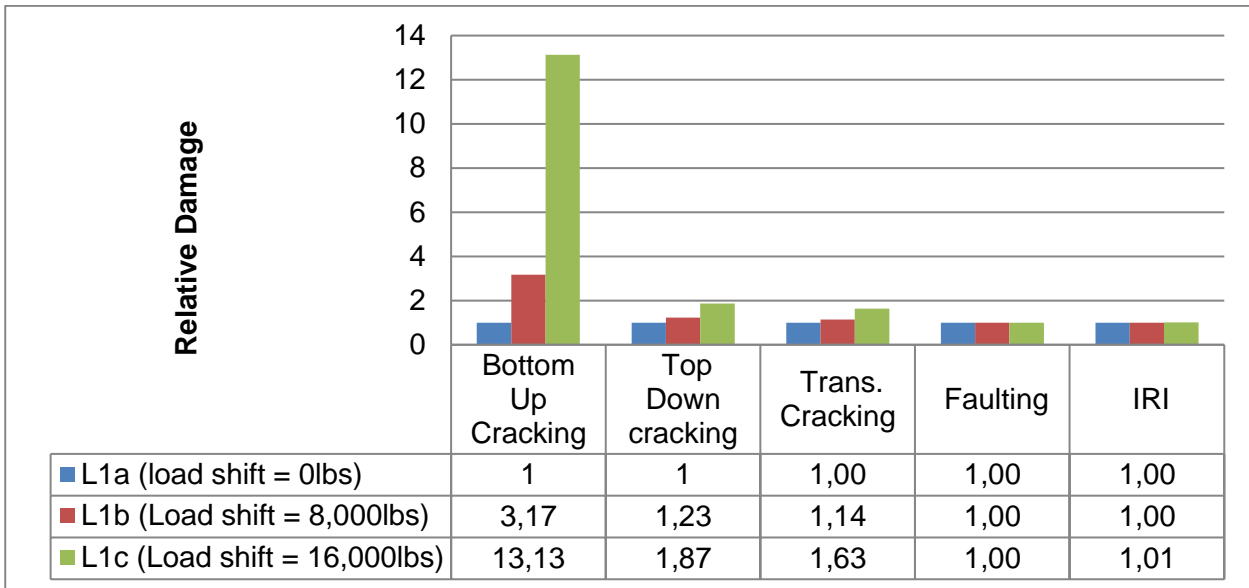


Fig. 13 - Truck Case L1– Effect of Shifting Loads between Equal Axles.

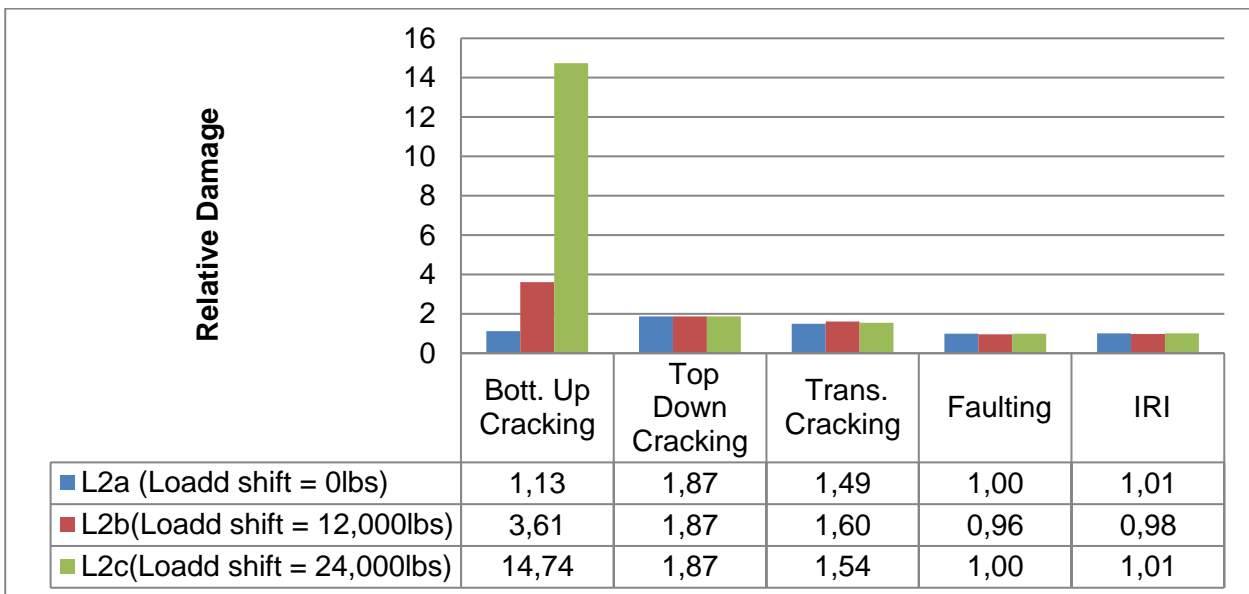


Fig. 14 - Truck Case L2– Effect of Shifting Loads between Equal Axles.

Effects of load shifting (unequal sized axles)

Figure 15 shows the MEPDG damage analysis results for trucks case L7, L8, and L9a. The truck cases represent the effects of load shifting for unequal sized axles (i.e., from tandem to quad axle). Relative to truck case L7, the shifted loads were 6,000lbs and 12,000lbs for truck cases L8 and L9a, respectively. The figure illustrates a decrease in cracking damage whenever the loads are shifted from tandem to quad axle. Likewise, negligible change in faulting and IRI damages was observed.

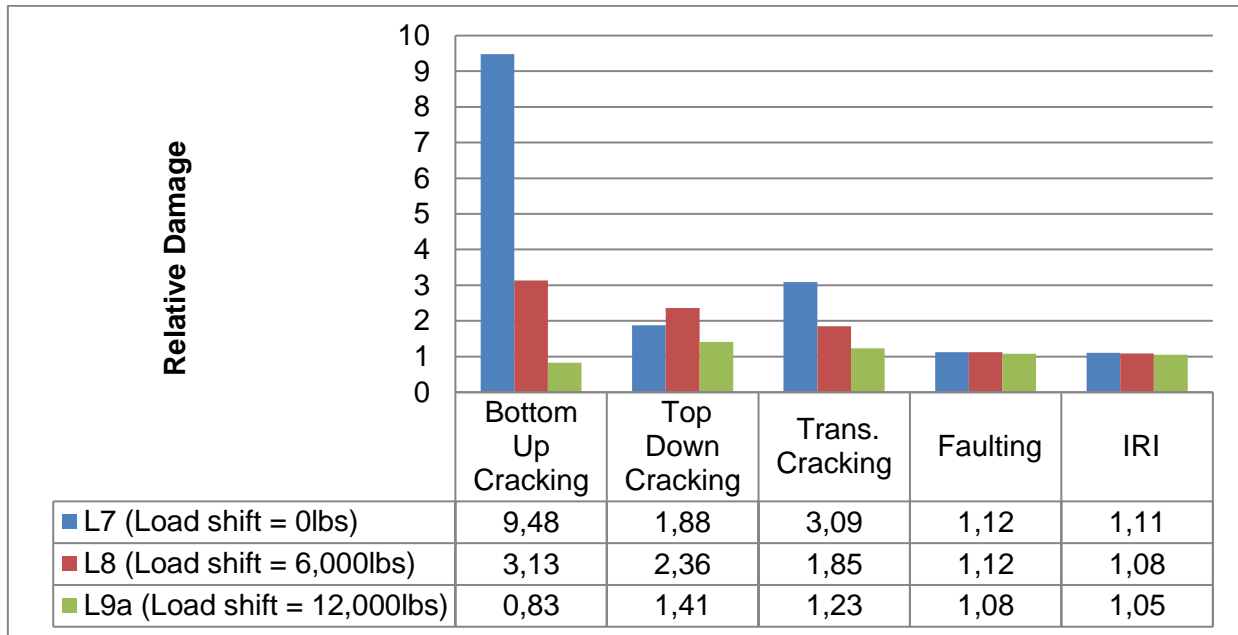


Fig. 15 - Effect of Load Shifting from Tandem to Quad.

Effects of increasing spaces between the axles of an axle group

Figure 16 shows relative damage to the JPCP pavement due to increase in the axle spacing of truck case L15. The wheel spacing for the axle group was 48", 60", and 90" for truck case L9a, L9b, and L9c, respectively. The MEPDG damage analysis results as shown in Figure 16, depict that JPCP is not sensitive to the spacing of the wheels in any axle group.

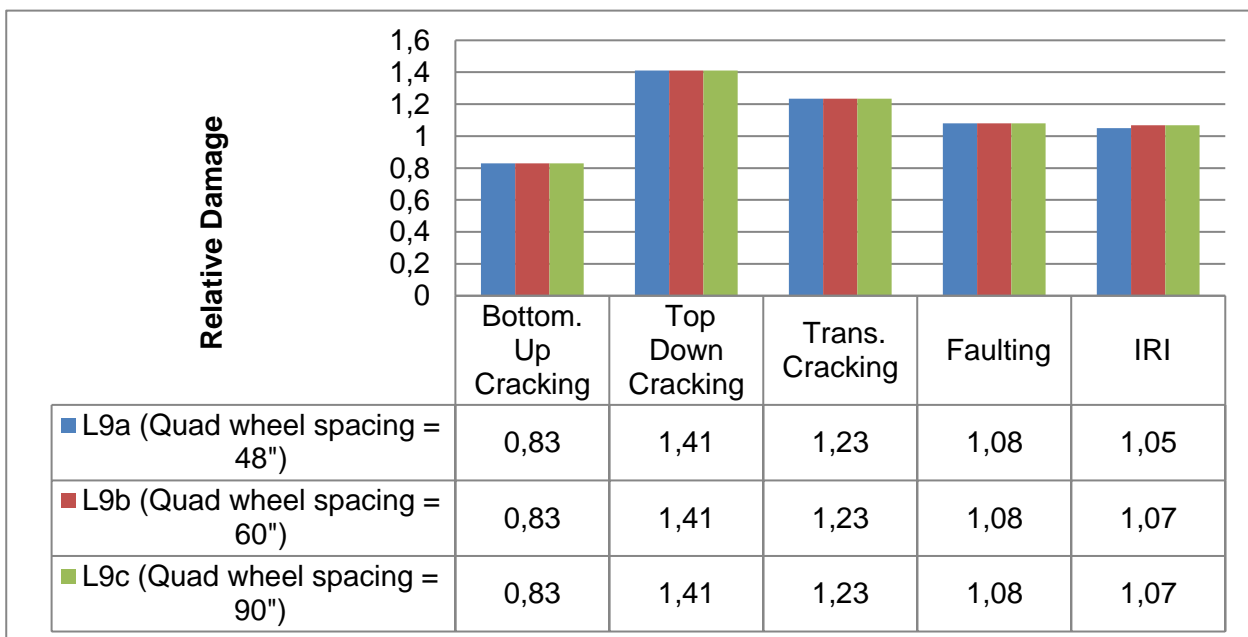


Fig. 16 - Effect of Changing Axle Spacing for Truck.

CONCLUSION

The aim of this study was to compare trucks in terms of major damages caused to concrete pavements. The study was successful not only at identifying the most damaging truck cases, but also at establishing the trends of truck damage when the axle loads were shifted, or when axle spacing in an axle's group were changed. Based on these results, the following conclusions can be made:

- When loads are shifted between the axles of the same size, on the same truck, the damage increases as the shifted load increases; the minimum damage occurs when the axles are loaded equally. Two sets of truck cases L1 (tandems) and L2 (tridem) were used to demonstrate this behavior.
- The rate of increase of truck damage due to load shifting between equal axles of the same size was higher for truck L1 (tandem axles) than L2 (tridem axles).
- As expected, at the same axle load, when a tandem axle is replaced by a tridem or quad axle, the damage to the pavement decreases. This was evidenced by a reduction in truck damage when truck case L7, having tandem axles, was replaced by truck cases L8 and L9a, which have tridem and quad axles, respectively.
- Based on the MEPDG analysis, increasing spacing in an axle group (i.e., quad axle group) does not change the extent of fatigue cracking, faulting, or roughness of the JPCP.
- As theoretically expected, trucks with excessive loads per wheel impacted more damage to the pavement as exemplified by truck case L7.

Overall, the study findings highlight the importance of evenly distributing the truck loading on the axles so as to minimize pavement damage. As was demonstrated in this paper, minimum damage occurred when the truck axles were loaded equally. However, the MEPDG damage analysis in this study was performed on a concrete pavement with a slab thickness of 12 inches that yielded relatively small damage levels. Therefore, future studies should consider thinner slabs where substantial damage from truck loading is theoretically expected.

ACKNOWLEDGEMENTS

This study is part of a research work conducted at the University of Texas-Arlington (UTA) based on truck configurations data provided by the New York State Department of Transportation (NYSDoT). The authors thank NYDoT for their support of this research work and all those who helped during the course of the study and documentation of this paper.

The contents of this paper reflect the views of the authors who are responsible for the facts and accuracy of the data presented herein and do not necessarily reflect the official views or policies of any agency or institute. This paper does not constitute a standard, specification, nor is it intended for design, construction, bidding, contracting, tendering, certification, or permit purposes. Trade names were used solely for information purposes and not for product endorsement, advertisement, or certification.

REFERENCES

- [1] Gillespie T.D., Karamihas S.M., Cebon D., Sayers M.W., Nasim M.A., Hansen W., Ehsan N., 1993. Effects of Heavy Vehicle Characteristics on Pavement Response and Performance. National Cooperative Highway Research Program Report 353, Transportation Research Board, (National Research Council, Washington, DC).

- [2] Hudson W.R., Monismith C.L., Dougan C.E., Visser W., 2003. Use Performance Management System Data for Monitoring Performance: Example with SuperPave. Transportation Research Record 1853, TRB, Washington DC.
- [3] Yu H. T., Khazanovich L., Darter M. I., Ardani, A., 1998. Analysis of Concrete Pavement Responses to Temperature and Wheel Loads measured from Instrumented Slabs. In Journal of Transportation Research Board No. 1639, TRB,(National Research Council, Washington, D.C.), 94–101 pp.
- [4] Zaghoul S., White T.D., 1994 Guidelines for permitting overloads – Part 1: Effect of overloaded vehicles on the Indiana highway network. FHWA/IN/JHRP-93–5. Purdue University, West Lafayette, Ind.
- [5] Chen H., Dere Y., Sotelino E., Archer G., 2002. Mid-Panel Cracking of Portland Cement Concrete Pavements in Indiana, FHWA/IN/JTRP-2001/14, Final Report
- [6] Ceylan H., Kim S., Gopalakrishnan K., Schwartz C.W., Li R., 2013. Sensitivity quantification of jointed plain concrete pavement mechanistic-empirical performance predictions. Construction and Building Materials 43, 545-556.
- [7] Vandenbossche J.M., Nassiri S., Ramirez L.C., Sherwood J.A., 2012. Evaluating the continuously reinforced concrete pavement performance models of the mechanistic-empirical pavement design guide. Road Materials and Pavement Design 13:2, 235-248.
- [8] Vandenbossche J.M., Mu F., Burnham T.R., 2011. Comparison of measured vs. predicted performance of jointed plain concrete pavements using the Mechanistic–Empirical Pavement Design Guideline. International Journal of Pavement Engineering 12:3, 239-251.
- [9] Wu C. P., Shen, P.A., 1996. Dynamic analysis of concrete pavements subjected to moving loads. J. Transp. Engrg., 122(5), 367–373.
- [10] Huang Y. H., 1974. Finite element analysis of slabs on elastic solids. Transp. Engineering. J., ASCE, 100(2), 403–416.
- [11] Chatti K., Monismith C. L., Mahoney J. P., 1995. Investigation of asphalt concrete pavement cracking from heavy vehicles, phase II, Tech. Rep. on Project. F89TL29, Inst. of Transp. Studies, University of California, Berkeley, Berkeley, CA.
- [12] NCHRP, March 2004. Guide for Mechanistic-Empirical Design of New and Rehabilitated Pavement Structures. Final Report for Project 1-37A, Part 1, 2 & 3, Chapter 4. National Cooperative Highway Research Program, Transportation Research Board, National Research Council, Washington, D.C.
- [13] WSDOT. WSDOT Pavement Guide, Washington State Department of Transportation, URL: <http://training.ce.washington.edu/WSDOT/>, Accessed May 2009.
- [14] Huang Y.H., 2004. Pavement Analysis and Design. Prentice Hall, Inc., New Jersey.
- [15] American Concrete Pavement Association (ACPA). http://metiebar.acpa.org/Concrete_Pavement/Technical/Fundamentals/Concrete_Types.asp, accessed January 2017.
- [16] American Association of State Highways and Transportation Officials (AASHTO), 1993. AASHTO Guide for Design of Pavement Structures, Washington, D.C.
- [17] Federal Highway Administration, September, 2005. Long-Term Plan for Concrete Pavement Research and Technology- The Concrete Pavement Road Map: Volume I, URL: <http://www.fhwa.dot.gov/pavement/pccp/pubs/05052/index.cfm>, Publication number: FHWA-HRT-05-0520,
- [18] Darestani M. Y., Nataatmadja A., Thambiratnam D.P., 2006. A Review of 2004: Austroads Rigid Pavement Design, 22nd ARRB Conference – Research into Practice, Canberra Australia..
- [19] Kim S.M., Won M.C., Mccullough B.F., 2002. Dynamic Stress Response of Concrete Pavements to Moving Tandem-Axle Loads, Transp. Res. Record, No. 1809, 32-41 pp.
- [20] Hiller J.E., Roesler J.R., 2002. Transverse Joint Analysis for Use in Mechanistic-Empirical Design of Rigid Pavements, Transportation Research Record 1809, TRB, National Research Council, Washington, DC, 42-51 pp.
- [21] Darestani M. Y., Thambiratnam P., Nataatmadja D.A., Baweja D., 2008. Influence of vehicular positions and thermal effects on structural behaviour of concrete pavement. Journal of Mechanics of Materials and Structures, 567-589 pp.
- [22] <https://www.fhwa.dot.gov/reports/tswstudy/Vol3-Chapter5.pdf>. Accessed January 2017
- [23] <https://waterdata.usgs.gov/ny/nwis/current/?type=gw>. Accessed January, 2017

FINITE ELEMENT ANALYSIS OF THE BEHAVIOUR OF REINFORCED CONCRETE COLUMNS CONFINED BY OVERLAPPING HOOPS SUBJECTED TO RAPID CONCENTRIC LOADING

Xiang Zeng^{1,2}

1. College of Civil Engineering and Architecture, Hainan University, No.58, Renmin Ave., Haikou 570228, China
Hainan Institute of Development on International Tourist Destination, No.58, Renmin Ave., Haikou 570228, China; E-mail: zengxce@hainu.edu.cn

ABSTRACT

The strain rate sensitivity of concrete material was discovered approximately one hundred years ago, and it has a marked effect on the behaviour of concrete members subjected to dynamic loadings such as strong earthquake and impact loading. Because of the great importance of the confined reinforced concrete (RC) columns in RC structures, the dynamic behaviour of the columns induced by the strain rate effect has been studied, but only few experiments and analyses have been conducted. To investigate the behaviour of overlapping hoop-confined square reinforced normal-strength concrete columns, considering the strain rate effect at a strain rate of $10^{-5}/\text{sec}$ to $10^{-1}/\text{sec}$ induced by earthquake excitation, an explicit dynamic finite element analysis (FEA) model was developed in ABAQUS to predict the behaviour of confined RC columns subjected to the rapid concentric loading. A locally modified stress-strain relation of confined concrete with the strain rate sensitivity of the concrete material and the confining effect of overlapping hoops were proposed to complete the simulation of the dynamic behaviour of concrete with the concrete plastic-constitutive model in ABAQUS. The finite element predictions are consistent with the existing test results. Based on the FEA model, a parametric investigation was conducted to capture more information about the behaviour of confined RC columns under varying loading rates.

KEYWORDS

Reinforced concrete columns, Rapid loading, Overlapping hoops, Confining effect, Strain rate sensitivity, Finite element analysis, Parametric investigation

INTRODUCTION

With the increasing strain rate of concrete and reinforcing steel, the properties of these materials change. This refers to the strain rate sensitivity of concrete and reinforcing steel, which has been documented in literature [1-5]. The strain rate sensitivity of the materials significantly affects the behaviour of reinforced concrete (RC) members under dynamic loading. As a typical type of dynamic load, earthquake loading induces strain rates on the structures. The quasi-static strain rate is commonly approximately $10^{-6}/\text{sec}$ to $10^{-5}/\text{sec}$. Bertero predicted that for a notably rigid RC structure with a fundamental natural period of approximately 0.1 s under earthquake action, the strain rate at some critical regions can be as high as 0.025/sec [6]. Generally, the strain rate of materials in RC structures under earthquake loading is approximately from $10^{-4}/\text{sec}$ to $10^{-1}/\text{sec}$ [7-9]. Asprone et al. conducted an earthquake evaluation analysis of RC structures to appreciate the effect of the strain rate sensitivity of concrete and reinforcing steel on the global seismic response of RC structures [10]. The result shows that considering the updated material properties, to

account for the earthquake-induced strain rate, a strength reserve of the structural system is experienced when only ductile failure mechanisms are considered; on the other hand, the structural capacity decreases when brittle failure mechanisms are included. The evaluation method with consideration of the strain rate effect of the behaviour of RC structures under earthquake loading appears to be more proper.

The RC column is an elementary member of RC structures. The strain rate effect on the dynamic behaviour of RC columns by directly imparting rapid loading protocols has been partially studied. Reinschmidt et al. conducted several static and dynamic tests on plain and RC columns with a slenderness ratio (L/D) of 3 to 25 under eccentric or concentric axial loads [11]. They observed a 30-40 percent increase in the strength of columns under dynamic loads compared with the contrast columns under quasi-static loads, except the notably slender columns with a slenderness ratio of 25 were 70 to 100 percent stronger under dynamic loads than those tested under quasi-static loads. Xu and Zeng [12] found that the lateral inertial effect played an important role in increasing the axial bearing capacity for slender columns under axially rapid loading. Iwai et al. investigated the effect of the axial loading rate on the behaviour of RC columns [13]. Four short columns ($L/D=6$) and eight long columns ($L/D=16$ and 26) were tested under concentric and eccentric loads. The experimental results show that the maximum load of dynamically loaded columns is 11-14% larger than that statically loaded for concentric compression and 17- 37% larger under dynamic load for eccentric compression.

The aforementioned studies did not fully account for the confined effect of hoops under high strain rates. Under a static load, various studies show that the confined concrete behaves better than unconfined concrete. Then, the behaviour of confined concrete under dynamic loading becomes an interesting topic. To investigate the behaviour of concrete confined by hoops under rapid loading, Scott et al. conducted a test programme on twenty-five square short RC columns with different longitudinal steel bars and arrangements of overlapping hoops, which were subjected to concentric and eccentric loads at different strain rates [14]. The compressive strain rate was either 0.000033/sec or 0.0167/sec. The test results show that a high longitudinal strain rate (0.0167/sec) increases the peak stress and descending branch of the core concrete by approximately 25%. A stress-strain curve for confined concrete loaded at a high strain rate was proposed by modifying Kent and Park's [15] stress-strain relation for confined concrete with a dynamic multiplying factor of 1.25 for the peak stress, strain at the peak stress and slope of the falling branch. Li et al. experimentally investigated the behaviour of short reinforced high-strength concrete columns [16]. Thirty specimens with different confining reinforcement configurations, yield strengths of transverse reinforcement and concrete compressive strengths, were tested under concentric loads at different strain rates (0.000011/sec and 0.0167/sec). The test results confirmed that high-strength concrete had lower strain rate sensitivity than low- and moderate-strength concrete. Under high strain rate loading, the modulus of elasticity and slope of the descending branch of the stress-strain curve increase, but the effect of the high strain rate on the compressive strength depends on the strength of the transverse reinforcement. Zeng and Xu [17] developed an FEA model in general-purpose finite element computer program ABAQUS to predict the behaviour of laterally confined short RC columns under rapid concentric loading, but the model had a shortcoming: the cover concrete and core concrete were simulated with the same identical constitutive models.

Despite two experimental programmes and limited numerical analyses that investigated the effects of the loading rates on RC columns confined by transverse reinforcement, the state of the art on the subject remains in its infancy. Until now, notably limited experimental data can be acquired to investigate the effect of different parameters at high strain rate, and there is notably little finite element modelling on the dynamic behaviour of RC columns. Because of the high requirement on loading instrument for the rapid loading test, the FEA modelling becomes a good choice for parametric studies. In this paper, the objective is to investigate the dynamic behaviour of square reinforced normal-strength concrete columns confined by overlapping hoops under rapid

concentric loading through finite element analysis. To model the behaviour of concrete confined by overlapping hoops (different from the hoops in the study by Zeng and Xu [17]) at high strain rates using the concrete damaged plasticity model in ABAQUS, a locally modified compressive stress-strain relation of concrete was developed based on the work by Zeng and Xu [17], which considers the confining effect of the overlapping hoops and strain rate effect of concrete. Then, an explicit dynamic FEA model was established in ABAQUS to evaluate and predict the behaviour of the overlapping-hoop-confined square reinforced normal-strength concrete columns with two different reinforcement arrangements (type A and type B, as shown in Figure 1). Finally, the effect of the parameters including the loading strain rate (3×10^{-5} - 3×10^{-1} /sec), reinforcement arrangement (type A and type B), longitudinal reinforcement ratios (ρ_s : 2.65% and 1.27%) and volumetric ratios of transverse reinforcement (ρ_{sv} : 3% and 1.5%) on the dynamic behaviour of confined RC columns was investigated.

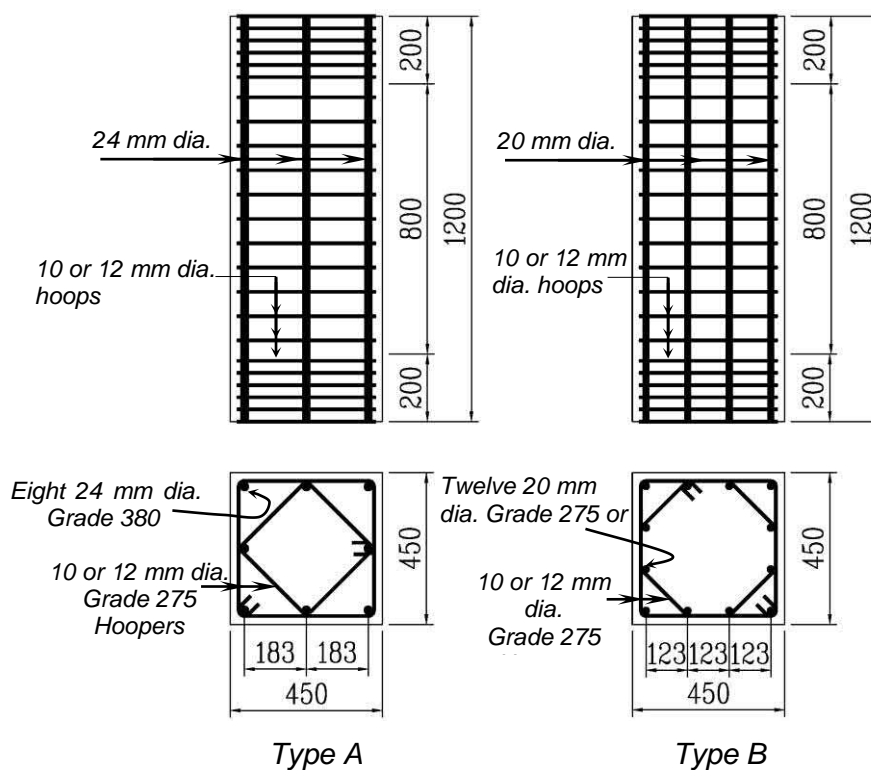


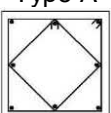
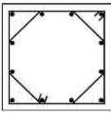
Fig. 1 - Typical details of the test units

BRIEF DESCRIPTION OF THE RAPID AXIAL LOADING EXPERIMENT ON RC COLUMNS

Until now, the experimental data of square reinforced normal-strength concrete columns confined by overlapping hoops under axial rapid loading have been notably limited and can only be acquired from literature [14]. In the paper, eight RC columns confined by overlapping hoops from the rapid concentric loading experiment of Scott et al. [14] were used to verify the following FEA model. Figure 1 shows that all test specimens have identical cross sections of 450 mm x 450 mm and are 1200 mm high. The longitudinal concrete strains in the test units were measured over the central 400-mm gage length of the units. Two reinforcement arrangements (type A and type B, as shown in Figure 1) were used. These arrangements are typical for 8-bar and 12-bar columns. The centre-to-centre spacing of longitudinal bars across the section for type-A and type-B arrangements was 183 mm and 123 mm, respectively. More details of the cross-sections in the test regions of different columns are shown in Table 1. The volumetric ratio of transverse

reinforcement ρ_{sv} is 0.0134 to 0.0309. The spacing of transverse hoops was reduced by one-half for 200 mm at each end of the test columns to provide extra confinement and ensure that failure occurred in the 800-mm-long central region. For columns under rapid concentric loadings, the strain rate was 0.0167/sec, which is representative of that expected during seismic loading. The quasi-static test columns with a strain rate of 0.0000033/sec were used for contrast.

Tab. 1 - Details of the cross-section of test columns

Specimens	Type of load	Reinforcement arrangement	Concrete compressive cylinder strength f_c (Mpa)	Longitudinal reinforcement			Transverse reinforcement			
				Number of bars	Diameter (mm)	Yield strength f_y (Mpa)	Diameter (mm)	Spacing (mm)	Yield strength f_{hy} (Mpa)	Volumetric ratio ρ_{sv}
Unit6	Quasi-static	 Type A	25.3	8	24	394	10	72	309	0.0174
Unit7	Rapid loading		25.3				10	72	309	0.0174
Unit17			24.8				10	98	309	0.0134
Unit19			24.8				12	88	296	0.0213
Unit20			24.8				12	64	296	0.0293
Unit2	Quasi-static	 Type B	25.3	12	20	434	10	72	309	0.0182
Unit3	Rapid loading		25.3				10	72	309	0.0182
Unit12			24.8				10	98	309	0.014
Unit14			24.8				12	88	296	0.0224
Unit15			24.8				12	64	296	0.0309

EXPLICIT DYNAMIC FEA MODELLING

To avoid numerical difficulty in convergence, the analysis module ABAQUS/Explicit was used to solve the quasi-static and dynamic analysis of RC columns under concentric loading.

The steel rebar was modelled using a 2-node linear 3D truss element (T3D2) in the explicit element library. The concrete was modelled using 8-node brick elements (C3D8R) in the explicit element library with three translational degrees of freedom at each node. The approximate global mesh size of 50 mm was used to discretize the concrete body, which can provide a precise simulation result. The load plate was modelled with an analytical rigid part, which is reasonable to save the computing cost because the load plate of the test machine is sufficiently stiff.

An embedded region constraint was used to simulate the interaction between the steel bars and concrete, which embedded the steel bars (embedded elements) into the concrete (host elements). In other words, the translational degrees of freedom of the embedded node were constrained to the interpolated values of the corresponding degrees of freedom of the host element, but these rotations were not constrained by the embedding [18]. General contact in the explicit module was used to simulate the interaction between the surfaces of the rigid load plate and the end of the column, which combines a rough friction formulation for the tangential behaviour and a contact pressure model for the normal direction behaviour.

In Figure 2, a quarter model with symmetric boundaries on the X-Y plane and Y-Z plane was used based on the symmetry, which reduced the computation cost. In ABAQUS, the motion of the rigid load plate at the end of the column was constrained to the motion of a reference point, so the axial load was applied to the top reference point with an allowable translational motion in the direction Z and an allowable rotational motion around the X-axis. The boundary conditions in the FEA model were selected according to the actual experimental boundary conditions.

Concrete material model

The concrete damaged plasticity model [18] was used to simulate the behaviour of concrete. The constitutive model uses concepts of isotropic damaged elasticity in combination with isotropic tensile and compressive plasticity to represent the inelastic behaviour of concrete. The damaged

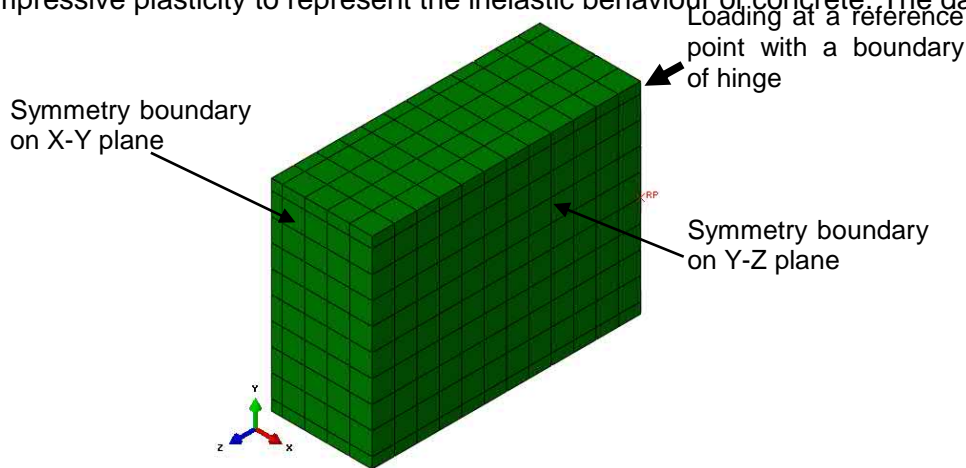


Fig. 2 - Illustration of the finite element model

model describes the irreversible damage that occurs during the fracturing process, which enables the user to control the stiffness recovery effects during cyclic load reversals. In this study, the test columns were under a monotonic load, there was no need to define the damaged model, and only the plasticity model was defined in the FEA model.

The plastic constitutive theory in the model is suitable to describe concrete and other quasi-brittle materials under fairly low confining pressures (less than four or five times the ultimate compressive stress in uniaxial compression loading) and can consider the strength improvement at the state of triaxial loading. It can also be defined as sensitive to the straining rate. The key parameters of the plasticity model are as follows: the dilation angle, eccentricity, ratio of the biaxial compression strength to the uniaxial compression strength of concrete, ratio of the second stress invariant on the tensile meridian to that on the compressive meridian and viscosity parameter are 30°, 0.1, 1.16, 0.667, and 0.0001, respectively [19]. Regarding the dynamic modulus of elasticity, Bischoff and Perry noted the confusion about whether the initial tangent modulus should change with the strain rate because of the confliction from different experimental results [2]. In this study, the modulus of elasticity is assumed to be constant for an effective numerical implementation in ABAQUS and is equal to $4730\sqrt{f_c}$ by ACI 318 [20], where f_c (N/mm²) is the compressive cylinder strength of concrete under a quasi-static load. Poisson's ratio of concrete is assumed to be constant under dynamic loading, as recommended by CEB [21], and is equal to 0.2. Moreover, an equivalent uniaxial compressive stress-strain relationship and tension stiffening are required in the plasticity model of concrete, which will be described as follows.

Uniaxial compressive stress-strain relation of confined concrete considering the strain rate effect

As previously mentioned, the range of strain rate of the materials in RC structures under earthquake loading is approximately 10⁻⁴/sec to 10⁻¹/sec [7-9]. To consider the strain rate sensitivity of concrete, the dynamic compressive cylinder strength f_{cd} of concrete can be estimated from Equations 1 and 2 provided by CEB-FIP Model Code 1990 [1].

$$f_{cd} / f_{cs} = \left(\frac{\dot{\epsilon}}{\dot{\epsilon}_{cs}} \right)^{1.02\alpha_s} \quad \dot{\epsilon} \leq 30s^{-1} \quad (1)$$

$$\alpha_s = \frac{1}{5 + 9f_{cs} / f_{co}} \quad (2)$$

where f_{cs} is the quasi-static compressive strength of unconfined concrete; $f_{cs}=0.85f_c$ considering a strength-reduction factor related to the column shape, size and the difference between the strength of in situ concrete and the strength determined from standard cylinder tests [22-23]; $\dot{\epsilon}$ is the strain rate (s^{-1}); $f_{co}=10$ Mpa; and $\dot{\epsilon}_{cs}=30 \times 10^{-6} s^{-1}$. f_{cd} increases with increasing strain rate; the other parameters in the following uniaxial compressive stress-strain curve correspondingly change, and the dynamic uniaxial compressive stress-strain curve is formed.

The uniaxial compressive stress-strain relation of confined concrete considering the strain rate effect is shown in Figure 3, which is suitable for the dynamic finite element analysis of concrete confined by overlapping hoops using ABAQUS. The basic equations (Equation 3 to 6) of the stress-strain relation, which were proposed by the author [17,19], are used.

$$y = \begin{cases} \alpha_a \cdot x + (3 - 2\alpha_a)x^2 + (\alpha_a - 2)x^3 & (x \leq 1) \\ \frac{x}{\alpha_d \cdot (x - 1)^2 + x} & (x > 1) \end{cases} \quad (3)$$

$$x = \frac{\epsilon}{\epsilon_{co}} ; \quad y = \frac{\sigma}{f_{cd}} \quad (4)$$

$$\alpha_a = 2.4 - 0.0125 f_{cd} \quad (5)$$

$$\alpha_d = \frac{\epsilon_{cc50} / \epsilon_{co}}{(\epsilon_{cc50} / \epsilon_{co} - 1)^2} \quad (6)$$

where parameters α_a and α_d control the slope of the ascending and descending branches of the stress-strain curve, respectively; ϵ and σ are the strain and stress of the confined concrete under dynamic loading, respectively; and ϵ_{co} is the peak strain of the confined concrete (as shown in Figure 3), which is expressed as [17]

$$\epsilon_{co} = (1300 + 12.5 \cdot \sigma_{co}) \cdot 10^{-6} + 800 \cdot \xi^{0.2} \cdot 10^{-6} \quad (7)$$

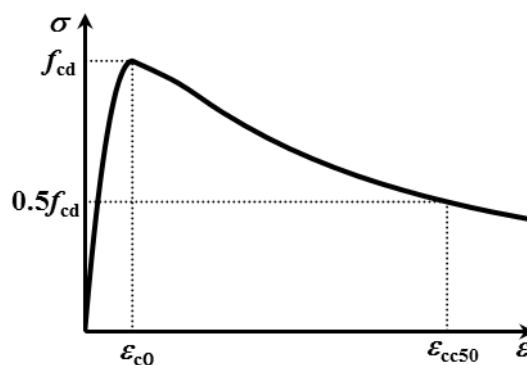


Fig. 3 - Dynamic stress-strain relation of confined concrete

where $\xi = \rho_{sv} f_h / f_{cd}$, ρ_{sv} is the volume ratio of the transverse hoop to the confined concrete core, and f_h is the stress in confinement reinforcement at the peak strength of confined concrete. f_h was proposed by Le'geron and Paultre [23] as follows:

$$f_h = \begin{cases} f_h = f_{hy} & \kappa \leq 10 \\ f_h = \min(f_{hy}, \frac{0.25 f_{cd}}{\rho_{se}(\kappa - 10)}) & \kappa > 10 \end{cases} \quad (8)$$

where f_{hy} is the yield strength of stirrups; ρ_{se} is the effective sectional ratio of confinement reinforcement in the x or y direction (Figure 4); and κ is a parameter to determine whether the transverse reinforcement yields at the peak strength of confined concrete. ρ_{se} and κ are expressed as follows:

$$\rho_{se} = k_e A_{sh} / sc \tag{9}$$

$$\kappa = f_{cd} / (\rho_{se} E_s \epsilon_c) \tag{10}$$

where s and c (as shown in Figure 4, $c=c_x=c_y$) are the spacing of transverse reinforcement and diameter of the core measured centre-to-centre of the hoops, respectively; A_{sh} is the total area of transverse bars in the x or y direction and is defined as 3.41 and 3.61 times the cross-section area of a single tie leg for the type-A and type-B configurations in Table 1, respectively [24]; E_s and ϵ_c are the modulus of elasticity of transverse reinforcement and the axial strain, which corresponds to the concrete cylinder strength, respectively; and k_e is the geometrical effectiveness coefficient of confinement, which represents the ratio of the smallest effectively confined concrete area at midway between two layers of stirrups to the nominal concrete core area. k_e was proposed by Mander et al. [25] as follows:

$$k_e = \frac{(1 - \frac{\sum w_i^2}{6c_x c_y})(1 - \frac{s'}{2c_x})(1 - \frac{s'}{2c_y})}{1 - \rho_c} \tag{11}$$

where w_i is the i th clear distance between adjacent longitudinal bars (as shown in Figure 4); s' is the clear spacing of transverse reinforcement; ρ_c is the ratio of the area of longitudinal steel to the area of the core of the section; and c_x and c_y are the core dimensions to centrelines of the perimeter hoop in the x and y directions, respectively.

In Equation 4, ϵ_{cc50} is the post-peak axial strain in confined concrete when the capacity decreases to 50% of the confined strength. Based on the expression of ϵ_{cc50} proposed by Le'geron and Paultre [23], the modified expression of ϵ_{cc50} is

$$\epsilon_{cc50} = \epsilon_{c50} (1 + 40 I_{e50}) \tag{12}$$

where ϵ_{c50} is the post-peak axial strain in unconfined concrete under quasi-static load when the capacity decreases to 50% of unconfined strength, and $\epsilon_{c50}=0.004$ according to the proposal of Le'geron and Paultre [23]; I_{e50} is the effective confinement index at ϵ_{cc50} ,

$$I_{e50} = \rho_{se} f_{hy} / f_{cd} \tag{13}$$

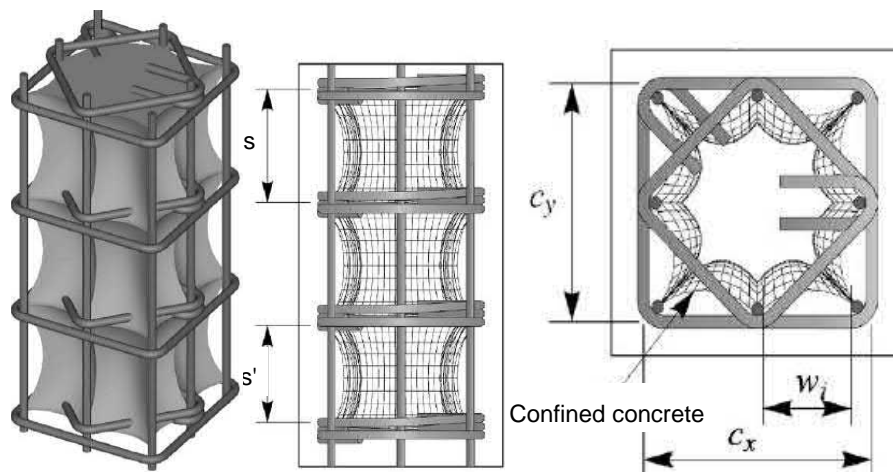


Fig. 4 - Diagram of the partial parameters [26]

Uniaxial compression stress-strain relations of cover concrete considering the strain rate effect

When the volume ratio of transverse steel is $\rho_v=0$ and the effective confinement index is $I_{e50}=0$ in Equations 7 and 10, respectively, Equation 1 to 13 describe the uniaxial compressive stress-strain relation of cover concrete with the strain rate effect, which can be used to analyse the behaviour of the cover concrete of RC columns.

Uniaxial tensile behaviour

In ABAQUS, the uniaxial tensile behaviour of concrete is taken as a linear elastic relation before reaching the tensile strength [18]. The post-failure behaviour for direct straining is modelled with tension stiffening, which enables the user to define the strain-softening behaviour for cracked concrete. This behaviour also enables the effects of the reinforcement interaction with concrete to be simulated in a simple manner. One method to specify tension stiffening is applying a fracture energy cracking criterion. The fracture energy is directly specified as a material property in the model, and a linear loss of strength after cracking is assumed. The fracture energy G_F in N/m is determined by the expression proposed by the *Fib Model Code for Concrete Structures 2010* [27],

$$G_F = 73f_c^{0.18} \quad (14)$$

where f_c is the compressive strength in MPa.

As suggested by available studies [28-30] on the dynamic fracture energy of concrete, the dynamic fracture energy of concrete can be assumed to be identical to the static fracture energy for the strain rate range from 10^{-4} to 10^{-1} under earthquake action.

Steel material model

An isotropic elastic-plastic model was used to describe the constitutive behaviour of the steel bar. The perfect elastic-plastic relation was used as the uniaxial stress-strain relation of steel. Based on the studies on the dynamic behaviour of steel, the steel modulus of elasticity has no relation to the strain rate. The steel modulus of elasticity is constant under dynamic loading. The dynamic yield strength of steel σ_{yd} is obtained using the Cowper-Symond equation,

$$\frac{\sigma_{yd}}{\sigma_{ys}} = 1 + \left(\frac{\dot{\varepsilon}}{C} \right)^{1/q} \quad (15)$$

where σ_{ys} is the static yield strength of steel, $\dot{\varepsilon}$ is the strain rate of steel, $C=1300 \text{ s}^{-1}$ and $q=5$ according to Munoz-Garcia et al. [31].

VERIFICATION OF FEA MODEL

Based on the FEA model, the quasi-static and dynamic behaviours of the columns in Table 1 were simulated. Figures 5 and 6 show that the predicted axial load (N) versus the axial strain (ε) curves are consistent with the tested N - ε curves under the conditions of quasi-static loading and rapid loading. Because the available tested N - ε curves under rapid loading from the literature are notably limited, the comparison between the predicted N - ε curves and the tested axial bearing capacity are shown in Figures 5 and 6. Table 2 shows the comparison between experimental and predicted axial bearing capacities (P_e and P_c) and the corresponding average axial strain (ε_c and ε_e). The largest error of the predicted axial bearing capacity is 7% for Unit19. The mean value and standard deviation of P_c/P_e are 0.97 and 0.03, respectively. The largest error of the predicted axial strain at the bearing capacity is 36% for Unit12, but the mean value and standard deviation of $\varepsilon_c/\varepsilon_e$ are 1.11 and 0.16, respectively. The comparison shows that the FEA model is effective to predict the quasi-static and dynamic behaviour of square reinforced normal-strength concrete columns with different volume ratios of transverse reinforcement.

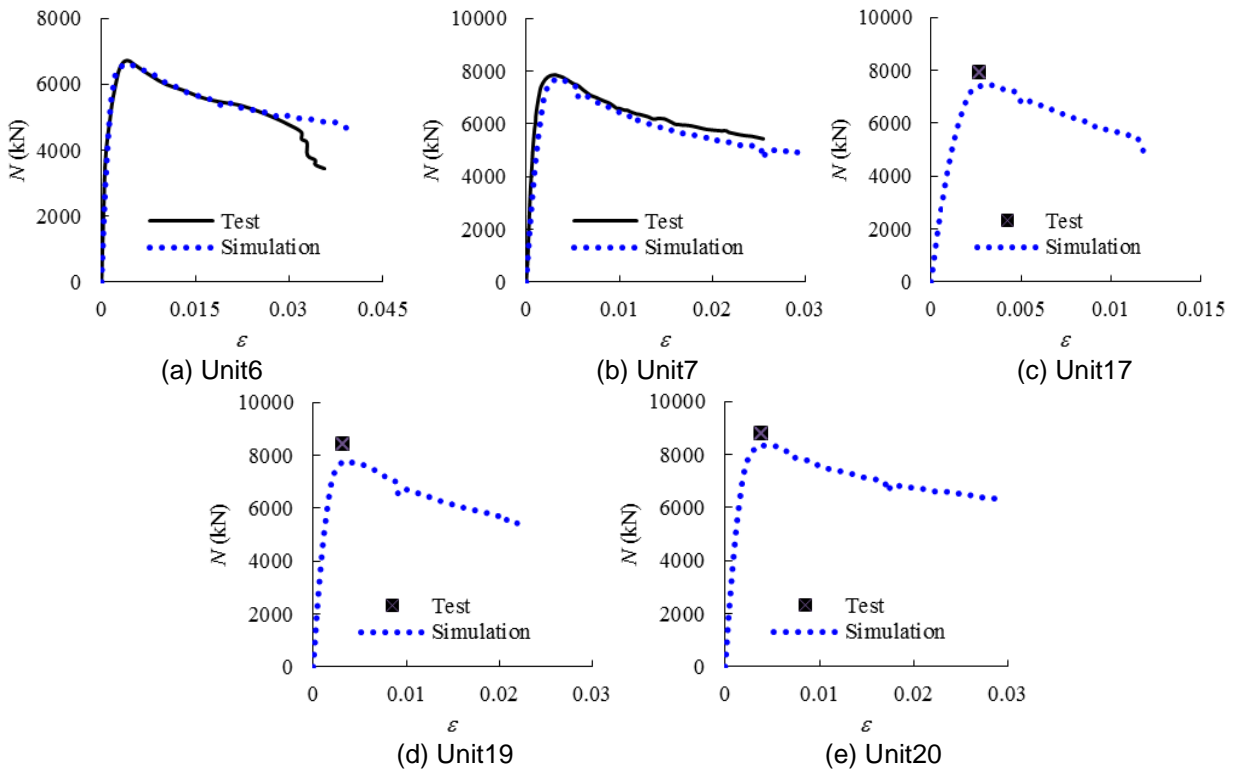


Fig. 5 - Comparison between experimental and predicted $N-\varepsilon$ curves of columns with type-A reinforcement arrangement

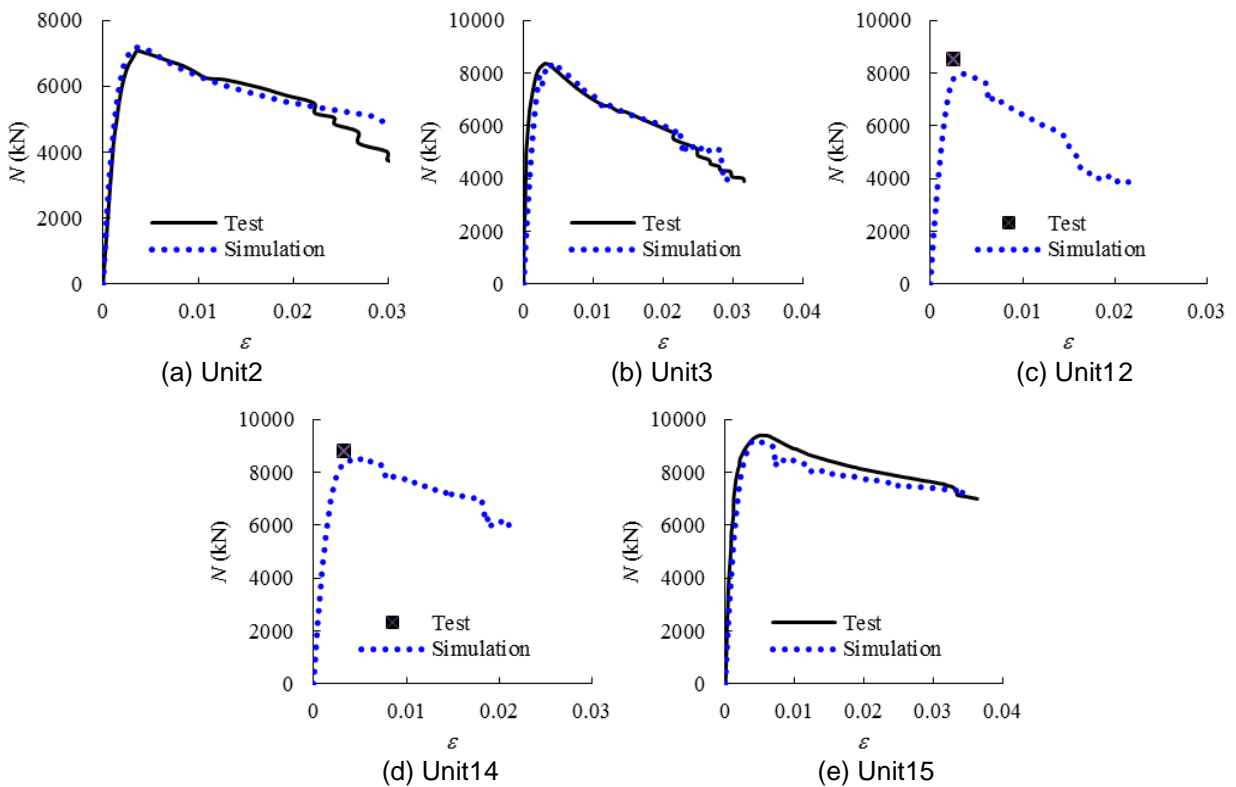


Fig. 6 - Comparison between experimental and predicted $N-\varepsilon$ curves of the columns with type-B reinforcement arrangement

Tab. 2 - Comparison between tested and predicted bearing capacities and the corresponding axial strain

Specimens	P_e /kN	P_d /kN	P_d/P_e	ε_e	ε_c	$\varepsilon_c/\varepsilon_e$
Unit6	6720	6628	0.99	0.0041	0.0041	1.00
Unit7	7850	7717	0.98	0.0032	0.0035	1.09
Unit17	7900	7455	0.94	0.0027	0.0032	1.19
Unit19	8400	7794	0.93	0.0032	0.0034	1.06
Unit20	8800	8362	0.95	0.0039	0.0037	0.95
Unit2	7070	7175	1.01	0.0036	0.0035	0.97
Unit3	8410	8360	0.99	0.003	0.0038	1.27
Unit12	8500	7974	0.94	0.0025	0.0034	1.36
Unit14	8800	8532	0.97	0.0033	0.0042	1.27
Unit15	9400	9188	0.98	0.0052	0.0047	0.90
Mean			0.97			1.11
Standard deviation			0.03			0.16

Note: P_e and P_c are the experimental and simulation axial-bearing capacity, respectively; ε_e and ε_c are the experimental and simulation axial strain at the axial-bearing capacity, respectively.

PARAMETRIC INVESTIGATION

Numerical simulation matrix

After the verification of the FEA model against the experimental results, this section presents a parametric investigation to capture more information about the behaviour of RC columns under varying loading rates. Various key parameters were considered, including the loading strain rate (3×10^{-5} , 3×10^{-4} , 3×10^{-3} , 3×10^{-2} and $3 \times 10^{-1} \text{ s}^{-1}$), reinforcement arrangement (type A and type B), longitudinal reinforcement ratios (ρ_s : 2.65% and 1.27%) and volumetric ratios of transverse reinforcement (ρ_{sv} : 3.0% and 1.5%). Table 3 summarizes the specimen characteristics of the simulation matrix. The titles of the specimens in Table 3 describe the varying parameters and have the following meaning. The first letter (A or B) in the titles represents the reinforcement arrangement of type A or type B. The number after the first letter indicates the ratio of longitudinal steel ρ_s . Numbers 2 and 1 correspond to $\rho_s=2.65\%$ and $\rho_s=1.27\%$, respectively. The numbers behind the middle hyphen represent the volumetric ratio ρ_{sv} of the transverse reinforcement. Numbers 3.0 and 1.5 indicate $\rho_{sv}=3\%$ and $\rho_{sv}=1.5\%$, respectively. All specimens are 1200 mm long and have identical section sizes of 450 mm \times 450 mm. The core size measured from the centre of the perimeter hoop was maintained constant at 400 mm \times 400 mm. The concrete compressive cylinder strength f_c was 30 MPa.

Influence analysis of investigated parameters

As shown in Figure 7, the loading rate has an obvious effect on the $N-\varepsilon$ curves. First, the axial bearing capacity increases with the increase in loading rate. The dynamic increasing factor (DIF) of the bearing capacity, namely, the ratio of dynamic bearing capacity to quasi-static bearing capacity at a strain rate of 0.000033/sec, is commonly used to describe the effect of the loading rate on the bearing capacity. In these cases, the maximum DIF is 1.28 for specimen A1-1.5 when the strain rate increases to 0.3/sec. Second, the ductility obviously decreases after the loading rate increases. The descending branches of $N-\varepsilon$ curves with different loading rates appear to converge

after the axial strain ϵ reaches a certain value.

Tab. 3 - Specimens for the parameter analysis

Specimen	Longitudinal reinforcement			Transverse reinforcement			
	Diameter (mm)	Ratio of longitudinal steel ρ_s	Yielding strength f_y (Mpa)	Diameter (mm)	Spacing (mm)	Yielding strength f_{hy} (MPa)	Volumetric ratio ρ_{sv}
A1-3.0	18	1.27%	400	10	43	300	3.0%
A1-1.5	18	1.27%	400	10	86	300	1.5%
A2-3.0	26	2.65%	400	10	43	300	3.0%
A2-1.5	26	2.65%	400	10	86	300	1.5%
B1-3.0	14.7	1.27%	400	9.7	43	300	3.0%
B1-1.5	14.7	1.27%	400	9.7	86	300	1.5%
B2-3.0	21.2	2.65%	400	9.7	43	300	3.0%
B2-1.5	21.2	2.65%	400	9.7	86	300	1.5%

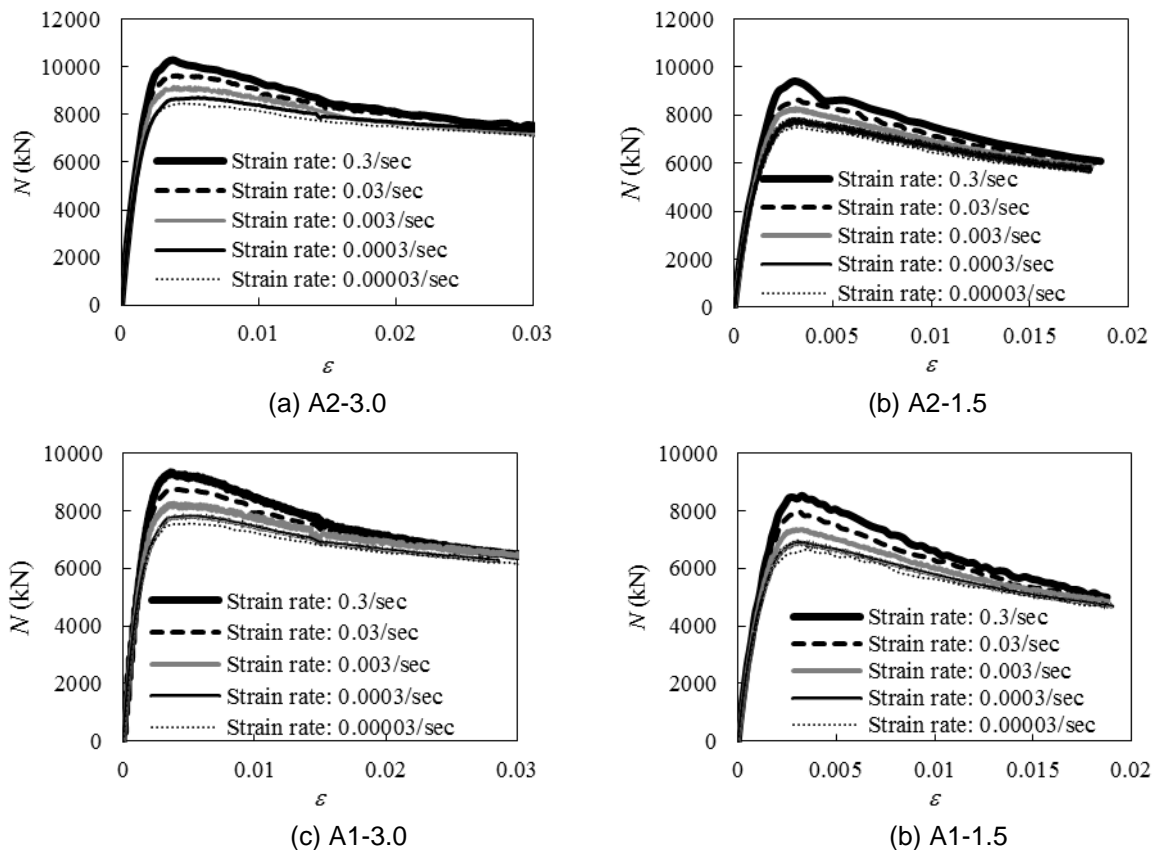


Fig. 7 - Effect of the loading rate on the $N-\epsilon$ curves

Figure 8 shows the effect of the transverse reinforcement volumetric ratio (ρ_{sv} : 3.0% and 1.5%) on the DIF . Improving the transverse reinforcement volumetric ratio reduces the DIF . With the increase in strain rate, the difference of the DIF with two different volumetric ratios of

transverse reinforcement increases. Compared with the specimens with type-A reinforcement arrangement, the difference of *DIF* with different volumetric ratios of transverse reinforcement is more obvious for the specimens with type-B reinforcement arrangement. However, the maximum difference of *DIF* is only 5.3%, which is notably small. Thus, the effect of the transverse reinforcement volumetric ratio in the range of 1.5% to 3% on the *DIF* can be ignored.

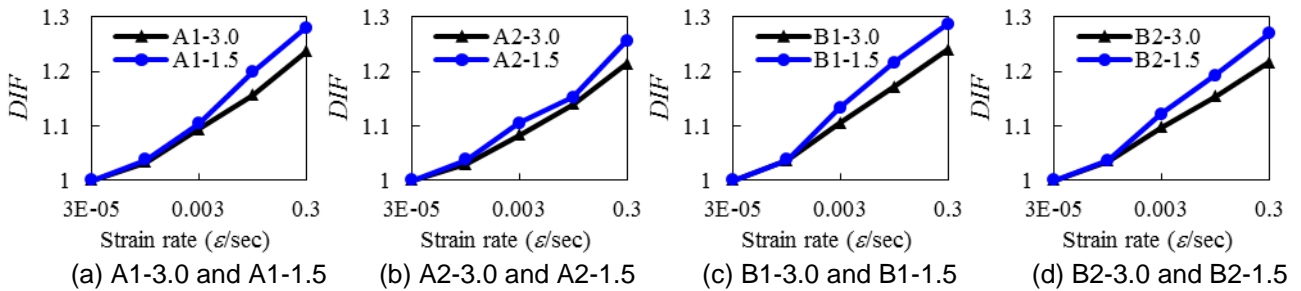


Fig. 8 - Effect of the transverse reinforcement ratio on *DIF*

Figure 9 shows that an increase in longitudinal reinforcement ratio from 1.27% to 2.65% makes the *DIF* slightly decrease. Figure 10 shows the effect of the reinforcement arrangement on the *DIF*. The two specimens in each group in Figure 10 have identical longitudinal reinforcement ratio and transverse reinforcement volumetric ratio but different reinforcement arrangements. The *DIF* of specimens with type-B reinforcement arrangement is slightly larger than the *DIF* of specimens with type-A reinforcement arrangement. In sum, the effect of the longitudinal reinforcement ratio and reinforcement arrangement on *DIF* is smaller than the effect of the transverse reinforcement ratio, and the effect is also commonly negligible.

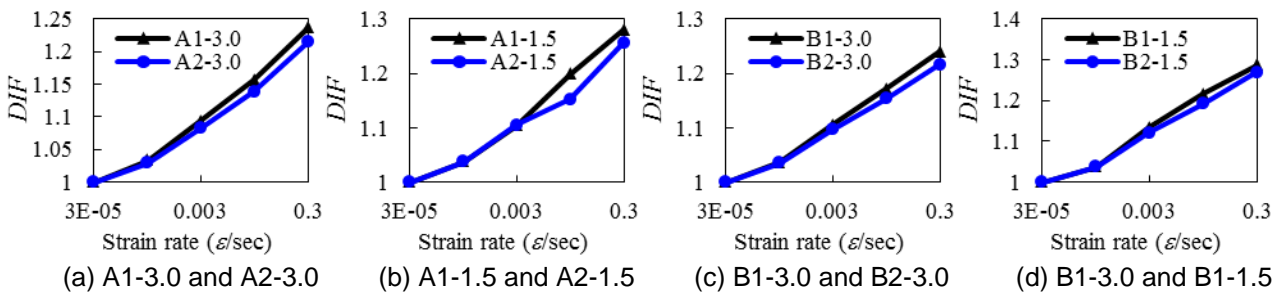


Fig. 9: Effect of the longitudinal reinforcement ratio on *DIF*

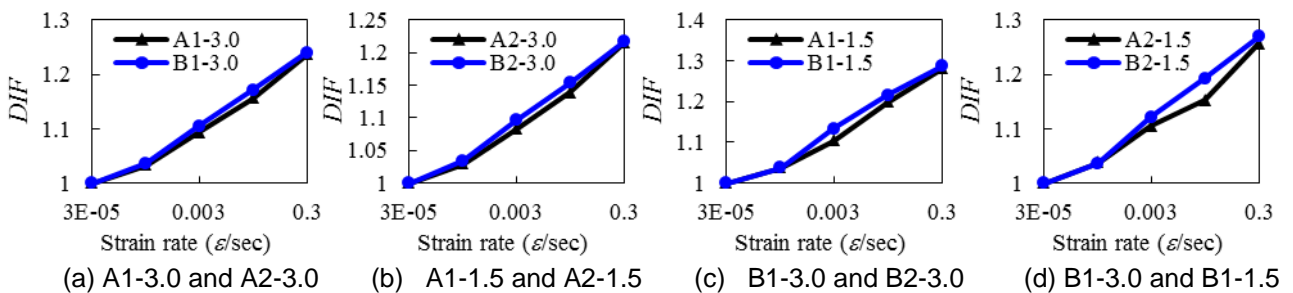


Fig. 10: Effect of the reinforcement arrangement on *DIF*

CONCLUSION

In this paper, a three-dimensional FEA model was developed to investigate the behaviour of RC columns with the overlapping hoop confining effect under different concentric loading rates. The predicted results by the FEA model were consistent with the test results. Based on the numerical results obtained in the study, the following conclusions were drawn.

- (1) A modified uniaxial compressive stress-strain relation of concrete was developed, including the confining effect of overlapping hoops and strain rate effect of concrete, and it is proper to simulate the quasi-static and dynamic behaviour of the overlapping hoop-confined concrete by introducing it into the concrete damaged plastic material model in ABAQUS.
- (2) Increasing the loading rate increases the axial bearing capacity but decreases the ductility of RC columns. Compared with the quasi-static bearing capacity, the increase in axial bearing capacity is obvious when the strain rate approaches 0.3/sec.
- (3) For the RC columns with the reinforcement arrangement of type A or type B, the transverse reinforcement volumetric ratio and longitudinal reinforcement ratio slightly affect the *DIF* of specimens under the strain rate of 0.00003/sec to 0.3/sec.
- (4) With the identical volumetric ratio of transverse reinforcement and longitudinal reinforcement ratio, the change of reinforcement arrangement between type A and type B slightly affects the *DIF* of specimens under the strain rate of 0.00003/sec to 0.3/sec.

ACKNOWLEDGEMENTS

The research reported in the paper is supported by the National Natural Science Foundation of China (No. 51608156) and the Project of the Natural Science Foundation of Hainan Province (No. 20165208). These sources of financial support are highly appreciated.

REFERENCES

- [1] Comité Euro-International du Béton, 1993. CEB-FIP Model Code 1990 (Redwood Books).
- [2] Bischoff P.H., Perry S.H., 1991. Compressive behaviour of concrete at high strain rates. *Materials and Structures*, 24(6): 425-450. <http://dx.doi.org/10.1007/BF02472016>.
- [3] Malvar L.J., Ross C.A., 1998. Review of strain rate effects for concrete in tension. *ACI Materials Journal*, 95(6): 735-739.
- [4] Fu H.C., Erki M.A., Seckin M., 1991. Review of effects of loading rate on reinforced concrete. *Journal of Structural Engineering*, 117(12): 3660-3679. [http://dx.doi.org/10.1061/\(ASCE\)0733-9445\(1991\)117:12\(3660\)](http://dx.doi.org/10.1061/(ASCE)0733-9445(1991)117:12(3660)).
- [5] Malvar L.J., Ross C.A., 1998. Review of static and dynamic properties of steel reinforcing bars. *ACI Materials Journal*, 95(5): 609-616.
- [6] Bertero V.V., 1972. Experimental studies concerning reinforced, prestressed and partially prestressed concrete structures and their elements. Introductory Report, Symposium on Resistance and Ultimate Deformability of Structures Acted on by Well Defined Repeated Loads, 67-99.
- [7] Soroushian P., Obaseki K., 1986. Strain rate-dependent interaction diagram for reinforced concrete section. *ACI Journal Proceedings*, 83(1): 108-116.
- [8] Al-Haddad M.S., 1995. Curvature ductility of reinforced concrete beams under low and high strain rates. *ACI Structural Journal*, 92(5): 526-534.
- [9] Lin G., Yan D.M., Xiao S.Y., Hu Z.Q., 2005. Strain rate effects on the behavior of concrete and the seismic response of concrete structures. *China Civil Engineering Journal*, 38(11): 1-8.
- [10] Asprone D., Frascadore R., Ludovico M.D., Prota A., Manfredi G., 2012. Influence of strain rate on the seismic response of RC structures. *Engineering Structures*, 35: 29-36. <http://dx.doi.org/10.1016/j.engstruct.2011.10.025>.
- [11] Reinschmidt K.F., Hansen R.J., Yang C.Y., 1964. Dynamic tests of reinforced concrete columns. *ACI Journal Proceedings*, 61(3): 317-334.
- [12] Xu B., Zeng X., 2014. Experimental study and finite element analysis on the dynamic

- behavior of slender RC columns under concentric compressive rapid loadings. *Engineering Mechanics*, 31(4): 210-217.
- [13] Iwai S., Minami K., Wakabayashi M., 1988. Stability of slender reinforced concrete members subjected to static and dynamic loads. In: *Proceedings of Ninth World Conference on Earthquake Engineering*, Vol. VIII 901-906.
- [14] Scott B.D., Park R., Priestley M.J.N., 1982. Stress-strain behavior of concrete confined by overlapping hoops at low and high strain rates. *ACI Journal Proceedings*, 79(1): 13-27.
- [15] Kent D.C., Park R., 1971. Flexural members with confined concrete. *Journal of the Structural Division*, 97(7): 1969-1990.
- [16] Li B., Park R., Tanaka H., 2000. Constitutive behavior of high-strength concrete under dynamic loads. *ACI Structural Journal*, 97(4): 619-629.
- [17] Zeng X., Xu B., 2014. Numerical simulation on the dynamic behavior of short RC columns subjected to concentric rapid loading considering confinement effect of stirrups. *Engineering Mechanics*, 31, 190-197.
- [18] Dassault Systemes Simulia Corp., 2014. Abaqus Version 6.14 Documentation- ABAQUS Theory Guide (Dassault Systemes Simulia Corporation).
- [19] Zeng X., 2016. Finite element modelling and analysis of concrete confined by stirrups in square RC columns. *The Civil Engineering Journal*, 3: Article no. 17. <https://doi.org/10.14311/CEJ.2016.03.0017>.
- [20] ACI Committee 318, 2008. Building code requirements for structural concrete (ACI 318-08) and commentary (American Concrete Institute) 109 pp.
- [21] CEB, 1988. Concrete Structures under Impact and Impulsive Loading. Synthesis Report, Bulletin d'Information No. 187 (Comité Euro-International du Béton).
- [22] Chung H.S., Yang K.H., Lee Y.H., Eun H.C., 2002. Strength and ductility of laterally confined concrete columns. *Canadian Journal of Civil Engineering*, 29(6): 820-830. <http://dx.doi.org/10.1139/l02-084>.
- [23] Légeron F., Paultre P., 2003. Uniaxial confinement model for normal- and high-strength concrete columns. *Journal of Structural Engineering*, 129(2): 241-252. [http://dx.doi.org/10.1061/\(ASCE\)0733-9445\(2003\)129:2\(241\)](http://dx.doi.org/10.1061/(ASCE)0733-9445(2003)129:2(241)).
- [24] Cusson D., Paultre P., 1995. Stress-strain model for confined high-strength concrete. *Journal of Structural Engineering*, 121(3): 468-477. [http://dx.doi.org/10.1061/\(ASCE\)0733-9445\(1995\)121:3\(468\)](http://dx.doi.org/10.1061/(ASCE)0733-9445(1995)121:3(468)).
- [25] Mander J.B., Priestley M.J.N., Park R., 1988. Theoretical stress-strain model for confined concrete. *Journal of Structural Engineering*, 114(8): 1804-1826. [http://dx.doi.org/10.1061/\(ASCE\)0733-9445\(1988\)114:8\(1804\)](http://dx.doi.org/10.1061/(ASCE)0733-9445(1988)114:8(1804))
- [26] Paultre P., Légeron F., 2008. Confinement reinforcement design for reinforced concrete columns. *Journal of Structural Engineering*, 134(5): 738-749. [http://dx.doi.org/10.1061/\(ASCE\)0733-9445\(2008\)134:5\(738\)](http://dx.doi.org/10.1061/(ASCE)0733-9445(2008)134:5(738)).
- [27] Fib, 2013. *Fib Model Code for Concrete Structures 2010* (Ernst & Sohn).
- [28] Van Doormaal J., Weerheijm J., Sluys L.J., 1994. Experimental and numerical determination of the dynamic fracture energy of concrete. *Journal de Physique IV*, 4(C8): 501-506.
- [29] Rericha P.A., 1998. *Structures Under Shock and Impact V*, edited by Jones N., Talaslidis D.G., et al. (Computational Mechanics Publications in Southampton, Boston) 461-470.
- [30] Ruiz G., Zhang X.X., Yu R.C., et al., 2011. Effect of loading rate on fracture energy of high-strength concrete. *Strain*, 47(6): 518-524. <http://dx.doi.org/10.1111/j.1475-1305.2010.00719.x>.
- [31] Munoz-Garcia E., Davison B., Tyas A., 2005. Structural integrity of steel connections subjected to rapid rates of loading. In: *Structures Congress 2005: Metropolis and Beyond*, 1-12. [http://dx.doi.org/10.1061/40753\(171\)217](http://dx.doi.org/10.1061/40753(171)217).

EXPERIMENTAL STUDY ON THE SOFTENING CHARACTERISTICS OF ARGILLACEOUS SLATE WITH WATER

Chengzhong Yang, Yuqiang Tang, Wei Wang, Shufang Wang

School of Civil Engineering and Architecture, East China Jiaotong University, Nanchang, Jiangxi, 330013, China, email: 274798959@qq.com, 1163437914@qq.com, 417453083@qq.com, 330013wsf@sina.com

ABSTRACT

Because the stratification of argillaceous slate developed well, the anisotropy is obvious and it is easy to soften when encountering water, in the excavation, tunnel is easy to cause large deformation and collapse. In order to understand the softening mechanism of argillaceous slate in water and mechanical anisotropy and to provide reference for solving practical engineering problems, in this paper, introducing an argillaceous slate highway tunnel project in Zixi County of Jiangxi province. By preparing standard specimens in field sampling, the mineral composition analysis, water rational test and uniaxial compression test were carried out. The result shows: The main mineral composition of argillaceous slate is sericite, inclusion of a few chlorite, quartz and so on. This composition makes obvious characteristics of soft rock. The influence of hydration on the mechanical properties of argillaceous slate is large. With the increase of water content, the peak strength shows a downward trend, while the Poisson ratio shows the characteristics of slow growth. At the same time, the mechanical properties of argillaceous slate are obviously anisotropic by the direction of stratification plane. The failure modes of argillaceous slate mainly include axial tension, local shear failure and shear failure along the stratification plane.

KEYWORDS

Argillaceous Slate, Tunnel Surrounding Rock, Compression Test, Water Rationality, Mechanical Properties

INTRODUCTION

In recent years, the number of tunnel construction in our country is increasing, and various complicated geological environment emerge in endlessly. Argillaceous slate, as a kind of stratified rock, its joint surface developed well and is easy to be softened by water. At present, engineers and technicians know little about the deformation and failure mechanism of the rock. In the process of tunnel excavation, it is easy to cause large deformation, collapse and other disasters and cause great losses, which brings some difficulties to the tunnel construction. Many scholars at home and abroad have carried out many theoretical and experimental researches on layered rock. The results obtained are helpful to further study the mechanical properties and deformation mechanism of layered rock mass. In the field of theoretical research, some scholars have studied the constitutive model and failure prediction of slate. Zuo Qingjun etc al[1] based on the basic constitutive model in the existing Burgers creep, by introducing the water deterioration factor, established the visco

elastic plastic creep constitutive equation of argillaceous slate considering water absorption, and divided the argillite creep into attenuation, steady state and accelerated creep three stages. Huang Shuling et al. [2] proposed a model of hardening and softening of layered rock composite materials, and described the strength and deformation anisotropy and progressive fracture (or slip) characteristics of these rock masses. Zhang Yujun et al. [3], thought the method of searching and trial calculation combing the empirical expression of the shear strength of layered rock mass varying with the direction of rock layer with the Mohr Coulomb criterion is used to predict the shear failure surface and orientation of slate, which is more in line with reality. In the field of experimental research, Yang Chunhe et al [4], by electron microscopy, X ray diffraction and other tests on slates, explained microscopically the softening mechanism of slate in water. It is considered that with the increase of soaking time, the capillary force and the surface tension between the mineral particles of slate decrease, and the cohesive force of the slate decreases. Fall M [5] studied the influence of interstitial water pressure on the strength of shaly shale by simulating the gas injection test. By three axial compression test, Nguyen T S et al [6-9] established the argillite constitutive model, and revealed the relationship between mechanical parameters of slate such as peak strength and elastic modulus and confining pressure, moisture content and jointed relationship, proof the slate rock has anisotropic mechanical characteristics, and proved that the slate rock mass has anisotropic mechanical characteristics. In the slate rock tunnel stability, Lisjak A et al [10,11], by using the numerical analysis software, for the excavation of slate tunnel with different stratification plane directions, carried out numerical analysis, explained the characteristics of stratification plane direction effecting on the stability of the tunnel. Su Zhendao [12], in the deformation and stress analysis of the tunnel lining, based on the field test of the argillite tunnel, he recommended that the radial grouting behind the lining of the tunnel should be taken to reduce the pressure of the lining so as to enhance the stability of surrounding rock. Although there are many researches on the engineering properties of slate, however, there are few studies on the physical and mechanical characteristics of argillaceous slate, and the results both theoretically and experimentally are very limited. In this article, for a highway tunnel project in Zixi County of Jiangxi, the mineral composition analysis, water rational test and uniaxial compression test of argillaceous slate are carried out. Furthermore, the mechanism of softening of argillaceous slate with water and its mechanical anisotropy are revealed. The physical and mechanical properties of argillaceous slate are established, which provides reference for engineering decision-making.

TEST OVERVIEW

Test equipment and method

The mineral composition analysis of argillaceous slate was carried out by D8ADVANCE X-ray diffractometer produced by Brook Company of Germany. The device can scan the sample at different angles and obtain the X ray diffraction pattern of different mineral components in the sample for analyzing the mineral composition of the sample. The scanning range of this experiment is 5° - 65° , and the scanning speed is $0.02^{\circ}/s$. The water rational test of argillaceous slate includes water absorption test and expansion test and so on. The test equipment includes electronic scales, thermometer, drying box, vacuum pump etc. The specific test methods can refer to the "water conservancy and hydropower engineering rock test procedures" edited by the Yangtze River academy of Sciences [13], here is no longer described. The uniaxial compression test was carried

out by use of a RMT-150 compression test machine, as is shown in Figure 1. The device has the advantages of simple operation, convenient loading and deformation controlling, high measuring accuracy, long continuous operation time, stable working performance and strong protection function and other advantages. It is widely used in a single three axial compression test of rock materials. In the test, the axial load is controlled by controlling the axial displacement; the axial deformation rate of the preset specimen is 0.002mm/s; the upper limit of axial displacement is set. After the axial load is started, the axial load is maintained until the specimen axial deformation reaches its preset upper limit or until the yielding failure of the argillaceous slate samples occurs, then the test is stopped. During the whole compression test, the experimental data are recorded automatically by the test system, and the fracture features and the failure modes of the argillaceous slate are observed and recorded by manual observation.



Fig. 1 - RMT-150 Compression Machine

Specimen preparation

The specimens used in the test are all argillaceous slates taken from the construction site of a highway tunnel in Zixi County of Jiangxi Province, as is shown in Figure 2. The weathering degree of argillaceous slate is different, and the degree of fracture development is different. In the field, a more complete block is selected. The maximum length of rock block is about 20cm. Because of the significant anisotropy of argillaceous slate, the drilling core sampling is respectively done in accordance with the stratification direction of vertical, 45° and parallel. The sample is a standard cylinder with a molding diameter of 50mm and a height of h of 100mm. In the process of specimen preparation, the roughness of the end face is controlled at about 0.005mm, and the axial direction is kept perpendicular to the radial direction. After the specimens were finished, selected the specimens with smooth surface, no obvious cracks and intact, studied the velocity of specimens using acoustic instrument to avoid the influence of the case of not dense or void in the test piece on the test result. Finally, covered with a layer of plastic wrap on the selected specimens and stored in the laboratory for test preparation.



Fig. 2 - Weathered argillaceous slate

EXPERIMENTAL RESULTS AND ANALYSIS

Mineral composition and water rationality test

Mineral composition analysis of argillaceous slate samples was carried out by using D8ADVANCE X- ray diffractometer, as shown in Figure 3. The mineral composition of argillaceous slate includes sericite, chlorite, quartz and a small amount of kaolinite and feldspar. The content of Sericite is the highest, which is 46.6%, which shows that it has the greatest influence on the engineering properties of argillaceous slate, followed by quartz and chlorite, and the content is about 20%. The analysis shows that the sericite intensity is low, and a loose and flaky structure, so that the argillaceous slate has the characteristics of water permeability, uneven and loose structure, which eventually leads that the strength of argillaceous slate becomes low and its stability becomes bad, and the properties of soft rock and schist are prominent.

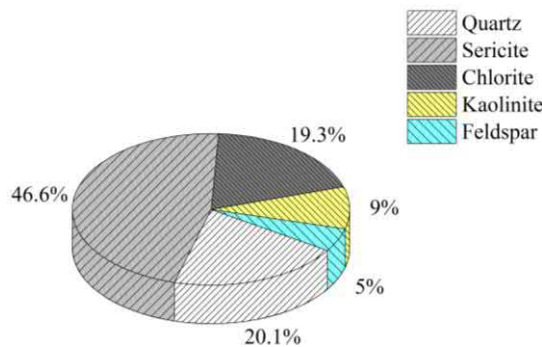


Fig.3 - Mineral composition of argillaceous slate

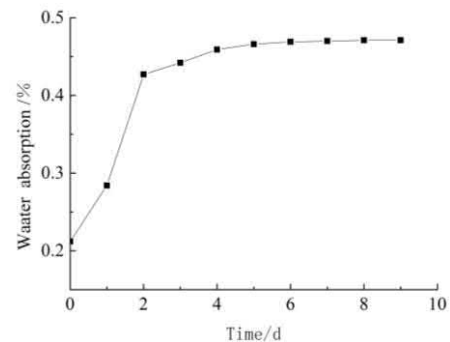


Fig.4 - The relationship between water absorption and time

The water rationality of argillaceous slate includes water absorption characteristics, swelling characteristics and disintegration characteristics. Through the field sampling, according to the standard, a group of specimens were prepared in the laboratory, and the corresponding tests were carried out. The results of water absorption test were shown in Figure 4. The swelling test results were shown in Table1.

Tab. 1 - Test results of natural swelling of argillaceous slate

Specimen number	The angle between the stratification plane and the axial direction	Axial expansion value (mm)	Radial expansion value (mm)	Axial expansion ratio (%)	Radial expansion ratio (%)
1	90°	0.0025	0.0165	0.0035	0.0234
2	90°	0.0009	0.0515	0.0013	0.0789
3	0°	0.0635	0.0031	0.1387	0.0057
4	0°	0.1578	0.0198	0.1231	0.0329

The experimental results show that the water quantity of argillaceous slate under natural condition in the early immersion was proportional to the immersion time. In fourth days, with the growth of time, the natural water absorption rate showed a decreasing trend, and eventually stabilized, the water absorption rate remained at about 0.45%; the swelling deformation is affected by water and stratification plane structure, no matter the angle between the axial and stratification plane of the specimens are either 0° or 90°, the rate of expansion in the direction parallel to the stratification plane is always higher than that in the direction perpendicular to the stratification plane. The reason is that the contact area between clay minerals parallel to the stratification plane and water is larger, and it is easier to absorb water and expand. But water is difficult to enter the clay minerals between the stratification plane, and the expansion rate is smaller; in the expansion test of argillaceous slate, it is observed that the disintegration of argillaceous slate is related to the integrity and weathering degree of the sample. Relevant tests show that the higher the degree of fragmentation, the stronger the disintegration. In addition, under dry conditions, argillaceous slate is more likely to disintegrate and more rapidly disintegrate than in natural conditions.

Uniaxial compression test

Through the uniaxial compression test of argillaceous slate specimens under different stress and moisture content, the mechanical properties, such as deformation, strength and failure of argillaceous slate, are studied.

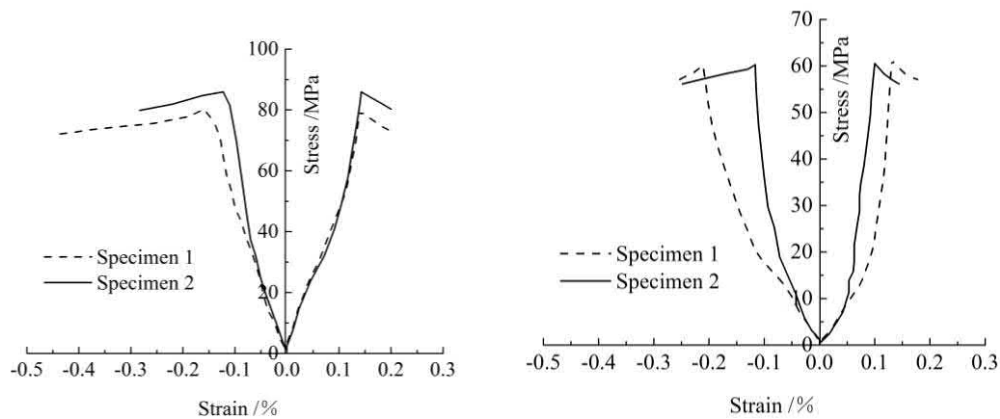
Deformation characteristics

Uniaxial compression specimens were divided into 3 groups: axial direction perpendicular to stratification plane direction, 45° degrees with stratification plane direction and parallel stratification plane direction. Each group is made of 2 specimens. The specimen size of the uniaxial compression test is shown in Table 2, and the stress-strain curve obtained in the test is shown in Figure 5.

Tab.2 Specimen size of uniaxial compression test

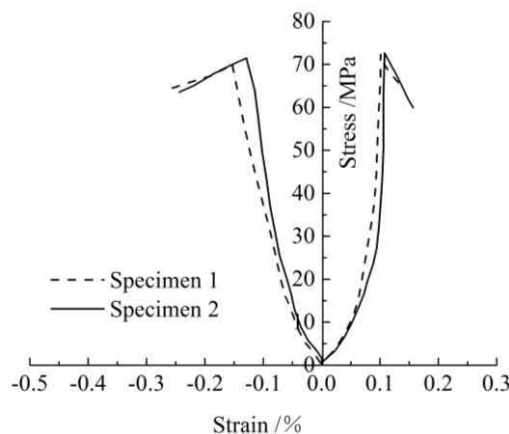
Specimen number	0-1	0-2	45-1	45-2	90-1	90-2
Specimen height (mm)	98.3	97.9	96.4	97.6	97.9	98.2
Specimen diameter (mm)	48.7	49.3	49.7	46.1	47.4	47.2
Height diameter ratio	2.02	1.99	1.94	2.11	2.06	2.08

Note: the first number indicates the angle between the axis of the specimen and the stratification plane. The second numbers indicate the number of the specimen in the group. The following is the same as this.



(a) The stratification plane is perpendicular to the axial direction of the specimen

(b) The angle between the stratification plane and the axial direction of the specimen is 45°



(c) The stratification plane is parallel to the axial direction of the specimen

Fig.5 - The stress-strain curves of argillaceous slate under uniaxial compression

Figure 5 shows the stress-strain curves of the argillaceous slate under different working stress from the beginning of the loading to the stage of failure. It can be seen from the figure, the trend is quite similar, contains the specimen compression phase, elastic deformation and crack development stage and failure stage, but the magnitude of the peak reflects a different, the rate of

deformation in each stage is obvious differences. The contrast analysis shows that: when the stratification plane perpendicular to the specimen axial, both the axial peak strain and lateral strain peak are at about 0.0015; while the stratification plane parallel to the specimen axial or 45°, the axial peak strain is greater 0.005 than lateral peak strain. It indicates that the strain has the characteristics of anisotropy significantly. In the compaction stage, nonlinear characteristics are exhibited, and the deformation rate is fast. The nonlinear characteristics are influenced by the fracture development of the argillaceous slate and the roughness of the end face of the specimen. The deformation of argillaceous slate develops from the elastic deformation stage to the fracture stage, showing the characteristics of elastic deformation, and the direct result of elastic deformation is the swelling deformation of its volume. In the failure stage of argillaceous slate specimens, axial deformation increases sharply and shows obvious brittle failure characteristics.

Strength characteristics

The uniaxial compression test results are shown in Table 3. It can be seen from the table that the uniaxial compressive strength of argillaceous slate is obviously affected by the dip angle of the stratification plane. When the argillaceous slate specimen axial is perpendicular to the rock stratification plane, the average value of the argillaceous slate compressive strength is 85.45MPa; it is the maximum value of the compressive strength of the test specimen into 3 groups. The failure mode is shear failure or splitting failure. When the angle between argillaceous slate specimen axial and the rock stratification plane is 45°, argillaceous slate compressive strength average value is 60.58MPa, it is the minimum value of the compressive strength of the test specimen into 3 groups. The specimen is sheared along the rock stratification plane. When the argillaceous slate specimen axial is parallel to the rock stratification plane, the average value of compressive strength of the argillaceous slate specimen is 73.84MPa, the compressive strength value is between that of the two groups test specimen mentioned above and the specimen appears to be in shear failure mode. Through further tests, it can be seen that, with the increase of stratification plane angle from 0° to 90°, the compressive strength and modulus of argillaceous slate changes similar to V type. The uniaxial compressive strength of argillaceous slate shows different characteristics of its mechanical properties in different directions, and it also shows that the rock is the most unfavorable state of force when the inclination of the stratification plane is close to 45°.

Tab.3 Results of uniaxial compression test

Number	Height (mm)	diameter (mm)	compressive strength (MPa)	average value (MPa)	elastic modulus (GPa)	average value (GPa)	Poisson ratio	failure modes and shear angles
90-1	98.3	48.7	86.04	85.45	32.25	33.22	0.22	shear failure
90-2	97.9	49.3	84.86		34.18		0.20	shear failure
45-1	96.4	49.7	64.44	60.58	25.31	25.00	0.18	A certain angle along the stratification plane
45-2	97.6	46.1	56.71		24.68		0.19	A certain angle along the stratification plane
0-1	97.9	47.4	74.12	73.84	28.48	26.82	0.23	vertical failure
0-2	98.2	47.2	73.56		25.15		0.25	vertical failure

Failure characteristics

The essence of argillaceous slate specimens from the beginning load to the final fracture is that, under external force, the gradual evolution process of generation, propagation and coalescence of the internal cracks. That is to say, rock failure is a macroscopic reflection of the accumulation of rock microstructure deformation. Figure 6 is the state of the specimen when it is broken.



Fig. 6 - Failure modes of rock specimen

Through the observation of the failure state characteristics of argillaceous slate and other specimens in the test, the failure forms of argillaceous slate specimens can be simply divided into three types: Cracks are formed parallel to the axial direction when tensile failure occurs in the axial direction; comprehensive local shear and tensile failure modes simultaneously with lateral expansion phenomenon; the shear failure modes along the stratification plane. By analyzing the failure evolution process and failure modes of rock samples, the stress path in the course of rock force, as well as the influence of different loading factors on rock failure characteristics can be obtained.

Effect of water content on mechanical properties of argillaceous slate

The forming method of uniaxial compression test of argillaceous slate sample with different water content is the same as that of front uniaxial compression test specimen. The specimens of argillaceous slate are perpendicular to the stratification plane direction. A total of 7 specimens are made to study the influence of water content on the mechanical properties of argillaceous slate. The soaking time of argillaceous slate samples is respectively 0d, 1d, 2d, 4d, 8d, 16d and 32d. Table 4 is the results of uniaxial compression test of argillaceous slate after soaking. Figure 7 shows the relationship between the uniaxial compressive strength and the length of immersion time of argillaceous slate specimens.

Tab. 4 - Results of uniaxial compression test of argillaceous slate under different saturated time

Specimen number	Soaking time (d)	Water content (%)	elastic modulus (GPa)	compressive strength (MPa)	Poisson ratio
1	0	0.136	31.46	76.32	0.21
2	1	0.203	32.56	68.54	0.27
3	2	0.236	30.64	62.25	0.31
4	4	0.251	28.65	55.18	0.34
5	8	0.262	34.16	53.31	0.36
6	16	0.268	32.22	45.27	0.36
7	32	0.270	30.65	41.26	0.37

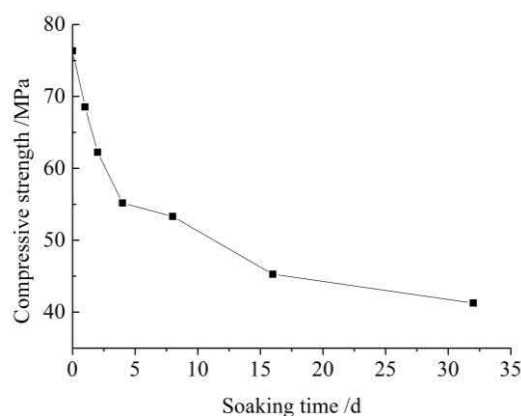


Fig. 7 - Relationship curves between strength and saturated time

Table 4 and Figure 7 shows: with the increase of argillaceous slate soaking time, the uniaxial compressive strength of argillaceous slate shows obvious decreasing trend; the decreasing rate is first fast and then slow; the variation law of modulus is discrete, while the Poisson ratio of argillaceous slate shows a trend of slow increase. In the natural water content state, the uniaxial

compressive strength of argillaceous slate is 76.32MPa, and the uniaxial compressive strength is minimum when submerged 32d, and the value is 41.26MPa. The longer the soaking time of argillaceous slate, the more the uniaxial compressive strength decreases. In the 5 days before immersion, the decreasing rate of uniaxial compressive strength is fastest. Subsequently, the decreasing rate of its uniaxial compressive strength gradually slow down, and it was basically stable after 16d. The analysis shows that when argillaceous slate after immersion, due to physical and chemistry of water on the argillaceous slate, argillaceous slate itself and its inner friction angle decreases, the cohesion of clay decrease, which lead to argillaceous slate strength will produce large losses. With the increasing of soaking time of argillaceous slate specimens, the Poisson ratio shows a trend of slow increasing. It reflects the increasing ability of its lateral expansion deformation.

CONCLUSIONS

By testing on the mineral composition of argillaceous slate analysis, water rational characteristic and uniaxial compression, the microstructure of argillaceous slate, stress-strain characteristic and failure characteristics in different stratification plane and soaking time were studied. The conclusions are as follows:

- (1) The argillaceous slate minerals used in the test are mainly sericite, followed by chlorite and quartz. Because the stability of sericite is poor, clay minerals are mixed between bedrock layers, it result obvious soft rock characteristics of argillaceous slate. Under the action of water, it is easy to expand, soften and even disintegrate. It has obvious water softening characteristics;
- (2) The strength characteristics of argillaceous slate show the anisotropy with angle of the specimen axial direction and the stratification plane. In the original test scheme, the angle of the specimen axial direction and the stratification plane only 0° , 45° and 90° , the test state is less. However, taking into account the continuity of rock mechanical properties, some basic conclusions can be obtained. It changes similar to the V type with the increase of angle. When the shale specimen is perpendicular to the rock stratification plane, its compressive strength is the largest, and the fracture mode of the specimen is shear failure or splitting failure; In the three set specimen, when the angle between the axial direction and the stratification plane of the argillaceous slate specimen is 45° , the compressive strength is the minimum, and the specimen appears shear failure along the stratification plane. When the argillaceous slate specimens are axially parallel to the stratification plane, the compressive strength is between that of the above-mentioned specimens, showing a shear failure.
- (3) Because of the physical and chemical effects of water on argillaceous slate, the mechanical properties and deformation characteristics of shale are obviously changed. With the increase of soaking time, the friction angle of clay rock itself and its clay layer decreases and cohesive force decreases, and then the compressive strength shows obvious decrease trend. When the soaking time is more than 15 days, the compressive strength reduction is almost 50%. With the increase of water content, the Poisson ratio of argillaceous slate samples shows a trend of slow increase, which indicates that the ability of lateral expansion deformation increases gradually under the influence of water.

ACKNOWLEDGEMENTS

The author is grateful for the support of the National Natural Science Foundation of China (51668017), the natural science foundation of Jiangxi (20152ACB20016) and the science and technology project of Jiangxi Provincial Department of Communications (2016D0038).

REFERENCES

- [1] Zuo Q J, Wu L, Li B, Lu Z L, Yuan Q, Chen F, et al. Creeping properties of water-rich argillaceous slate surrounding tunnel[J]. Chinese Journal of Rock Mechanics and Engineering, 2015(10):2047-2056, in Chinese.
- [2] Huang S L, Xu J S, Jing X L, Wu A J, et al. Study of layered rock mass composite model based on characteristics of structural plane and its application[J]. Chinese Journal of Rock Mechanics and Engineering, 2010(04):743-756, in Chinese.
- [3] Zhang Y J, Liu Y P, et al. Anisotropy of shear strength of layered rocks and determination of shear failure plane [J]. Rock and Soil Mechanics, 2001(03):254-257, in Chinese.
- [4] Yang C H, Mao H J, Wang X C, Li X H, Liu J W, et al. Study on variation of microstructure and mechanical properties of water- weakening slates [J]. Rock and Soil Mechanics, 2005(12):2090-2098, in Chinese.
- [5] Fall M. Simulation of a gas injection test in a layered argillaceous rock[C]// International Conference on Computational Geomechanics, Comgeo II. 2011.
- [6] Nguyen T S, Le A D. Development of a constitutive model for a bedded argillaceous rock from triaxial and true triaxial tests1[J]. Canadian Geotechnical Journal, 2015, 52(8):1072-1086.
- [7] Gao C Y, Xu J, LI Z H, Deng J H, et al. Experimental study of anisotropic ally mechanical characteristics of sandy slate in Xuefeng mountain tunnel [J]. Rock and Soil Mechanics.2011 (05):1360-1364, in Chinese.
- [8] Wang M, Zhu Z M, Feng R Q, et al. Experimental study on failure behaviors of cracked rocks around tunnels under true triaxial unloading [J]. Journal of China Coal Society. 2015(02):278-285, in Chinese.
- [9] Wang L, Liu Z Y, et al. Triaxial Compression Test of weakly cemented mudstone [J]. Journal of Yangtze River Scientific Research Institute.2016 (08):86-90+95, in Chinese.
- [10] Lisjak A, Garitte B, Grasselli G, et al. The excavation of a circular tunnel in a bedded argillaceous rock (Opalinus Clay): Short-term rock mass response and FDEM numerical analysis [J]. Tunnelling and Underground Space Technology incorporating Trenchless Technology Research, 2015, 45(45):227-248.
- [11] Tan X, Fu H L, Chen C, Zhao M H, Liu Y S, et al. Numerical simulation analysis of tunnel in rock-mass[J]. Journal of Railway Science and Engineering.2016 (06):1108-1113, in Chinese.
- [12] Su Z D, Luo J J, et al. Experimental study and prediction on large section tunnel construction deformation of surrounding rock in soft ground [J]. Chinese Journal of Rock Mechanics and Engineering.2016 (S2):4029-4039, in Chinese.
- [13] Yangtze River Water Resources Commission, Yangtze Academy of Sciences. Water conservancy and hydropower engineering rock test gauge (JGJ SL264-2001) [S]. Beijing: China Water Conservancy and Hydropower Press, 2001, in Chinese.

HOW MUCH DOES A MINUTE OF COMMUTING TIME COST?

AN EXAMINATION OF PROPERTY PRICES IN RELATION TO DISTANCE TO THE CITY CENTER IN PRAGUE, CZECH REPUBLIC

Martin Lukavec¹, Božena Kadeřábková²

1. *University of Economics, Department of Regional Studies, Prague, W. Churchill Sq. 4, Czech Republic; xlukm902@vse.cz*
2. *Czech Technical University, Faculty of Civil Engineering, Prague, Thákurova 7, Czech republic; kaderabb@fsv.cvut.cz*

ABSTRACT

This paper sets out to explore the strength of the relationship between the proximity of a property to the city center and its price. Buyers are willing to pay extra for apartments or houses closer to the city center, but the extent of this willingness remains largely unexplored. Our research question is: How much does a minute of commuting time influence the price of an apartment in Prague? In other words, with every minute of commuting time, how much more is paid for a house or an apartment closer to the central business district (CBD)?

Our analysis has found that on average, every minute of commuting time closer to the city center corresponds to an additional cost of CZK 43,390.45 for an average sized apartment in Prague. A regression analysis is graphically plotted in the Chart 1. We have also found that this relationship changes according to distance from the city center. For a commuting time of 1-20 minutes to the city center, the price increase is the highest: CZK 259,466.18 per minute. However, this figure is only CZK 55,809.01 for the interval of 21-40 minutes, and CZK 33,924.29 per minute for the interval of 41-55 minutes.

KEYWORDS

Property Prices, Proximity to the CBD, Cities, Prague

INTRODUCTION

Among the reasons that people and companies cluster together to form communities, towns and cities, economists most often mention economies of scale and agglomeration economies (Brueckner, 2011). The specialization of work and the scale of production result in more efficient and competitive production, and therefore lower prices. An automobile production company, for example, manufacturing 10 million cars per year is more efficient than a smaller company that produces only a few hundred. In fact, a town's existence can be dependent on a small number of large companies located in them, or even on the existence of only one large company. A good example of this is Wolfsburg, Germany, hometown of Volkswagen.

Agglomeration economies are a more elusive concept and are related to the economies of scale in many respects. They derive their added value from companies in close proximity to each other. They are thus able to create wider range of production chains, and enjoy a larger pool of workers able to highly specialize (and be secure in their future employment prospects). A small town may be able to host a hospital with a few doctors, but their field of specialization will be significantly restricted by the size of the population. On other hand, doctors in large cities can be highly specialized, you might find intestinal tract oncologists or brain surgeons there. Higher specialization results in a higher added value for these professions, a byproduct of being located in a large city (Brueckner, 2011). Technological clusters are another example of agglomeration economies – a pool of workers and companies are able to work more effectively at a larger scale. Put simply, frontier technological advancements are implemented faster when people and companies cluster in close proximity to each other.

These observations led to the development of the Urban Model, originally developed by William Alonso in 1964. The Urban Model describes the relationship between the distance from the city center (or central business district – CBD), and the price of a property (or “land rent,” in the model’s terminology). The model explains decreasing property prices with increasing distance from the city CBD. Properties in city centers are, predictably, more expensive than their counterparts in city suburbs (Alonso, 1964).

This relationship changes over time, as cities grow and/or become more or less congested. Larger cities reap more of the benefits of the economies of scale and agglomeration economies, and it can be observed that central locations in today’s megacities are comparatively more expensive than in cities of a smaller size. Central London, Manhattan and the center of Tokyo regularly lead in high property prices (Cushman & Wakefield, 2016). Moreover, higher differences in property prices between the CBD and the suburbs can be observed in cities with insufficient infrastructure and long commuting times.

New technology has been envisioned to change this relationship between distance and property price. Extensive literature has been written about how ever cheaper transport and information flowing freely across borders will reshape the economy. An influential book by Frances Cairncross argues that proximity to other people, the main reason for the existence of highly concentrated cities, will lose its added value. The book envisions a much less concentrated economy where people are capable of living in a location of their choosing, working distantly, and communicating with ease with their colleagues around the world (Cairncross, 1997).

To a certain degree, this future has arrived. A new class of digital nomads has formed largely around young entrepreneurs and office workers, who may work for companies based in London or San Francisco, yet are personally based in Thailand or Bali (or change locations a few times a year according to their preference) (The Economist, 2008).

However, the phenomenon of being located in proximity to large offices has not yet come to an end. On the contrary, it seems to matter more than ever. Production has spread its supply chains around the world, but the office environment has not (Glaeser, 2011). Many international companies have established numerous local offices in many countries, but paradoxically, this was done to serve the local markets closely. Therefore, even in this case location still plays a significant role. It follows, then, that people are willing to pay ever higher price to be closer to each other (Avent, 2016). Agglomeration economies seem to play an ever-increasing role in the formation of the cities.

Aim of this paper is to explore the strength of the relationship between proximity and price. For all of the reasons mentioned above, people are willing to pay extra money for apartments or houses closer to the city center, but the extent of this willingness is often unexplored. The research question at hand is: How much does a minute of commuting time influence the price of an apartment in Prague? In other words, with every minute of commuting time, how much more is paid for a house or an apartment closer to the central business district (CBD)? Similar research was conducted by Carl Bialik (2016) into the case of New York City, but based solely on asking prices and without the theoretical underpinnings of the Urban Model. This paper conducts an analysis of the relationship between distance and property price with a wider theoretical foundation and with a data set of property prices adjusted to real transaction level.

METHODOLOGY

For this analysis, a data set of apartment asking prices has been collected. A data mining tool ParseHub was used to collect the asking prices from the biggest Czech real estate listing website, Sreality.cz. During a data mining session on 13th November 2016, 2542 property prices were collected, together with the size of the property and location (street name, land registry districts, city district), and number of rooms. After removing duplicate entries and those with missing information, the data set included 2038 unique properties for sale at the time (Sreality.cz, 2016).

This data set is sufficiently large and the properties listed are distributed across Prague land registry areas (95 out of 112 land registry areas included at least one listing), so an average property asking prices per square meter in each district has been calculated. Because asking prices deviate from real transaction costs, we then corrected them using average transaction costs, available at the city district level (Deloitte, 2016). As real transaction costs are published only at the city district level (Prague 1-10), the option of using only available transaction prices was not possible, as the analysis would be influenced by the districts' excessive size.

Instead, listed asking prices available at the land registry area were adjusted according to the real transaction prices. This combination of two resources of property prices gives us a data set reasonably close to the real transaction prices while maintaining the variety present among city neighborhoods.

The CBD was set at Můstek metro station, a commuting hub with the highest number of commuters in Prague (DPP, 2008). Commuting times were collected from Google Maps between 8 and 9am on Monday, 14th of November 2016, purposely chosen at the height of the commuting rush.

The relation between property prices and commuting time is examined based on the Alonso Urban model, which states that:

$$r = y - td, \quad (1)$$

where r represents rent form land, y signifies income, t the cost of traveling per unit of distance, and d distance. For simplicity, the urban model assumes all city inhabitants have the same income y , so the rent decreases with increasing distance from the CBD (Alonso, 1964).

I here conduct a similar analysis, but instead of rent r , I am going to find the relationship between property price p and distance, for our purposes measured in minutes of commuting time.

This examination is based on a regression analysis. In the first step, we found a simple linear regression in the following format:

$$p = a - bt, \quad (2)$$

where p is the property price per meter square, t is commuting time in minutes, a represents the price at commuting time zero, and b represents the slope of the regression and our research objective – the property price per square meter, increased per minute of commuting time. We can state that:

$$p_t = bs_{average} \quad (3)$$

By multiplying the slope b by the average size of an apartment in Prague at the time of the analysis $s_{average}$, we receive an average cost of property price increase equivalent to one minute closer to the CBD, p_t .

While the linear regression offers simple and telling information for our problem, it is not without drawbacks. Our rigorous analysis of the residuals has pointed to systematic errors these residuals display when simple linear regression is applied. This is a serious flaw in the analysis. For this reason, we have conducted a regression analysis of higher orders and along other mathematical functions, in order to find out that the systematic error disappears from the analysis when a logarithmic regression is used in combination with other so far excluded factors, such as existence of large part (of a minimum size of 80ha), which is included linearly as a dummy variable. This confirmed that the logarithmic regression analysis is the most suitable for our problem at hand, even though it lacks the simplicity of a simple linear regression.

We can adjust our regression formula to:

$$p = a - b \log(t) + c \text{ dummy (green)}, \quad (4)$$

where p is the property price per meter square, t is the commuting time in minutes, dummy (green) is a dummy variable representing a proximity of a large park, a represents the price at commuting time zero, b is the constant representing the slope of the logarithmic regression and c is the constant representing the slope associated with the proximity of a large park.

Our research objective – to determine the relationship between property price and commuting time – is more complicated when using a logarithmic regression, as the slope changes with the distance from the CBD.

ANALYSIS

The dataset of average asking property prices per meter square at the land registry level, real transaction prices at the city district level, and property prices per land registry level adjusted for the difference between asking and real prices, are included in Appendix 1. The same appendix also includes commuting times from each land registry area to the CDB.

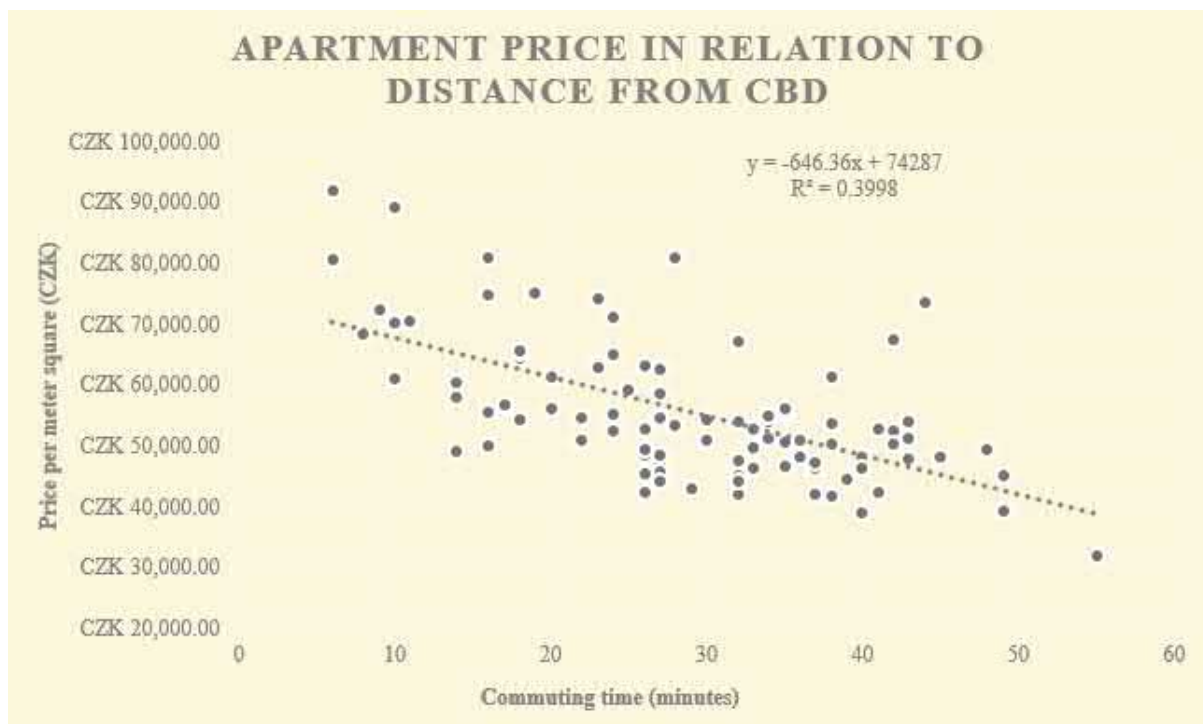
A simple linear regression analysis was conducted after removing 4 outliers with a standardized residual higher than 3, as per Appendix 2. The result is the following relationship:

$$p = 74287 - 646.36t$$

$$R^2 = 0.3998$$

This relationship is plotted in the Figure 1.

Fig. 1 – Linear Regression chart



The slope in this equation, $-646,36t$ is equivalent to the price per square meter decrease associated with one extra minute of commuting time to the CBD. Substituting in the formula (3), t with an average flat size in Prague of 67.13 square meters (Cenová Mapa, 2016), we find:

$$p_t = - CZK 646.36 * 67.12 = - CZK 43,390.45$$

In conclusion, one extra minute of commuting time saves CZK 43,390.45 of the price of an average apartment in Prague.

As stated above, linear regression has a number of drawbacks. The high systematic error in the residuals resulted in the need to remove of 4 outliers, especially in the areas close to the CBD. This is apparent from the coefficient a , which in this analysis is only CZK 74,287, and does not truly represent the mean property price per meter square in the CBD. The systematic error in regression residuals has also resulted in a comparatively smaller value of R^2 .

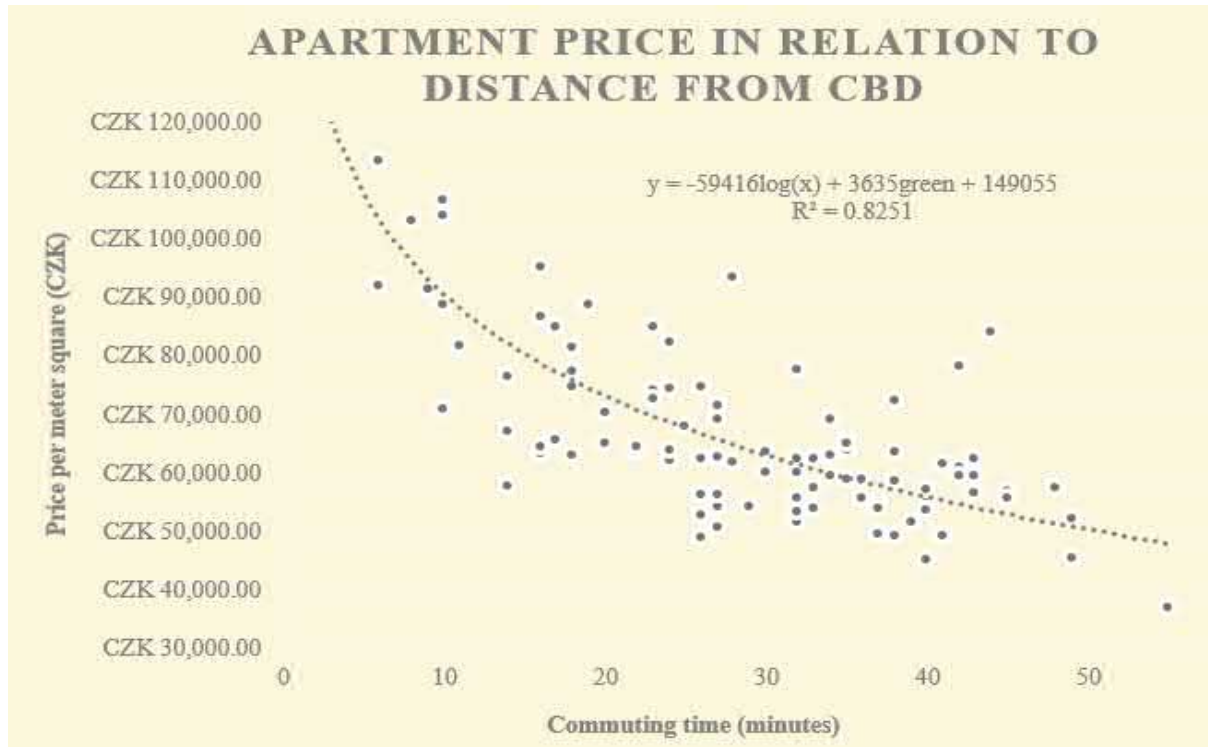
A logarithmic regression with a linear inclusion of a proximity of a larger park (minimum size of 80ha) was conducted, as per Appendix 3, and I have found the following relationship:

$$y = -59416\log(t) + 3635green + 149055$$

$$R^2 = 0.8251$$

This relationship is graphically illustrated in the Figure 2. The I-shaped curve of the plotted relationship signifies a very steep slope in the proximity of the CBD, which is gentler with increasing distance from the city center.

Fig. 2 – Logarithmic regression chart



To simplify our interpretation of this relationship, we can split the distance between the city districts and the CBD according to commuting time into 3 intervals (1-20, 21-40 and 41-55 minutes from the CBD, with 55 minutes being the longest commuting time for any of the land registry areas). We can then calculate linear increases in price.

Interval 1-20 minutes of commuting time: slope CZK 3,865.13

Interval 21-40 minutes: slope CZK 831.36

Interval 41-55 minutes: slope CZK 505.35

Substituting in formula (3), we find that with an average flat size in Prague of 67.13 square meters (Cenová Mapa, 2016).

Interval 1-20 minutes of commuting time: CZK 259,466.18 per minute of commuting time

Interval 21-40 minutes: CZK 55,809.01 per minute of commuting time

Interval 41-55 minutes: CZK 33,924.29 per minute of commuting time

The proximity of a large park increases the price per meter square by CZK 3,635.26. This increase translated to CZK 244,034.71 for an average apartment in Prague.

CONCLUSION

Our analysis has found that on average, every minute of commuting time closer to the city center corresponds with an additional cost of CZK 43,390.45 for an average-sized apartment in Prague. A regression analysis is graphically plotted in the Chart 1. We have also found that this relationship changes with the distance from the city center. For a commuting time of 1-20 minutes to the city center, the price increase is the highest: CZK 259,466.18 per minute. However, this cost drops to CZK 55,809.01 for the interval of 21-40 minutes, and CZK 33,924.29 per minute for the interval of 41-55 minutes from the central business district.

The proximity of a large park increases the price per meter square by CZK 3,635.26. This increase translates to CZK 244,034.71 for an average apartment in Prague.

REFERENCES

- [1] BRUECKNER, Jan K. *Lectures on urban economics*. Cambridge: MIT Press, 2011.
- [2] ALONSO, William. *Location and Land Use*. Cambridge: Harvard University Press, 1964.
<https://doi.org/10.4159/harvard.9780674730854>
- [3] CUSHMAN & WAKEFIELD. Main Streets across the world 2016/2017. *Cushman & Wakefield* [online]. 2016 [cit. 2016-11-20]. Dostupné z: <http://www.cushmanwakefield.com/en/research-and-insight/2016/main-streets-across-the-world-2016-2017/>
- [4] CAIRNCROSS, Frances. *The death of distance: how the communications revolution will change our lives*. Boston, Massachusetts: Harvard Business School Press, 1997.
- [5] THE ECONOMIST. Nomads at last. *The Economist* [online]. 2008 [cit. 2016-11-20]. Dostupné z: <http://www.economist.com/node/10950394>
- [6] GLAESER, Edward. *Triumph of the city: how our greatest invention makes us richer, smarter, greener, healthier, and happier*. New York, New York: Penguin Books, 2011. ISBN 978-014-3120-544.
- [7] AVENT, Ryan. *The wealth of humans: work, power, and status in the twenty-first century*. New York: St. Martin's Press, 2016.
- [8] BIALIK, Carl. New Yorkers Will Pay \$56 A Month To Trim A Minute Off Their Commute. *FiveThirtyEight* [online]. [cit. 2016-11-20]. Dostupné z: <http://fivethirtyeight.com/features/new-yorkers-will-pay-56-a-month-to-trim-a-minute-off-their-commute/>
- [9] SREALITY.CZ. Byty na prodej Praha. *Sreality.cz* [online]. 2016 [cit. 2016-11-13]. Dostupné z: <https://www.sreality.cz/hledani/prodej/byty/praha>
- [10] DELOITTE. Deloitte Real Index Q2 2016: Skutečné ceny prodaných bytů v ČR. *Deloitte* [online]. 2016 [cit. 2016-11-20]. Dostupné z: https://www2.deloitte.com/content/dam/Deloitte/cz/Documents/real-estate/Deloitte_Real_Index_Q2_2016_CZ.pdf
- [11] DPP. Pražské metro v den přepravního průzkumu přepravilo 1 272 143 cestujících. *Dopravní podnik hlavního města Prahy* [online]. 2015 [cit. 2016-11-20]. Dostupné z: <http://www.dpp.cz/prazske-metro-v-den-prepravnio-pruzkumu-prepravilo-1-272-143-cestujicich/>
- [12] CENOVÁ MAPA. Byty v září byly letos čtvrté nejdražší. Na trh jich přibylo přes 550. *Transaction price map* [online]. 2016 [cit. 2016-11-21]. Dostupné z: https://www.cenovamapa.org/Default.aspx?menu=Blog_Article&culture=en&BlogPostID=8

APPENDICES

Appendix 1 – Dataset

City district (land registry)	Average of Price per m ²	Deloitte real transaction index (q2 2016)	Distance to CBD	Distance Log	Greenery	Price adjusted
Praha 1	CZK 131,868.96	CZK 107,300.00				CZK 107,300.00
Josefov	CZK 185,272.13		3	0.477121	0	CZK 150,753.44
Malá Strana	CZK 141,291.69		14	1.146128	1	CZK 114,967.15
Nové Město	CZK 113,167.57		6	0.778151	0	CZK 92,082.93
Staré Město	CZK 166,042.84		1	0	0	CZK 135,106.83
Praha 10	CZK 65,992.91	CZK 56,600.00				CZK 56,600.00
Dolní Měcholupy	CZK 54,008.01		33	1.518514	0	CZK 46,320.94
Dubeč	CZK 55,924.80		40	1.60206	1	CZK 47,964.90
Horní Měcholupy	CZK 58,729.61		38	1.579784	1	CZK 50,370.50
Hostivař	CZK 62,918.18		34	1.531479	1	CZK 53,962.90
Kolovraty	CZK 37,107.44		55	1.740363	0	CZK 31,825.86
Malešice	CZK 56,493.55		26	1.414973	0	CZK 48,452.71
Michle	CZK 52,885.17		26	1.414973	0	CZK 45,357.91
Petrovice	CZK 49,238.98		41	1.612784	1	CZK 42,230.69
Pitkovice	CZK 61,039.40		42	1.623249	1	CZK 52,351.53
Štěrboholy	CZK 61,639.34		41	1.612784	1	CZK 52,866.09
Strašnice	CZK 63,703.16		22	1.342423	0	CZK 54,636.16
Uhřetíněves	CZK 59,599.77		43	1.633468	1	CZK 51,116.81
Vinohrady	CZK 104,068.66		10	1	0	CZK 89,256.35
Vršovice	CZK 74,091.99		23	1.361728	0	CZK 63,546.32
Záběhlice	CZK 63,466.15		30	1.477121	1	CZK 54,432.88
Praha 2	CZK 104,614.54	CZK 69,300.00				CZK 69,300.00
Nové Město	CZK 103,159.91		8	0.90309	0	CZK 68,336.40
Nusle	CZK 71,305.56		27	1.431364	0	CZK 47,235.07
Vinohrady	CZK 106,653.26		10	1	0	CZK 70,650.51
Vyšehrad	CZK 85,000.00		17	1.230449	0	CZK 56,306.70
Praha 3	CZK 81,338.40	CZK 64,300.00				CZK 64,300.00
Strašnice	CZK 64,382.80		22	1.342423	0	CZK 50,896.18
Vinohrady	CZK 88,752.38		10	1	0	CZK 70,160.93
Vysočany	CZK 63,220.79		16	1.20412	0	CZK 49,977.59
Žižkov	CZK 81,316.08		18	1.255273	0	CZK 64,282.36
		Deloitte real transaction index (q2 2016)				
City district (land registry)	Average of Price per m ²	Deloitte real transaction index (q2 2016)	Distance to CBD	Distance Log	Greenery	Price adjusted
Praha 4	CZK 63,766.16	CZK 53,900.00				CZK 53,900.00
Braník	CZK 74,668.33		26	1.414973	0	CZK 63,115.34

Chodov	CZK 54,819.80		37	1.568202	1	CZK 46,337.86
Cholupice	CZK 56,567.16		43	1.633468	1	CZK 47,814.86
Háje	CZK 54,236.14		27	1.431364	1	CZK 45,844.50
Hodkovičky	CZK 65,489.59		35	1.544068	0	CZK 55,356.77
Kamýk	CZK 57,133.93		40	1.60206	0	CZK 48,293.93
Komořany	CZK 65,674.16		35	1.544068	1	CZK 55,512.78
Krč	CZK 62,087.37		24	1.380211	0	CZK 52,480.95
Kunratice	CZK 63,693.21		38	1.579784	1	CZK 53,838.33
Lhotka	CZK 49,409.89		38	1.579784	0	CZK 41,764.99
Libuš	CZK 72,411.50		38	1.579784	1	CZK 61,207.70
Michle	CZK 62,515.12		26	1.414973	0	CZK 52,842.53
Modřany	CZK 62,492.11		33	1.518514	1	CZK 52,823.07
Nusle	CZK 69,253.74		27	1.431364	0	CZK 58,538.52
Písnice	CZK 59,601.97		42	1.623249	1	CZK 50,380.11
Podolí	CZK 88,843.09		19	1.278754	0	CZK 75,096.92
Šeberov	CZK 49,598.43		37	1.568202	0	CZK 41,924.35
ÚjezduPrůhonic	CZK 56,870.03		45	1.653213	0	CZK 48,070.87
Záběhlice	CZK 60,171.06		30	1.477121	0	CZK 50,861.15
Praha 5	CZK 73,648.71	CZK 64,400.00				CZK 64,400.00
Břevnov	CZK 85,018.83		23	1.361728	1	CZK 74,342.28
Hlubočepy	CZK 67,872.32		25	1.39794	1	CZK 59,349.00
Jinonice	CZK 70,292.26		20	1.30103	1	CZK 61,465.05
Košíře	CZK 74,368.64		24	1.380211	1	CZK 65,029.52
MaláStrana	CZK 138,775.61		14	1.146128	1	CZK 121,348.34
Motol	CZK 50,633.21		27	1.431364	1	CZK 44,274.76
Radlice	CZK 74,714.21		18	1.255273	1	CZK 65,331.69
Radotín	CZK 53,944.16		37	1.568202	1	CZK 47,169.92
Řeporyje	CZK 51,489.82		32	1.50515	1	CZK 45,023.79
Slivenec	CZK 84,016.43		44	1.643453	1	CZK 73,465.76
Smíchov	CZK 92,079.13		6	0.778151	0	CZK 80,515.95
Stodůlky	CZK 62,622.27		27	1.431364	1	CZK 54,758.25
VelkáChuchle	CZK 71,493.12		27	1.431364	1	CZK 62,515.10
Zbraslav	CZK 56,435.50		26	1.414973	1	CZK 49,348.40
Zličín	CZK 62,907.23		34	1.531479	0	CZK 55,007.42

City district (land registry)	Average of Price per m ²	Deloitte real transaction index (q2 2016)	Distance to CBD	Distance Log	Greenery	Price adjusted
Praha 6	CZK 74,379.23	CZK 64,300.00				CZK 64,300.00
Břevnov	CZK 72,739.11		23	1.361728	1	CZK 62,882.13
Bubeneč	CZK 86,704.77		16	1.20412	1	CZK 74,955.28
Dejvice	CZK 81,656.46		11	1.041393	1	CZK 70,591.07
Hradčany	CZK 70,776.12		10	1	0	CZK 61,185.15
Liboc	CZK 93,500.15		28	1.447158	1	CZK 80,829.82
PředníKopanina	CZK 57,600.97		33	1.518514	1	CZK 49,795.38
Řepy	CZK 53,694.38		40	1.60206	0	CZK 46,418.18
Ruzyně	CZK 61,922.65		28	1.447158	1	CZK 53,531.42
Střešovice	CZK 82,201.39		24	1.380211	0	CZK 71,062.17
Suchdol	CZK 56,209.44		27	1.431364	1	CZK 48,592.42
Veleslavín	CZK 65,670.20		17	1.230449	1	CZK 56,771.14
Vokovice	CZK 65,038.91		20	1.30103	1	CZK 56,225.39
Praha 7	CZK 80,420.02	CZK 68,300.00				CZK 68,300.00
Bubeneč	CZK 95,119.53		16	1.20412	1	CZK 80,784.17
Holešovice	CZK 77,367.50		18	1.255273	0	CZK 65,707.52
Libeň	CZK 57,777.78		14	1.146128	0	CZK 49,070.15
Praha 8	CZK 74,179.98	CZK 58,700.00				CZK 58,700.00
Bohnice	CZK 58,970.70		35	1.544068	1	CZK 46,664.62
Čimice	CZK 53,269.85		32	1.50515	1	CZK 42,153.43
Ďáblice	CZK 63,900.72		35	1.544068	1	CZK 50,565.83
DolníChabry	CZK 69,209.19		34	1.531479	1	CZK 54,766.53
Karlín	CZK 91,483.95		9	0.954243	0	CZK 72,392.96
Kobylisy	CZK 54,299.67		29	1.462398	1	CZK 42,968.34
Libeň	CZK 76,425.42		14	1.146128	0	CZK 60,476.86
Střížkov	CZK 55,842.70		32	1.50515	0	CZK 44,189.37
Troja	CZK 60,027.55		32	1.50515	1	CZK 47,500.92

City district (land registry)	Average of Price per m ²	Deloitte real transaction index (q2 2016)	Distance to CBD	Distance Log	Greenery	Price adjusted
Praha 9	CZK 60,765.89	CZK 52,500.00				CZK 52,500.00
Běchovice	CZK 62,519.69		43	1.633468	1	CZK 54,015.23
Čakovice	CZK 55,707.54		45	1.653213	0	CZK 48,129.73
ČernýMost	CZK 48,879.22		26	1.414973	0	CZK 42,230.25
DolníPočernice	CZK 78,246.38		42	1.623249	1	CZK 67,602.65
Hloubětín	CZK 62,904.84		18	1.255273	0	CZK 54,348.00
HorníPočernice	CZK 59,433.31		34	1.531479	0	CZK 51,348.69
Hrdlořezy	CZK 77,718.09		32	1.50515	0	CZK 67,146.22
Kbely	CZK 51,645.59		39	1.591065	0	CZK 44,620.32
Klánovice	CZK 45,431.47		49	1.690196	1	CZK 39,251.50
Kyje	CZK 65,070.15		35	1.544068	0	CZK 56,218.76
Letňany	CZK 58,932.74		36	1.556303	0	CZK 50,916.21
Libeň	CZK 67,237.80		14	1.146128	0	CZK 58,091.55
Miškovice	CZK 57,351.42		48	1.681241	0	CZK 49,550.00
Prosek	CZK 63,859.95		24	1.380211	0	CZK 55,173.18
Satalice	CZK 55,789.47		36	1.556303	0	CZK 48,200.52
Střížkov	CZK 62,556.95		32	1.50515	0	CZK 54,047.42
ÚjezdnadLesy	CZK 52,292.40		49	1.690196	1	CZK 45,179.14
Vinoř	CZK 45,237.17		40	1.60206	0	CZK 39,083.63
Vysočany	CZK 64,396.51		16	1.20412	0	CZK 55,636.75



Appendix 2 – linear regression

<i>Regression Statistics</i>	
Multiple R	0.632292955
R Square	0.39979438
Adjusted R Square	0.393669833
Standard Error	8761.535175
Observations	100

ANOVA

	<i>df</i>	<i>SS</i>	<i>MS</i>	<i>F</i>	<i>Significance F</i>
Regression	1	5010985216	5010985216	65.2773783	1.71675E-12
Residual	98	7522920864	76764498.61		
Total	99	12533906080			

	<i>Coefficients</i>	<i>Standard Error</i>	<i>t Stat</i>	<i>P-value</i>	<i>Lower 95%</i>	<i>Upper 95%</i>	<i>Lower 95.0%</i>	<i>Upper 95.0%</i>
Intercept	74286.62731	2467.240975	30.10919001	2.51321E-51	69390.46789	79182.78673	69390.46789	79182.78673
Distance to CBD	-646.364576	80.00114358	-8.079441707	1.71675E-12	-805.1242418	-487.6049103	-805.1242418	-487.6049103



Appendix 3 – Logarithmic regression with a dummy variable

<i>Regression Statistics</i>	
Multiple R	0.825182264
R Square	0.680925769
Adjusted R Square	0.67441405
Standard Error	9930.802848
Observations	101

ANOVA					
	<i>df</i>	<i>SS</i>	<i>MS</i>	<i>F</i>	<i>Significance F</i>
Regression	2	20625421579	10312710790	104.5692801	4.90563E-25
Residual	98	9664842831	98620845.21		
Total	100	30290264410			

	<i>Coefficients</i>	<i>Standard Error</i>	<i>t Stat</i>	<i>P-value</i>	<i>Lower 95%</i>	<i>Upper 95%</i>	<i>Lower 95.0%</i>	<i>Upper 95.0%</i>
Intercept	149054.7708	5739.22573	25.97123337	9.93033E-46	137665.4642	160444.0775	137665.4642	160444.0775
Distance Log	-59416.46516	4178.618097	-14.21916619	1.46892E-25	-67708.79678	-51124.13355	-67708.79678	-51124.13355
Greenery	3635.255696	2074.375381	1.752457983	0.082822719	-481.2747368	7751.786129	-481.2747368	7751.786129